Karlsruhe Institute of Technology

Characterization and Optimization of the KATRIN Tritium Source

Zur Erlangung des akademischen Grades eines
Doktors der Naturwissenschaften
von der KIT-Fakultät für Physik
des Karlsruher Instituts für Technologie
genehmigte
Dissertation
von

M. Sc. Alexander Curt Marsteller

aus Bühl

Referent:	Prof. Dr. G. Drexlin
	Institut für Experimentelle Teilchenphysik, KIT
Korreferent:	Prof. Dr. B. Holzapfel
	Institut für Technische Physik, KIT

Tag der mündlichen Prüfung: 04.12.2020

Declaration of authorship Herewith I affirm that I wrote the current thesis on my own and without the usage of any other sources or tools than the cited ones and that this thesis has not been handed neither in this nor in equal form at any other official commission.

Erklärung der Selbstständigkeit Hiermit versichere ich, die vorliegende Arbeit selbstständig angefertigt zu haben und keine Hilfsmittel jenseits der kenntlich gemachten verwendet zu haben. Weiterhin habe ich weder diese noch eine äquivalente Version dieser Arbeit bei einer anderen Prüfungskommission vorgelegt.

Karlsruhe, December 14, 2020

. . . . . .
Alexander Marsteller

Abstract

The Karlsruhe Tritium Neutrino (KATRIN) experiment aims to measure the effective electron anti-neutrino mass via high-precision spectroscopy of the energy spectrum of β-decay electrons of tritium near the 18.6 keV endpoint with an unprecedented accuracy. The specifications of the KATRIN experiment result in an experimental setup with a target discovery potential of $5\,\sigma$ for a neutrino mass of $350\,\mathrm{meV}/c^2$ and the expected capability to push the upper limit on the neutrino mass down to a target of $200\,\mathrm{meV}/c^2$ (90 % C. L.) if no neutrino mass signal is detected. To achieve this unprecedented sensitivity, both statistical and systematical uncertainties have to be stringently minimized. The reduction of statistical uncertainties requires a total measurement duration of 3 years with a windowless gaseous tritium source (WGTS) capable of producing 10^{11} β-electrons per second. To keep the systematical uncertainties at the level required to reach the target sensitivity, the activity of this β-electron source needs to be stable at the level of 0.1 %. This stability is influenced by several factors such as the purity and pressure of the tritium gas, as well as the temperature of the WGTS beam tube enclosing the gaseous tritium. Therefore, in order to minimize systematical uncertainties, a very stable injection of tritium gas into the beam tube is necessary. This is achieved by the tritium loop system. The main focus of this thesis is the optimization of stabilized injection of tritium gas into the WGTS, the in-depth characterization and modeling of the isotopic gas composition inside of the WGTS, as well as the measurement and continuous monitoring methods of the WGTS column density.

A suite of extensive commissioning measurements of the stabilized injection system has revealed that the stability at the 0.1 %-level required by the KATRIN experiment was surpassed by one order of magnitude. A further opportunity to improve the system was found in the lacking digital resolution of the pressure readout, which limited the stabilization. In order to minimize the impact of the pressure stabilization on the neutrino mass measurement and to constrain the systematic uncertainty budget, the pressure readout of the injection pressure stabilization was replaced by a high resolution data acquisition (DAQ) system. As a result, the pressure stability could be increased by another factor of about 5, leading to a stability of $<0.002\,\%$. This value can be maintained on the time scale of a typical measurement campaign of the KATRIN experiment of about 60 d.

Similarly, the residual gas analyzer (RGA) and laser Raman (LARA) spectroscopy system used for gas composition measurements were fully characterized with respect to their consistency. In particular, the question whether LARA measurements yield representative values for the gas composition inside the WGTS beam tube was investigated. A time shift between both systems due to finite travel times of gas batches through the tritium loop system was measured with different methods, calculated theoretically, and found to not impact the neutrino mass measurements negatively. As the gas composition measurements cannot be obtained for all tritium loop op-

eration modes, and in order to gain a deeper understanding of isotopic exchange effects in the tritium loop system, a simulation model was developed. After successful verification of the model predictions using LARA data gained from operating the tritium loop for neutrino mass measurements, the model was transferred to a different operation mode which is used to investigate systematic effects. This modeling process not only allows an inference of the gas composition without direct continuous measurement, it also gave new insights to the dynamics of the involved isotopic exchange effects and their dependence on operating parameters of the tritium loop system.

Transitioning from the stabilities of subsystems to that of the WGTS column density, a continuous monitoring scheme with periodic calibrations for the column density was developed. Using this monitoring scheme, the impact of all relevant external influences on the column density was investigated. These influences are changes in temperature of the WGTS cryostat, changes in the gas composition, as well as changes of the injection geometry due to deposition of radiochemically produced impurities. Finally, the achieved stability of the column density in different measurement modes of the tritium loop system was determined. This showed that, even under the influence of all external effects, the column density stability requirement of 0.1 % can be achieved more than 99 % of the time.

Summarizing the results presented in this thesis, it was shown that the stability of the tritium column density of the WGTS meets the requirement of 0.1 %. A variety of column density monitoring methods were implemented and have been used to derive the best current upper limit on the neutrino mass from direct measurement of $1.1\,\mathrm{eV}/c^2$. This outstanding performance in both stability and monitoring can be achieved reliably and reproducibly. This is necessary for the upcoming measurement campaigns, which are needed by the KATRIN experiment in order to meet its scientific goal of a $200\,\mathrm{meV}/c^2$ sensitivity on the neutrino mass.

Contents

1. Introduction

Neutrinos are among the most elusive particles of the Standard Model of particle of physics. They are however also the most abundant massive particles in the universe [LLS14], giving them a large potential impact on the formation of large-scale structures in the early universe [Pee73]. The fact that neutrinos do possess a non-zero rest mass, despite the assumptions of the Standard Model predicting otherwise, is interesting as a possible pathway to physics beyond the Standard Model.

The existence of a non-zero neutrino mass was discovered in neutrino flavor oscillation experiments [Fuk+98; Ahm+01], which require different mass eigenstates for flavor oscillation to occur [Pon58; MNS62; Pon68]. These oscillation experiments are however conceptually incapable of providing an absolute mass measurement. They are only sensitive to the difference between squared neutrino masses, only allowing them to put a lower bound of $50\,\mathrm{meV}/c^2$ on the biggest neutrino mass [Est+19]. In contrast, a wide variety of upper limits on the neutrino mass exist, which are based on different measurement principles [CH19; LL02; AR87]. Among these principles, the precise spectroscopy of β-decay kinematics only relies on conservation of energy and momentum, making it the conceptually most model-independent method. Experiments using β-decay spectroscopy have been performed since the 1950s [LM52; HAG53; Lub+80; Rob+91; Kra+05; Ase+11], steadily improving their sensitivity, which culminated in an upper limit of $2.05\,\mathrm{eV}/c^2$ (95 % C.L.) derived by the Mainz and Troitsk experiments in the 2000s [Ase+11].

The Karlsruhe Tritium Neutrino (KATRIN)[1]experiment [KAT05], as the successor to these experiments, aims to measure the effective electron anti-neutrino mass via spectroscopy of β-decay electrons of tritium with an unprecedented accuracy. KATRIN measures the shape of the β-decay energy spectrum of tritium near the kinematic endpoint at 18.6 keV. The specifications of KATRIN result in an experimental setup with a target discovery potential of $5\,\sigma$ for a neutrino mass of $350\,\mathrm{meV}/c^2$ which is equivalent to an upper limit on the neutrino mass down of $200\,\mathrm{meV}/c^2$ (90 % C. L.) if no neutrino mass is detected [KAT05]. As the observable in β-decay spectroscopy is the squared mass, this factor of 10 in sensitivity gain compared to the Mainz and Troitsk experiments corresponds to an improvement in both statistical and systematical uncertainties by a factor of 100. As a consequence, both uncertainties have to be stringently minimized in order to achieve the unprecedented sensitivity of KATRIN. The reduction of statistical uncertainties requires a total measurement duration of 3 net years with a windowless gaseous tritium source (WGTS) capable of producing 10^{11} β-electrons per second [KAT05]. To keep the systematical uncertainties at the low level required to reach the target sensitivity, the β^- activity of this source needs to be stable to 0.1 % [KAT05].

[1]For the sake of a smooth flow of reading, the abbreviation KATRIN will also be used with the meaning of "the Karlsruhe Tritium Neutrino experiment" in this thesis.

This stability level is governed by the stability of the tritium gas column in the WGTS beam tube, which is influenced by

- the pressure with which gas is injected into the gas column,
- the pumping speed with which gas is removed at the ends of the gas column,
- the purity of the tritium gas, as well as
- the temperature of the WGTS beam tube enclosing the gaseous tritium.

The topics of pumping speed and WGTS temperature were investigated in previous works [Pri13; Sei19]. This thesis is therefore focused on the topics of the injection pressure, gas purity, as well as the monitoring of the overall column density. All above paramters are controlled by the tritium loop system of KATRIN.

Accordingly, the main part of this doctoral project is the commissioning and thorough characterization of the tritium loop system. This comprises three main tasks which were accomplished during the characterization process:

- Optimization of the stabilized injection of tritium into the WGTS
- Characterization and modeling of the isotopic composition inside of the WGTS
- Development of continuous monitoring methods for the column density and characterization of its stability

This thesis is therefore structured as follows: Following an introduction to the topic of neutrino masses in chapter 2, different measurement methods for the neutrino mass will be presented, with a focus on tritium β-decay spectroscopy and the KATRIN experiment. Then a detailed description of the tritium loop system of KATRIN, which is the focus of this thesis, will be given in chapter 3. Chapter 4 then briefly illustrates the experimental challenges faced during long-term operation of the tritium loop system. The following chapters 5 to 7 present the employed methodology and obtained results. Finally, chapter 8 summarizes the obtained results and gives an outlook on open questions which became apparent over the course of this doctoral project.

2. Determination of the Neutrino Mass

The neutrino is one of the most elusive known particles with its unknown mass being in the center of interest. Section 2.1 gives a short overview of the history of key neutrino discoveries and details our current understanding of neutrinos in the Standard Model of particle physics. In section 2.2, the discovery of a non-zero neutrino mass via neutrino oscillations will be introduced. The methods which can be used to measure the neutrino mass are described in section 2.3. One of these methods, the precise spectroscopy of the β-decay spectrum, is laid out in more detail in section 2.4. Then, an overview of the most advanced experiment making use of this method, the Karlsruhe Tritium Neutrino (KATRIN) experiment, is given in section 2.5.3. Finally, the objectives of this doctoral project and thesis are presented in section 2.6.

2.1. Neutrinos in the Standard Model

The first indication for the existence of the neutrino was found in early investigations of nuclear β-decays by Chadwick [Cha14] in 1914. What at the time had been thought of as being a two-body process,

$$ {}^{A}_{Z}X \rightarrow {}^{A}_{Z+1}X + \beta^{-} \,, \tag{2.1} $$

should have led to discrete spectral lines. Surprsingly, these decays showed continuous energy spectrum. As this would violate either conservation of energy or momentum, this discovery sparked a controversy. This prompted Pauli [Pau30] to postulate the existence of a novel particle produced in β-decay in 1930. This was central to our modern understanding of the underlying weak interaction reaction:

$$ \mathrm{n} \rightarrow \mathrm{p} + \mathrm{e}^{-} + \bar{\nu}_{\mathrm{e}} \,. \tag{2.2} $$

On the basis of the assumption of this new particle, which he named "*neutrino*" due to it being neutral and having a very small mass, Fermi [Fer34] formulated his theory of the β-decay in 1934. Due to the lack of charge and very small interaction cross-sections with normal matter, the experimental detection of the neutrino (and, subsequently of the different flavors of neutrinos known today) was only possible several decades later:

- The first experimental proof of the existence of neutrinos was obtained by Reines and Cowan [RC53; Cow+56] in the 1950s, making use of the emerging nuclear reactors. They used the high flux of electron antineutrinos there,

which is produced in nuclear fission induced decay chains. Their observation was based on the now classical antineutrino capture process:

$$\mathrm{p} + \bar{\nu}_\mathrm{e} \rightarrow \mathrm{e}^+ + \mathrm{n}\,. \tag{2.3}$$

The signature consists of a coincidence of two angular correlated γ photons from $\mathrm{e}^+\mathrm{e}^-$ annihilation with a delayed γ from nuclear deexcitation of cadmium, after capture of the free neutron. This provided irrefutable proof of the existence of the neutrino.

- A decade later in 1962, evidence for the existence of more than one flavor of neutrino came from investigations of pion decays [Dan+62]:

$$\pi^+ \rightarrow \mu^+ + \nu_\mu\,, \tag{2.4}$$
$$\pi^- \rightarrow \mu^- + \bar{\nu}_\mu\,. \tag{2.5}$$

The particles generated by charged current interaction of the neutrinos with a steel target were identified to be muons only. The lack of electron production showed that the muon neutrino ν_μ associated with the production of muons differs from the electron neutrino associated with the β-decay.

- The third neutrino flavor, the tau neutrino ν_τ, was confirmed to exist at the turn of the millennium in 2001 [Kod+01]. Here, an accelerator beam expected to contain a smaller number of tau neutrinos, primarily from the decay of D_S-mesons:

$$D_S^+ \rightarrow \tau^+ + \nu_\tau\,, \tag{2.6}$$
$$D_S^- \rightarrow \tau^- + \bar{\nu}_\tau\,, \tag{2.7}$$

was directed onto a target containing a layered system of steel plates and photosensitive emulsions. Interactions of the ν_τ with the steel plates produced a small number of charged tau-leptons. Their signature consists of characteristic kinks in particle tracks in the emulsion. Identification of a kink after a short length on the mm-scale is characteristic for the tau-leptons given their short lifetime. The discovery of a few of such tracks in the emulsion brought proof of the tau neutrino as third neutrino flavor state.

The existence of these three neutrino flavors, and in particular the prediction of the tau neutrinos, are key to our modern understanding of the Standard Model (SM) of particle physics [Mün19]. The Standard Model is a quantum field theory describing the interactions of three fundamental forces - the electromagnetic, weak, and strong interactions - with a small set of elementary particles (see fig. 2.1 for all particles of the Standard Model). The SM has been very successful in predicting the discovery of the top quark, the tau neutrino, and finally the Higgs boson. In particular, the SM allows high precision descriptions of the properties of weak interactions. However, not all properties of the neutrinos can be explained in the framework of the Standard Model.

One of the interesting and unexpected properties of the neutrino is connected to its helicity. The helicity of a particle describes the direction of the particle spin in relation to its momentum, and is differentiated into right-handed (spin and momentum

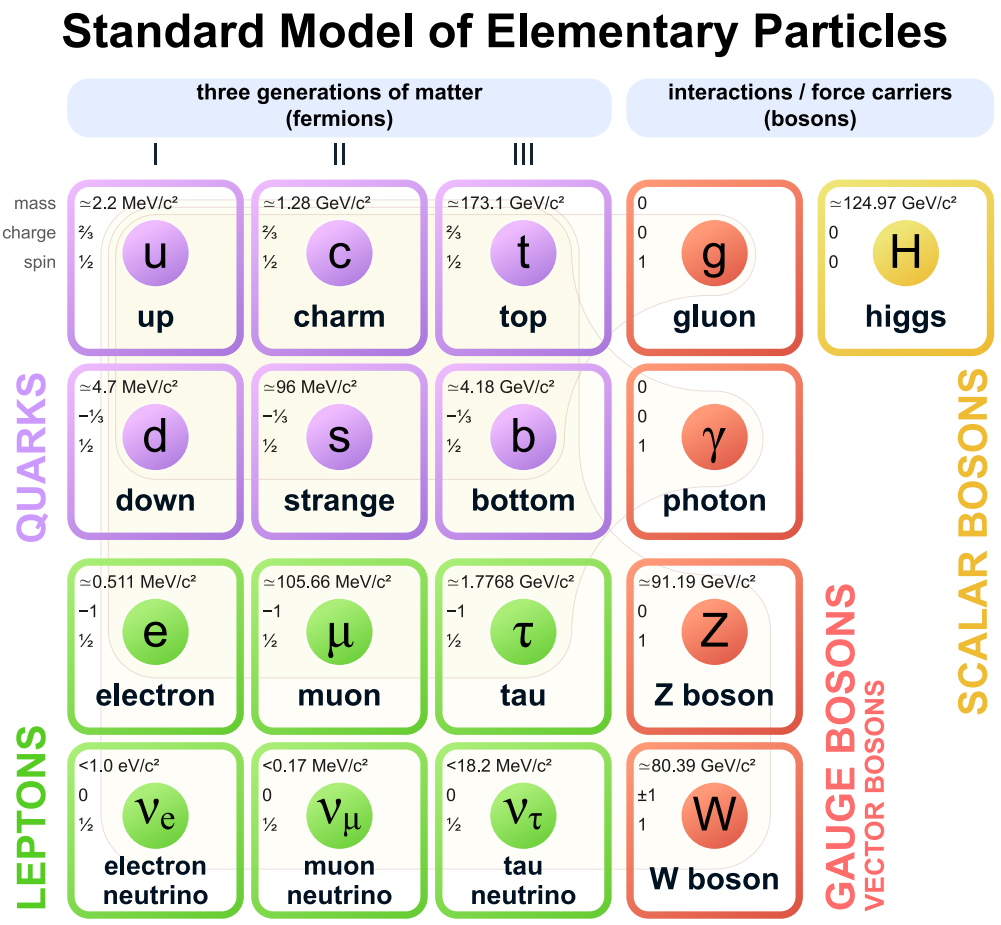

Figure 2.1.: **Particles of the Standard Model.** Shown are the particles of the Standard Model with their charge, mass, and spin. The Fermions are ordered by their flavor generations. The Bosons (excluding the Higgs) are grouped via lightly colored bubbles with the Fermions the interact with. The data included in this graphic are taken from [Ber+12] with updates from [Aab+18; Kar19; Ass+96; Bar01]. The image is taken from [Com20] and public domain.

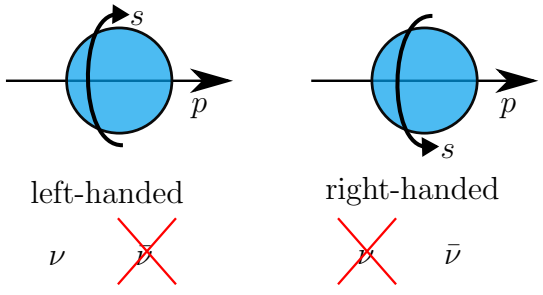

Figure 2.2.: **Illustration of helicity and neutrino parity violation.** The terms left- and right-handed are derived from pointing one's thumb in the direction of the momentum and representing the spin direction via the remaining digits. As has been shown by the Wu and Goldhaber experiments [Wu+57; GGS58], no left-handed antineutrinos or right-handed neutrinos exist.

are aligned) and left-handed (spin and momentum point in different directions), see fig. 2.2. Under parity transformation - a flip of all spatial coordinates - the momentum will change sign while the spin remains invariant, causing a flip of the helicity. The parity of processes involving neutrinos was found to be maximally violated by Wu [Wu+57], who investigated the β-decay of magnetically spin aligned ^{60}Co nuclei for different magnetic field directions. Interestingly, she found an exclusive preference for β-electron emission in the opposite direction of the nuclear spin. This finding was followed up by Goldhaber experiment [GGS58], which showed that only left-handed neutrinos and right-handed antineutrinos appear in weak interaction processes. As the Standard Model is a chiral theory, this property has direct implications. Chirality and helicity are closely linked, and even identical for massless particles; chirality however is an inherent quantum mechanical property of a particle which stays invariant under Lorentz transformations, whereas, for massive particles, one can cause a flip of the helicity by boosting the reference system. The Wu and Goldhaber experiments showed that neutrinos and antineutrinos only exist in one chirality and thus require them to be massless. In view of the Higgs mechanism [Hig64] of mass creation, which was observed at the LHC in 2012 [Cha+12; Aad+12], massless neutrinos do not interact with the Higgs field, as these interactions change the chirality of the interacting particle.

However, as will be discussed in the following section, neutrinos and antineutrinos are in fact massive particles, which makes neutrino physics one of the most promising fields for discovering new physics beyond the SM.

2.2. Discovery and Impact of the Non-Zero Neutrino Mass

The discovery of non-vanishing neutrino masses is directly linked to the observation of neutrino oscillations.

2.2.1. Neutrino Oscillation Theory

The theory behind neutrino oscillations was pioneered by Pontecorvo [Pon58; Pon68], Maki, Nakagawa, and Sakata [MNS62] starting around the 1960s. It is based on the implications of the difference between neutrino states which interact with other particles via the weak force, and states which propagate through space. The neutrinos interact via flavor eigenstates $|\nu_\alpha\rangle$ ($\alpha \in \{e^-, \mu^-, \tau^-\}$) which correspond to the electron, muon, and tau, whereas they propagate as mass eigenstates $|\nu_i\rangle$ ($i \in \{1, 2, 3\}$). For neutrino flavors to oscillate, a difference between flavor and mass eigenstates is needed. This means that each mass eigenstate is a superposition of different flavor eigenstates and vice versa:

$$|\nu_i\rangle = \sum_\alpha U_{\alpha i} |\nu_\alpha\rangle \,, \tag{2.8}$$

or

$$|\nu_\alpha\rangle = \sum_i U_{\alpha i}{}^* |\nu_i\rangle \,. \tag{2.9}$$

The factors $U_{\alpha i}$ can be understood as the elements of a 3×3 rotation matrix, switching from a flavor basis to a mass basis. It is named the PMNS matrix U, after Pontecorvo, Maki, Nakagawa, and Sakata. The PMNS matrix

$$U = \begin{pmatrix} U_{\mathrm{e}1} & U_{\mathrm{e}2} & U_{\mathrm{e}3} \\ U_{\mu 1} & U_{\mu 2} & U_{\mu 3} \\ U_{\tau 1} & U_{\tau 2} & U_{\tau 3} \end{pmatrix} \tag{2.10}$$

is commonly parametrized using the following parameters [Eid+04]:

- θ_{ij}, representing three mixing angles,
- δ_{CP}, which represents a single CP-violating phase.
- α_j ($j \in 1, 2$), which represent two additional so called "Majorana phases". These phases become relevant only if neutrinos are their own antiparticles. The phases are related to lepton number violating processes.

As the entire PMNS matrix can be described by the θ_{ij}, δ_{CP}, and α_j, these 6 parameters are commonly used to describe neutrino mixing in literature.

To go from these fundamental parameters to the experimentally measurable flavor oscillation probabilities, one needs to look at the temporal evolution of a mass eigenstate during propagation. For this, the Schrödinger equation is solved using a plane wave approach [Zub20]. The solution can be used to express the time and space dependent transition probability:

$$P_{\alpha\to\beta} = \sum_{i,j} U^*_{\alpha i} U_{\beta i} U_{\alpha j} U^*_{\beta j} e^{-\mathrm{i}/\hbar \cdot ((E_i t - p_i x_i) - (E_j t - p_j x_j))} \,. \tag{2.11}$$

From this equation one can see that neutrino oscillations necessarily require that mass and flavor eigenstates be different. For an exact match (e.g. $\nu_{\mathrm{e}} = \nu_1$, etc.), the PMNS matrix would become a unit matrix and the elements would simplify to ${U_{\alpha i}}^* = \delta_{\alpha i}$, causing all transition probabilities $P_{\alpha\to\beta}, \alpha \neq \beta$ to vanish.

Considering the fact that basically all experimentally accessible neutrinos have kinetic energies in the ultra-relativistic regime, the exponent of the plane wave solution of eq. (2.11) can be simplified. Using the approximations of $v = c$ and $x = L = c \cdot t$, the exponent then becomes:

$$E_i t - p_i x_i = \left(p_i c + \frac{m_i^2 c^4}{2E} \right) \cdot t - p_i L = \frac{m_i^2 c^3 L}{2E} \,. \tag{2.12}$$

With this expression and the introduction of a term $\Delta m^2_{ij} = m_i^2 - m_j^2$ describing the difference between the squared masses, eq. (2.11) can be written as:

$$P_{\alpha\to\beta} = \sum_{i,j} U^*_{\alpha i} U_{\beta i} U_{\alpha j} U^*_{\beta j} \mathrm{e}^{-\mathrm{i}/\hbar \cdot \frac{\Delta m^2_{ij} c^3 L}{2E}} \,, \tag{2.13}$$

which now only depends on the energy of the neutrino E and the distance L between its creation and observation as experimental parameters. This formula also shows that neutrino oscillation experiments on a fundamental level only allow to measure differences between the mass eigenstates, but not absolute values.

A useful simplification of this formula is to assume oscillations between only two neutrino flavors. In such a case one considers a simple 2×2 mixing matrix, for which the above equation becomes:

$$P_{\alpha\to\beta}(E, L) = \sin^2(2\theta)\sin^2(\frac{\Delta m^2 c^3 L}{4\hbar E})\,. \tag{2.14}$$

Numerous experiments around the world have been performed with different scales of the parameters E and L.

2.2.2. Neutrino Oscillation Experiments

The neutrino sources for these experiments can largely be split into the following categories:

Solar neutrino experiments

Neutrinos produced in nuclear fusion processes inside the sun exhibit energies in the MeV-range. Measured neutrino fluxes can then be compared to predictions from the Standard Solar Model [Bah64b; Bah64a], or one can search for temporal variations of the flux. This allows the investigation of length-scales on the order of the diameter of the earth of $\approx 13\,000\,\mathrm{km}$ or of the $1\,\mathrm{AU}$ distance between earth and sun. Early investigations include the the Homestake, GALLEX, and SAGE experiments [DHH68; Bah97]. These radiochemical experiments were impacted by neutrino oscillations, resulting in a missing flux of electron neutrinos coming from the sun, which was referred to as the solar neutrino problem. Examples for later experiments are Super-Kamiokande, which uses Cherenkov light produced from electrons on which relativistic neutrinos elastically scattered [Fuk+98], as well as the SNO experiment, which used D_2O to gain access to ν_μ and ν_τ via neutral current reactions [Ahm+01]. This experiment finally solved the solar neutrino problem.

Atmospheric neutrino experiments

Atmospheric neutrinos are produced from pion decays in particle showers caused by cosmic rays hitting the upper atmosphere of the earth. There, charged pions decay to muons, which further decay into electrons, electron antineutrinos, and muon antineutrinos (or the respective antiparticles). These neutrinos have energies on the GeV-scale. Given a sensitivity to the incident direction of the neutrino, such as is the case for the Super-Kamiokande experiment [Fuk+98], the scale of L which can be probed with these neutrinos ranges from the height of the top of the atmosphere of $L \approx 15\,\mathrm{km}$ for neutrinos created directly above the detector, to that of the diameter of the earth. For reviews of atmospheric neutrino experiments see [WO15; Cho16]

Long baseline accelerator neutrino experiments

Particle accelerators can produce beams of sign-selected pions via proton bombardment of a light target. The sign-selevted pions then decay to produce neutrinos or

antineutrinos, which follow the direction of the original pion beam. Neutrinos produced in this way are then usually detected at both, a near detector located several hundred meters from the point of neutrino generation, and at a far detector located several hundred km away, allowing for a comparison of rates and energy spectra at both places. Examples for experiments using these neutrinos are OPERA, MINOS, and T2K [Acq+09; Aga+15; Ada+11; Abe+11; Abe+17].

Reactor neutrino experiments

The decay chains of radioactive isotopes in the core of nuclear fission reactors produce a high flux of electron antineutrinos with energies on the scale of several MeV. Two approaches are used to investigate these neutrinos. The first approach used by the KamLAND [Egu+03] experiment makes use of a large amount of nuclear reactors with distances on the scale of 180 km from the detector. The second approach uses a near detector several hundred meters and a far detector between 1 km to 2 km away from the reactor, for which the difference in flux is measured. Examples for this type of experiment are RENO, Double Chooz, and Daya Bay [RA10; Ahn+12; Las06; Abe+14; Day07; AAP20].

2.2.3. Results from Neutrino Oscillation Experiments

The best values for the parameters of the PMNS matrix θ_{ij} and δ_{CP} as well as the differences of the squared masses Δm^2_{ij} determined by these experiments are listed in table 2.1. An observed hierarchy in the mass splittings of $\Delta m^2_{12} \ll |\Delta m^2_{31}| \simeq |\Delta m^2_{32}|$ allows two different ordering scenarios for neutrino masses:

- **Normal ordering (NO):** The mass eigenstate ordering follows $m_1 < m_2 < m_3$, which is qualitatively similar to mass orderings of the other fermions in the SM, thus labeled “normal”.
- **Inverted ordering (IO):** The mass eigenstates are ordered as $m_3 < m_1 < m_2$, which would stand in contrast to the ordering of the quarks and charged leptons.

A visualization of both ordering schemes is shown in fig. 2.3. A further important distinction with regard to the absolute scale of the smallest neutrino mass can be made. In case of $m_1^2 \gg |\Delta m^2_{31}|$ for NO and $m_3^2 \gg |\Delta m^2_{32}|$ for IO, the neutrino masses are called degenerate. An important result for the absolute mass of neutrinos which can be gained from these measurements refers to the largest of the mass splittings, as it serves as a lower limit on the heaviest mass eigenstate [Est+19]:

$$m_3 > \sqrt{|\Delta m^2_{31}|} = 0.05\,\mathrm{meV}/c^2 \qquad \text{for NO}\,, \tag{2.15}$$

$$m_2 > \sqrt{|\Delta m^2_{32}|} = 0.05\,\mathrm{meV}/c^2 \qquad \text{for IO}\,. \tag{2.16}$$

Even without an absolute value as of yet, the existence of neutrino masses and this lower limit have interesting implications for different fields of physics:

Table 2.1.: **Neutrino oscillation parameters.** Data taken from [Est+19].

Oscillation Parameter	Normal Ordering	Inverted Ordering
θ_{12} in $^\circ$	$33.82^{+0.78}_{-0.76}$	$33.82^{+0.78}_{-0.76}$
θ_{23} in $^\circ$	$49.6^{+1.0}_{-1.2}$	$49.8^{+1.0}_{-1.1}$
θ_{13} in $^\circ$	$8.61^{+0.13}_{-0.13}$	$8.65^{+0.13}_{-0.13}$
δ_{CP} in $^\circ$	215^{+40}_{-29}	284^{+27}_{-29}
Δm^2_{12} in $(\mathrm{eV}/c^2)^2$	$7.39^{+0.21}_{-0.2} \times 10^{-5}$	$7.39^{+0.21}_{-0.2} \times 10^{-5}$
Δm^2_{31} in $(\mathrm{eV}/c^2)^2$	$2.525^{+0.033}_{-0.032} \times 10^{-3}$	-
Δm^2_{32} in $(\mathrm{eV}/c^2)^2$	-	$-2.512^{+0.034}_{-0.032} \times 10^{-3}$

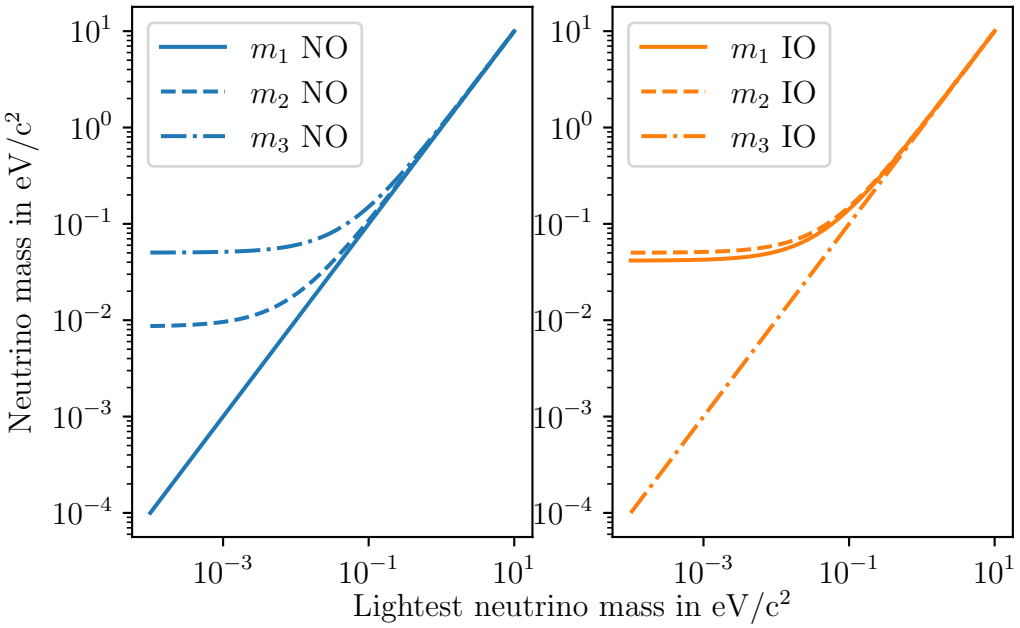

Figure 2.3.: **Neutrino mass ordering.** Neutrino masses are displayed as function of the lightest neutrino mass for the normal and inverted ordering scenario. The masses are calculated based on the mass splitting data from [Est+19] shown in table 2.1.

- **Sterile neutrinos:** As mentioned in chapter 1, the Higgs mechanism in the SM can not explain the masses of the purely left-handed neutrinos observed in nature. It would require the existence of new neutrino states which would require an extension to the SM.

  The most straightforward extension is the introduction of right-handed neutrinos ν_{R} which do not interact via the weak force [Eid+04], usually called *sterile neutrinos*. In terms of the Lagrangian of the system, one can now construct a so called Dirac mass term which is analogous to the one responsible for generating the masses of quarks and charged leptons:

  $$\mathcal{L}_{\mathcal{D}} = -m_D \ \bar{\nu}_L \ \nu_R + \mathrm{h.c.}\,. \tag{2.17}$$

  In contrast to quarks and leptons however, the neutrino carries no charge. As such, no fundamental symmetry explicitly forbids the equality of neutrino and antineutrino, apart from the concept of lepton number conservation. Neutrinos then would be Majorana particles, in which case an additional so called Majorana mass term can be written:

  $$\mathcal{L}_{\mathcal{M}} = -m_R \ \bar{\nu}_R{}^c \ \nu_R + \mathrm{h.c.}\,. \tag{2.18}$$

  If Neutrinos are Majorana particles and this term exists, it would allow violation of lepton number conservation by $\Delta L = 2$.

  Both options, purely Dirac neutrinos as well as neutrinos of Majorana nature, would allow the solution of several open questions in physics besides that of the neutrino mass, such as the baryon asymmetry of the universe [Moh+07; Brd+19]. However, a distinction between the two scenarios arises with regards to the mass scale. While Dirac neutrinos would result in relating all particle masses directly to the Higgs, it would require extremely small Yukawa-like coupling constants ($\mathcal{O}(10^{-12})$) as well as imposing conservation of the lepton number as an exact global symmetry. In the case of Majorana neutrinos, the mass scale of neutrinos is not related to the Higgs, but results from the so called see-saw mechanism, which can explain the small observed left-handed neutrino masses on condition that right-handed neutrinos possess very large masses, possibly up to the GUT scale of $10^{16}\,\mathrm{GeV}/c^2$ [Eid+04; Moh+07].

- **Structure formation in the early universe:** In the moments shortly after the Big Bang, an enormous number of neutrinos was created, with the current number density of these relic neutrinos being $336\,\mathrm{cm}^{-3}$ [LLS14]. This density is much larger compared to that of baryons of $2.5 \times 10^{-7}\,\mathrm{cm}^{-3}$ [Tan+18]. After the universe cooled down below $\approx 1\,\mathrm{MeV}$, the mean time between weak interactions became longer than the age of the universe, freezing out the weak interactions of neutrinos with the other particles [Cyb+16]. Despite their small mass, the vast amount of neutrinos allows them to perturb the early universe by their gravitational effect alone. In combination with their large free-streaming length in the early universe, this impacts the formation of large-scale structures at certain length scales [Pee73]. This effect can still be observed today in the power spectrum of galaxies or of the cosmic microwave background (CMB) [BS04; TM05].

In order to solve the neutrino mass puzzle and gain insights for the above fields, various methods for neutrino mass measurement have been developed, which will be introduced in the following.

2.3. Neutrino Mass Measurement Methods

There are several complementary measurement principles which can be employed to determine the neutrino mass:

- derivation of the neutrino mass from cosmological observations
- time-of-flight measurement of supernova neutrinos
- measurement of the neutrinoless double β-decay
- precise measurement of β-decay kinematics

These principles and the sensitivities on the neutrino mass obtained are described briefly in the following.

Derivation of the neutrino mass from cosmological observations

As stated above, neutrino masses have an impact on the galaxy power spectrum and the CMB. Therefore, information about neutrinos can be derived from cosmological observations, however only under the assumption of a specific cosmological model. From this cosmological approach, upper limits of the sum of active neutrino masses have been derived for the ΛCDM cosmological model [CH19]:

$$\sum m_i < \begin{array}{ll} 0.146\,\mathrm{eV/c^2} & \text{for normal ordering}\,, \\ 0.172\,\mathrm{eV/c^2} & \text{for inverted ordering}\,, \\ 0.121\,\mathrm{eV/c^2} & \text{for degenerate masses}\,. \end{array} \tag{2.19}$$

While these limits are the lowest currently available numbers, and already encroach upon the lower mass limit from neutrino oscillations, their model dependency makes independent investigation in laboratory experiments mandatory.

Time of flight measurement of supernova neutrinos

Core-collapse supernovae (SN) of type Ib, Ic, and II emit 99 % of their energy in a 10 s long burst of neutrinos with energies at the MeV-scale. About a dozen SN-neutrinos from the famous supernova SN1987A were detected on earth [Hir+87]. Over the large travel distance of $L = 1.586 \times 10^{21}$ m [Pan03], the non-zero neutrino mass will cause a measureable difference in arrival time Δt depending on the neutrino energy. For two neutrinos with energies E_1 and E_2, it is given by:

$$\Delta t = \Delta t_{\mathrm{em}} + \frac{L c^3 {m_\nu}^2}{2} \left(\frac{1}{E_1^2} - \frac{1}{E_2^2} \right) . \tag{2.20}$$

The above equation includes a time difference Δt_{em} due to different emission times of the neutrinos. This unknown emission time difference can be obtained using models of the supernova collapse, explosion and subsequent cooling.

With significant differences depending on the used supernova model and analysis, the upper limits on the neutrino mass derived from SN1987A are in the range of [AR87; LL02]:

$$m_\nu \leq 5.7\,\mathrm{eV}/c^2 - 12\,\mathrm{eV}/c^2\,. \tag{2.21}$$

Neutrinoless double β-decay

The neutrinoless double β-decay ($0\nu\beta\beta$) is disctinct from the second order weak process of the double β-decay with neutrinos ($2\nu\beta\beta$). Of experimental interest are only isotopes where the simple β-decay is forbidden. As $2\nu\beta\beta$ is a second order process its comparatively small rates would be undetectable otherwise. In the $0\nu\beta\beta$-decay, a virtual neutrino emitted by the decay of a neutron is absorbed by another neutron, inducing its decay. This process is only possible if neutrinos are Majorana particles. For this decay, the rate Γ is given by [VEŠ12]:

$$\Gamma = G|M_{\mathrm{nuc}}|^2|m_{\beta\beta}|^2\,. \tag{2.22}$$

The mass $m_{\beta\beta}$ entering this equation is called effective Majorana mass which is formed by the coherent sum of the neutrino mass eigenstates:

$$m_{\beta\beta} = \sum_i m_i U_{ei}^2\,, \tag{2.23}$$

with U_{ei} being the elements of the PMNS-Matrix relevant to electron neutrinos.

If $0\nu\beta\beta$-decay events would be observed, it would confirm the Majorana nature of neutrinos, and one could derive $m_{\beta\beta}$ from the measured half-life of the decay. Relying on the Majorana nature of neutrinos, searches for $0\nu\beta\beta$ will yield no positive results if neutrinos are Dirac particles. Further issues of this type of experiment are the possibility of cancellations of the PMNS-Matrix elements due to the Majorana phases α_j, which could result in a vanishingly small $m_{\beta\beta}$ value. Moreover, there are large uncertainties on the nuclear matrix elements M_{nuc}, which are necessary to calculate the expected decay rates.

So far, no $0\nu\beta\beta$-decay event has been observed. This lack of an observation, combined with the amount of target material used in experiments, allows to derive an upper limit on the decay rate. This can then be translated to a limit on the effective Majorana mass $m_{\beta\beta}$. The current best upper limits (90 % C.L.) on the effective Majorana mass are [Gan+16]:

$$m_{\beta\beta} < 0.61\,\mathrm{eV}/c^2 - 0.165\,\mathrm{eV}/c^2\,. \tag{2.24}$$

Precision measurement of the β-decay kinematic

A laboratory-based method complementary to neutrinoless double β-decay is the precise measurement of the single β-decay electron spectrum. In the kinematics of a β-decay

$${}^A_Z X \rightarrow {}^A_{Z+1} Y + \mathrm{e}^- + \bar{\nu}_\mathrm{e}\,, \tag{2.25}$$

the Q-value corresponding to the mass difference between the nuclei X and Y is shared between a small recoil of the nucleus E_{rec}, the excitation of the daughter nucleus into a state with energy V_j, kinetic energies of the electron and antineutrino, and their respective rest masses. This direct access to the mass of the neutrino, only relying on the conservation of energy and momentum is the biggest advantage of this method. As the effect of the neutrino mass on the β-spectrum is most pronounced close to the endpoint energy, β-decays with low Q-values are desirable in order to precisely measure this endpoint region. Two isotopes currently in use for this purpose are (molecular) tritium (^{3}H) [Kra+05; Ase+11; Ake+19] with an endpoint energy of 18.6 keV [Mye+15] and more recently holmium-163 (^{163}Ho) [Gas+14; Fav+16] with an endpoint energy of 2.8 keV [Eli+15].

The current best upper limit on the incoherent sum of neutrino mass eigenstates from β-decay, to which the results of this thesis contributed, is [Ake+19]:

$$m_\nu = \sum_i |U_{ei}|^2 m_i < 1.1\,\mathrm{eV}/c^2\,. \tag{2.26}$$

This limit, conceptually free of any particle-physics-related model assumptions, was derived by the KATRIN experiment [KAT05] using an unprecedented tritium source. The following sections will explain the β-spectroscopy of tritium in more detail, before describing the implementation in the KATRIN experiment.

2.4. Tritium β-electron Spectroscopy

The impact of a non-zero neutrino mass on the β-spectrum was already discussed in the first formulation of the theory behind the β-decay by Fermi [Fer34]. Using Fermi's Golden Rule, the energy-dependent rate of the β-spectrum of a nucleus (shown in fig. 2.4 is the case for tritium) can be expressed after [OW08] as:

$$\begin{aligned}\frac{\mathrm{d}\Gamma}{\mathrm{d}E}(\epsilon) =& \frac{G_{\mathrm{F}}^2 \cos^2\Theta_{\mathrm{C}}}{2\pi^3(\hbar c)^3} |M_{\mathrm{nuc}}|^2 F \cdot (E_0 + m_{\mathrm{e}}c^2 - \epsilon) \\ & \cdot \sqrt{(E_0 + m_{\mathrm{e}}c^2 - \epsilon)^2 - {m_{\mathrm{e}}}^2c^4} \sum_{i,j} |U_{ei}|^2 P_j \cdot (\epsilon - V_j) \\ & \cdot \sqrt{(\epsilon - V_j)^2 - {m_i}^2c^4} \cdot \Theta(\epsilon - V_j - {m_i}^2c^4)\ ,\end{aligned} \tag{2.27}$$

with:

- $E_0 = Q - E_{\mathrm{rec}}$, the endpoint energy of an energy spectrum with a vanishing neutrino mass ($m_\nu = 0\,\mathrm{eV/c^2}$) and the daughter system in its ground state ($V_j = V_0 = 0$),
- $E = E_0 - \epsilon$, the kinetic energy of the emitted electron,
- $\epsilon = E_0 - E$, the missing energy, shared between the total neutrino energy and V_j,
- G_{F}, the Fermi constant,
- Θ_{C}, the Cabbibo angle,

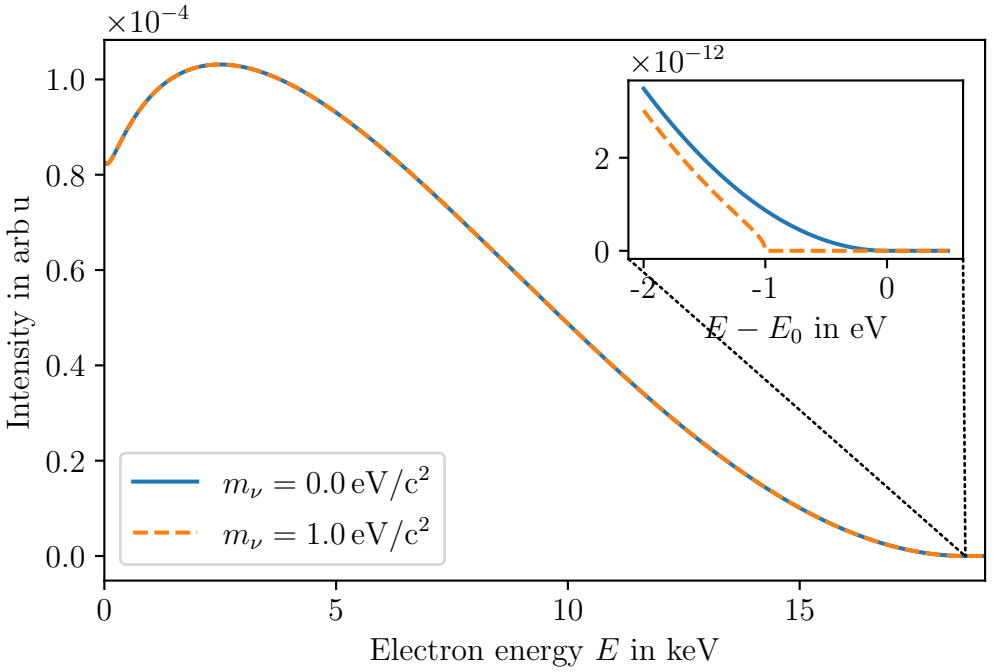

Figure 2.4.: **β-spectrum of tritium.** Shown are two β-spectra calculated according to eq. (2.27) with neutrino masses of $0\,\mathrm{eV}/c^2$ and $1\,\mathrm{eV}/c^2$. The region near the endpoint of the β-decay, where the sensitivity to the neutrino mass is best, is zoomed in in the inset to illustrate the size of the shape distortion induced by the neutrino mass.

- $M_{\mathrm{nuc}}(E)$, the nuclear Matrix element,
- F, the Fermi function,
- m_{e}, the electron rest mass,
- P_j, the probability for the daughter system to be in the j-th excited final state, and
- $\Theta(\epsilon - V_j - {m_i}^2)$, the Heaviside function ensuring conservation of energy.

Tritium in particular is suitable for investigation of the neutrino mass due to several of its properties:

- The β-decay of tritium is super-allowed. This leads to an energy-independent M_{nuc} [WA03], greatly simplifying the analysis.
- The comparatively short half-life of 12.3 yr [LU00] and the correspondingly high specific activity ($1.79 \times 10^{-9}\,\mathrm{s}^{-1}$) is highly favorable with regard to the construction of a high intensity β-electron source with low density, and therefore low opacity for electrons.
- The simple structure of the T_2 molecule allows for detailed, quantitative calculations of the decay process and the resulting final state distribution of the daughter molecule [SJF00; BPR15; Lin+20].
- The low Q-value of the decay of 18.6 keV [Mye+15], and therefore low endpoint energy E_0 of the spectrum. This permits the use of high precision spectroscopy of the endpoint region with electrostatic filters.

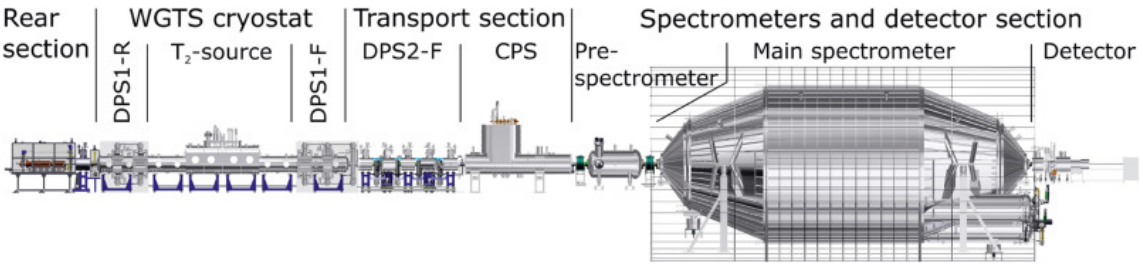

Figure 2.5.: **CAD model of the KATRIN experiment.** Shown is a rendering of the KATRIN beam line with labels describing the different sections. Illustration as published in [Fri+19] under the CC BY license https://creativecommons.org/licenses/by/4.0/.

These properties have lead to a multitude of measurements of the tritium β-decay since the 1950s (e.g. [LM52; HAG53; Lub+80; Rob+91; Kra+05; Ase+11]), which have improved their methodology continuously to derive smaller and smaller limits on the neutrino mass. A common issue occurring in these experiments was the measurement of negative values for $m_\nu{}^2$ due to imperfect treatment of systematic effects. The culmination of the efforts to reduce the impact of such systematic effects resulted in the currently best upper limit for the neutrino mass derived by the KATRIN experiment [Ake+19]. Future experiments such as Project 8 [Esf+17; Pet20] or PTOLEMY [Bet+19; Coc19], aim to push the sensitivity beyond that of the KATRIN experiment. However, going to sensitivities equal to the lower limit from neutrino oscillations requires substantial research and developement effort, and all new projects are currently still in their early design phases.

2.5. The KATRIN Experiment

The **KA**rlsruhe **TRI**tium **N**eutrino experiment, located at the Tritium Laboratory Karlsruhe (TLK) of the Karlsruhe Institute of Technology, is the direct successor to the Mainz [Kra+05] and Troitsk [Ase+11] neutrino mass experiments. A technical design report was finished in the early 2000s [KAT05]. The experiment principally consists of a β-electron sourse, and an energy spectrometer. The source is a windowless gaseous tritium source (WGTS) from which β-electrons can leave without needing to cross any physical barrier. These electrons are filitered by a spectrometer combining magnetic adiabatic collimation with an electrostatic filter (MAC-E type filter [Pic+92]), which only lets electrons above a certain energy pass to be finally detected on a segmented detector. An illustration of the experiment is shown in fig. 2.5.

The spectrometer and detector are breifly described in section 2.5.1, followed by an in-depth description of the source and the section connecting it to the spectrometer in section 2.5.2. Finally in section 2.5.3, the importance of operating a stable tritium source is discussed.

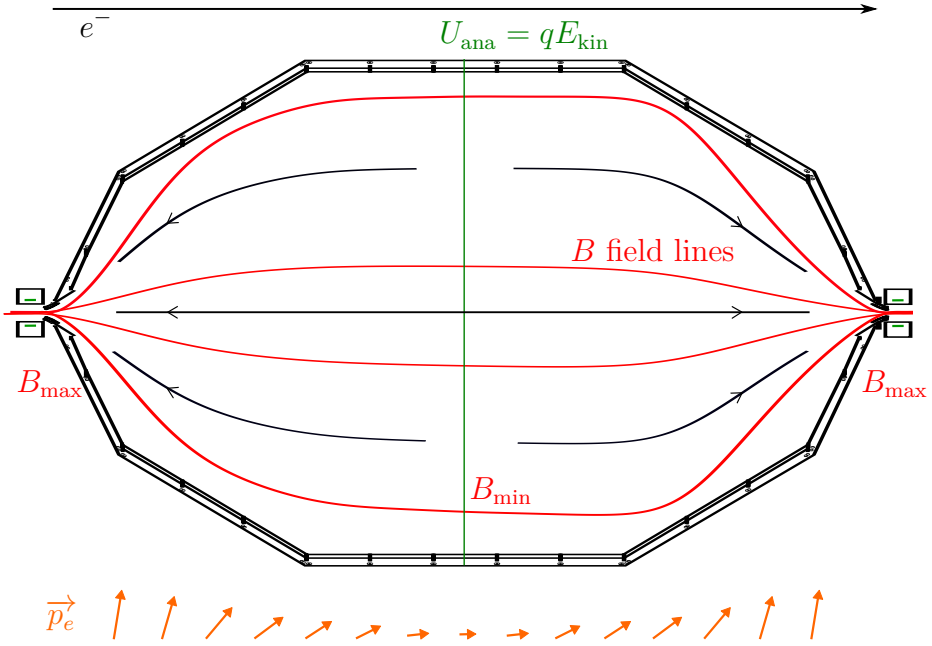

Figure 2.6.: **Schematic of the MAC-E filter principle.** The combination of magnetic and electric fields allows for high resolution energy spectroscopy for a big solid angle of an isotropically emitting electron source. Figure adapted from [Hei19].

2.5.1. Spectrometer and Detector Section

The spectrometer and detector section (SDS) consists of two MAC-E type filters called the Pre- and Main Spectrometer (PS and MS), as well as the focal plane detector (FPD). The PS and MS both work under the principle of magnetic adiabatic collimation with an electrostatic filter (MAC-E type filter) [BPT80; LS85; Pic+92] as sketched in fig. 2.6. A maximum value of the electrostatic potential is applied at the center of the spectrometer, the so called analyzing plane. This barrier can only be overcome by electrons with kinetic energies above this potential, meaning the spectrometer serves as a high-pass filter. In addition to the electrostatic potential, a strong magnetic field B_{max} is applied at the entrance and exit of the spectrometer, while the magnetic field strength in the center B_{min} almost vanishes. The purpose of this magnetic field is the collimation of electron momenta at the analyzing plane via the magnetic gradient force:

$$\vec{F} = \vec{\nabla}(\vec{\mu} \cdot \vec{B})\,. \tag{2.28}$$

This force converts the energy of cyclotron motion $E_\perp$ of all electrons moving along the magnetic field lines into kinetic energy $E_\parallel$ parallel to the field lines. If the relative change of the magnetic field strength is small over the scale of a cyclotron radius of an electron, this conversion is adiabatic and the magnetic moment μ is conserved:

$$\mu = \frac{E_\parallel}{B}\,. \tag{2.29}$$

This setup drastically increases the accepted solid angle of electrons from isotropic β-decays which can be analyzed without sacrificing energy resolution. The resolution

of the spectrometer results from the remaining orthogonal component of the kinetic energy $E_\perp$ which is not converted due to the non-zero magnetic field strength $B_{\min}$ in the analyzing plane. Taking this $E_\perp$ as the width of the energy distribution of transmitted electrons ΔE, the energy resolution of a MAC-E type filter is given by

$$\frac{\Delta E}{E} = \frac{B_{\min}}{B_{\max}} \cdot \frac{\gamma + 1}{2}\,, \tag{2.30}$$

with the relativistic gamma factor γ of transmitted electrons. The resolution is limited by the achievable maximal magnetic field, as well as the need to keep the minimal field strength $B_{\min}$ in the center to ensure guiding of electrons along the field lines, which causes a small residual $E_\perp$. For the KATRIN design values of $B_{\min} = 0.3\,\mathrm{mT}$ and $B_{\max} = 6\,\mathrm{T}$, the energy resolution of the MS close to the tritium β-decay endpoint of 18.6 eV is $\Delta E = 0.93\,\mathrm{eV}$ [KAT05]. The conservation of magnetic flux,

$$\Phi = \int_A B \mathrm{d}A\,, \tag{2.31}$$

requires a much larger diameter in the central section of the spectrometer than at its entrance and exit. The ratio of $B_{\max}/B_{\min}$ of 20 000 in combination with the maximal spectrometer diameter of $d \approx 10\,\mathrm{m}$ for which construction was feasible leads to a transported magnetic flux of $191\,\mathrm{T\,cm^2}$. To ensure a small enough magnetic field gradient in order to have adiabatic collimation of the electrons, the length of the MS is 23.3 m [KAT05]. To prevent background from affecting the precision measurement of the endpoint region of the β-spectrum, residual gas ionization needs to be suppressed, requiring the MS to be operated at an UHV pressure level of $<10^{-11}$ mbar [KAT05]. In order to make proper use of the high resolution and small background, the high voltage applied to the MS which establishes the potential of the analyzing plane needs to be stable on the ppm-level [KAT05; Are+18; Res+19].

The PS works similarly to the MS, however its purpose is not the final energy filtering of the electrons, but the reduction of electrons entering the MS by removing a large fraction of low energy electrons from the β-spectrum. This minimizes ionization processes of the remaining gas in the MS, which otherwise would cause an elevated background.

The FPD is a silicon p-i-n diode wafer, which is segmented into 148 pixels [Ams+15]. The detector has a high efficiency of $\varepsilon_{\mathrm{FPD}} \geq 90\,\%$ for electrons in the signal region and is calibrated regularly using an americium calibration source. In order to reduce backscattering of electrons from the FPD, a post-acceleration electrode (PAE) gives the electrons additional 10 keV of energy. This, as well as the energy resolution of typically about 1.5 keV FWHM, is no issue for KATRIN, as the FPD only needs to count events after the energy filtering by the MS with high resolution.

2.5.2. Source and Transport Section

The source and transport section (STS) consists of the following components:

- the windowless gaseous tritium source (WGTS)
- the differential pumping section (DPS)

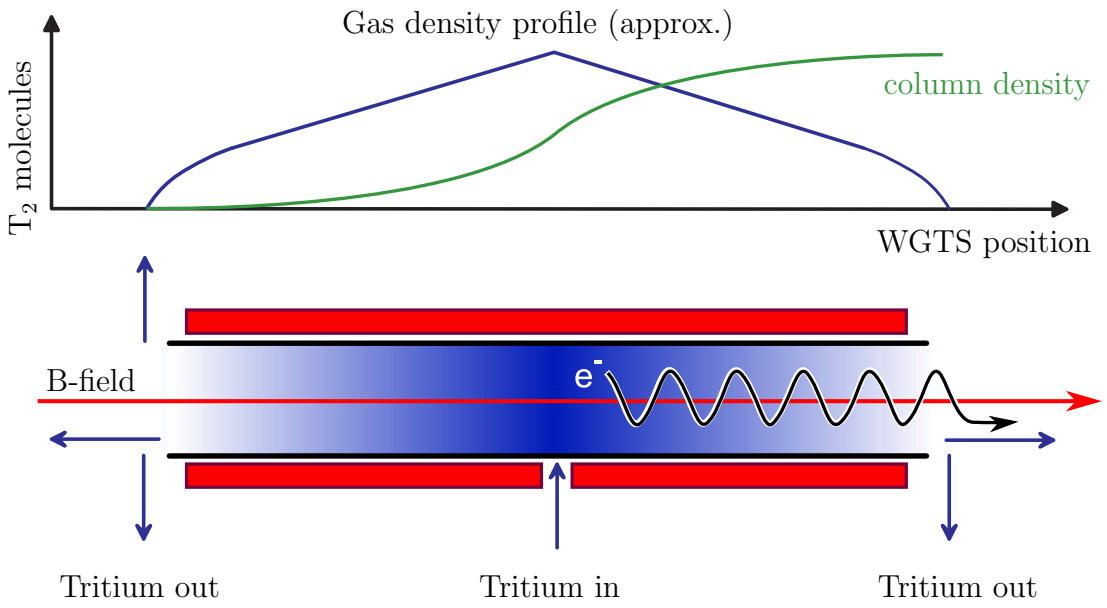

Figure 2.7.: **Schematic of the Windowless Gaseous Tritium Source Principle.** Shown is a schematic WGTS with central tritium gas injection and pumping at both sides of the source tube. The source tube is surrounded by super conducting magnets, depicted in red, which provide the necessary magnetic field to adiabatically guide β-electrons towards the spectrometers. In addition, at the top an illustration of the nonuniform gas density profile inside the WGTS is shown. The integration of this density along the length of the WGTS is the so called column density shown in green.

- the cryogenic pumping section (CPS)
- the rear section (RS)
- the tritium loops system interconnecting all above components

The WGTS is a column of gas containing mostly tritium inside the WGTS source tube, formed via continuous circulation [Bor06]. For an illustration of the principle of the WGTS, refer to fig. 2.7. Gas is continuously injected in the center of the source tube and then streams towards both ends, where it is pumped out, forming a stationary gas density profile. This profile is characterized by the so called tritium column density ρd, which is a measure of the amount of tritium atoms N_T inside the WGTS:

$$N_\mathrm{T} = \rho d \cdot A_\mathrm{WGTS} \cdot \varepsilon_\mathrm{T} \cdot 2\,, \tag{2.32}$$

with A_WGTS being the cross section of the source and ε_T the atomic fraction of tritium in the gas. The β-electrons, which are produced in decays during the free streaming phase of tritium molecules, are used by KATRIN to determine the neutrino mass. In order for these electrons to reach the SDS, a strong magnetic field of 3.6 T, which guides the electrons adiabatically, is applied to the WGTS via superconducting solenoids surrounding the source tube.

As a means of decreasing systematic effects and increasing the source strength, the WGTS can be operated at temperature levels around 30 K, 80 K or 100 K. This is realized via a sophisticated two-phase cooling system, which allows a temperature

stabilization of the source tube on the sub-permille level [Gro+08; Gro+11; Sei19]. The entirety of the source tube, its cooling system, as well as the superconducting magnets are housed inside the WGTS cryostat.

Following the WGTS in direction of the spectrometers is the DPS. Its purpose is the reduction of the tritium flow rate from the WGTS towards the SDS by a factor of at least 10^7 via differential pumping using turbo molecular pumps (TMPs). The DPS is followed by the CPS, which reduces the tritium flow rate towards the SDS by another factor of at least 10^7 by cryogenically trapping tritium on a layer of argon frost at a temperature level of $\approx 3\,\mathrm{K}$ [Gil+10]. Together, the DPS and the CPS constitute the transport section, and reduce the tritium flow to a level which does not cause an observable increase in background rate in the spectrometers, while also adiabatically transporting the electrons towards them.

The RS terminates the beam line at the rear end, in opposite direction of the FPD. It contains the Rear Wall, which is a gold-plated disk. It can be biased and allows to influence the starting potential of the β-electrons inside the WGTS. In addition, it contains several calibration and monitoring devices [Bab14].

To provide all of the above systems with tritium and vacuum pumping is the key task of the tritium loop system [PSB15; Pri+20]. It is responsible for all matters pertaining to the handling of tritium in the KATRIN experiment. As the loops system is the focus of this thesis, its relation to the other STS components is described in more detail in chapter 3.

2.5.3. The Importance of Source Stability

The stability of the WGTS is essential for the entire KATRIN experiment. While the most intuitive signal of the neutrino mass is a vanishing of the event rate above a certain energy, this method of determining the neutrino mass is not applicable in a real experiment. Background and endpoint shifts due to work function changes of source and spectrometer make the direct observation of this impossible. Instead of searching for a vanishing rate, KATRIN measures the tiny distortion of the shape of the differential spectrum close to the endpoint energy. Also, due to the MAC-E type filter being a high-pass filter, KATRIN can only measure the integrated count rate of electrons with energies above the analyzing potential, instead of the more direct differential spectrum. The integral spectrum is obtained by varying the analyzing potentials [Bab+12; Ake+20].

This scanning of the spectrum by varying the analyzing potentials requires the activity of the source to remain stable at least on the time scale of a scan [Sib19]. Otherwise, fluctuations of the source are imprinted onto the differential spectrum, distorting it. Such distortions can not be distinguished from those caused by the neutrino mass, potentially causing biased results for m_ν. An illustration of this effect is shown fig. 2.8. Therefore, the stability of the WGTS is of utmost importance for KATRIN.

Experimentally, stabilizing the source means to stabilize the column density ρd. This key parameter depends on the pressure of gas being injected into the WGTS, the pumping speed of the TMPs of the DPS, the temperature of the WGTS beam

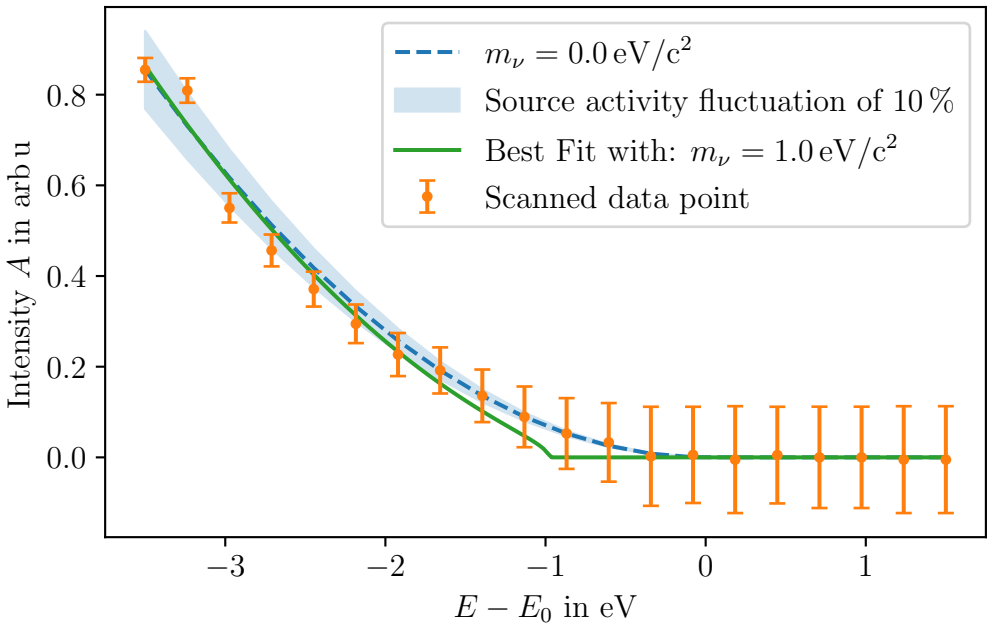

Figure 2.8.: **Illustration of the importance of source stability.** Shown is the endpoint region of a simplified, theoretical tritium β-spectrum for a neutrino mass of $m_\nu = 0\,\mathrm{eV}/c^2$. A temporal activity fluctuation was added to the spectrum and a scanning "measurement" of several points with a fixed duration was taken. The model used to create the spectrum was then fitted to these points, leading to a non-zero neutrino mass fit result purely due to temporal activity fluctuations.

tube, and the composition of the injected gas. Previous investigations have shown the temperature and TMP pumping speed to meet the 0.1 % stability requirement [Pri13; Sei19]. The remaining parameters are the focus of this thesis, as lined out in the following section.

2.6. Objectives of this Thesis

As laid out in the previous section, to meet the requirement of a 0.1 % source activity stability is imperative for the KATRIN experiment to be able to reach its sensitivity goal of $0.2\,\mathrm{eV}/c^2$ (90 % C.L.). The stability of the injection pressure and gas composition, as well as of the column density as the combination of all parameters are the topic of this thesis. It is split according to three main tasks:

Optimization of the stabilized injection of tritium into the WGTS
The stable injection of tritium gas into the WGTS is essential for a stable column density and thereby activity. As such, a thorough characterization of the injection system is necessary to verify that the KATRIN stability requirements are fulfilled. It is furthermore of interest to find ways in which any observed fluctuations can be mitigated in order to minimize the contribution of the injection pressure stability to the systematic uncertainty budget of the experiment.

Characterization and modeling of the isotopic composition inside of the WGTS
The isotopic composition of the gas circulating through the WGTS not only directly impacts the activity, but also affects the scattering probabilities of electrons on gas molecules as well as the overall gas dynamical properties of the gas and therefore the shape of the gas density profile inside the WGTS. For this reason monitoring tools exist which measure the gas composition. First, it needs to be verified that these measurements are indeed representative of the gas composition in the WGTS beam tube. This task can be answered by comparing the different monitoring tools. However, these monitoring tools are not available in all operation modes of the tritium loops. For operation modes where the tools are unavailable, a different approach needs to be taken by simulating the gas circulation to infer the gas composition and changes in it.

Development of continuous monitoring methods for the column density and characterization of its stability
Being the most important quantity of the WGTS for neutrino mass analyses, the column density needs to be known to a high degree of accuracy in addition to being kept stable. In order to achieve this accurate knowledge of the column density, a measurement scheme allowing the continuous monitoring of the column density needs to be developed. Once such measurements are possible, the WGTS can be investigated with respect to the impact of external influences on the column density.

All of these tasks are intrinsically connected to the performance and properties of the tritium loops system of KATRIN, which makes a detailed understanding of this system necessary. Therefore, the next chapter 3 is dedicated to an overview of this system, before the chapters 5 to 7 will address achievements in the main tasks named above. Finally, a summary of the results and an outlook are given in chapter 8.

3. The Tritium Loop System of KATRIN

All beam line components of KATRIN, besides the spectrometers, are interconnected by the extensive *tritium loop system* of KATRIN. Its purpose is to provide a stable circulation for high flow rates of tritium through the WGTS as well as the recuperation of tritium pumped out by the DPS, CPS, and RS. In addition, it is the key interface between KATRIN and the tritium loop system of the Tritium Laboratory Karlsruhe (TLK). A simplified flow scheme is shown in fig. 3.1.

The loop system of the TLK is divided into the so called *inner loop* (IL) and *outer loop* (OL). The IL, explained in detail in section 3.3, is responsible for the stabilized gas circulation through the WGTS. In section 3.2, the different operation modes of the IL are presented. The OL consists of the TLK infrastructure described in the following section 3.1, as well as of *feed loop* (FL) and *exhaust loop* (EL) (see section 3.4) in the KATRIN tritium loop system which are responsible for both receiving high purity tritium gas from and returning tritiated waste gas back to the TLK infrastructure.

3.1. Integration of the KATRIN Loop System into the TLK Infrastructure

The integration of the loop system into the TLK infrastructure is realized in the form of a closed loop system [Dör+05]. A schematic of this can be seen in fig. 3.2. The tritium gas is processed by the TLK facilities as follows:

- When it is not in use, tritium is safely stored in the *Tritiumlager* (TLG) on getter beds made of uranium or zirconium-cobalt [BPB02].
- From these beds, the tritium is transferred via the *Tritium Transfer System* (TTS) to the experiments or facilities. Besides connecting the facilities of the TLK, the TTS is also responsible for bookkeeping of the tritium inventory.
- One such facility connected to the TTS is the *Isotope Separation System* (ISS) [Doe+02]. From it, gas can be either transferred to the FL or purified if it does not meet the KATRIN requirements. This is done using displacement gas chromatography to separate T_2 from the other hydrogen isotopologues via the difference in time the isotopologues need to pass through a chromatography column. By this process the ISS is capable of reliably providing gas enriched to a tritium purity >98 % [Wel+17].

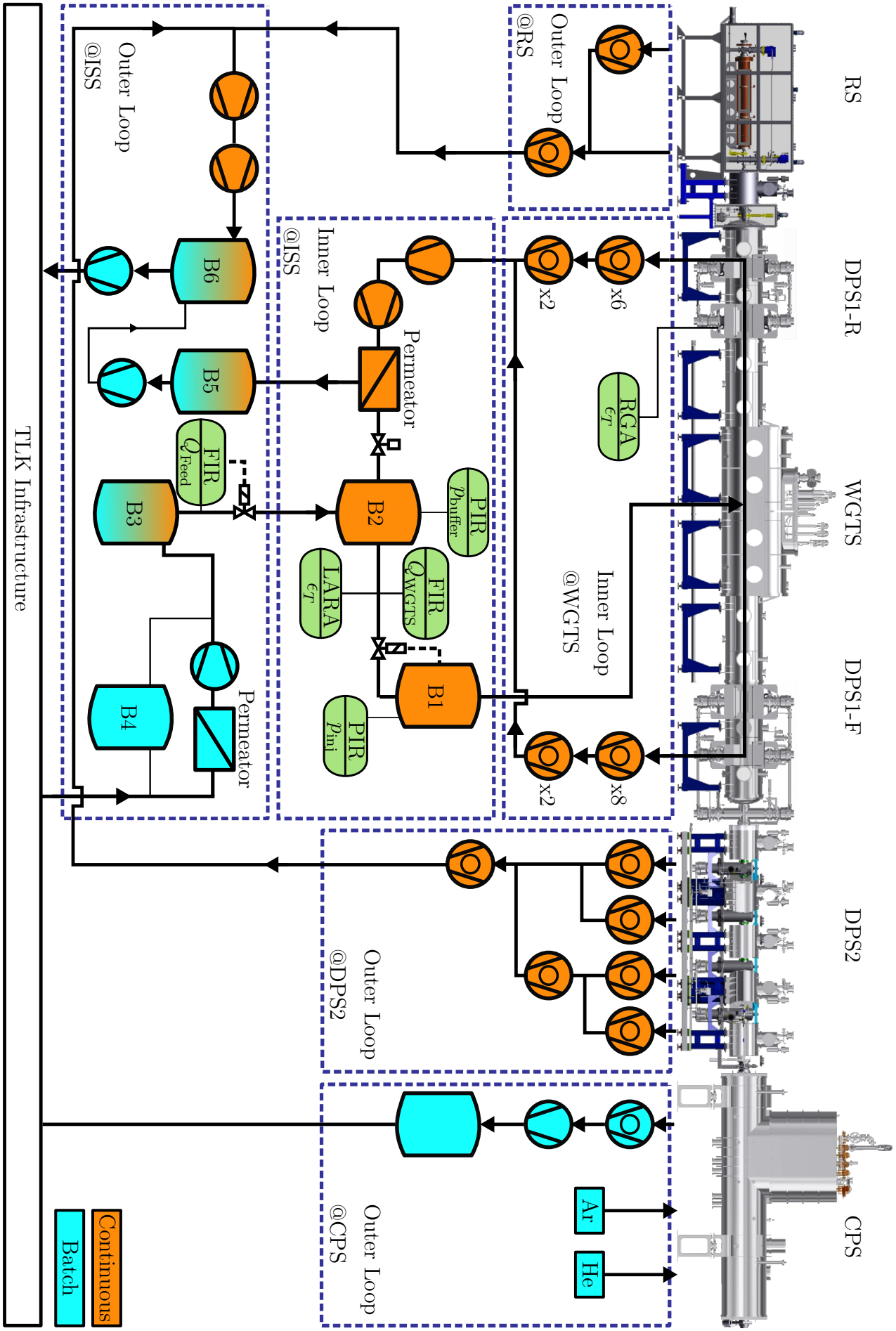

Figure 3.1.: **Schematic of the KATRIN tritium loops system.**

- After the tritium gas has passed through the KATRIN experiment, it consists of a mixture of hydrogen isotopologues containing less tritium than originally supplied, as well as other impurities from outgassing of the vacuum systems and pumps in the IL and OL [PB13]. From the EL, this gas is transferred to the *CAPER facility*. In the first stage of the CAPER process, Q_2 ($Q \in$ H, D, T) is separated from non-Q_2 molecules such as e.g. Q_2O or CQ_4, leaving a pure mixture of hydrogen isotopologues [Bor+05b; Dem+15]. In further steps, the tritium atoms bound in the non-Q_2 molecules is converted to Q_2 before being separated.
- After being purified by the CAPER facility, the hydrogen isotope mixture can either be sent to the ISS via the TTS for isotopic separation, to the TLG for long term storage, or back to KATRIN if the Q_2 gas mixture still fulfills the KATRIN tritium purity requirements.
- In addition to the above, there are connections from the EL, CAPER and the CPS to the *Zentrales Tritiumrückhaltunssystem* (ZTS). The ZTS converts tritium gas to tritiated water, which is then bound on molecular sieves. As the tritium is not recovered from this water, only waste gas with low tritium content is transferred to the ZTS to minimize losses. The resulting tritium free waste gas can then be disposed via the laboratory exhaust air without releasing tritium into the environment [BDG08].

The exchange of gas between the loop system and the TLK infrastructure is done batch wise. This is necessary due to the discontinuous nature of the involved purification processes. Typically, transfers from ISS to FL happen once a week and returns from EL to CAPER twice a week [Wel+20].

While the low endpoint energy of tritium makes external exposition irrelevant, incorporating tritium and the resulting internal exposure to β-radiation is hazardous. To prevent this, all systems which come into contact with tritium directly (primary systems) need to adhere to strict regulations [Wel+15]. Further ensuring the containment and safe handling of tritium, all primary systems are enclosed by glove boxes, which form a second containment. These glove boxes are held slightly below atmospheric pressure and the atmosphere inside of them is continuously purified. This is done to remove tritium from possible leakages or opening of the primary system for e.g. maintainance. As such, all primary systems inside the TLK, including those belonging to the KATRIN experiment, are contained within glove boxes [Sch+91]. Exceptions to this are the beam tubes of the WGTS and CPS, for which the cryostat isolation vacuum serves as the second containment.

3.2. Operation Modes of the Loop System

The KATRIN experiment requires excellent control and knowledge of the systematics affecting the neutrino mass measurement. To accommodate these requirements on the systematics, the loop system can be operated in three different operation modes:

- **Neutrino Mass Mode:** The mode which is used to take the data that will be used for neutrino mass analysis. (see section 3.2.1)

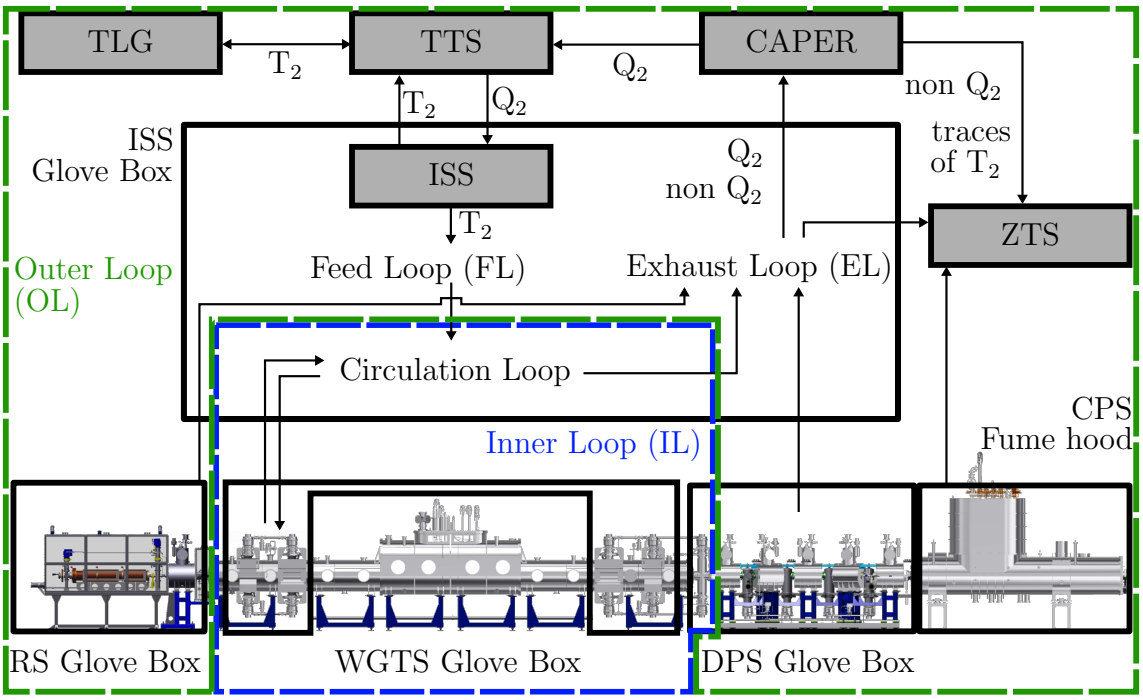

Figure 3.2.: **Integration of KATRIN into the TLK infrastructure.** Shown schematically are the connections between the components of the KATRIN tritium loops system to the different transfer, purification, and storage systems of the TLK

- **Tritium+Krypton Mode:** An operation mode of the IL in which gaseous krypton is circulated through the beam tube together with tritium. (see section 3.2.2)
- **Pure Krypton Mode:** In this mode, pure krypton is circulated through the source, without any tritium. (see section 3.2.3)

For the sake of providing a complete overview of the operation modes in their optimized versions, some results which will be derived in later chapters are already incorporated in the descriptions of the modes in the following subsections.

3.2.1. Neutrino Mass Measurement Mode

The neutrino mass measurement mode is the main configuration in which the loop system is operated. This mode is the most stable in terms of both gas injection as well as gas composition. It incorporates the stabilized buffers (section 3.3.1) and the gas purification system (section 3.3.5) as integral components. Thereby, this mode ensures the smallest possible impact on the source stability. A WGTS beam tube temperature at the 30 K-level is the standard for this mode, but it can in principle be run at every temperature achievable by the cooling system.
A schematic depiction of this operation mode is shown in fig. 3.3. It is operated as described in the following:

- Highly pure tritium gas from vessel B3 in the FL is continuously fed into B2 via mass flow controller RV2 with a flow rate (q_{feed}) of around 1 sccm to 2 sccm.

The setpoint of RV2 is automatically adapted to regulate the pressure inside of B2 to a setpoint from 100 mbar to 250 mbar.

- From B2, the tritium gas is fed to B1 over a laser Raman (LARA) cell for gas composition analysis, a mass flow meter (q_{WGTS}), and the regulation valve RV1. In a steady state, the flow rate q_{WGTS} is representative of that through the WGTS. Regulation valve RV1 controls the pressure of B1. The opening degree of RV1 is regulated by the pressure p_{inj} inside of B1. The pressure inside B1 is the main experimental parameter which can be used to set the column density inside of the source. It is set in the range of 1 mbar to 30 mbar for this mode, depending on the required column density.
- From B1, the gas is expanded via the tritium transfer line and the tritium injection capillary (section 3.3.2.1) into the injection chamber (section 3.3.3) inside the WGTS cryostat. The pressure p_{Kr} inside the injection chamber can be monitored by the pressure sensor connected to the tritium+krypton injection capillary (section 3.3.2.2).
- After being injected into the beam tube, the tritium gas freely streams towards the pumps of the DPS1 (section 3.3.4), where >99.9 % of it is pumped out. This gas is transferred back towards the ISS glove box via the tritium return line.
- In the next step, the gas is pushed through the permeator, a hydrogen isotopologue selective membrane filter (section 3.3.5). A small fraction of the circulating flow rate of up to 2 sccm is extracted and collected in B5.

  The loss of gas due to this is compensated by q_{feed}.
- After passing the permeator, the gas is fed back into B2, completing the cycle.

3.2.2. Tritium+Krypton Mode

The tritium+krypton mode is a special operation mode used to investigate systematic effects of the WGTS. In this mode, traces of gaseous $^{83\mathrm{m}}$Kr from the krypton generator (section 3.3.6) are mixed into tritium gas circulating through the WGTS. It has several key differences and limitations compared to the neutrino mass measurement mode:

- $^{83\mathrm{m}}$Kr would freeze out at low temperatures around 30 K, so the tritium+krypton mode needs to be operated at an elevated beam tube temperature of $T > 80$ K.
- The permeator of the IL would remove the $^{83\mathrm{m}}$Kr from the gas stream, so it can not be used to purify the gas stream during this mode.
- The concentration of $^{83\mathrm{m}}$Kr needs to be as high as possible to achieve the highest possible activity of $^{83\mathrm{m}}$Kr inside of the beam tube. This in turn means a minimization of the circulating tritium inventory while maintaining the desired tritium column density.
- As a result of a minimized gas amount coupled with the lack of a gas purification, isotopic exchange effects and impurity accumulation can be greatly magnified in the tritium+krypton mode.

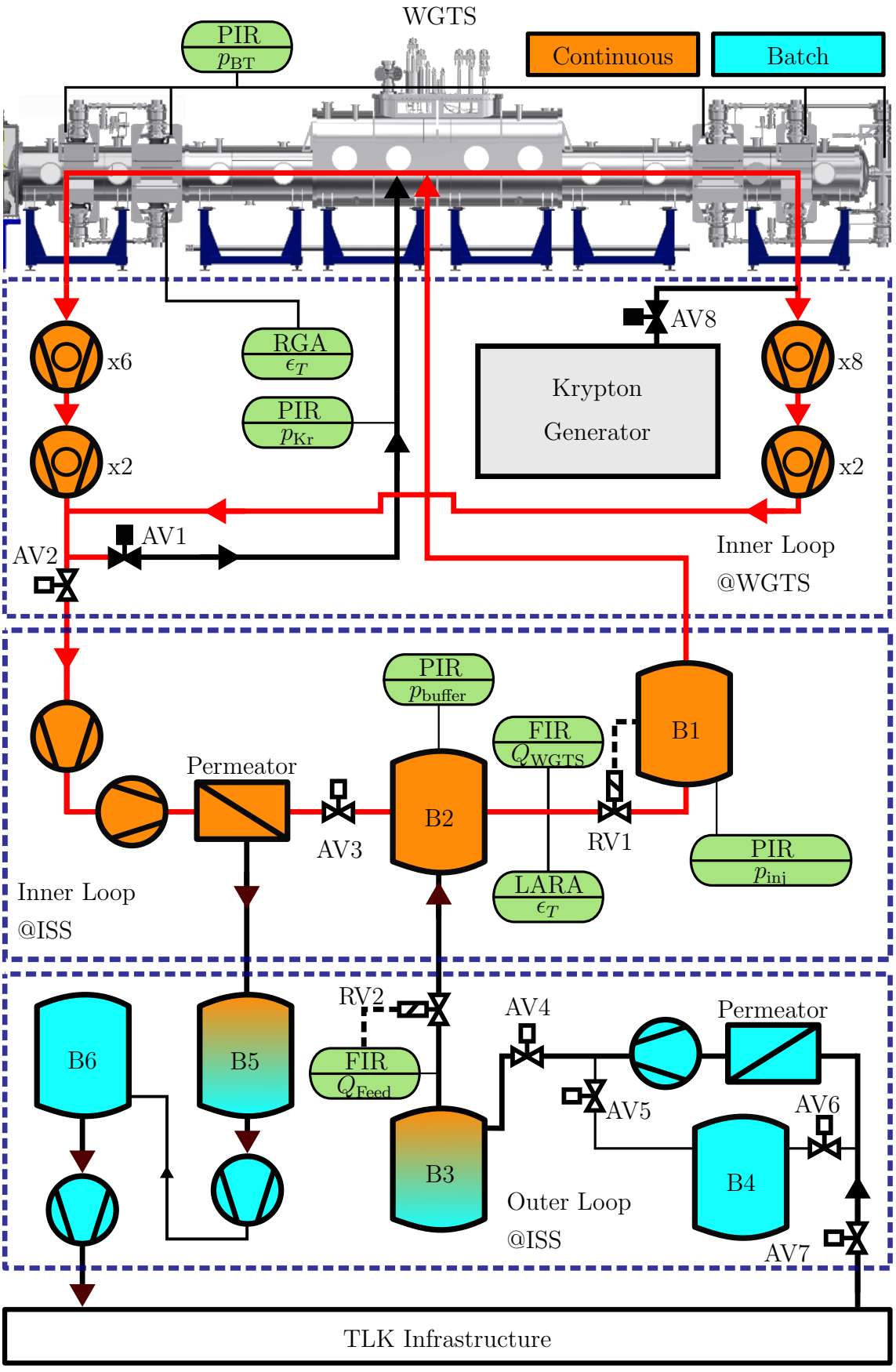

Figure 3.3.: **Schematic of the loop system in neutrino mass measurement mode.**

The operating scheme of the tritium+krypton mode is described in the following according to the schematic shown in fig. 3.4:

- By switching the valve states of AV1 and AV2 with regard to the neutrino mass measurement mode, the exhaust of the DPS1 pumps is circulated back into the injection chamber via the tritium+krypton injection capillary. The volume between the DPS1 pumps and the capillary serves as a buffer for the circulating tritium. The pressure inside this volume determines the column density of the WGTS.
- ^{83m}Kr from the krypton generator is injected at the bottom pump port of DPS1-F2 (see section 3.3.4). From there, the ^{83m}Kr mixes with the cycling tritium.
- As the DPS1 only recycles >99.9 % of the circulating gas, a fraction of the circulating tritium krypton mixture is continuously lost towards the DPS2 (section 3.4.2) and the RS (section 3.4.4). To compensate for this, a minuscule flow of tritium from B1 into the injection chamber is established, represented by the dashed red line in fig. 3.4. The extremely small flow of $\approx 10^{-4}\,\mathrm{mbar}\,\ell\,\mathrm{s}^{-1}$ needed for this necessitates the operation of the pressure stabilization at greatly reduced pressures on the order of 0.1 mbar to 0.5 mbar in B1. As the developement of this replenishment scheme of tritium in the tritium+krypton was part of the focus of this thesis, it is thematized in sections 5.1.2, 5.2.2 and 5.3.2.

3.2.3. Pure Krypton Mode

The pure krypton mode is a modification of the tritium+krypton operation mode where ideally only ^{83m}Kr is circulated through the WGTS beam tube. This mode is used to investigate source as well as spectrometer systematic effects. In terms of operation, this mode is executed identically to the tritium+krypton mode except for the lack of tritium. As such, fig. 3.4 without the dashed red line from B1 towards the WGTS is a schematic representation of this mode.

An issue inherent to this mode is the suppressed transport of the ^{83m}Kr through the system without carrier gas. A more detailed discussion of this can be found in sections 5.1.2, 5.2.2 and 5.3.3.

3.3. The Inner Loop of KATRIN - Stabilized Gas Circulation

The inner loop (IL) is responsible for the stable circulation of tritium through the WGTS. To reach the required source luminosity, a high tritium flow rate of $1.8\,\mathrm{mbar}\,\ell\,\mathrm{s}^{-1}$ ($\approx 40\,\mathrm{g}\,\mathrm{d}^{-1}$) is necessary. To realize this high flow rate, the IL of KATRIN was designed as a circulation loop with inline gas purification. For a schematic depiction refer to fig. 3.3. The design as a loop keeps the tritium inventory in the IL as low as possible, needing only on the order of <0.4 g ($\approx 1.4 \times 10^{14}$ Bq) tritium to operate. A downside of circulating gas is the accumulation of impurities. These

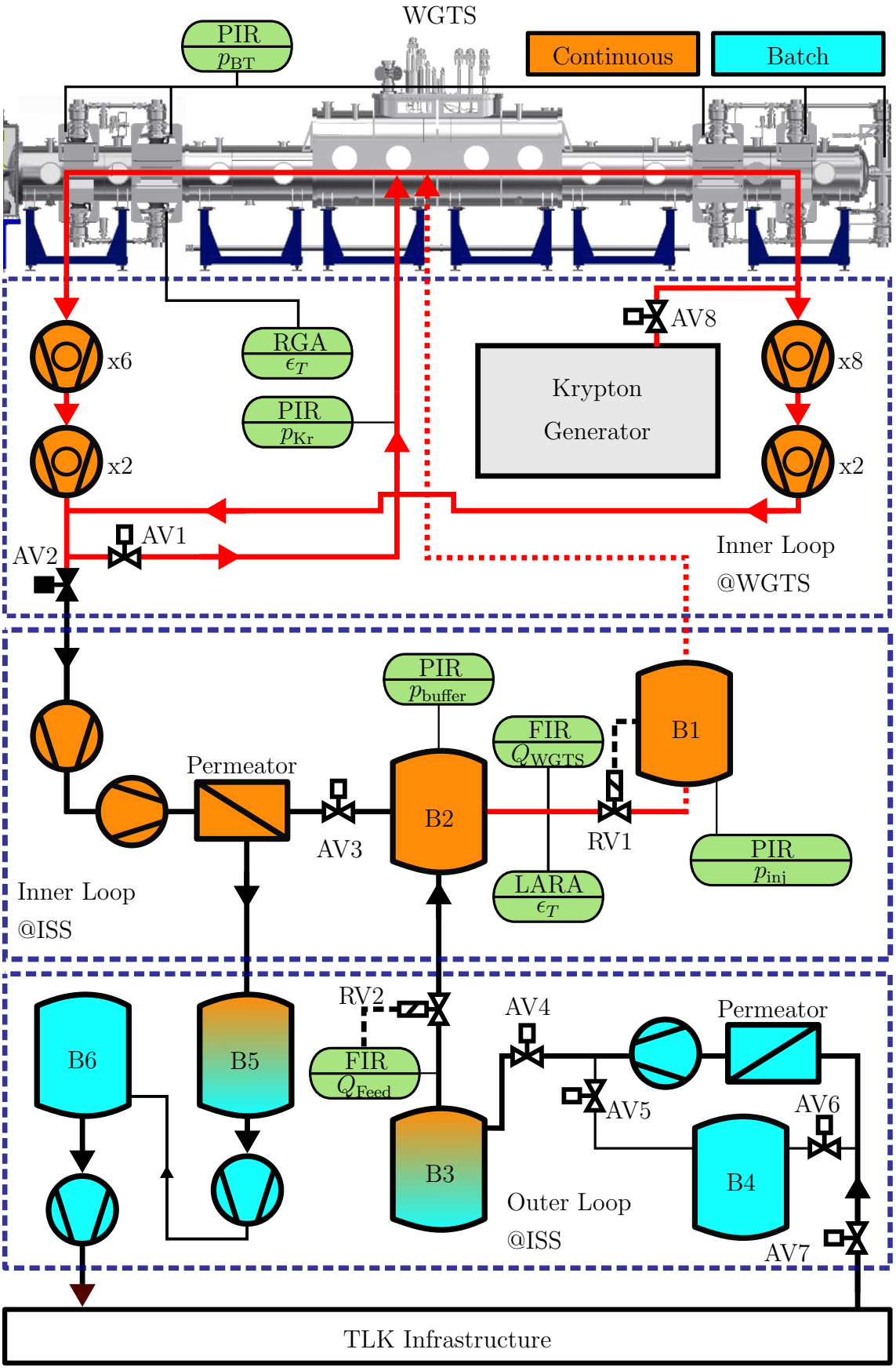

Figure 3.4.: **Schematic of the loop system in tritium+krypton mode.**

impurities are filtered from the tritium gas stream by the inline gas purification system.

For the ease of explanation, the IL has been partitioned into several sections. The stabilized buffer vessels (section 3.3.1) provide the stable tritium injection pressure which is then transferred via the tritium transfer line and tritium injection capillary (section 3.3.2) into the injection chamber (section 3.3.3). Once the tritium has passed through the WGTS, it is pumped by the DPS1 (section 3.3.4) before being filtered by the inline gas purification system (section 3.3.5).

3.3.1. The Stabilized Buffer Vessels

The IL contains two buffer vessels (B1 and B2 in fig. 3.1), which are pressure stabilized to ensure a stable injection pressure into the WGTS.

- **Buffer B1** has a volume of $\approx 15\,\ell$ and can be operated in a pressure range of 0 mbar to 30 mbar. The pressure inside of B1 is measured and regulated by two `MKS 690A` high accuracy capacitance manometers[1]. The flow of tritium gas coming from B2 to B1 is regulated by a `MKS 148J` type all-metal flow control valve. To ensure constant injection conditions, the temperature of vessel B1 can be stabilized at 40 °C.
- **Buffer B2** has a volume of $2\,\ell$ and can be operated in a pressure range of up to 300 mbar. The pressure inside of B1 is measured by a `MKS 626` capacitance manometer[2]. The flow of pure tritium from the FL pure tritium buffer vessel B3 to B2 is regulated by a `MKS M200` flow controller with a F.S. of 2 sccm ($\approx 0.034\,\mathrm{mbar}\,\ell\,\mathrm{s}^{-1}$). This flow controller is set to regulate on the pressure setpoint for the pressure inside B2. Between B2 and B1, a `MKS 179` all-metal mass flow meter with a full scale (F.S.) of 200 sccm ($\approx 3.4\,\mathrm{mbar}\,\ell\,\mathrm{s}^{-1}$) measures q_{WGTS} if the system is in a steady state.
- **A cell for laser Raman spectroscopy (LARA)** is installed in the connection between the two buffer vessels B1 and B2 [Fis+11; Sch+13]. This LARA system allows for contact free gas composition analysis of molecules and is able to differentiate between H_2, HD, D_2, HT, DT, and T_2. It is however unable to detect atomic gas species such as ^{3}He from tritium decay. In the IL however, this is not important as the inline gas purification (see section 3.3.5) ensures that gas components other than hydrogen isotopologues are reduced to the sub-ppm level. The intensity of the LARA signal is proportional to the number of gas molecules and therefore the pressure inside the LARA cell.

3.3.2. The Injection Lines

The injection lines of the IL feed gas into the injection chamber inside the WGTS cryostat:

[1] `MKS 690A12TRC` and `690A12TRA`, F.S.: 133 mbar, accuracies: 0.12 %rdg and 0.05 %rdg
[2] `MKS 626AX13MBD`, F.S.: 1000 mbar, accuracy: 0.15 %rdg

- The tritium transfer line and the tritium injection capillary connect the stabilized buffer vessel to the injection chamber. It is described in section 3.3.2.1.
- The tritium+krypton capillary runs in parallel to the tritium injection capillary, and is used in the krypton operation modes. For details on this capillary, see section 3.3.2.2.

Detailed information on the geometry of the tritium transfer line and injection capillaries as it is used for simulations can be found in appendix B.2.

3.3.2.1. The Tritium Transfer Line and Tritium Injection Capillary

The tritium transfer line connects the primary system of the IL inside the ISS glove box to that inside of the WGTS cryostat. It consists of ≈10.5 m of stainless steel piping with an internal diameter of 25 mm, followed by an automatic valve and a ≈80 cm section of 10 mm internal diameter. A `MKS 627` capacitance manometer[3] is connected to this section. The tritium transfer line can be separated from the tritium injection capillary via a manual valve.

The tritium injection capillary consists of two sections with different diameters. Over its length, the temperature drops from room temperature to the source tube temperature level of 30 K during standard operation. A depiction of the capillary along with more information on its geometry can be found in fig. 3.5.

3.3.2.2. The Tritium + Krypton Injection Capillary

The tritium+krypton injection capillary is used in the tritium+krypton and the pure krypton operation modes to inject gas pumped by the DPS1 (see section 3.3.4) directly back into the source. It runs in parallel to the tritium injection capillary. The difference between both capillaries is that the tritium+krypton injection capillary has a uniform inner diameter of 6 mm over its entire length. Similarly to the tritium injection capillary, a `MKS 627` capacitance manometer[4] is connected to the tritium+krypton injection capillary, with which the injection chamber pressure can be monitored during neutrino mass measurements.

3.3.3. The Injection Chamber

The injection chamber is located in the central part of the WGTS source tube and is responsible for the axially homogeneous injection of tritium gas into the source tube. A cross section of the injection chamber surrounding the source tube can be seen in fig. 3.6.

The injection chamber is a hollow cylinder surrounding the source tube. It has a width of ≈4 mm between inner and outer diameter, and a length of 95 mm. The injection capillaries are connected to its downstream end. Gas entering through the capillaries is injected homogeneously into the source tube by an array of 415 orifices

[3] `MKS 627F.1MBD5B`, F.S.: 0.1 mbar, accuracy: 0.15 %rdg
[4] `MKS 627FU2TBE5B`, F.S.: 0.02 torr, accuracy: 0.25 %rdg

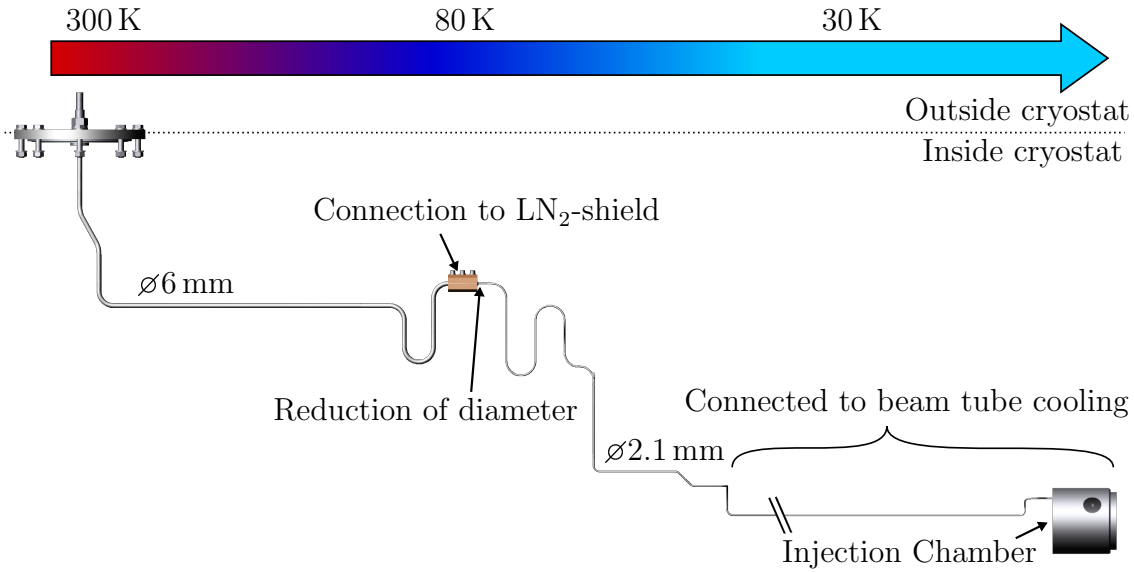

Figure 3.5.: **CAD model of the tritium injection capillary.** Shown is the tritium injection capillary inside the WGTS together with the flange at which it enters the WGTS cryostat on the left. From that point, the capillary is a ≈1.2 m long pipe of 6 mm inner diameter up to the copper colored connection to the LN_2 shield of the WGTS cryostat. At this point, a concentric reducer with a length of <2 mm connects to the second section of the capillary with a 2.1 mm inner diameter. This section continues for ≈5.8 m until it reaches the injection chamber at the center of the source tube to the right. The final ≈4.9 m of the capillary is brazed to the source tube cooling system. The CAD part of this illustration is based on a CAD model provided by S. Lichter.

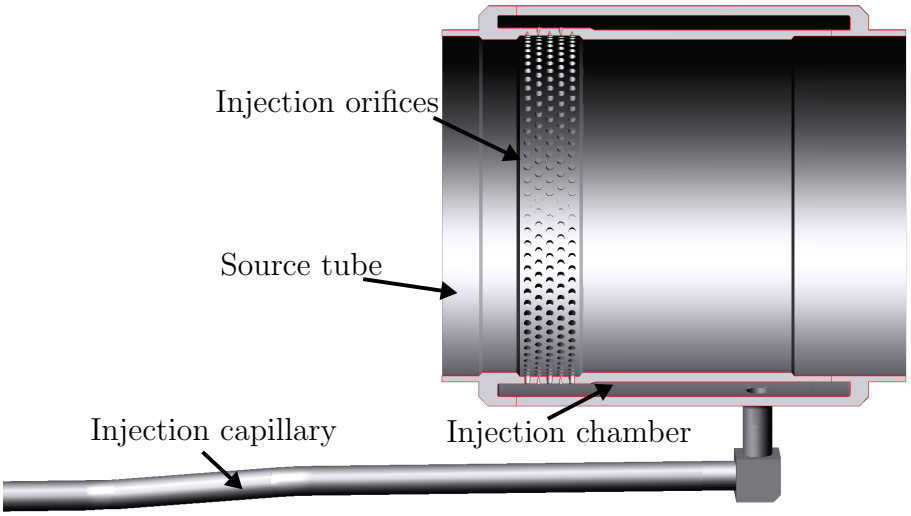

Figure 3.6.: **Cross section view of the injection chamber.** Shown is the central section of the WGTS source tube with the injection chamber surrounding it. The pipe entering the injection chamber is the tritium+krypton injection capillary. The tritium injection capillary is connected similarly but not shown as it is cut out due to the cross section. The CAD part of this illustration is based on a CAD model provided by S. Lichter.

of 2 mm diameter. The number and dimension of orifices was chosen to avoid the formation of shock waves and their accompanying temperature variations, as well as gas flow vortices [Sha10].

3.3.4. The Differential Pumping System DPS1 of the WGTS

After the tritium gas is injected into the the center of the source tube, it freely flows towards both ends, where it is pumped at differential pumping ports, called DPS1-R (rear) and DPS1-F (front).

DPS1-R and DPS1-F each consist of two pump ports connected by a tube of 1 m length. The pump ports DPS1-R1 and DPS1-F1 closer to the injection chamber are connected via gate valves to 4 `MAG W2800`[5] turbo molecular pumps. The pump ports DPS1-R2 and DPS1-F2 further outward are only connected to 2 `MAG W2800` pumps. Between the DPS1-F2 and the DPS2 of the OL, an additional pump port called pump port 0 (PP0) with 2 `MAG W2800` pumps is installed to minimize gas loss from the IL to the OL.

The forepressure for these 14 `MAG W2800` pumps is provided by 4 `HiPace`[6] TMPs. The `MAG W2800` are connected to the `HiPace` grouped by front (DPS1-F, PP0) and rear (DPS1-R), as well as top and bottom of the cryostat. An image of the instrumentation of the top part of DPS1-F outside of the WGTS cryostat is shown in fig. 3.7.

[5] `Oerlikon Leybold MAG W2800`, pumping power: $2100\,\ell\,s^{-1}$ for H_2
[6] `Pfeiffer HiPace 300`, pumping power: $220\,\ell\,s^{-1}$ for H_2

Figure 3.7.: **DPS1-F top pumps and piping during commissioning.** Shown are the top pumps and piping of the DPS1-F1 and DPS1-F2 pumping ports. The instrumentation on the bottom of DPS1-F1 and DPS1-F2 is similar. This setup is mostly mirrored by DPS1-R.

The pressure inside each pump port is monitored by a `MKS 423` cold cathode gauge[7]. In addition, a `MKS HPQ3` residual gas analyzer (RGA) is connected to DPS1-R2, allowing the monitoring of the gas composition of the source if no magnetic field is applied to it. The forepressure of the `MAG W2800` pumps is measured by 4 `MKS 317` Pirani gauges[8], while the forepressure of the `HiPace` pumps is measured by a `MKS 750`[9] and a `MKS 722`[10] capacitance manometer.

3.3.5. The Inline Gas Purification

During circulation of gas inside the IL, impurities in the gas stream build up. These are either caused by isotopic exchange with hydrogen isotopologues from the vessel walls, radiochemical reactions, ^{3}He buildup from tritium decay, or outgassing, leakages, and permeation from components of the vacuum system. Of particular note for the latter are the used turbomolecular pumps, which release a variety of gas species on their exhaust side [PB13]. These impurities would adversely impact KATRIN's search for the neutrino mass. Non-tritium molecules can serve as additional targets for electron scattering, thereby reducing the statistics near the endpoint region of the β-decay. They also smear the spectrum of energy loss via scattering, which is needed

[7] `MKS 104230002`, range: 1×10^{-11} mbar to 1×10^{-2} mbar, reproducibility: 5 %rdg
[8] `MKS 103170012SH`, range: 1.3×10^{-3} mbar to 1.3×10^{3} mbar, reproducibility: 5 %rdg
[9] `MKS 750C51TCD4GA`, F.S.: 50 torr, accuracy: 0.25 %rdg
[10] `MKS 722B21TCE2FA`, F.S.: 20 torr, accuracy: 1.0 %rdg

to interpret the measured spectra [Rod21]. Furthermore, tritium atoms bound in molecules other than T_2, in general, have a different binding energy, which causes a shift in the effective endpoint energy of the β-spectrum emitted by these atoms [Bab+12; Kle+19]. The overlay of these shifted spectra over the molecular tritium spectrum once again causes a smearing of the experimentally measured spectrum.

As a countermeasure, the IL implements an inline gas purification system. This system consists of a palladium silver (PdAg) membrane filter (permeator). Hydrogen isotopes can pass this permeator as atoms, leading to a high selectivity with which purities >99.9999 % of hydrogen can be achieved [Got70; Bor+05a]. The permeator can remove all impurities from the gas stream aside from non-T_2 hydrogen isotopologues. To address these remaining impurities, a constant flow of gas of up to $0.034\,\mathrm{mbar}\,\ell\,\mathrm{s}^{-1}$ (2 sccm) is extracted on the retentate side of the permeator and transferred to the EL. The amount of gas removed from the system this way is compensated by high purity tritium from the FL.

A side effect of the atomic permeation of hydrogen isotopes through the permeator is the catalyzation of isotopic exchange between different hydrogen isotopologues. To illustrate this, one can take a look at the protium deuterium equilibration reaction:

$$H_2 + D_2 \rightleftharpoons 2HD \tag{3.1}$$

For protium and deuterium at standard conditions, this reaction is heavily suppressed [HAS81] with large time constants. The radioactivity of tritium provides a source of ions which catalyze this as well as many other radiochemical reactions. This effect can shorten equilibration time constants significantly [DM53].

Upon permeating through the PdAg membrane however, the isotopes are immediately equilibrated to the equilibrium concentrations corresponding to the membrane temperature [TK79].

3.3.6. The Krypton Generator

In order to gain a detailed understanding of the systematic effects of the WGTS, gaseous ^{83m}Kr can be injected into it in special operating modes described in section 3.2.2 and section 3.2.3.

^{83m}Kr is a meta-stable state of krypton with a half life of (1.862 ± 0.002) h [Sen+18]. This meta-stable state decays via the cascade of two electromagnetic transitions with energies of 32.2 keV and 9.4 keV [McC15] to the ground state. These transitions in turn produce narrow conversion electron lines. The ^{83m}Kr is generated via electron capture of its parent isotope ^{83}Rb, which has a half life of (86.00 ± 0.44) d [Gin76]. On one hand, the short half life of ^{83m}Kr allows the injection into the source without a lasting contamination. On the other hand, the sizable half life of ^{83}Rb allows for the construction of a generator of ^{83m}Kr with ex-situ produced ^{83}Rb. For the KATRIN experiment, this has been realized by the synthesis of $\approx 10^9$ Bq of ^{83}Rb at the Řež cyclotron with subsequent deposition of the ^{83}Rb in zeolite beads [Vén+05].

The krypton generator inside the IL consists of such a zeolite ^{83}Rb source, surrounded by lead shielding which blocks the γ-radiation from the ^{83}Rb decay. This source is connected to the pumping duct of the bottom side of DPS1-F2.

3.4. The Outer Loop of KATRIN - Tritium Supply and Gas Flow Reduction

The purpose of the outer loop (OL) of the KATRIN tritium loop system is twofold. One of its tasks is to provide the interface between KATRIN and the TLK infrastructure in the form of the feed loop and exhaust loop (FL and EL, section 3.4.1). The second responsibility is the further reduction of the tritium gas flow rate towards the spectrometer section to reach a total of 14 orders of magnitude of reduction with regard to the injection flow rate. This is needed to prevent tritium induced background in the spectrometers [KAT05; Mer+13].

The so called *transport section* is responsible for gas flow reduction, and consists of the second differential pumping (DPS2, section 3.4.2) and the cryogenic pumping (CPS, section 3.4.3) sections. In addition, the OL also provides the vacuum infrastructure for the rear section (RS, section 3.4.4).

3.4.1. The Feed Loop and Exhaust Loop

The FL and the EL are situated inside of the ISS glove box. They are the interface to the TLK infrastructure. Both subsytems are interconnected with each other and the IL to allow for flexible gas processing.

- **The FL** consists of two buffer vessels B4 and B3 with $\approx 25\,\ell$ and $\approx 4\,\ell$ volume. Between both vessels, a PdAg permeator followed by a combination of a Normetex and a Metal Bellows pump are installed. When pure tritium gas from the TLK infrastructure arrives via a connection to the ISS, it can be pumped into B4 directly or passed through the permeator first. From B4 the gas is then transferred into B3 once per day during standard operation, passing through the FL permeator. From B3, the gas is continuously fed into B2 of the IL.
- **The EL** consist of two buffer vessels B5 and B6 with $\approx 106\,\ell$ and $\approx 25\,\ell$ volume. It furthermore contains two Normetex and a Metal Bellows pump combinations as well as one TMP[11]. The vessel B5 is pumped out daily into B6 to maintain a pressure <20 mbar inside of it. Driven by the pressure gradient, the retentate gas of the IL permeator at a pressure >100 mbar is continuously extracted into B5. The gas transferred daily from B5, as well as the continuous stream of exhaust gas from DPS2 and RS, are collected inside B6. During standard operation, the gas is transferred twice a week from B6 to the CAPER facility, which forms the first step in purifying the exhaust gases.

3.4.2. Differential Pumping in the DPS2

The second differential pumping section, DPS2, as shown in fig. 3.8 and simplified in fig. 3.1, consists of four pump ports (PP1-PP4) in series. To increase pumping efficiency for neutral tritium gas and prevent a direct line of sight between the WGTS

[11] Pfeiffer TMU 200 M

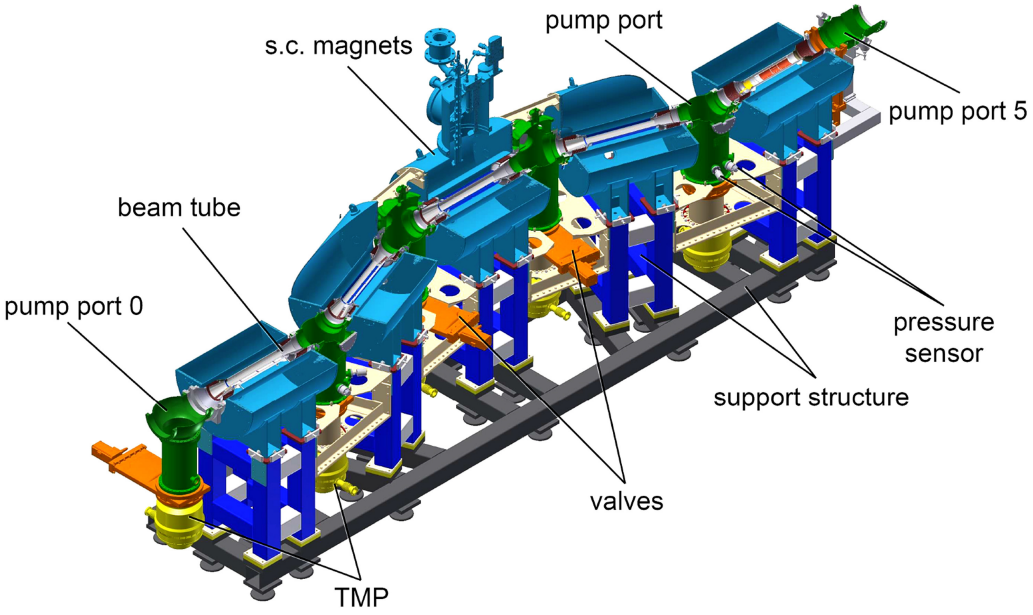

Figure 3.8.: **Cross sectional CAD drawing of the DPS2.** Shown is the DPS2 vacuum and magnet system. In addition, pump port 0 of the DPS1 and pump port 5 of the CPS is also depicted as the interface to the connecting components. Illustration as published in [Fri+19] under the CC BY license https://creativecommons.org/licenses/by/4.0/.

and the spectrometers, the beam tube inside the DPS2 forms a chicane. The beam tube leaves PP1 at an angle of 20° and is brought back onto a parallel axis by PP2. PP3 & PP4 mirror this to return the beam tube back onto its original axis.
The β-electrons are guided through this chicane by super conducting magnets through whose warm bore the beam tube segments run between the pump ports.

Besides this chicane, the beam tube of the DPS2 also contains dipole and ring electrodes for tritium ion monitoring and blocking [KG17]. While this instrumentation inside the beam tube reduces its diameter, and therefore conductance, making the differential pumping more effective, they also negatively impact the vacuum conditions inside the beam tube by partially trapping volumes and outgassing.

The pumping system of the DPS2 consists of four `MAG W2800` TMP connected to each pump port. The forepressure of these pumps is provided by two cascaded `HiPace` pumps. In this cascaded setup, the two `MAG W2800` pumps at the pump ports closest to the DPS1 (PP1 & PP2) and the two closest to the CPS (PP3 & PP4) are grouped together and each group is pumped directly by one of the `HiPace` pumps. To achieve the lowest possible ultimate pressure at the entrance of the CPS, the `HiPace` pump providing the forepressure for the PP3 & PP4 `MAG W2800` pumps in turn is provided its forepressure by the `HiPace` pump providing the forepressure for PP1 & PP2. This last pump is connected to the DPS2 return line, through which the pump exhaust is pumped into the EL in the ISS glove box by a Normetex + Metal Bellows combination.

Similarly to the DPS1, the pressure inside the pump ports is monitored by `MKS 423` cold cathode gauges. In addition, a `MKS HPQ3` RGA is connected to PP4, allowing to monitor the gas composition when no magnetic field is applied to the DPS2.

3.4.3. Cryogenic Pumping in the CPS

The cryogenic pumping section, CPS, aims to reduce the flow rate of tritium towards the spectrometers by trapping the tritium on a cold layer on argon frost. The cryogenic pump itself consists of the gold coated beam tube inside of the CPS cryostat, onto which a layer of argon frost can be deposited to form the actual cryogenic pump. By cooling down this layer to the 3 K-level with a dedicated LHe-cooling system, a reduction of the gas flow rate by at least 7 orders of magnitude can be achieved [Röt17; Röt19]. The cryogenic pump of the CPS is limited by the maximum amount of 3.7×10^{10} Bq (1 Ci) of tritium allowed to be adsorbed on the Ar frost. To regenerate the pump and remove the tritium, the beam tube is heated and the Ar frost is purged by a flow of He gas. This results in a mixture of mostly He with a small admixture of Ar and traces of tritium. Due to the comparatively low amount of tritium in this purged gas, it is transferred to the ZTS.

Attached to the CPS cryostat are the *forward beam monitor* (FBM) and *condensed krypton source* (CKrS). The FBM consists of a detector for electrons and a magnetic field sensor. Its main purpose is the continuos monitoring of the source activity by measuring the electron rate at the outer rim of the beam tube. It can however be moved inside the beam tube to scan for inhomogeneities along its cross section [Ell+17; Ell19; Hau19]. The CKrS consists of ^{83m}Kr frozen onto a substrate, providing a source with ≈2 mm diameter of mono-energetic conversion electrons for calibration purposes. Similar to the FBM, it can be moved across the beam tube [Ful18; Dyb19].

3.4.4. The Rear Section

The rear section, RS, forms the electrical and vacuum technical termination of the WGTS in the direction facing away from the spectrometers. The main components of the RS are the *rear wall* (RW), the *beta induced X-ray spectrometry* (BIXS) detectors, the *electron gun* (E-Gun) [Bab+12], as well as the vacuum system surrounding them:

- The **RW** is a gold plated stainless steel disk, which serves as the electrical termination of the WGTS. Electrons leaving the WGTS towards the RS are guided by magnetic fields towards the RW, connecting the potential of the RW to the potential in which tritium decays inside the source [Bab14].
- A side effect of the source electrons impinging on the RW is the creation of X-rays. The resulting spectrum of bremsstrahlung and characteristic X-ray lines of the gold are then used by the **BIXS detectors** to monitor the activity of the WGTS [Röl15].
- The **E-Gun** of the RS is a calibration source which produces quasi mono-energetic electrons with selectable incident angle with regards to the magnetic field lines [Bab14; Beh+17]. It is based on the production of photo-electrons on a thin gold target by monochromatic UV-light. These electrons are then accelerated towards the WGTS by high voltage electrodes, which can be coupled to the main spectrometer high voltage.

- Tritium gas entering the RS via gaps around and a central hole in the RW is pumped by a **pumping system** consisting of two TMPs. The TMP pumping the chamber containing the E-Gun is provided its forepressure by the second TMP. The second TMP also pumps the section of the RS closer to the RW. This TMPs is provided its forepressure by the same pumps in the EL as the DPS2. This pumping setup is needed to reach a low pressure of 1×10^{-8} mbar to 1×10^{-7} mbar inside the RS, which is necessary to prevent high voltage break downs of the E-Gun.

4. Overview of Initial Measurements

Over the course of the commissioning of the loop system with deuterium and tritium, followed by the first neutrino mass measurements, the loop system has been thoroughly characterized. An overview of the different phases will be given in section 4.1. Sections 4.2 and 4.3 sketch out improvements of the system which have been identified during these initial measurements, before being addressed in detail in chapter 5. A short preview of the characterization of monitoring tools of gas composition and column density will be given in sections 4.4 and 4.5, with details following in chapters 6 and 7.

4.1. Overview of the KATRIN Measurement Campaigns So Far

As of the writing of this thesis, five distinct measurement phases with the loop system, summarized in table 4.1, have been carried out:

- After the completion of the loop system in early 2018, a **Loop Commissioning** phase using pure D_2 was performed. In this measurement phase the principal functionality of the system was verified. Furthermore, no magnetic fields were used during this phase, allowing for a characterization of the gas composition inside of the source using the installed RGA.
- After the **Very First Tritium** (VFT) test phase with strictly limited trace amounts of tritium, the first measurement phase, called **First Tritium** (FT), using trace amounts of tritium in deuterium, followed this commissioning phase. This allowed a first check of the entire KATRIN setup while minimizing contamination of the system.
- The low contamination was desirable in order to keep the tritium background inside the source as low as possible for systematic measurements with deuterium in the following **STS3a** measurement phase.
- With the commissioning completed and important systematics measured, the KATRIN experiment then went on to using highly pure tritium in its first neutrino mass measurement campaign **KNM1**. The new upper limit on the neutrino mass of $1.1\,\mathrm{eV}/c^2$ (90 % confidence level) from this campaign has been published in [Ake+19].
- Following this proof of the capabilities of KATRIN, the tritium column density was increased to a level close to the design value of $5 \times 10^{21}\,\mathrm{m}^{-2}$ for the second neutrino mass measurement campaign **KNM2**.

Table 4.1.: **Overview of the KATRIN measurement phases.**

Name	Date	Circulated gas	ϵ_T in %
Loop Commissioning	Spring 2018	D_2	0.0
First Tritium	Summer 2018	D_2 with DT traces	≈0.5
STS3a	Fall 2018	D_2	0.0
KNM1	Spring 2019	T_2	>95.0
KNM2	Fall 2019	T_2	>97.0

4.2. Readout Limitation of the Injection Pressure Stabilization

The stability of the injection pressure is an essential parameter for a stable column density of the WGTS. This pressure is stabilized by a PID[1] regulation using the pressure p_{inj} in B1 as an input to control the opening degree of the regulation valve RV1. To facilitate this, p_{inj} is monitored with a high degree of accuracy by two `MKS 690A` capacitance manometers.

Already during commissioning of the loop system with D_2, a stabilization of the pressure on a level below 0.1 % has been achieved. The presence of digitization steps (see fig. 5.4) in the pressure signal however showed that the readout system did not make full use of the pressure sensor's capabilities. The improvement of the pressure readout as well as its impact on the regulation system are presented in sections sections 5.2.1 and 5.3.1.

4.3. Instability of the Krypton Operation Modes

Due to the limitations stemming from low gas inventory and the lack of gas purification, inherent to the krypton modes as described in sections 3.2.2 and 3.2.3, these modes cannot be stabilized to the same level which can be achieved in the neutrino mass measurement mode. In the original operating scheme for the tritium+krypton mode, tritium gas is filled into the WGTS only discontinuously. The loss of gas towards the DPS2 and the RS from the WGTS leads to a sawtooth structure in the pressure which is shown in fig. 5.2. To counteract this effect, a continuous refilling scheme has been developed and successfully put to use. This enhanced operation scheme is presented in sections 5.2.2 and 5.3.2.

In the pure krypton mode, a steady increase of ^{83m}Kr activity inside of the source is observed. This increase is due to the necessity of a carrier gas to transport the ^{83m}Kr through the tritium+krypton injection capillary. Due to outgassing of the WGTS beam tube and the DPS1 pumps and piping, the pressure inside the IL increases with time, providing more carrier gas. A detailed investigation of this phenomenon and a possible solution to it is given in sections 5.2.3 and 5.3.3.

[1] proportional-integral-derivative

4.4. Isotopic Exchange effects in the Inner Loop

The gas composition of the WGTS is highly important for the stability of the source activity. Due to the difficulty of actively controlling the gas composition while maintaining the highest possible tritium concentration, the loops system employs a gas filtration system combined with a precise laser Raman monitoring system.

Despite this, however, changes in the gas composition as shown in fig. 6.5 on the 1 %-level have been observed. A detailed discussion of the observed effects and attempts at modeling them are presented in chapter 6.

4.5. In-Situ Column Density Monitoring Methods

For neutrino mass measurements, the column density of gas inside the WGTS needs to be known precisely to account for systematic effects such as the energy loss of electrons via scattering on the gas. The most direct method to measure this is to use the E-Gun of the RS to measure this scattering of electrons. With it, accuracies on the column density times cross section $\rho d\sigma$ on a level $<0.2\,\%$ can be reached. However, this method can not be used in parallel to the neutrino mass measurements and uses up a non-negligible amount of time. Therefore making frequent use of it, e.g. after every run, would significantly extend the KATRIN run time.

To overcome this limitation, in-situ monitoring methods which can be applied during normal neutrino mass measurements have been developed and characterized. These methods and studies on the influence of external effects on the column density using them are presented in chapter 7.

5. Optimization of the Stabilization of Tritium Injection into the WGTS

One of the key parameters influencing the source activity stability is the injection pressure p_{inj} of tritium into the source tube. This chapter describes the accurate control and stabilization of this parameter. In the neutrino mass measurement mode, this stabilization is realized via a respective PID-regulation system for the temperature of and pressure p_{B1} in buffer vessel B1 (see fig. 3.3). In the tritium+krypton mode, it is the pressure p_{DPS1} behind the DPS1 HiPace TMPs (the volume containing AV1 in fig. 3.4) which needs to be held constant. Gas dynamical effects due to the transfer line and injection capillary between B1 or the volume behind the DPS1 TMPs and the injection chamber are discussed in more detail in section 7.2.1.2 and section 7.2.3.

This chapter is segmented into three parts. Section 5.1 contains an overview of the pressure stabilities in the different operation modes which were achieved with the system as it was first commissioned. In addition, the issues which limit the pressure stability are identified. This is followed by the measures which were taken to improve upon the pressure stability in all operation modes in section 5.2. Finally, the achieved pressure stability after these modifications is shown and discussed in section 5.3.

5.1. Results of Stability Measurements before Optimizations

The following subsections show the injection pressure stability achieved with the Loop system during the First Tritium and STS3a measurement campaigns in 2018. At this point, no modifications to the initially commissioned setup were done, and no refined operation schemes had been worked out. Exemplary data for all operation modes will be shown and the peculiarities of stabilization in each mode will be addressed.

5.1.1. Achieved Stability in Neutrino Mass Measurement Mode

For the stability measurements in neutrino mass measurement mode, gas is circulated in the IL at a constant pressure setpoint in B1. Figure 5.1 shows the p_{B1} pressure

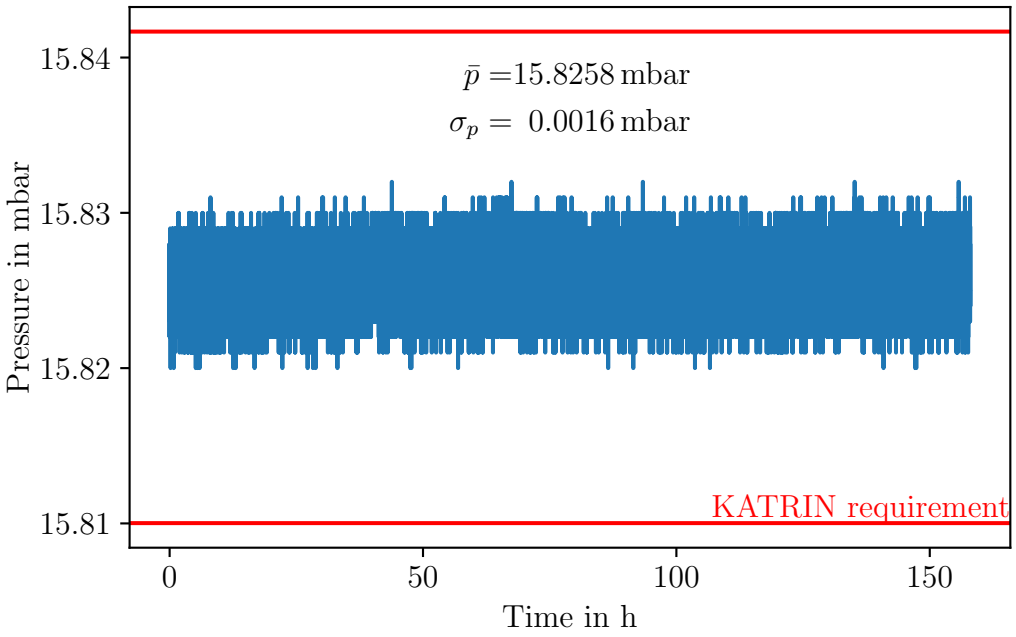

Figure 5.1.: **Pressure inside the stabilized buffer vessel B1.** Shown is the pressure p_{B1} during a <150 h period of stable IL operation during the First Tritium campaign. Additionally, the KATRIN stability requirements of 0.1 % are shown in red.

readout in B1 during a stable operation period of the First Tritium measurement phase. For this particular set of data, the relative values for the peak-to-peak and standard deviation as a measure of stability are:

$$\frac{\Delta p_{\mathrm{ptp}}}{\bar{p}} = 0.038\,\%\,, \tag{5.1}$$

and

$$\frac{\sigma_p}{\bar{p}} = 0.0098\,\%\,. \tag{5.2}$$

The pressure stability surpasses the requirement of a standard deviation <0.1 % by one order of magnitude, and even the peak-to-peak value surpasses it by more than a factor 2. This result verifies the stability of <0.1 % seen in test measurements done prior to complete commissioning of the loop system, where the missing IL components outside of the ISS glovebox were substituted with a bypass between the stabilized buffer and the inline gas purification system [PSB15].

Analyzing the data on short timescales on the order of the regulation parameters, one can find a non-Gaussian fluctuation in the pressure. Despite already surpassing the initial KATRIN design [KAT05], further reduction of fluctuations potentially allows a larger budget for other systematics, or a better sensitivity on the neutrino mass. Therefore, the origin of these fluctuations has been investigated and a countermeasure devised and implemented. The details on this can be found in section 5.2.1, while the results of this improvement are shown in section 5.3.1.

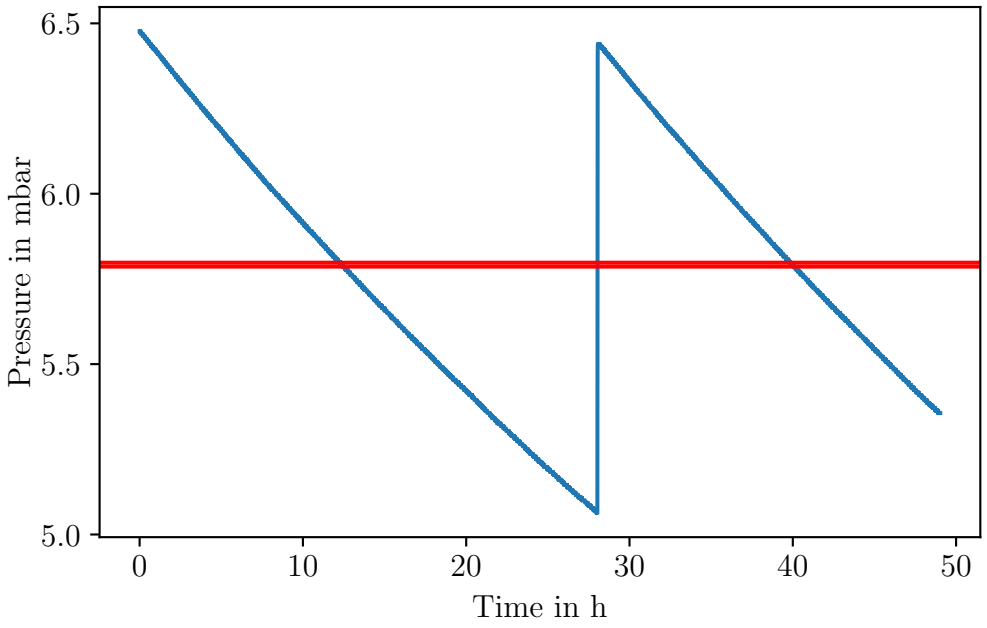

Figure 5.2.: **Pressure decrease in IL during tritium+krypton mode.** Shown is the pressure at the inlet of the tritium+krypton capillary. In the original tritium+krypton operation mode, gas loss towards the DPS2 and RS cause a steady decrease of pressure in the IL, resulting in big changes in the column density.

5.1.2. Achieved Stability in Tritium+Krypton Mode

In the original design of the tritium+krypton mode, no stabilization of the injection pressure was forseen. As a result of this, gas loss towards the DPS2 and RS causes a steady decrease in injection pressure and thereby column density. This is counteracted by periodic refilling, generating a sawtooth profile in the pressure (see fig. 5.2). From this data, one derives a relative decrease in injection pressure due to gas loss of:

$$\Delta p_{\text{loss}} = 0.9\,\%\,\text{h}^{-1}\,. \tag{5.3}$$

After initial measurements with $^{83\text{m}}$Kr were carried out in this configuration during STS3a, the necessity of a better source stability during the tritium+krypton became apparent. Over the course of this thesis, a modification to the operation mode which counteracts the pressure decrease was proposed and successfully implemented (see sections 5.2.2 and 5.3.2).

5.1.3. Achieved Stability in Pure Krypton Mode

The pure krypton mode would ideally consist of only $^{83\text{m}}$Kr freely streeming from the krypton generator into the DPS1. After being pumped by the TMPs, the $^{83\text{m}}$Kr would then be injected via the tritium+krypton injection capillary into the source. Due to the low pressure of $^{83\text{m}}$Kr of $<2 \times 10^{-7}$ mbar in the entire circulation loop, accurately measuring its stability directly via pressures is not possible given the instrumentation. Instead, the rate of $^{83\text{m}}$Kr conversion electrons at the FPD for one main spectrometer voltage can be used to monitor the $^{83\text{m}}$Kr amount inside of the

source. This has been done for a MS voltage of 30 kV, to exclude the signal from residual tritium.

The measured rate increases over time, in coincidence with an increase of pressure p_{DPS1} behind the DPS1 TMPs (see fig. 5.3). The increasing rate $r(t)$can be fitted well by the following limited growth exponential function:

$$r(t) = c - A \cdot \exp^{-\frac{t}{\tau}} , \tag{5.4}$$

with parameters:

- $c = (1.1100 \pm 0.0027) \times 10^5$ cps the rate in equilibrium,
- $A = (0.9420 \pm 0.0024) \times 10^5$ cps the scale of the rate growth,
- $\tau = (2.46 \pm 0.10)$ d the time constant of the equilibration process.

Translating this drift into a relative stability for the highest pressure and rate, the following results are obtained:

$$\frac{\Delta p}{p} < 2\,\%\,\mathrm{h}^{-1} , \tag{5.5}$$

$$\frac{\Delta r}{r} < 1\,\%\,\mathrm{h}^{-1} . \tag{5.6}$$

The explanation for this increase as well as an idea to improve the stability of this mode are given in section 5.2.3. The results of implementing this improvement are shown in section 5.3.3.

5.2. Optimization of the System

In the previous section, the performance of the loop system as it was built and designed was presented. From the data gathered during these measurements, much about the peculiarities of the different operation modes was learned. Bottlenecks limiting the stability of the system were identified as targets for a more thorough investigation and search for mitigation possibilities, which is the topic of this section.

5.2.1. Improvement of the Stabilization by Readout Upgrade of the Regulation circuit

A closer look at the remaining fluctuations in the pressure signal (depicted in fig. 5.4) of the pressure stabilization system of vessel B1 shows that some structure is visible in the readout of the redundant sensor. In comparison, the sensor readout used for regulation of the pressure stabilization only jumps between two analog digital converter (ADC) values. As a result, the deviation of the pressure p_{B1} from the set point needs to be large enough to overcome the threshold needed to flip from one ADC step to the next, making it impossible for the regulation to smooth out fluctuations below the level of the ADC step width. The reason for the difference

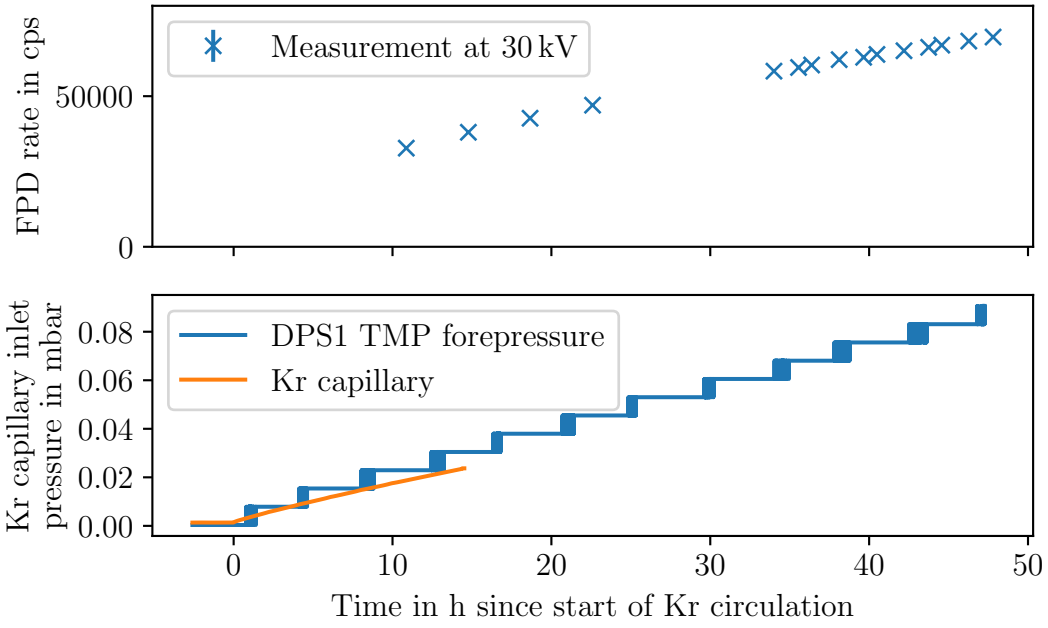

Figure 5.3.: **FPD rate increase during pure krypton mode with coinciding pressure rise in the IL.** Shown are the rate of ^{83m}Kr conversion electrons measured by the FPD at one voltage. Below that, the pressure p_{DPS1} behind the DPS1 TMPs is shown. The Kr capillary pressure sensor, which is connected to the same volume, is only shown for the time period in which the pressure is not outside of its range.

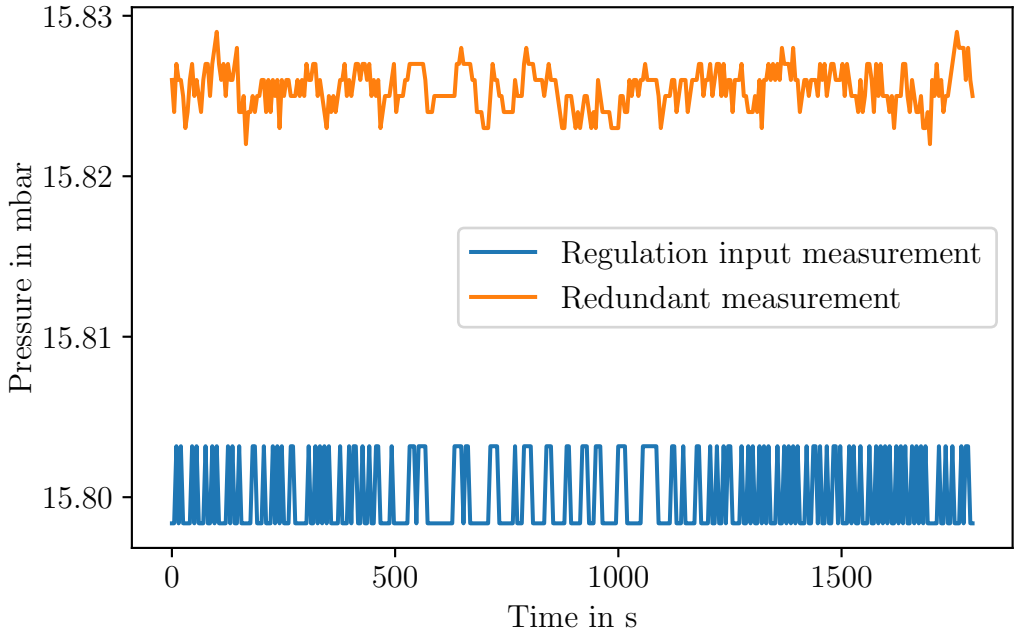

Figure 5.4.: **Limitation of injection pressure measurement by digitization.** Shown is the pressure p_{B1} as measured by the two pressure sensors connected to the injection buffer vessel B1.

between both sensor outputs is their different readout: Each `MKS 690A` sensor is connected to a `MKS 670` signal conditioner. The signal of the sensor used for regulation is put out by its signal conditioner as a 0 V to 10 V signal, which is read out by the Siemens PCS7 process control system via a 16-bit ADC card[1]. The redundant signal is digitized internally by its signal conditioner and then read out via RS232 delivering $5^1/_2$ digits of precision. As an additional digital signal converter is needed to translate between RS232 and the ProfiBus protocol used by PCS7, this signal was not used as a regulation input. Based on the difference in signal shape depending on the readout, the data acquisition chain is the factor limiting the resolution of the measurement instead of any intrinsic property of the sensor. Test measurements, detailed in appendix C, showed that a significant improvement can be made by exchanging the PCS7 readout of the signal conditioner analog output. This readout was replaced by a 24 bit Delphin Technologies ProfiMessage DAQ system[2].

A comparison of the new readout with the signal directly digitized by the signal conditioner is shown in fig. 5.5. No ADC steps are visible with the new readout and it has a much smaller spread of data points compared to the best old readout:

$$\sigma_{p,\mathrm{old}} = 8.15 \times 10^{-5}\,\mathrm{mbar}\,, \tag{5.7}$$

$$\sigma_{p,\mathrm{new}} = 1.50 \times 10^{-5}\,\mathrm{mbar}\,. \tag{5.8}$$

The hardware upgrade of the DAQ has improved the pressure readout of the pressure stabilization system by more than a factor of 5. The effect of this improvement on the pressure stability is presented in section 5.3.1.

5.2.2. Development of a Stabilization Procedure for the Tritium+Krypton Mode

The main issue of the tritium+krypton mode is the loss of circulating gas towards the DPS2 and RS. The solution to this problem is both simple in principle and difficult in execution: compensating the lost gas with fresh tritium gas.

The technical challenge of feeding the required gas amount needed to keep the tritium+krypton mode stable is the implementation of an extremely small compensation flow with sufficient stability. The loss flow towards the DPS2 and RS can be determined from the measured pressure decrease in the tritium+krypton mode to be approximately:

$$q_{\mathrm{loss}} \approx 4 \times 10^{-4}\,\mathrm{mbar}\,\ell\,\mathrm{s}^{-1}\,. \tag{5.9}$$

Comparing this to the design value for the tritium flow from the stabilized buffer system of $1.8\,\mathrm{mbar}\,\ell\,\mathrm{s}^{-1}$, the disparity between design and new requirement becomes apparent.

These four orders of magnitude can be bridged by making use of the characteristics of the tritium injection capillary. The conductance C of such a long and thin pipe in the laminar flow regime is proportional to the mean pressure $\bar{p}$ across the pipe. For a

[1] The card measures both positive and negative voltages, and uses one bit for the sign, leading to an effective resolution of 15 bit for the 0 V to 10 V range.

[2] 31000-GBDP ProfiMessage-Master device with a 32090-ADIT measurement module

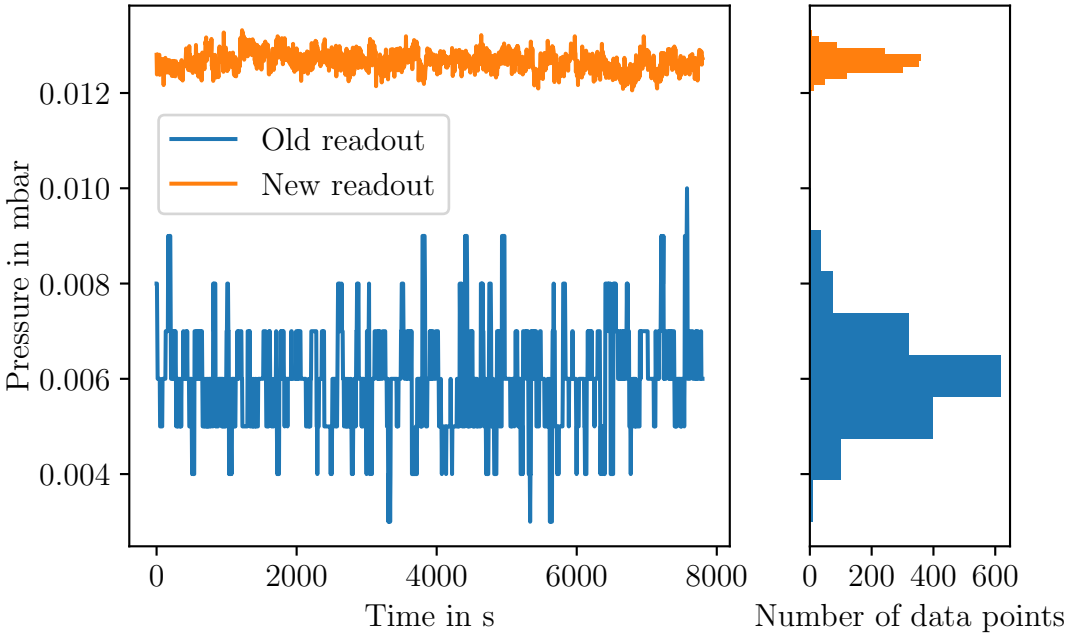

Figure 5.5.: **Comparison of pressure signal resolution with old RS232 readout and the new Delphin readout.** Shown are traces of the pressure p_{B1} measured with both `MKS 690A` sensors read out with the different systems. To the right side, histograms of the traces are shown. The offset between both signals is due to a small zero offset between the two sensors.

pipe where one side is pumped to a much lower pressure than the other, such as the injection capillary, the flow q through it can be approximated well by a quadratic dependence [Jou04] on the higher injection pressure p_{inj}:

$$q \propto {p_{inj}}^2 . \tag{5.10}$$

This means that, in order to stabilize a four orders of magnitude smaller flow, the pressure stabilization needs to work at an approximately two orders of magnitude lower pressure regime of $p_{B1} \approx 0.15\,\text{mbar}$.

When implementing a stabilized buffer pressure on the 0.15 mbar scale several related issues arose:

- The small outflow of gas from B1 into the WGTS necessitates an equally small flow from B2 to B1 (see fig. 3.4). When B2 is kept at its normal operating pressure of >100 mbar, the internal leak rate through the regulation valve[3] is bigger than the flow into the WGTS, causing a steady pressure rise in B1. Therefore, the operating pressure in B2 needs to be lowered to values in the range from 1.5 mbar–5 mbar to properly stabilize the pressure in B1.
- The same issue presented itself for the gas flow from the pure tritium buffer vessel B3 to B2 (see lower part of fig. 3.4), requiring its operating pressure to be dropped from the normal 350 mbar–850 mbar range to 1.5 mbar–5 mbar.

[3]This kind of internal leak rate is normal for the used regulation valve in its tritium compatible variant, see fig. H.20 for the datasheet.

- The refilling B3 from the FL storage vessel B4 cannot be achieved via pumping as in the normal case. Instead, the gas is expanded from B4 into the FL permeator and through the inactive Normetex and Metal Bellows pumps, which throttle the flow enough to allow some measure of control when refilling B3.
- An automatic regulation of the pressure set point of B1 is highly impractical. The reason for this are long time constants of the regulation process as well as the inability to reliably quantify the small fluctuations which need to be regulated out. These issues arise due to extremely small relative changes in the gas inventory of the WGTS of $2.6\,\mathrm{ppm\,s^{-1}}$ ($0.9\,\%\,\mathrm{h^{-1}}$) and buffer vessels, as well as limited sensor resolutions.
- Instead of being able to employ an automatic regulation, the set point value of B1 is iteratively tuned by hand to achieve an optimum stability of the pressure p_{DPS1} in front of the tritium+krypton injection capillary.
- Quick changes between different column density set points are impossible. Adding gas requires a filling and emptying of the IL buffer vessels, which takes several hours, while removing gas also removes $^{83\mathrm{m}}$Kr, leading to a waiting time of at least several time constants of 1.86 h until the concentration of $^{83\mathrm{m}}$Kr is back in equilibrium with its ^{83}Rb mother. Furthermore, the iterative set point tuning is a time consuming process.

With all of these modifications to the normal operation mode, the pressure p_{B1} in B1, as shown in fig. 5.6, could be stabilized during KNM2 at a setpoint value of:

$$p_{\mathrm{B1}} = 0.115\,\mathrm{mbar} \tag{5.11}$$

with relative peak-to-peak and standard deviation stabilities of:

$$\frac{\Delta p_{\mathrm{B1,ptp}}}{\bar{p}} = 0.90\,\%\,, \tag{5.12}$$

and

$$\frac{\sigma_{p_{\mathrm{B1}}}}{\bar{p}_{\mathrm{B1}}} = 0.17\,\%\,. \tag{5.13}$$

This novel stabilization of minuscule flows allows the continuous compensation of gas losses from the WGTS towards both DPS2 and RS. Furthermore, the capability to operate at such small pressures is of high interest in view of possible future operations at extremely small column densities on the order of $10^{17}\,\mathrm{m^{-2}}$–$10^{18}\,\mathrm{m^{-2}}$ (0.01 %–0.1 % of the nominal value) where a good stability is required, such as in the case of sterile neutrino searches [Dre+17; Hub20].

The results of the achieved pressure stability resulting from this novel operating scheme are presented in section 5.3.2.

5.2.3. Development of a Procedure for Accelerated Self-Stabilization in the Pure Krypton Mode

In the pure krypton mode, a steady increase of the $^{83\mathrm{m}}$Kr content inside the WGTS was observed via the detected rate of $^{83\mathrm{m}}$Kr conversion electrons. This increase

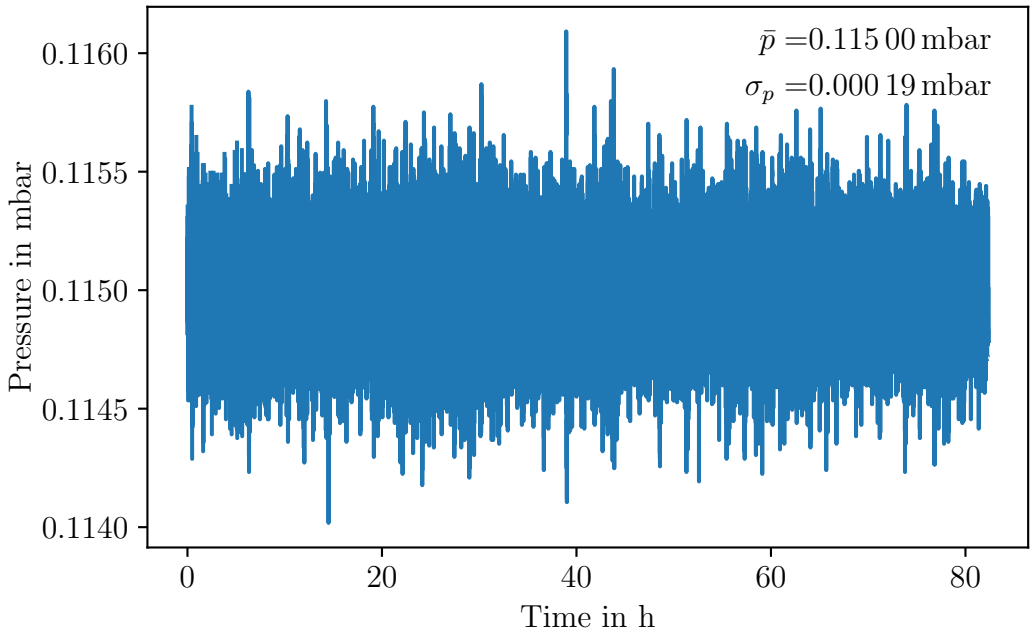

Figure 5.6.: **Pressure stabilization at very low pressures.** Shown is the pressure p_{B1} during >80 h of continuous operation of the tritium+krypton mode in the KNM2 campaign. Values for the mean pressure $\bar{p}$ and standard deviation σ_p are given in the upper right corner.

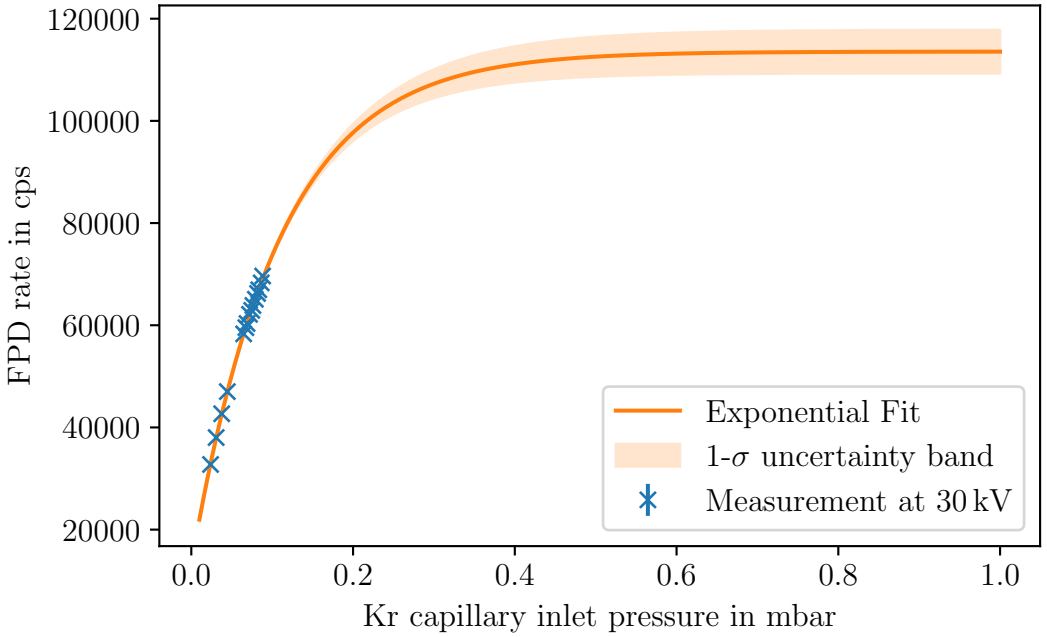

Figure 5.7.: **Rate increase in pure krypton mode over pressure behind DPS1 TMPs.** The ^{83m}Kr rate exhibits a limited exponential growth as a function of the inlet pressure p_{DPS1}.

correlates with a rising pressure p_{DPS1} in the volume behind the DPS1 pumps, which serves as a buffer in the krypton modes. A graph of the FPD rate over this pressure is shown in fig. 5.7.

The reason for the correlation between rate and pressure is the flow of $^{83\mathrm{m}}$Kr through the tritium+krypton injection capillary. The suppression of $^{83\mathrm{m}}$Kr activity in the beam tube can be understood by considering the circulation of only krypton first. In equilibrium between decay and production by the ^{83}Rb mother isotope, a maximum amount $<5 \times 10^{-7}\,\mathrm{mbar}\,\ell$ $^{83\mathrm{m}}$Kr can be present inside the IL. For such low gas amounts and the resulting low pressures inside the IL, the flow regime is molecular. This throttles the flow through the capillary due to two effects:

- the small conductance of the capillary for krypton for tritium in the molecular flow regime of $\approx 10^{-3}\,\ell\,\mathrm{s}^{-1}$ compared to a laminar flow regime at higher pressures in tritium+krypton mode with a conductance of $\approx 0.2\,\ell\,\mathrm{s}^{-1}$.
- the phenomenon of thermal creep flow [Sha96]: The temperature difference between the 100 K cold beam tube and the room temperature vacuum system behind the DPS1 causes a gas flow along the capillary in the inverse direction from the beam tube towards the outside of the cryostat.

Both effects are significant only for the molecular and transitional flow regimes. As the pressure inside the IL rises due to outgassing of the system in pure krypton mode, the flow regime inside the capillary grows progressively to a more laminar one, with the pressure gradient driven flow dominating the above effects more and more. Therefore, impurities act as a carrier gas, pushing the $^{83\mathrm{m}}$Kr through the capillary, which explains the dependence of the $^{83\mathrm{m}}$Kr activity inside the WGTS on the pressure.

A stabilization of the $^{83\mathrm{m}}$Kr rate can thus only be achieved by stabilizing the pressure of the carrier gas. In the pure krypton mode, this can be achieved by reaching the natural equilibrium of the system where the rate of outgassing q_{out} is equal to the rate of gas flow q_{loss} into the DPS2 and RS:

$$p \stackrel{!}{=} const. \qquad \Longrightarrow \qquad q_{\mathrm{out}} = q_{\mathrm{loss}} \tag{5.14}$$

Combining the data from the tritium+krypton and pure krypton mode, one can estimate the needed equilibrium pressure p_{eq} by assuming an exponential approach to the equilibrium value for datasets from both modes. This is shown in fig. 5.8. It is apparent that the two exponential functions do not converge to the same limit. The reasons for this are:

- The limited length and granularity of the datasets: Each dataset does not even cover one time constant ($\tau \approx 10\,\mathrm{d}$), and covers at most 30 discrete digitized values. Extrapolation to large times is therefore prone to some errors, as can be seen from the pressure decrease uncertainty band.
- The gas composition has an effect on the transport properties. As such, pure tritium as a carrier gas in general has a different equilibrium than the mixture of outgassed gas species. The impact of this effect can be larger than the uncertainty band shown in fig. 5.8, but quantification is practically impossible without precise knowledge of the gas composition. Even if such knowledge was

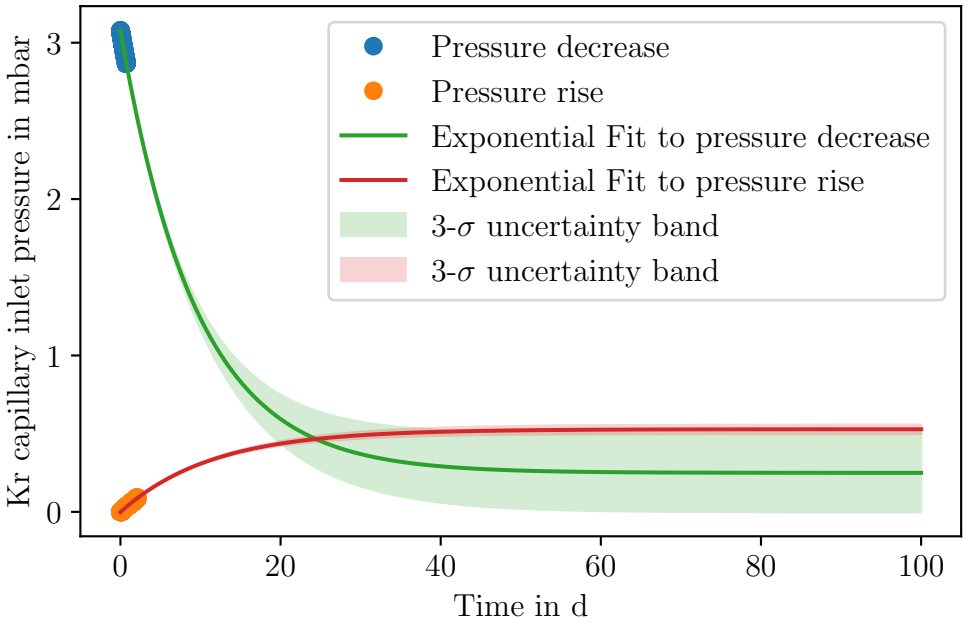

Figure 5.8.: **Pure krypton mode pressure extrapolation.** The pressure decrease during tritium+krypton and pressure increase during pure krypton mode has been fitted with an exponential function to determine the equilibrium pressure p_{eq}. This simple approach neglects gas composition dependent effects due to changes in flow regime or other transport properties of the gas. For details refer to the text.

available, for example by using the RGA of the WGTS, there is no experimental data on the transport of traces of krypton in a variety of carrier gases available, which would be needed for the calculation.

- In general, q_{out} and q_{loss} are not independent of the pressure in the system. This causes a deviation from the purely exponentially asymptotic behavior. And while the pressure dependence of q_{loss} could in principle be derived from simulations [Kuc+18], q_{out} is highly dependent on material surfaces as well as the history of the system in terms of prior exposure to hydrogen isotopologues, which makes getting a handle on its pressure dependence impractical.

Despite the lack of a precise value for p_{eq}, an approximate region can be given using the measured pressure rise and fall as an over- and underestimate:

$$0.25\,\mathrm{mbar} < p_{\mathrm{eq}} < 0.53\,\mathrm{mbar}\,. \tag{5.15}$$

Furthermore, the time constant for the equilibration derived from this extrapolation using only outgassing is on the order of 10 d. For a pure krypton measurement phase, which is usually on the scale of several days at maximum, this large time constant makes reaching the equilibrium by waiting for the accumulation of outgassing gas impossible. Therefore, the only feasible method of stabilizing the pure krypton mode is to intentionally add a small amount of carrier gas corresponding to p_{eq} when starting circulation. While this does not shorten the time constant, it brings the system closer to its equilibrium and reduces the relative change of pressure per time and thereby change of $^{83\mathrm{m}}$Kr rate.

Using tritium as a carrier gas is the easiest option, as it does not require purging gas from the FL and IL. This allows for reasonably fast switching times between

the pure krypton mode and the other operation modes. The tritium column density ρd_{carrier} when using pure tritium as a carrier gas can be estimated based on the range of pressures from eq. (5.15):

$$\rho d_{\text{carrier}} = (1.2 - 4.3) \times 10^{19}\,\text{m}^{-2} \mathrel{\hat{=}} (0.2 - 0.9)\,\%\,\text{of nominal}\,. \tag{5.16}$$

This amount of tritium might pose an issue for measurements interested in the lower energetic $^{83\text{m}}$Kr lines, such as the K line at 17.8 keV, due to an overlap with the tritium β-spectrum. For measurements negatively affected by this overlap, a different carrier gas such as H_2 (with traces of HT) can be used, but this makes a lengthy changing process necessary and disturbs the isotope equilibrium of the vacuum vessel walls, which can lead to a negative impact on the tritium purity stability for tritium measurements done afterward.

The result of using this stabilization by accelerated arrival at the equilibrium are presented in section 5.3.2.

5.3. Results of Stability Measurements after Optimizations

In this section, the achieved injection stabilities for the different operation modes, after application of the optimizations done over the course of this thesis, are presented. For all three different operation modes, a much better performance relative to the initial setup was reached.

5.3.1. Achieved Stability in Neutrino Mass Measurement Mode

After upgrading the readout hardware, the pressure stabilization of the buffer vessel B1 performs much better, as can be seen in fig. 5.9. During the KNM2 campaign, B1 was operated in a stable manner at a pressure setpoint similar to the initial measurements presented in section 5.1.1 for over 50 d without interruption. The achieved peak-to-peak and standard deviation over this entire time period were:

$$\Delta p_{\text{ptp}} = 5.6 \times 10^{-3}\,\text{mbar} \mathrel{\hat{=}} 0.018\,\%\,, \tag{5.17}$$

and

$$\sigma_p = 0.27 \times 10^{-3}\,\text{mbar} \mathrel{\hat{=}} 0.0017\,\%\,. \tag{5.18}$$

While the peak-to-peak value was lowered by a rather moderate factor of ≈ 2, the more relevant standard deviation was decreased by a factor of ≈ 5. The reason for this discrepancy are spikes which can be identified in fig. 5.9. Excluding these spikes (they last only ≈ 1 min each) the peak-to-peak stability value improves to:

$$\Delta p_{\text{ptp}} = 1.37 \times 10^{-3}\,\text{mbar} \mathrel{\hat{=}} 0.0087\,\%\,, \tag{5.19}$$

which corresponds to an improvement by a factor of > 4 compared to the initial setup.

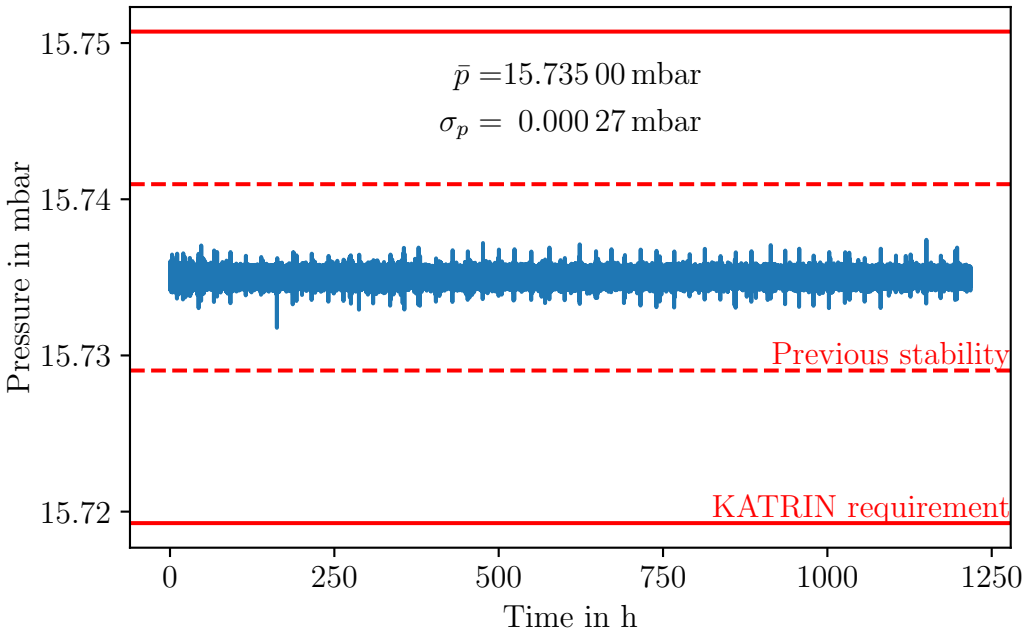

Figure 5.9.: **Injection pressure stabilization after improvements.** Shown is the pressure p_{B1} inside the stabilized buffer vessel B1 over a period of more than 50 d. Marked in solid red is the KATRIN stability requirement, while the dashed red lines show the stability which had been achieved prior to the readout upgrade. In a qualitative difference to the data before the upgrade, as shown in fig. 5.1, periodic spikes are visible in the pressure.

A closer look at the spikes reveals them to be caused by the daily refilling of the pure tritium buffer vessel B3 from the tritium storage vessel B4. A stacked plot illustrating this is shown in fig. 5.10. While no effect is resolved in the pressure of buffer B2, the pressure inside B1 spikes, causing the opening degree of the regulation valve between B2 and B1 to change significantly to compensate this. As will be demonstrated later in chapter 7, this effect is too small to be seen in the column density, and should therefore have no significant impact on the neutrino mass measurements.

The improvement of the pressure stabilization has reached the limit imposed by other IL components. The improved stability surpasses the design stability requirement of <0.1 % by a factor of at least 5. The overall column density stability with this stabilized buffer performance is presented in section 7.3.1.

5.3.2. Achieved Stability in Krypton + Tritium Mode

With the refilling scheme described above in section 5.2.2, the stability of the injection pressure into the tritium+krypton capillary has been improved greatly. This is shown in fig. 5.11. Compared to previous results, the pressure p_{DPS1} readout behind the TMPs is now stable to within 2 ADC steps during the majority of time during the tritium+krypton mode operation. For the shown data, the relative values for the peak-to-peak and standard deviation of the pressure are:

$$\frac{\Delta p_{ptp}}{\bar{p}} = 0.53\,\%\,, \tag{5.20}$$

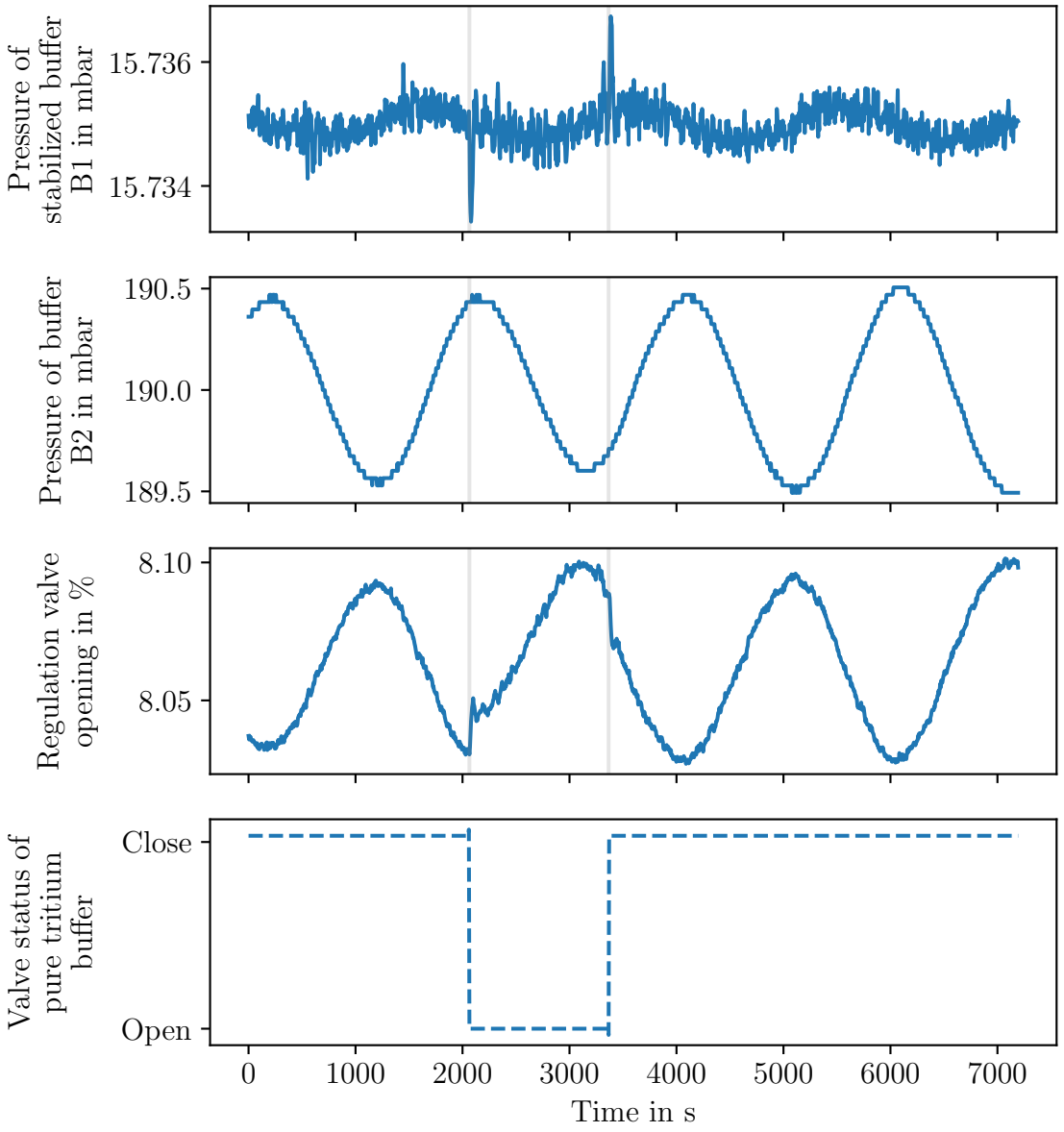

Figure 5.10.: **Behavior of improved pressure stabilization on short timescales.** Shown are the pressure p_{B1} in the stabilized buffer vessel B1 and the buffer vessel B2, as well as the opening degree of the regulation valve RV1 between them. In the bottom graph the status of the refilling valve AV4 of the pure tritium buffer B3 is shown.

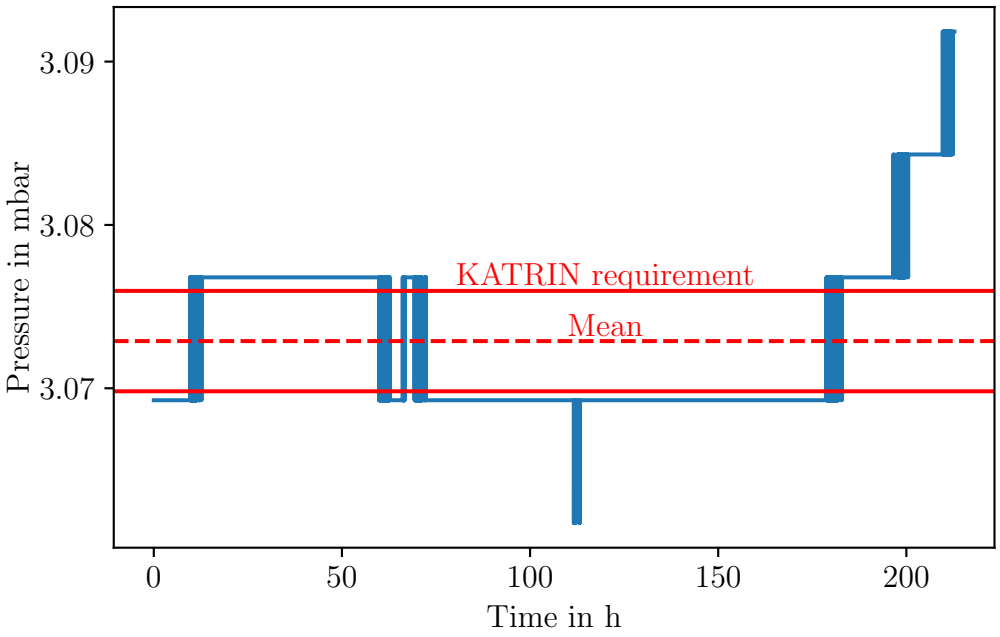

Figure 5.11.: **Stability of pressure behind DPS1 TMPs in tritium+krypton mode.** Although it was not specified as a requirement in [KAT05], a stability band of 0.1 % is drawn around the mean value as a comparison to the neutrino mass mode.

and

$$\frac{\sigma_p}{\bar{p}} = 0.17\,\%\,. \tag{5.21}$$

While these values do not meet the requirements of the neutrino mass measurement mode of 0.1 %, such stringent requirements were not considered for the tritium+krypton mode during the design stage [KAT05]. The rise observed around 175 h in fig. 5.11 is caused by a shift of the pressure p_{B1} reading of the stabilized buffer vessel regulation by ≈ 0.002 mbar. Reasons for such a small shift can range from fluctuations of the sensor zero point, which would be well within the sensor specification, to effects such as additional crosstalk on the cable connection between sensor and ADC on the µV-scale.

Regardless of this however, due the new operation scheme, the tritium+krypton mode is capable of providing a tritium source containing $^{83\mathrm{m}}$Kr with the stability necessary to investigate source systematics such as the source potential [Mac20] for the first time. The overall column density stability with this improvement is presented in section 7.3.2.

5.3.3. Achieved Stability in Pure Krypton Mode

After the KNM2 campaign, the accelerated self-equilibration of the pure krypton mode was tested at a WGTS source tube temperature of 80 K. For this purpose, accumulated gas (hydrogen, air, methane) in the WGTS return line originating from outgassing of the WGTS source tube and DPS1 TMPs was used as a carrier gas. The pressure p_{DPS1} between the DPS1 TMPs and the tritium+krypton injection capillary as well as the rate of $^{83\mathrm{m}}$Kr at a fixed voltage point are compared in fig. 5.12.

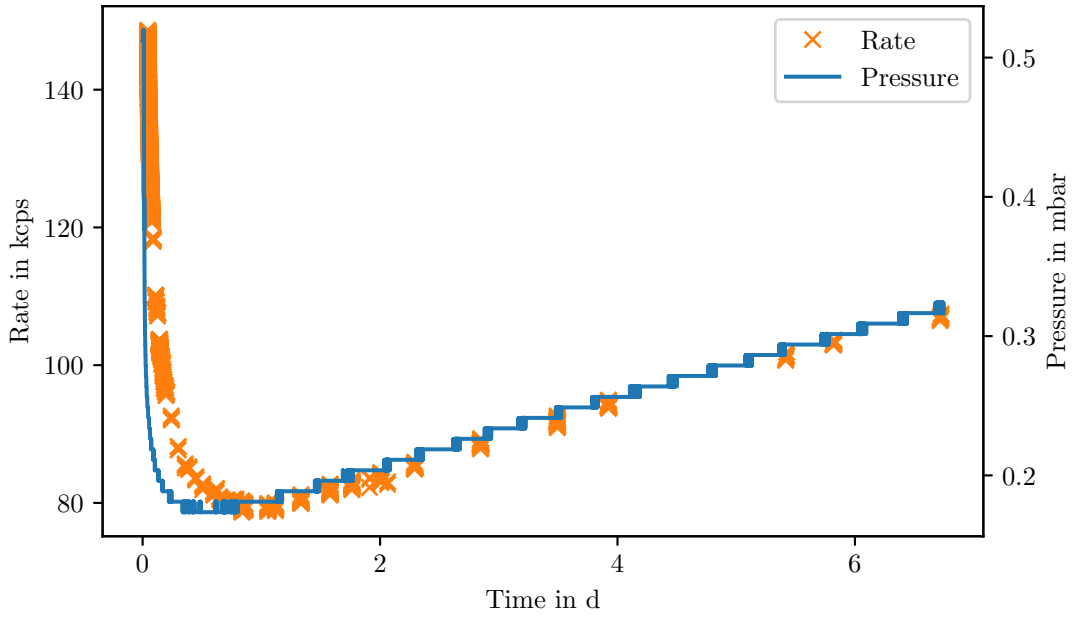

Figure 5.12.: **Pressure and ^{83m}Kr activity stability in the pure krypton mode.** Shown is the ^{83m}Kr rate measured by the FPD at a MS voltage of 30 470.5 V and the pressure p_{DPS1} applied to the tritium+krypton injection capillary.

Two regions of different behavior can be identified in the data. In region 1, upon starting circulation of the accumulated gas, the pressure p_{DPS1} quickly dropped from ≈ 0.5 mbar to a level less than 0.2 mbar, which is a much larger drop than would be expected from just expansion into the volumes forming the circuit. This was expected, as the prior thorough investigation of the `MAG W2800` pumps used in the DPS1 has shown that they gas out various species of hydrocarbons beyond methane when operated with tritium [Pri13; PB13]. Considering the vapor pressure of such hydrocarbons (see appendix I) and the pressure as well as the temperature distribution along the injection capillary, these molecules are expected freeze out inside the tritium+krypton injection capillary; it serves as a cryo pump. This is supported by the vastly smaller pressure rise of only ≈ 0.01 mbar, that was observed when stopping the circulation in this mode. The magnitude of this increase is in good agreement with the expectation from compression of the gas in the additional volumes during circulation and would have been the expectation for the pressure drop upon start of the circulation without any deposition of gas. The composition of the remaining gas which circulated could be analyzed qualitatively, showing the gas to consist of nitrogen, oxygen, hydrogen, as well as candidates for tritiated water or methanes. Hydrogen is easily explained via outgassing of the steel vessels, while nitrogen and oxygen originate from air leakage through the polymer sealing of the DPS1 TMPs. Tritiated water or methane can be created via exchange with surface water of the not baked out loops piping, radiochemical production of tritiated methane, or via fragmentation of higher hydrocarbons.

In region 2, after this initial drop in pressure and activity due to freezing of high-vapor pressure components of the carrier gas, the pressure p_{DPS1} and ^{83m}Kr rate slowly rise over time. The magnitude of this pressure increase is $\approx 8 \times 10^{-6}$ mbar $\ell\,\mathrm{s}^{-1}$. It amounts to approximately half of the observed outgassing rate of the WGTS and

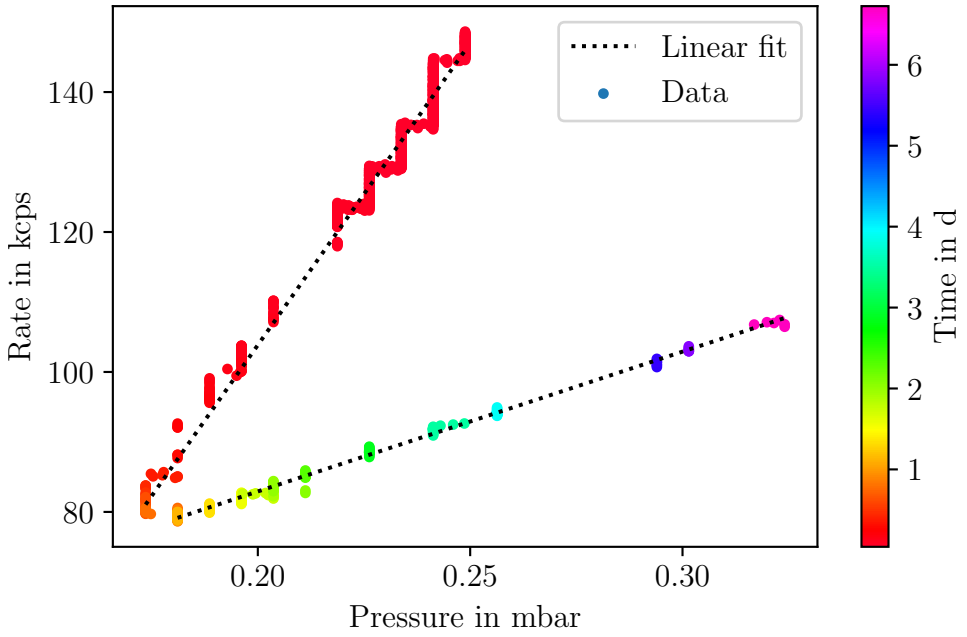

Figure 5.13.: **Dependence of ^{83m}Kr activity in the WGTS on the pressure applied to the tritium+krypton injection capillary.** Shown is the ^{83m}Kr rate measured by the FPD at a MS voltage of 30 470.5 V. The different slopes in rate over pressure are most likely caused by different transport properties of the circulating carrier gas and a change in composition due to freezing out of a part of the gas. Linear fits were applied to the two regions of different behavior.

DPS1 of $(1.5 \pm 0.2) \times 10^{-5}\,\mathrm{mbar}\,\ell\,\mathrm{s}^{-1}$ (for details see appendix D), which is in agreement with the observed initial pressure drop of approximately half the pressure inside the system. In comparison, the pressure increase during the pure krypton mode operation during the KNM1 campaign was $(1.4 \pm 0.1) \times 10^{-5}\,\mathrm{mbar}\,\ell\,\mathrm{s}^{-1}$, showing that the impurities frozen out at an 80 K setting after KNM2 were able to pass the tritium+krypton capillary at the 100 K setting in KNM1.

Despite operation over a time span of more than 6 d, no saturation or indication thereof was observed, resulting in a maximum measured pressure p_{DPS1} of 0.32 mbar at the end of the measurement period.At the maximal observed pressure p_{DPS1} in the volume between DPS1 and the tritium+krypton injection capillary during this measurement, the pressure in the source tube as measured by a Penning gauge at the DPS1-R1 pumping duct already reached $\approx 4\,\%$ of the value during maximal pressure operation of the tritium+krypton mode. From the behavior of the ^{83m}Kr rate to pressure p_{DPS1} shown in fig. 5.13 however, the applied pressure was still not sufficient to transport the maximal amount of ^{83m}Kr into the source tube. In addition, the amount of transported ^{83m}Kr per applied pressure changed significantly. The time of this change in behavior coincides with the transition of region to region 2. Linear fits to both regions show a ≈ 4.3 times greater increase of ^{83m}Kr rate per pressure. From this, it can be concluded that the gas composition most likely has a significant impact on the transport of the ^{83m}Kr trace gas. In particular, the gas components being deposited on the cold WGTS cryostat surfaces contribute significantly more to the transport than other gas components.

Looking only at region 2, where the circulating pressure increased, a relative change in the pressure p and mean rate r of

$$\frac{\Delta p}{p} < 0.5\,\%\,\mathrm{h}^{-1}\,, \tag{5.22}$$

$$\frac{\Delta r}{r} < 0.3\,\%\,\mathrm{h}^{-1}\,, \tag{5.23}$$

due to the pressure drift has been achieved. This is an improvement by a factor of 3 to 4 compared to the previous operation scheme of this mode. This improvement originates from the freeze out of a fraction of the carrier gas and an accordingly slower increase in the pressure p_{DPS1} per time unit. In exchange for this better stability, the strong initial pressure decrease poses a strong decrease in stability, which impacts approximately the first day of measurement time in pure krypton mode.

Further improvements of the stability in the pure krypton mode are rather unlikely. The steady increase of gas circulating through the source from air leakages can not be prevented. The high equilibrium pressure expected from this increase means that a significant density of impurity gas will be present inside the WGTS source tube at such an equilibrium. $^{83\mathrm{m}}$Kr electrons scatter on this residual gas and lose energy [Rod21] or ionize the gas and form a plasma, which could negatively impact the $^{83\mathrm{m}}$Kr line measurements. Therefore, the attainable equilibrium in this mode is most likely not desirable.

Summarizing the measurements discussed above, a carrier gas for the pure krypton mode is preferable in order to quickly gain a sufficiently high $^{83\mathrm{m}}$Kr activity inside the WGTS. The pressure increase of the circulating gas is caused by outgassing and air leakages of the TMPs, approximately half of which freezes out at cold surfaces inside the WGTS cryostat at temperature settings between 80 K–100 K. As the equilibrium pressure is likely to affect the $^{83\mathrm{m}}$Kr line measurements, the reduced rise in pressure, and the accordingly improved stability per time unit, during the 80 K setting makes this operation mode of the WGTS favorable for the pure krypton mode.

5.4. Conclusive Remarks on the Tritium Injection Stabilization

The stabilized injection of gas into the WGTS is one of the most important factors in achieving the required source stability of 0.1 %. Over the course of this doctoral project, the stabilization of gas injection in all different operation modes has been optimized, resulting in a significantly improved performance. By upgrading the read-out of the stabilized buffer B1, the stability in the neutrino mass measurement mode was improved by a factor of ≈ 5, reaching a level of almost 2 orders of magnitude better than required. For the resulting overall stability of the column density refer to section 7.3.

The upgrade also allows for the stabilization of very low pressures in B1, which in turn was used to establish minuscule gas flows. These small flows are essential to compensate the gas loss towards DPS2 and RS. By incorporating such a continuous

refilling, the newly developed operation scheme made it possible to establish a stable circulation in the tritium+krypton mode for the first time. As a result, the requirements for precise investigations of the source systematics in the tritium+krypton mode can be met with this new operating scheme. Additionally, the upgrade enables the direct provision of a reduced column density for sterile neutrino measurements with KATRIN with the required stability.

6. Measurement and Modeling of the Gas Composition inside the Loop System

Exact knowledge of the gas composition of tritium gas flowing through the loop system and in particular the WGTS is essential for an accurate neutrino mass analysis. In particular the *tritium purity*, namely the atomic fraction of tritium inside the gas, impacts several aspects of the experiment. These aspects are:

- The direct scaling of the source intensity with tritium purity: Less tritium purity at the same column density directly leads to a smaller activity.
- The differences in binding energies and final state distributions of HT, DT, T_2 and possibly more complex molecules. These differences produce shifted β-spectra, whose overlap smears the measured spectrum [Kle+19].
- The gas dynamical properties depend on the gas composition. Thus, changes in the isotopic composition change the gas density profile of the source.
- The scattering processes of β-electrons on gas particles need to be included when analyzing the β-spectrum. The probability to scatter and the corresponding energy losses in such collisions depend on the gas species the electrons scatter on.

To maximize luminosity while minimizing systematic effects, the neutrino mass measurements need to achieve a tritium purity as high as possible, as well as exact knowledge of the non-tritium contributions to the gas composition. For this reason, dedicated gas composition measurement systems are included in the IL.

The characterization, applicability and limitations of these systems are presented in section 6.1. Based on measurements with these diagnostic tools, the isotopic exchange effects in the IL have been investigated and characterized, which is presented in section 6.2. In section 6.3, corresponding simulation models are described, which have been developed to predict the gas composition for operation modes where a gas composition analysis can not be performed. The conclusions drawn from these measurements and simulations are summarized in section 6.4.

6.1. Monitoring of the Gas Composition

The IL contains two systems for gas composition analysis, which use complementary measurement principles. These systems are:

- A laser Raman (LARA) system, which has been developed specifically for KATRIN to meet the requirements of achieving an 0.1 % precision on the tritium purity over sampling times less than 250 s [Sch+13]. As the measurement time is defined by the time required to accumulate the necessary statistics, a high pressure at the point of spectroscopy is needed. As a result, the LARA cell is installed close to the buffer vessel B2, in a section with the highest stable pressure level in the IL.
- A residual gas analyzer (RGA) in the DPS1-R2, which possesses a high dynamic range and shows no restrictions on the detectable gas species. It is however limited in usability, as it does not measure correctly inside the stray magnetic fields needed for KATRIN operation. Additionally, translating intensities measured with the RGA into a gas composition with a high accuracy is impossible without repeated calibration with well known gas samples. Such a regular calibration is not possible in the setup, making the installed RGA more suited to the qualitative detection of trace gases and characterization of the applicability of LARA data for the gas composition inside the source as presented in sections 6.1.1 and 6.1.2.

For the krypton operation modes, neither the RGA nor LARA can be used. This issue and a possible method to infer tritium purites from WGTS activity measurements is discussed in section 6.1.3.

6.1.1. Representativeness of LARA for the WGTS Gas Composition

During the Loop Commissioning phase, the gas circulation was tested with inactive deuterium and gas composition measurements were done with both LARA and the RGA. One such measurement showing the concentration as measured with LARA, as well as the concentration derived from relative RGA peak heights, is depicted in fig. 6.1. For the RGA, an uncorrected curve showing the raw data as well as a curve with an inverse sixth power law correction [PM68] applied to it are displayed. This correction is necessary to account for differences in real gas molecule abundance relative to the signal strength due to the different ionization probabilities of H_2, HD, and D_2. Normalized to the H_2 intensity, these correction factors range from 1.03 to 1.18 for HD and from 1.15 to 1.43 for D_2, depending on the applied correction [PM68]. These kinds of systematics, and in particular the lack of corresponding literature values for tritiated hydrogen isotopologues, make an accurate concentration determination on the percent-level with the RGA without dedicated and repeated calibration impossible. Figure 6.1 also clearly shows the precision dependence of the concentration measured with LARA on the total number of molecules inside the LARA cell: the higher the number of molecules, and therefore partial pressure, the smaller the uncertainty on the measured concentration value. Furthermore, it can be seen that hydrogen concentrations below the percent-level are below the level of detection for this LARA setup at such short sampling times.

A comparison of LARA and RGA data shows good agreement between both systems once corrections are applied to the RGA values. As such, LARA is a highly qualified tool to monitor the concentration inside of the WGTS during normal KATRIN operation.

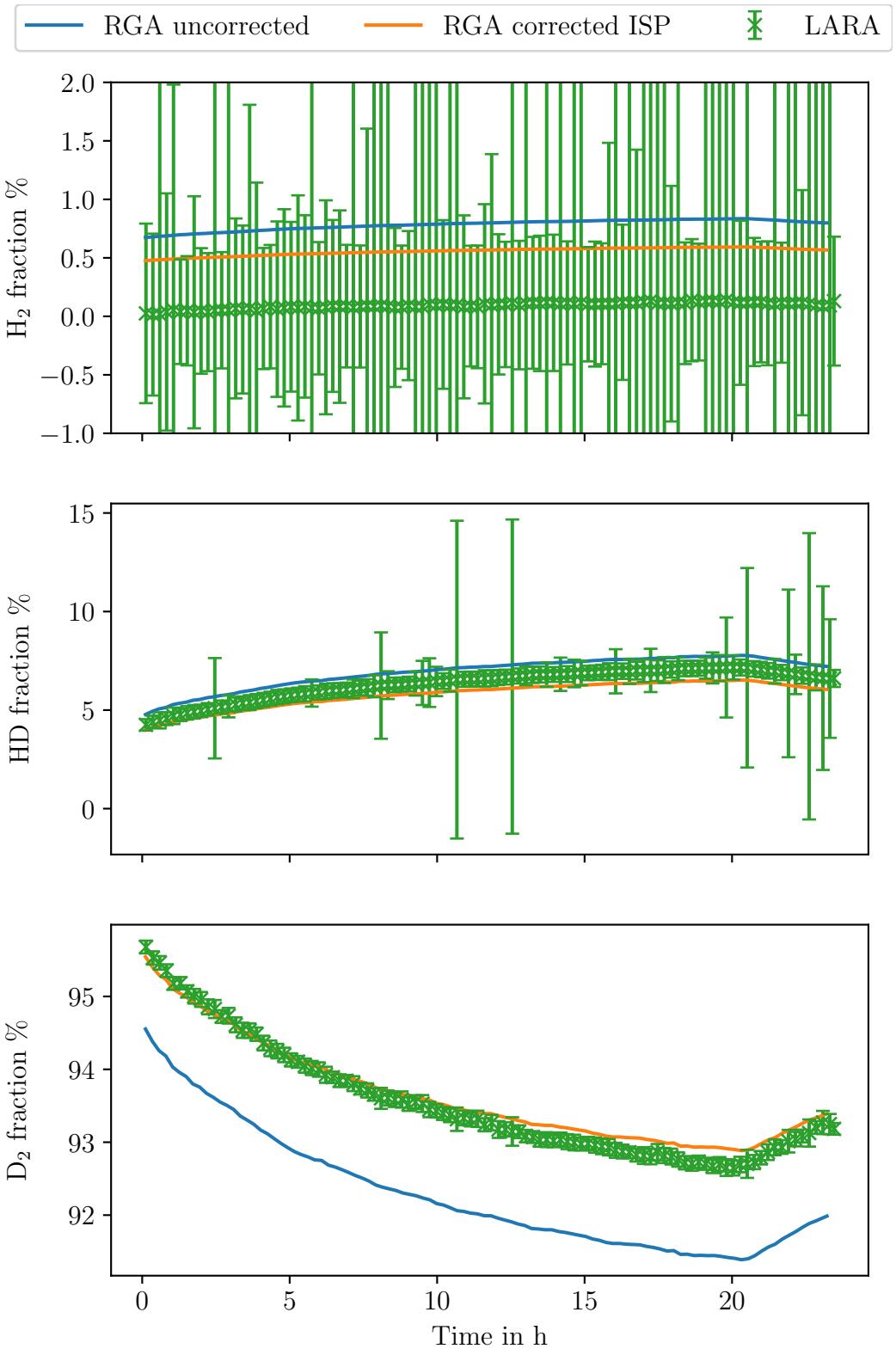

Figure 6.1.: **Comparability of the gas compostion as measured by LARA and RGA.** Shown are the H_2, HD, and D_2 fractions as a function of time, measured with both LARA and the RGA. Sampling times are 60 s for LARA and 20 s for the RGA. The blue curve shows the uncorrected RGA data, the orange curve RGA data corrected with the inverse sixth power (ISP) correction from [PM68].

6.1.2. Time Shift between LARA and RGA

When looking at the data presented in fig. 6.1 on a short time scale, a time shift between LARA and the RGA is visible, with the RGA being retarded with regards to LARA. This shift is caused by the finite time the gas needs to travel from the LARA cell through the stabilized buffer and via the tritium injection capillary into the beam tube, where the RGA is located.

6.1.2.1. Time Shift observed with the RGA

To determine the magnitude of the shift, a correlation analysis has been done. For this analysis, the signals of LARA and RGA were shifted against each other to determine the time shift for which the Pearson correlation coefficient [KD19] between the signals becomes maximal. The time shift derived from this analysis is:

$$\Delta t = (110 \pm 79)\,\mathrm{s}\,. \tag{6.1}$$

It is possible to experimentally investigate this effect in further detail by using data from the First Tritium measurement campaign.

6.1.2.2. Time Shift observed with the FPD

During the Very First Tritium phase of the FT measurement campaign, tests using only trace amounts of tritium were performed. For these tests, pure D_2 was circulated in the IL and traces of DT were injected into the gas stream from small sample cylinders. Each such injection causes a fast change of the gas composition on a time scale shorter than a single circulation of the gas through the IL, which can be used to investigate the time delay between LARA and the WGTS. As a measure for the gas composition in the source, in particular the tritium purity, the β-electron rate on the FPD can be used.

One such injection of tritium into the system is shown in fig. 6.2. To determine the shift, a correlation analysis has been done. For this analysis, the signals of LARA and the FPD were shifted against each other to determine the time shift for which the correlation becomes maximal. This is shown in in fig. 6.3. Due to the much steeper change in gas composition and the smaller time steps between FPD measurement values compared to the RGA, the measured value is much more accurate. The result of this analysis is:

$$\Delta t_{\mathrm{data}} = (126 \pm 4)\,\mathrm{s}\,. \tag{6.2}$$

This value agrees well with the RGA measurement, but is much more precise. Finally, aside from measurements, the time shift can also be calculated theoretically.

6.1.2.3. Theoretical calculation of the Time Shift

The expected size of this shift Δt_{theo} can be estimated from the system geometry and the measured pressures in different sections. By negelecting any significant mixing of

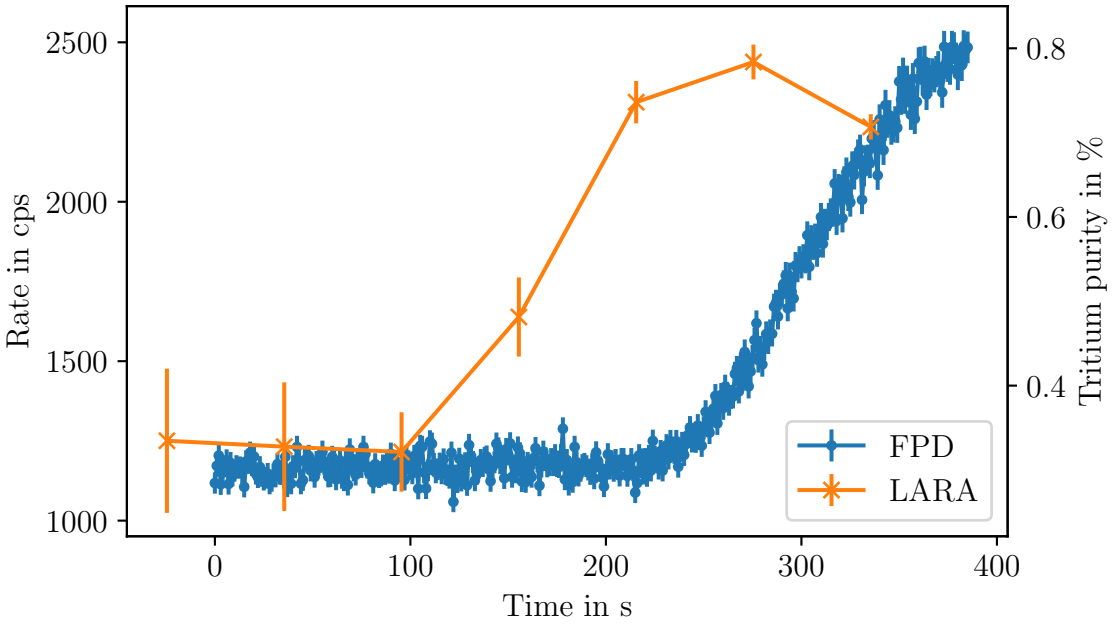

Figure 6.2.: **Time delay between FPD rate and LARA concentration.** Shown are the tritium purity measured by LARA and the countrate measured by the FPD. A clear delay of the change in FPD rate compared to the change in LARA composition is visible.

gas due to the assumption of dominantly laminar flow inside the pipes, one obtains:

$$\Delta t_{\text{theo}} = \frac{L_{\text{pipe}}}{v_{\text{gas}}} \,. \tag{6.3}$$

Here L_{pipe} is the length of the piping and v_{gas} the macroscopic velocity of a gas bunch. This velocity is given by:

$$v_{\text{gas}} = \frac{q}{p \cdot A_{\text{pipe}}} \,, \tag{6.4}$$

with

- the flow rate through the pipe q,
- the pressure inside the pipe p, and
- the pipe cross section area A_{pipe}.

To account for different pipe diameters and pressure drops along the system, the piping is sliced into small segments of length $\Delta L_{\text{pipe},i}$ each with local gas velocity of $\Delta v_{\text{gas},i}$. For each of these small slices, a local time shift $\Delta t_{\text{theo},i}$ can be calculated. The sum of these shifts then gives the total time shift:

$$\Delta t_{\text{theo}} = \sum \Delta t_{\text{theo},i} = \sum \frac{\Delta L_{\text{pipe},i}}{\Delta v_{\text{gas},i}} \,. \tag{6.5}$$

For the actual geometry of and observed pressures in the IL this formula leads to the following time shift between the LARA cell and the injection chamber:

$$\Delta t_{\text{theo}} = (119 \pm 8)\,\text{s} \,, \tag{6.6}$$

which is in good agreement with the measured values of $(110 \pm 79)\,\text{s}$ and $(126 \pm 4)\,\text{s}$.

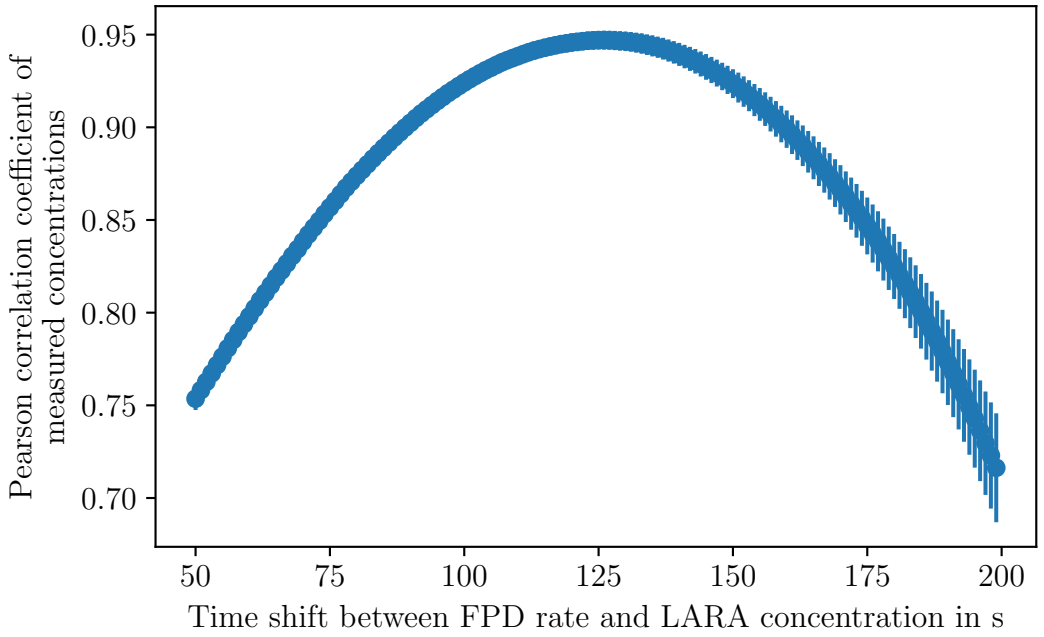

Figure 6.3.: **Correlation analysis of FPD rate and LARA concentration.** Shown is the Pearson correlation coefficient between shifted FPD rate and LARA concentration data as a function of of the time shift. The maximum of the correlation gives the best estimate of the real time shift between both systems.

6.1.2.4. Consequences of the Time Shift for KATRIN

For the later long-term operation, this transient effect of quick concentration changes can be neglected, as long as the concentration stays in quasi-equilibrium with time constants which are much larger than the measured time shift.

6.1.3. Unavailability of Gas Composition Monitoring in the Krypton Modes

When comparing the two gas composition measurement methods, only LARA provides a continuous monitoring of the composition due to the magnetic field at the source. However, this fact only applies for the neutrino mass measurement mode. For the krypton modes, LARA can not be used. In the tritium+krypton mode, the circulating tritium gas does not pass the LARA cell. The minuscule flow of tritium being continuously fed into the cycle is not representative of the composition of the circulating gas, and requires pressures in the stabilized buffers which are too low for LARA to measure with sufficient precision. Similarly, the gas composition in pure krypton mode is not accessible by either LARA or RGA.

Despite this, the modeling and simulations developed here can be used to get a handle on the gas composition. A validation of these simulations with regards to the tritium purity can be performed using the total gas amount and the tritium β-electron rate. As an example, the BIXS rate during stable tritium+krypton mode operation is shown in fig. 6.4. During the measurement, the total gas amount was

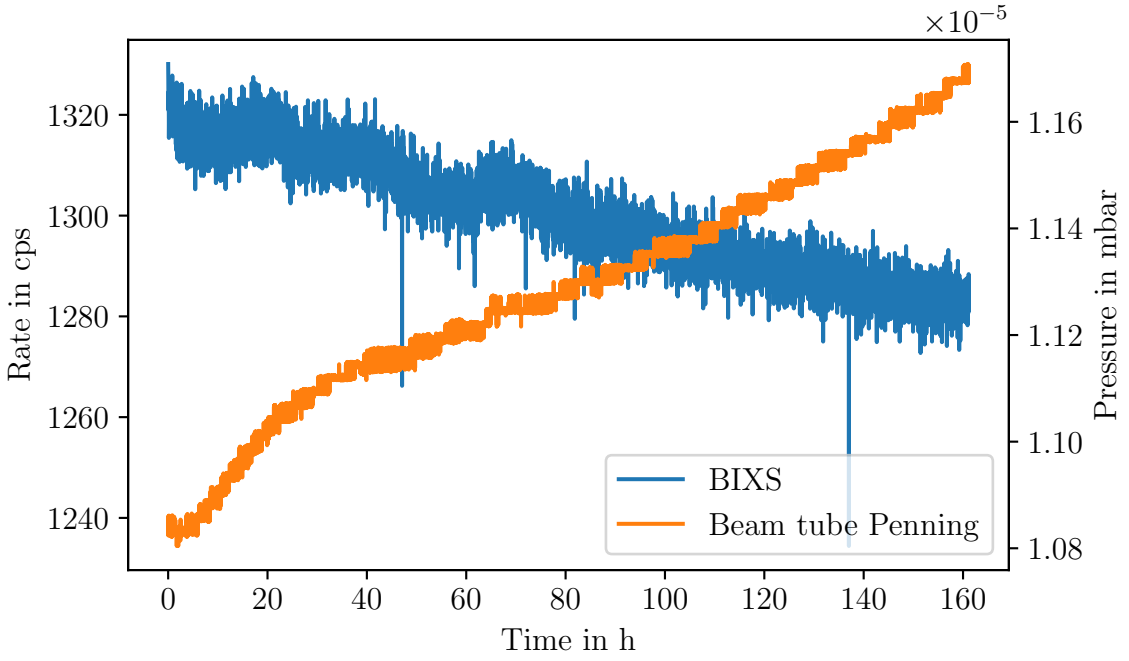

Figure 6.4.: **Measurements indicating a gas composition change in tritium+krypton mode.** Shown is the decrease in the BIXS rate during operation with constant total gas inventory. As an additional indicator of a change in gas composition, the pressure measured by a cold cathode gauge inside the DPS1-R1 pump port is shown. These gauges are sensitive to the gas composition via the differences in the ionization energies, causing a different reading for e.g. hydrogen or deuterium at the same pressure. Furthermore, the gas dependence of the conductances and TMP pumping speeds also changes the gas distribution inside the pump ports, leading to a different total pressure at the location of the gauge.

kept constant. The observed rate decrease therefore implies a decrease of the tritium purity of the gas. This decrease most likely results from:

- Loss of pure tritium towards the DPS2 and RS.
- Tritium ad- and absorption by the WGTS beam tube wall and IL piping.
- Outgassing of H_2 from vessel walls and other vacuum components.
- Permeation of air (N_2, O_2, Ar, ...) through the elastomer sealings of the DPS1 TMPs.
- Hydrocarbons gassing out from the high pressure side of the DPS1 TMPs.

A model for the tritium+krypton mode describing this decrease using only quantities as an input which can be measured independently, and its validation via the BIXS rate, can be found in section 6.3.3.

6.2. Time Behavior of Isotopic Composition inside the Circulation Loop

The composition of the tritium gas provided by the TLK infrastructure is analyzed before it is transferred to the FL. This composition, however, is not the composition which settles in equilibrium in the IL due to isotope dependent gas transport and isotopic exchange effects. This section focuses on the time dependency of these effects, which are visible in the measured data. In section 6.2.1 the time needed to reach an equilibrium gas composition in the IL after starting circulation is determined. Following that, the impact of the discontinuous transfer of tritium gas with slightly varying composition from the TLK infrastructure is addressed in section 6.2.2.

6.2.1. Equilibration Time after Starting the Circulation

When the circulation inside the IL is started, the stabilized buffer vessels B1 and B2, as well as the permeator, are filled with high purity tritium from the FL. The tritium purity in this gas is the maximum value which can be achieved in the IL. As discussed in section 3.3.5, isotopic exchange reactions of tritium with hydrogen from surfaces inside the primary system, as well as with outgassing molecules from the DPS1 pumps, cause a loss of tritium purity. To counteract this, a fraction of the gas on the retentate side of the permeator is continuously removed and high purity tritium gas from the FL is added in exchange. As a result, the system reaches an equilibrium tritium purity below that of the FL gas. How far this equilibrium is shifted from the feed concentration depends on the ratio of flows of isotopic exchange and the feed gas. This ratio also impacts the time until equilibrium is reached.

Figure 6.5 shows the tritium purity during a 24 d period of KNM1, in which the circulation had to be restarted several times. In KNM2, the circulation was only started a total of three times. Due to various factors such as changes to the circulation conditions shortly after start of the circulation, these data are not comparable to each other or to KNM1. After each start, which is marked by a dashed line in fig. 6.5, an exponential decay of the tritium purity to a new equilibrium value can be seen. For the shown data, the time constants of these equilibrations vary by about a factor of 2 and are in the following range:

$$\tau = (0.20 - 0.37)\,\mathrm{d}\,. \tag{6.7}$$

This means that the tritium purity in the IL only reaches equilibrium[1] after >1 d of stable circulation. Therefore, a stable circulation should be maintained whenever possible to minimize the downtime in data taking due to waiting for stabilization.

6.2.2. Composition Changes after Weekly Transfer of Tritium from the TLK Infrastructure

During normal operation of the loop system in neutrino mass measurement mode, fresh high purity tritium gas is typically transferred from the TLK infrastructure

[1] Assuming 5 time constants as the duration until the equilibrium value is approximately reached.

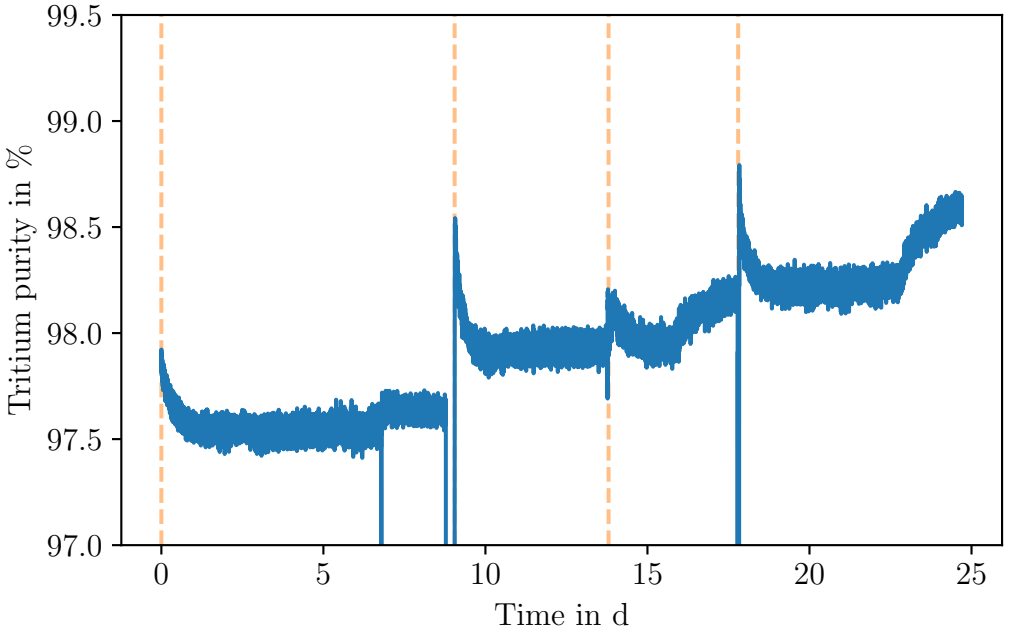

Figure 6.5.: **Changes in and equilibration of tritium purity after starting of gas circulation.** Shown is the tritium purity as measured by LARA over a time period with several restarts of the gas circulation. The dashed lines mark the starts of the gas circulation.

to the FL once per week. Due to the necessary purification processes of tritium in the TLK infrastructure, the gas composition provided to the FL can vary on the sub-percent-level. For the tritium purity in the IL, this means that once per week, the equilibrium tritium purity can change. This is shown in fig. 6.6.

The magnitude of these changes is on a similar scale to those observed during the start of the gas circulation. The time constant of this change to a new equilibrium value can be estimated by fitting an exponential to the data. For the KNM1 and KNM2 datasets, this results in time constants of:

$$\tau_{\mathrm{KNM1}} = (0.94 \pm 0.22)\,\mathrm{d}\,, \tag{6.8}$$

and

$$\tau_{\mathrm{KNM2}} = (1.54 \pm 0.55)\,\mathrm{d}\,. \tag{6.9}$$

Interestingly, the data shows a significant difference in the observed time constant when going from higher to lower tritium purity levels compared to the opposite. If the changes in purity are split by whether they go up or down in tritium purity, the following time constants can be derived:

$$\tau_{\mathrm{KNM1,up}} = (1.19 \pm 0.09)\,\mathrm{d}\,, \tag{6.10}$$
$$\tau_{\mathrm{KNM1,down}} = (0.77 \pm 0.07)\,\mathrm{d} \tag{6.11}$$

and

$$\tau_{\mathrm{KNM2,up}} = (2.05 \pm 0.27)\,\mathrm{d}\,, \tag{6.12}$$
$$\tau_{\mathrm{KNM2,down}} = (1.05 \pm 0.07)\,\mathrm{d}\,. \tag{6.13}$$

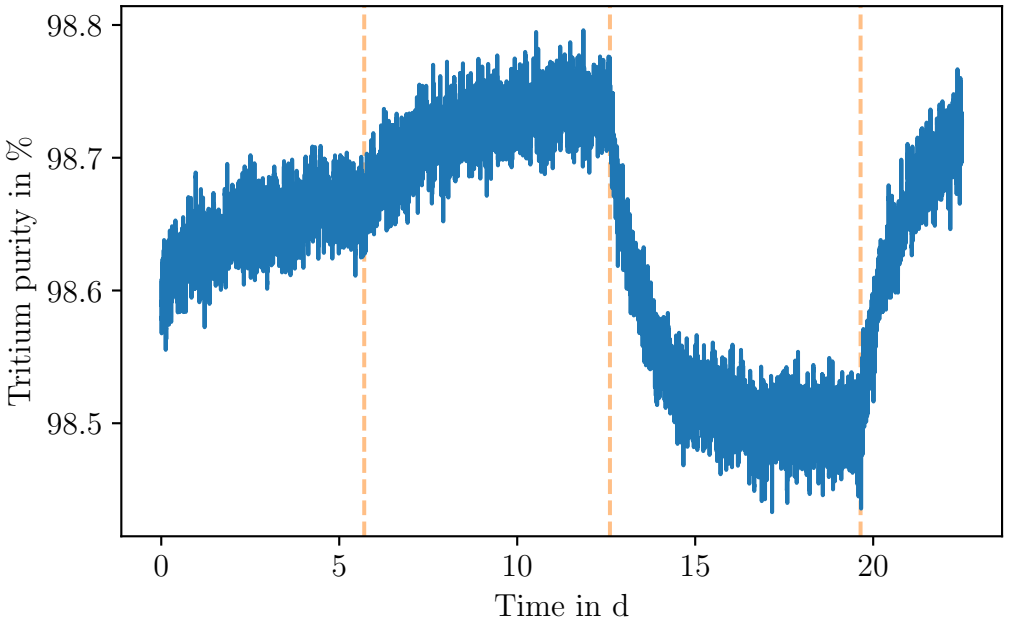

Figure 6.6.: **Change in tritium purity equilibrium due to weekly gas transfers from the TLK infrastructure.** Shown is the tritium purity measured with LARA over a period with continuous gas circulation. The times at which first transfer of a new batch to B3 are marked with dashed lines.

These different behaviors are the result of the different operating parameters during KNM1 and KNM2. The ratios of the time constants in up and down direction between KNM1 and KNM2 match within the uncertainties the ratio of the different gas inventories in the IL during KNM1 and KNM2, which is to be expected for constant flow rates of the feed and permeator bleed flows. An in-depth analysis of this behavior using simulations is performed in the following section 6.3.

6.3. Gas Composition Modeling

The aim of modeling the gas composition is to gain a deeper understanding of the impact different operation parameters have on the gas composition. With this understanding, predictions for the gas composition in operating modes without gas composition monitoring can be made. This section starts with a general formulation of the modeling problem in section 6.3.1. The model developed this way will be compared to LARA data in section 6.3.2 to validate it and derive otherwise inaccessible system parameters. It will then also be applied to the tritium+krypton mode in section 6.3.3 and verified using BIXS data. Finally, a short parameter study regarding the impact of the feed tritium purity will be presented in section 6.3.4.

6.3.1. Formulation of the Gas Composition Model

To model the gas composition inside the IL, the distribution of the amount of substance of the different gas species inside the IL needs to be calculated. Due to the low

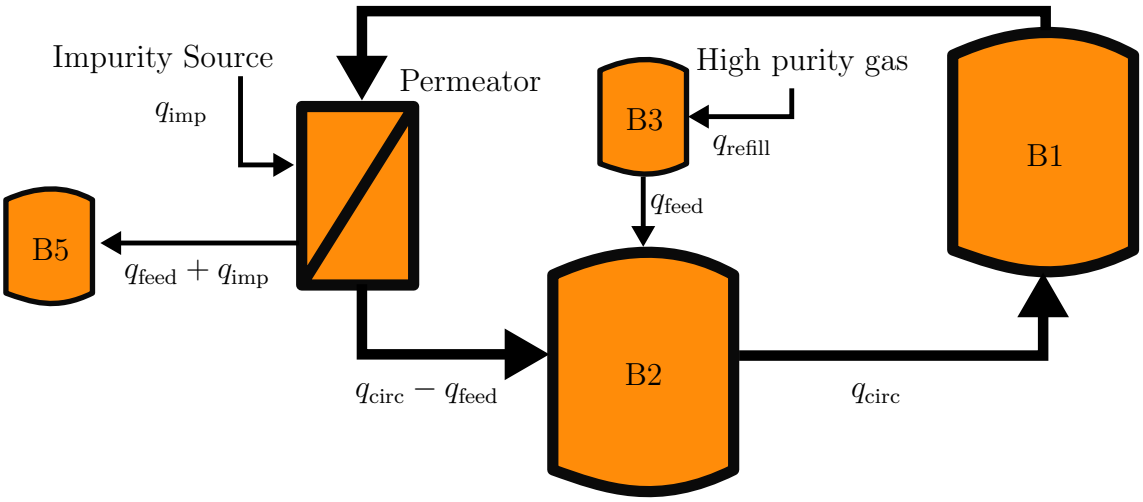

Figure 6.7.: **Schematic of the simplified model loop structure.** The complex structure of the IL and its connections to the FL and EL is reduced to the key components necessary to describe the system on an abstract level.

pressures present inside the system, the ideal gas law can be applied throughout the entire system to calculate the amount of substance. In order to keep computational effort low, a gas network model is used to describe the IL. This model simplifies the IL into a set of nodes which represent the buffer vessels and the permeator, as well as a set of connections between these nodes representing the piping. The most simple such partitioning in nodes and connections, which still reflects important properties of the IL, is illustrated in fig. 6.7. The parameters entering this model are:

- For each node (B1, B2, B3, B5, and the permeator) a set of pressure, volume, and temperature values is needed to calculate the amounts of substance inside the vessels ,
- the circulating flow rate through the IL, q_{circ},
- the feed flow rate from B3 to B2, q_{feed},
- the effective flow rate q_{imp} and concentration c_{imp} of impurities due to outgassing and isotopic exchange effects, and
- the boundary condition of the refilling flow rate q_{refill} and concentration c_{refill} from B4 to B3.

By characterizing the model in terms of total amounts of substance $n_{\mathrm{tot},j}$ and gas species independent flow rates q_j for each of the j nodes, the model can be mathematically formulated in terms of a system of differential equations of the form:

$$\frac{\mathrm{d}n_{\mathrm{tot},j}}{\mathrm{d}t} = \sum q_j \,. \tag{6.14}$$

As the concentrations $c_{i,j}$ of the i gas components are of higher interest than the total amounts of substance $n_{\mathrm{tot},j}$, the differential equations can be rewritten to reflect this:

$$\frac{\mathrm{d}}{\mathrm{d}t} c_{i,j} = \frac{\mathrm{d}}{\mathrm{d}t} \frac{n_{i,j}}{n_{\mathrm{tot},j}} \,. \tag{6.15}$$

This can be expressed more explicitly in terms of flow rates $q_{k,j}$ entering and flow rates $q_{j,l}$ leaving a node j:

$$\frac{\mathrm{d}}{\mathrm{d}t}c_{i,j} = \frac{\mathrm{d}}{\mathrm{d}t}\frac{n_{i,j}}{n_{\mathrm{tot},j}} = \frac{1}{n_{\mathrm{tot},j}} \cdot \left(\sum_k c_{i,k,j} \cdot q_{k,j} - \sum_l c_{i,j} \cdot q_{i,j,l} + f_{i,j}(t) \right) , \tag{6.16}$$

with

- $n_{i,j}$, the amount of substance of gas species i in component j,
- $n_{\mathrm{tot},j} := \sum_i n_{i,j}$, the total amount of substance of all gas species in component j,
- $q_{i,k,j}$, the gas flow of gas species i from component k to component j, and
- $f_{i,j}(t)$ is a boundary condition term which can be used to represent e.g. wall interactions. This could in principle also be realized as an interaction with an additional node, but was listed in this way for the sake of a better understanding.

At this point, several simplifications are made:

- Only H, D, and T are used as gas species instead of all different isotopologues H_2, HD, D_2, HT, DT, and T_2. This decouples the different isotopes:

$$\frac{\partial}{\partial n_{i,j}} n_{k,l} = 0, \qquad \forall j, l \quad \forall i \neq k \,, \tag{6.17}$$

  which allows treatment of the permeator as a simple node. Without this simplification, the concentrations in the permeator would need to be changed according to the thermal equilibration of isotopologues in each computation step.

- The gas flow dynamics are radically simplified by assuming gas species independent, constant flows, or at least pressure independent flows. This simplification can be made due to the conservation of mass inside the system and the flow control used at several points in the experimental setup:

$$q_{i,k,l} = q_{k,l}, \qquad \forall i \,, \tag{6.18}$$

$$\frac{\partial}{\partial p_{i,j}} q = 0, \qquad q \in \{q_{\mathrm{circ}}, q_{\mathrm{feed}}, q_{\mathrm{imp}}, q_{\mathrm{refill}}\} \,, \tag{6.19}$$

$$\frac{\mathrm{d}}{\mathrm{d}t} q = 0, \qquad q \in \{q_{\mathrm{circ}}, q_{\mathrm{feed}}\} \,. \tag{6.20}$$

- Based on the above assumption, only the quasi-steady state case is considered. This means that the initial filling of the IL and the time until the system has settled in the gas dynamical equilibrium is not simulated. The simulation starts from a state in which gas already circulates through the IL.

- The amount of gas inside the IL is constant, so for B1, B2 and the permeator the sum of flows vanishes:

$$\frac{\mathrm{d}}{\mathrm{d}t} n_{\mathrm{tot},j} = 0, \qquad j \in \{\mathrm{B1}, \mathrm{B2}, \mathrm{perm}\} \,, \tag{6.21}$$

$$\sum_i \frac{\mathrm{d}}{\mathrm{d}t} n_{i,j} = 0, \qquad j \in \{\mathrm{B1}, \mathrm{B2}, \mathrm{perm}\}, i \in \{\mathrm{H}, \mathrm{D}, \mathrm{T}\} \,. \tag{6.22}$$

With the help of these simplifications, the following system of differential equations can be derived:

$$\frac{\mathrm{d}}{\mathrm{d}t}c_{i,\mathrm{B1}} = \frac{q_{\mathrm{circ}}}{n_{\mathrm{tot,B1}}} \cdot \left(\frac{n_{i,\mathrm{B2}}}{n_{\mathrm{tot,B2}}} - \frac{n_{i,\mathrm{B1}}}{n_{\mathrm{tot,B1}}} \right) \tag{6.23}$$

$$\frac{\mathrm{d}}{\mathrm{d}t}c_{i,\mathrm{B2}} = \frac{1}{n_{\mathrm{tot,B2}}} \cdot \left(q_{\mathrm{feed}} \cdot \frac{n_{i,\mathrm{B3}}}{n_{\mathrm{tot,B3}}} + (q_{\mathrm{circ}} - q_{\mathrm{feed}}) \cdot \frac{n_{i,\mathrm{Perm}}}{n_{\mathrm{tot,Perm}}} - q_{\mathrm{circ}} \cdot \frac{n_{i,\mathrm{B2}}}{n_{\mathrm{tot,B2}}} \right) \tag{6.24}$$

$$\frac{\mathrm{d}}{\mathrm{d}t}c_{i,\mathrm{B3}} = \frac{1}{n_{\mathrm{tot,B3}}} \cdot \left(-q_{\mathrm{feed}} \cdot \frac{n_{i,\mathrm{B3}}}{n_{\mathrm{tot,B3}}} + q_{\mathrm{refill}} \cdot c_{\mathrm{refill}} \right) \tag{6.25}$$

$$\frac{\mathrm{d}}{\mathrm{d}t}c_{i,\mathrm{B5}} = \frac{q_{\mathrm{feed}} + q_{\mathrm{imp}}}{n_{\mathrm{tot,B5}}} \cdot \frac{n_{i,\mathrm{Perm}}}{n_{\mathrm{tot,Perm}}} \tag{6.26}$$

$$\frac{\mathrm{d}}{\mathrm{d}t}c_{i,\mathrm{Perm}} = \frac{1}{n_{\mathrm{tot,Perm}}} \cdot \left(q_{\mathrm{circ}} \cdot \frac{n_{i,\mathrm{B1}}}{n_{\mathrm{tot,B1}}} + q_{\mathrm{imp}} \cdot c_{i,\mathrm{imp}} - \left(q_{\mathrm{circ}} + q_{\mathrm{imp}} \right) \cdot \frac{n_{i,\mathrm{Perm}}}{n_{\mathrm{tot,Perm}}} \right) \tag{6.27}$$

This system can then be solved numerically for arbitrary parameters (q_{circ}, q_{feed}), initial values ($n_{i,j}(t_0)$) and boundary conditions ($q_{\mathrm{refill}}(t)$, $c_{\mathrm{refill}}(t)$, $q_{\mathrm{imp}}(t)$, $c_{\mathrm{imp}}(t)$).

The numerical solution is performed using Python [Van10] and the `scipy` [Vir+20] implementation of an implicit Runge-Kutta method of the Radau IIA family of order 5 [HW91]. An implicit method was chosen due to the stiffness of the differential equation, which arises when the actual values representing the usual IL operation are used. The huge difference in magnitude between $q_{\mathrm{circ}} \approx 1.8\,\mathrm{mbar}\,\ell\,\mathrm{s}^{-1}$ and $q_{\mathrm{feed}} \approx 0.023\,\mathrm{mbar}\,\ell\,\mathrm{s}^{-1}$ or $q_{\mathrm{imp}} \approx 1 \times 10^{-5}\,\mathrm{mbar}\,\ell\,\mathrm{s}^{-1}$ forces explicit numerical solvers to use very small step widths, which is impractical for simulations of long time scales, and the results suffer from numerical noise.
The particular solver was chosen among the implicit solvers implemented in `scipy`, as it has shown to converge on the fastest time scale for this particular problem.

6.3.2. Application of Model to Data in the Neutrino Mass Measurement Mode

To compare how well the gas composition model is able to describe the measurement data, it is necessary to use correct parameters as well as initial and boundary values to solve the underlying differential equations. In the following sections 6.3.2.1 and 6.3.2.2, this is done for both effects described in section 6.2, which require slightly different input parameters. After that, a short summary on the applicability of the model to KATRIN is given in section 6.3.2.3

6.3.2.1. Application of the Model to Starting of the Circulation

In order to describe the start of circulation, the initial parameters and boundary conditions were chosen as described in the following paragraphs.

Definition of Model Parameters and Assumptions

The parameters used as input for the model are:

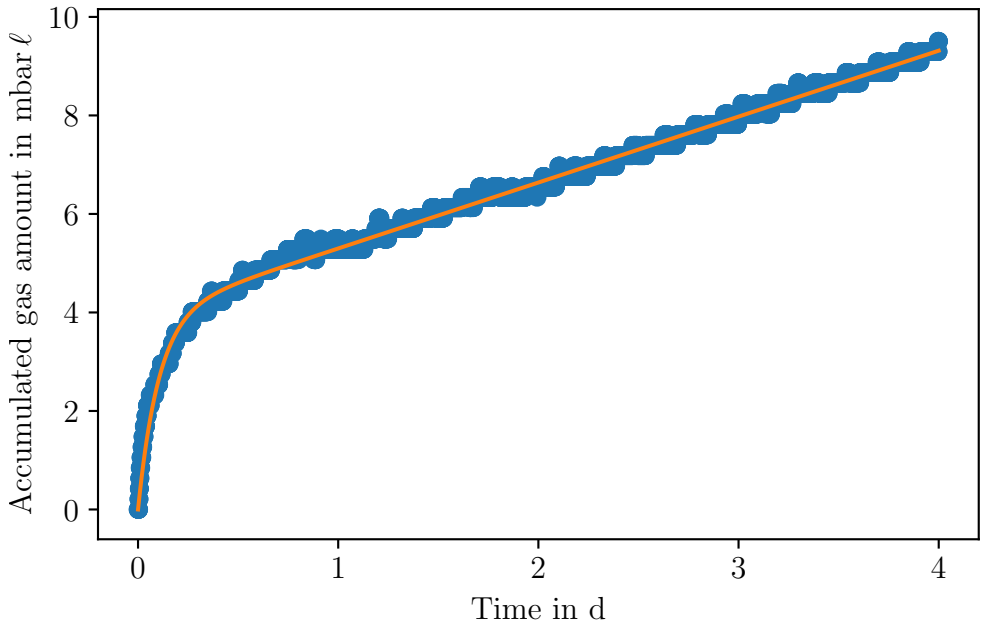

Figure 6.8.: **Behavior of WGTS outgassing.** Shown is the accumulation of gas behind the TMPs of the DPS1 due to outgassing of the WGTS beam tube and the TMPs. A fit combining an initially exponential increase followed by a long term linear increase was applied to the data. The derivative of this fit can be taken as an estimate for the behavior of q_{imp}

- The feed concentration c_{refill}, which can in principle be measured in the TTS of the TLK infrastructure before transferring the gas to KATRIN. Due to possible changes in composition during the transfer, as well as due to slight differences in the setup between the LARA systems of the TTS and IL, and taking into account a missing cross-calibration between both systems, differences on the $<1\,\%$ level have been found to occur. These differences would cause the model to deviate greatly from the actual measurement when using the TTS gas composition values as input. Therefore, the first ≈ 10 values measured by the IL LARA system after filling of the loop are used to determine c_{refill}. It is assumed to stay constant until a new batch of gas from the TTS is added to it.
- The initial gas composition inside the IL is taken to be $c_{\mathrm{refill}}(t_0)$.
- The initial amounts of substance $n_{i,j}$ for the different gas species and vessels are calculated based on their measured pressure and temperature as well as their known volume via the ideal gas law, combined with the initial gas composition.
- The flows q_{circ} and q_{feed} are taken as measured by the mass flow meters in the IL.
- In a simplifying assumption, the concentration of impurities c_{imp} is taken as constant and to consist purely of H.

With all of the above parameters determined, only the effective flow rate of impurities q_{imp} is missing. This parameter is not easily accessible by external measurement. This is due to the fact that this flow rate is closely related to isotopic exchange, on the surfaces of the vacuum system as well as with impurities in the gas phase, and therefore highly non-trivial. An estimation of the general behavior of q_{imp} can be

made by looking at the measured accumulation of outgassing gas of the WGTS when no tritium is being circulated. Such a measurement is shown in fig. 6.8, together with a fit of the form:

$$f = c + q_{\mathrm{imp},0} \cdot t - A\tau \cdot \mathrm{e}^{-\frac{t}{\tau}} \,. \tag{6.28}$$

The derivative of f can be taken as an approximation of the behavior of q_{imp}:

$$q_{\mathrm{imp}}(t) = q_{\mathrm{imp},0} + A \cdot \mathrm{e}^{-\frac{t}{\tau}} \,. \tag{6.29}$$

The parameters extracted from the fit in fig. 6.8 are:

$$q_{\mathrm{imp},0} = (1.55 \pm 0.07) \times 10^{-5}\,\mathrm{mbar}\,\ell\,\mathrm{s}^{-1}\,, \tag{6.30}$$
$$A = (4.42 \pm 0.02) \times 10^{-4}\,\mathrm{mbar}\,\ell\,\mathrm{s}^{-1}\,, \tag{6.31}$$
$$\tau = (8.964 \pm 0.015) \times 10^{3}\,\mathrm{s} = (2.490 \pm 0.004)\,\mathrm{h}\,. \tag{6.32}$$

This equation can be understood as the combination of a fast equilibration process between the gas and H atoms on the vessel surface described by the exponential function and a quasi-constant contribution. The quasi-constant contribution is a combination of H atoms stemming from outgassing of the steel vessel after diffusion of H from the bulk material, outgassing of hydrocarbons from the DPS1 TMPs, and air leakages through the TMP O-ring sealings.

Application to the Data

With the above assumptions, a model with 3 free parameters is used to fit to the measured data. An attempt of constraining $q_{\mathrm{imp},0}$ from outgassing measurements, leading to a scale of $2 \times 10^{-5}\,\mathrm{mbar}\,\ell\,\mathrm{s}^{-1}$, can be found in appendix D. For this fit, only the residuals of the T concentration between measurement and model were considered, leaving the simulated H and D concentrations as a cross-check. The model fits well to the data with a reduced χ^2 of 0.9. A fit of the model to a specific start of the gas circulation during the KNM2 campaign is shown in fig. 6.9. The derived parameters for q_{imp} are:

$$q_{\mathrm{imp},0} = (1.35 \pm 0.06) \times 10^{-4}\,\mathrm{mbar}\,\ell\,\mathrm{s}^{-1}\,, \tag{6.33}$$
$$A = (9.23 \pm 0.05) \times 10^{-3}\,\mathrm{mbar}\,\ell\,\mathrm{s}^{-1}\,, \tag{6.34}$$
$$\tau = (1.093 \pm 0.009) \times 10^{4}\,\mathrm{s} = (3.037 \pm 0.025)\,\mathrm{h}\,. \tag{6.35}$$

Using this approach on the KNM1 time intervals for which time constants of equilibration were derived in eq. (6.7), the data can be replicated by the model. The corresponding fitted parameters for q_{imp} for one such KNM1 interval are:

$$q_{\mathrm{imp},0} = (1.52 \pm 0.02) \times 10^{-4}\,\mathrm{mbar}\,\ell\,\mathrm{s}^{-1}\,, \tag{6.36}$$
$$A = (1.50 \pm 0.01) \times 10^{-3}\,\mathrm{mbar}\,\ell\,\mathrm{s}^{-1}\,, \tag{6.37}$$
$$\tau = (1.891 \pm 0.027) \times 10^{4}\,\mathrm{s} = (5.253 \pm 0.075)\,\mathrm{h}\,. \tag{6.38}$$

The constant contribution $q_{\mathrm{imp},0}$ in both measurements is very similar with the relative deviation between the measurements being on the same scale as the relative variation observed in outgassing measurements. The dynamic component however

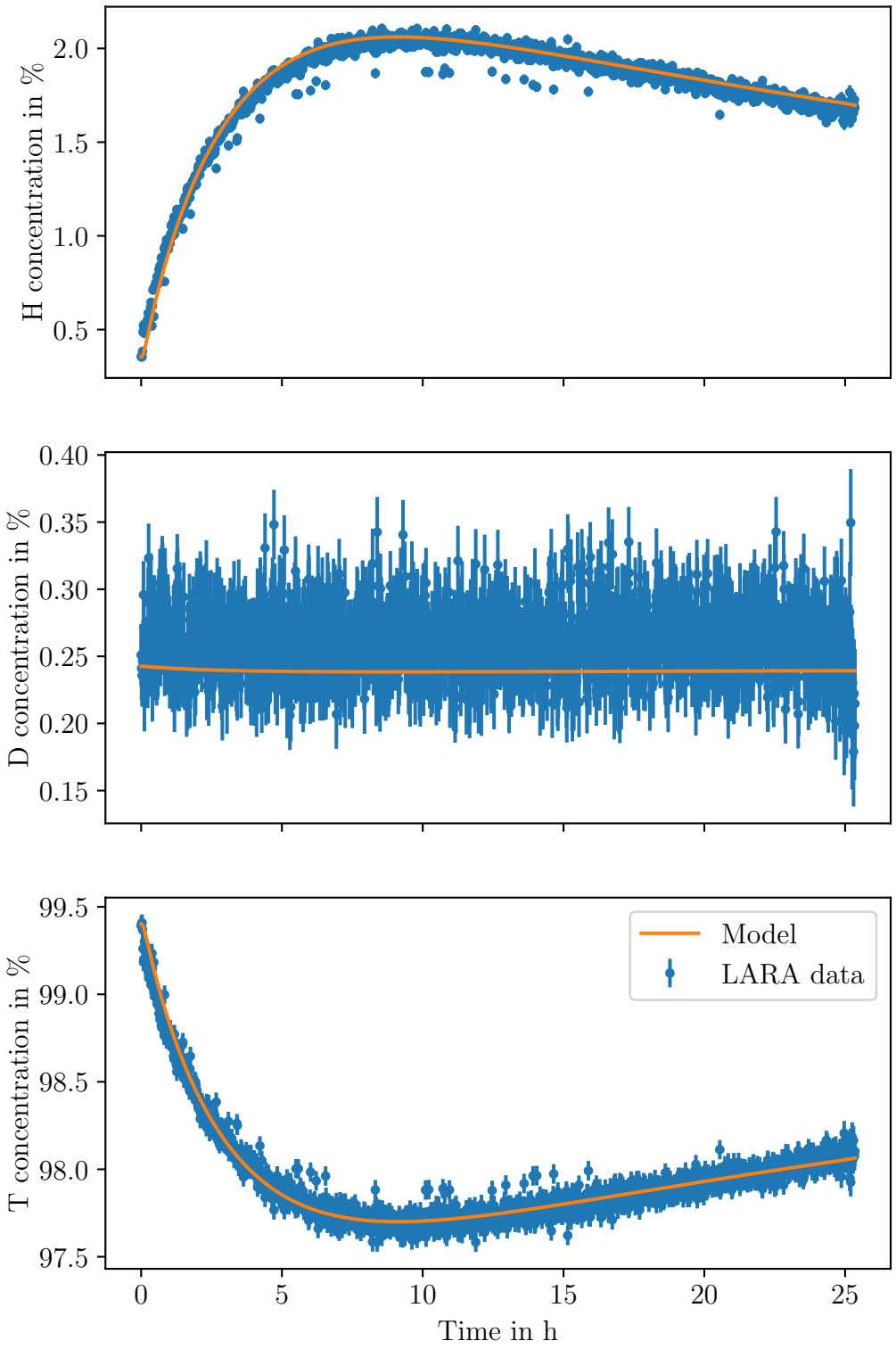

Figure 6.9.: **Comparison of gas composition model to measured data after starting the gas circulation.** Shown is LARA data from KNM2 where the gas circulation was started from a state without any gas inside, allowing a precise determination of the initial conditions. The below average D_2 value of the simulation is an artifact of a statistical underfluctuation in the first 10 LARA values used to initialize the simulation.

differs greatly. In KNM2, the magnitude of the dynamic component of the impurity flow rate is larger by a factor of 6, while the time constant is only about half of that of KNM1. As the main difference between the KNM1 and KNM2 campaigns is the respective circulating flow rates, the difference in impurity flow behavior is most likely related to this parameter. A possible explanation is the higher pressure inside the system at higher flow rates, leading to a stronger isotopic exchange and thus a bigger value for the parameter A.

Comparing these values to the ones expected from outgassing data listed in eqs. (6.30) to (6.32), both simulation results show much larger values for $q_{\mathrm{imp},0}$ and A. The lower value of A is most likely a continuation of the positive correlation between A and the circulating flow rate. The lower value of $q_{\mathrm{imp},0}$ is a result of the absence of the permeator in the static outgassing measurement. As demonstrated in section 5.3.3, the accumulation of gas due to TMP outgassing implies a large fraction of hydrocarbons. In view of the rise in pressure they cause, these hydrocarbons (CH_4, C_2H_4, C_2H_6, ...) provide much more H atoms which can undergo isotopic exchange once cracked by the permeator than pure hydrogen (H_2) from the vessel walls.

6.3.2.2. Application of the Model to Batches of different Isotopic Composition

A similar approach as above can be taken to model the observed concentration changes due to variations in the gas supplied from the TLK infrastructure.

Definition of Model Parameters and Assumptions

In the case of the effect of the isotopic composition of different batches of gas, the initial parameters, in particular the gas composition of the pure tritium buffer vessel B3, are not readily available. As seen in the above data and simulation, impurities will shift the concentrations in the IL away from those in B3. To still be able to gain some insight, and due to the steady state nature of the gas circulation investigated here, the influence of impurities can be approximated as a constant offset in the gas concentrations. With this, one can choose the parameters as listed below.

- The concentration of impurities is assumed to be constant and taken into account via a shift of the initial and final concentration and therefore the impurity flow is set to $q_{\mathrm{imp}} = 0$.
- The initial gas composition $c(t_0)$ inside the IL and B3 is assumed to correspond to $\overline{c_{\mathrm{LARA}}(t_0)}$, the average of the first ≈10 values measured by LARA.
- The boundary condition of the concentration being fed into B3 is given by:

$$c_{\mathrm{refill}} = \begin{cases} c_{\mathrm{LARA}}(t_0), & \text{if } t < t_{r,1} \\ \overline{c_{\mathrm{LARA}}(t_{\mathrm{end}})}, & \text{if } t \geq t_{r,1} \end{cases} \tag{6.39}$$

  with $t_{r,1}$ being the time of first injection of a fresh gas batch and $\overline{c_{\mathrm{LARA}}(t_{\mathrm{end}})}$, the average final equilibrium gas composition as measured by LARA.

- The feed flow into B3 is given by:

$$q_{\text{refill}} = \begin{cases} \frac{\Delta p_i \cdot V_{\text{B3}}}{\Delta t} - q_{\text{feed}}, & \text{if } t_{r,i,\text{start}} < t < t_{r,i,\text{end}} \\ 0, & \text{otherwise} \end{cases} \tag{6.40}$$

  with $t_{r,i,\text{start}}$ and $t_{r,i,\text{end}}$ being the start and stop time of the i-th refill of B3, and the associated measured total pressure change Δp_i of the refill.

Application to the Data

As the above assumptions leave no free parameters, the gas composition can be computed directly from the model without requiring a fit to the data. The result of a calculation of the gas composition model based on these input parameters is shown in fig. 6.10. The model solution for the gas composition is given by an exponential function with stepwise changing equilibrium concentration value governed by the concentration in B3. The refilling of B3 with fresh gas is performed while it still contains some remaining gas. Thus, the concentration in B3 changes stepwise with the steps exponentially approaching the final equilibrium value.

The model agrees very well with the data despite the simplifying assumptions concerning q_{imp}. A slight discrepancy between model and data is visible in the residuals. In the region directly after the refilling, the concentrations do not change as steeply as expected. This smoothing is most likely a buffering effect caused by long time constants of diffusion into and from the bulk material of the vacuum vessels. These time constants cause the surface concentration of hydrogen isotopes to be retarded with regard to the gas phase. The overabundance/depletion counteracts the change of concentration in the gas phase, slightly slowing the equilibration process until the surface and bulk are in equilibrium with the gas phase.

This surface buffering effect also explains the different time constants between between increasing and decreasing tritium purity, as observed in section 6.2.2: When the differential equations from section 6.3.1 are solved analytically for constant flow rates, the resulting solution consists of exponential functions whose time constant depends on the flow rates. The buffering effect induces a value of q_{imp} which depends on the isotopic composition and its history, and in second order on the flow rate of circulating gas. Such a changing q_{imp} behavior is the most simple explanation for time constants, which changes depending on the isotopic composition and history of the system.

6.3.2.3. Evaluation of the Applicability of the Isotopic Composition Model

The model presented in this section is capable of describing the time dependency of isotopic exchange effects in the inner loop using only a minimal set of parameters. Given appropriate input parameters, it can replicate within the experimental uncertainties the behavior of the gas composition upon starting the circulation as well as the impact of changing feed gas composition. These were the two major observed effects on the gas composition. As a result of this good performance, the original goal of gaining deep insight into the gas composition during the neutrino

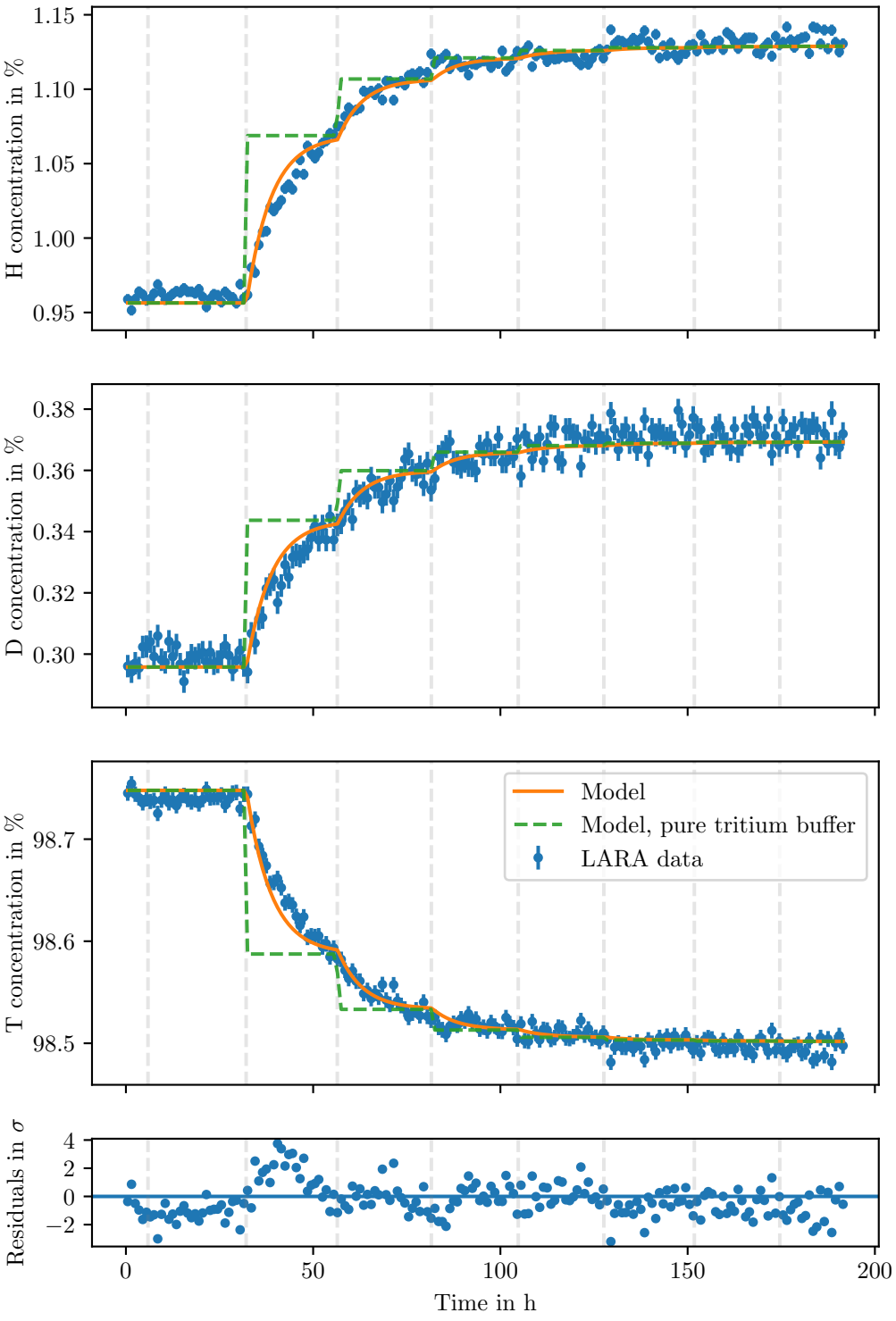

Figure 6.10.: **Comparison of gas composition model to measured data for weekly gas transfers from the TLK infrastructure.** Shown is data from the KNM2 campaign with constant gas circulation and changes in the gas composition due to a change in the feed gas composition supplied by the TLK infrastructure. Additionally, the residuals for the tritium concentration are given. The dashed line shows the simulated composition in the pure tritium buffer vessel B3, whose step-wise exponential changes are caused by the daily refilling of the not completely empty B3.

mass mode can be surpassed by extending the predictive power of the simulation to the tritium+krypton mode, where LARA composition monitoring is unavailable.

6.3.3. Time evolution of the Gas Composition in Tritium+Krypton Mode

To apply the above described model to the tritium+krypton mode, it needs to be adjusted slightly. The lack of complexity compared to the neutrino mass mode means that the tritium+krypton mode can be accurately described by a single vessel, grouping the WGTS, DPS1, and the piping between them with an inflow q_{in} and outflow q_{out} of gas, as well as an effective flow of impurities q_{imp}.

The effective volume V_{eff} of this "pseudo-vessel" can be obtained via the ideal gas law by considering the bulk of gas to be contained in the room temperature components and measuring the transferred amount of gas when starting the tritium+krypton mode:

$$V_{eff} = 28.1\,\ell\,. \tag{6.41}$$

With this volume, the outflow can be derived from the original operation scheme of the tritium+krypton mode, where gas is continuously lost to the DPS2 and RS while not being replaced:

$$q_{\mathrm{out}} = 4 \times 10^{-4}\,\mathrm{mbar}\,\ell\,\mathrm{s}^{-1}\,. \tag{6.42}$$

Assuming this outflow to be constant for small changes of the pressure in the pseudo-vessel, the inflow can be derived from the pressure change:

$$q_{\mathrm{in}} = \frac{\Delta p}{\Delta t} - q_{\mathrm{out}} - q_{\mathrm{imp}}\,. \tag{6.43}$$

A value for the impurity flow of $q_{\mathrm{imp}} = 1.5 \times 10^{-5}\,\mathrm{mbar}\,\ell\,\mathrm{s}^{-1}$ is chosen based on the scale of outgassing rates, which were measured under similar conditions in appendix D.

Running such a modified simulation for a tritium purity[2]of $\varepsilon_{\mathrm{T},0} = 98.4\,\%$, the resulting solution can described by an exponential function with an equilibrium tritium purity of:

$$\varepsilon_{\mathrm{T,eq}} = 94.8\,\%\,, \tag{6.44}$$

with a time constant of

$$\tau = 4.87\,\mathrm{d}\,. \tag{6.45}$$

This shows that even without gas purification, relying solely on feeding of high purity tritium with gas losses to the DPS2 and RS, the tritium purity can be kept close to the target value of >95 % set for the neutrino mass mode. Considering the usual time scale of tritium+krypton mode operation, the rather long time constant prohibits to reach equilibrium due to the measurement schedule. However, the long time constant also implies small relative changes on shorter time scales, causing

[2]The initial concentrations were taken from the LARA measurements at the initial filling of the pseudo-vessel during KNM1

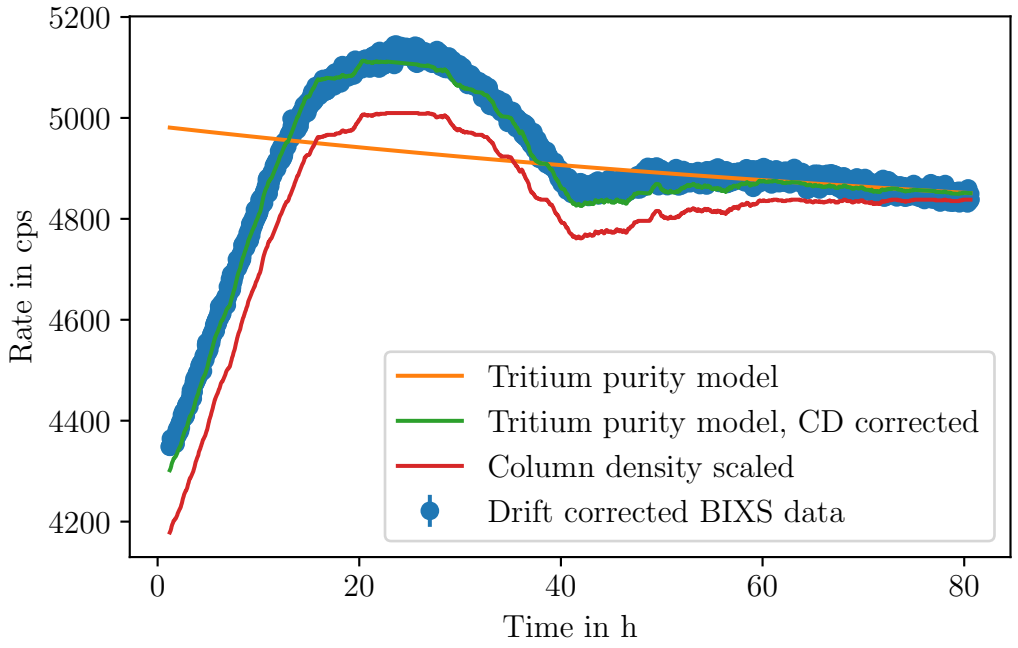

Figure 6.11.: **Validation of gas composition model for tritium+krypton mode using BIXS data.** Shown are the tritium purity calculated using the gas composition model, the column density calculated from pressure measurements, as well as their combination, referenced to the BIXS data. The BIXS data is corrected for a long term drift of the BIXS detectors.

the stability of the tritium purity to be better than $0.1\,\%\,\mathrm{h}^{-1}$, meeting the stability requirements.

Finally, to validate the application of the gas composition model to the tritium+krypton mode, the source activity as measured by BIXS is used. For this, it is necessary to include both the tritium purity derived from the model, as well as the column density of gas inside the WGTS, which is derived via gas dynamics simulations from measured pressures. The result of this is shown in fig. 6.11, with all model curves normalized to the last point of the BIXS data. The combination of the calculated column density with the decreasing tritium purity describes the observed shape of the BIXS data well, validating the application of this model to the tritium+krypton mode.

6.3.4. Tritium Purity Parameter Study

The tritium purity is a key parameter for the neutrino mass analysis. A higher tritium purity results in a better ratio of β-electrons to molecules on which these electrons can scatter, leading to a higher fraction of unscattered electrons. Similarly, a higher tritium purity means less HT and DT, whose different final state distribution causes a smearing of the β-spectrum. It is therefore of great interest to determine the factors limiting the equilibrium tritium purity $\varepsilon_{\mathrm{T,eq}}$. For this purpose, the simulations of the previous sections 6.3.2.1 and 6.3.3 have been run again with different input values for the feed tritium purity $\varepsilon_{\mathrm{T,feed}}$ and the long-term impurity flow rate $q_{\mathrm{imp,0}}$.

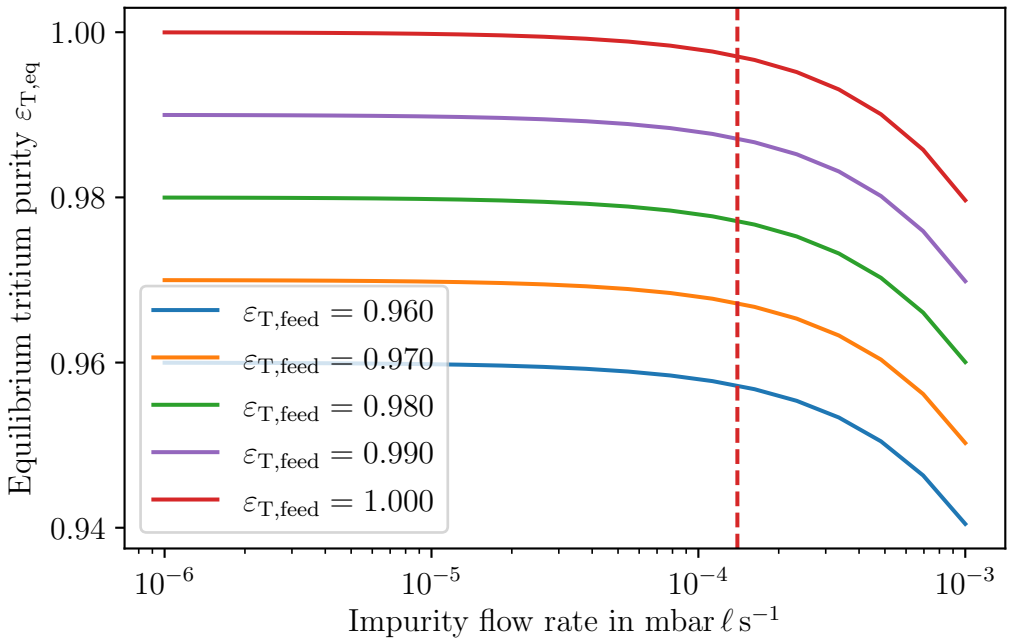

Figure 6.12.: **Equilibrium tritium purity parameter study for the neutrino mass measurement mode.** Shown is the simulated equilibrium tritium purity $\varepsilon_{T,eq}$ in the neutrino mass measurement mode as a function of the impurity flow rate $q_{imp,0}$ for several different feed tritium purities $\varepsilon_{T,feed}$. The dashed red line shows the level of impurity flow rate observed in the experiment.

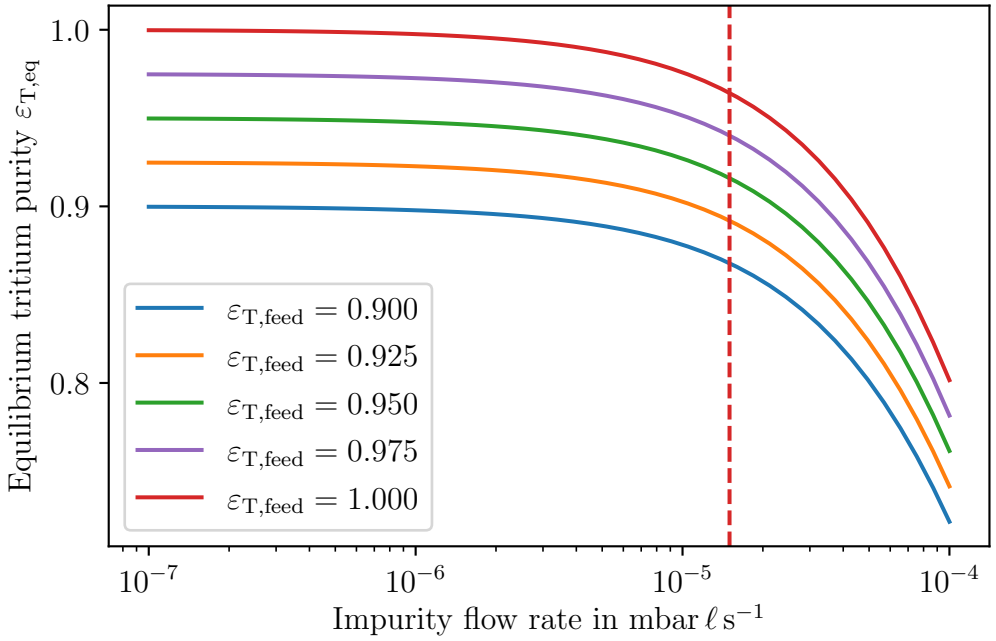

Figure 6.13.: **Equilibrium tritium purity parameter study for the tritium+krypton mode.** Shown is the simulated equilibrium tritium purity $\varepsilon_{T,eq}$ in the tritium+krypton mode as a function of the impurity flow rate $q_{imp,0}$ for several different feed tritium purities $\varepsilon_{T,feed}$. The dashed red line shows the level of impurity flow rate observed in the experiment.

The results of these simulations are shown in figs. 6.12 and 6.13. As can be seen in both figures, the impurity flow rate in both operation modi is on a level where it negatively impacts the tritium purity to a small degree. Furthermore, for realistic levels of impurity flow rate, an increase of the feed tritium purity $\varepsilon_{\mathrm{T,feed}}$ translates directly into an increase of the equilibrium tritium purity $\varepsilon_{\mathrm{T,eq}}$.

From these observations the following conclusions with regards to improving the system can be drawn:

- A decrease of the impurity flow rate would slightly increase $\varepsilon_{\mathrm{T,eq}}$. However, the majority of the impurity flow rate is caused by outgassing of the DPS1 TMPs. There is currently no alternative for these pumps available, so improving this parameter would involve a disproportionate amount of R&D effort on top of the expected several months of downtime associated with an exchange of these pumps.

- An increase of the feed tritium purity $\varepsilon_{\mathrm{T,feed}}$ will increase $\varepsilon_{\mathrm{T,eq}}$ in equal measure. This could be realized by a more aggressive operation scheme of the ISS and transport from the ISS to the IL with less isotopic exchange. Such strategies, which sacrifice throughput per process cycle for purity, would increase the number of times the exhaust gas would have to be processed in the ISS, which increases the workload on the ISS and the operators. Reduction of the tritium purity due to isotopic exchange during transport from the ISS to the IL can be reduced by saturating the the transfer lines with high purity tritium. Both measures could, at least in principle, be implemented in the current experimental configuration, but would require a significant amount of effort. In practice, a significant increase of the average tritium purity would most likely make modifications to the ISS necessary, which would mean a long downtime of the KATRIN experiment.

Summarizing the above consideration, a decrease of the amount of impurities is not feasible. The only realistic possibility to push the already excellent $\varepsilon_{\mathrm{T,eq}}$ of $>98\,\%$ to an even higher level is the increase of the feed tritium purity $\varepsilon_{\mathrm{T,feed}}$.

6.4. Results of Investigating Gas Composition Changes in the Loop System

As described above, the gas composition inside the inner loop has been thoroughly investigated using both RGA and LARA measurements. Monitoring of the source composition during neutrino mass mode operation with LARA has been qualified using the RGA.

Based on LARA measurements made during several KATRIN measurement campaigns, several important effects which impact the gas composition have been identified. The most prominent effects are those associated with the start of the circulation and changes of the equilibrium gas composition due to different gas batches prepared by the TLK infrastructure. With a time period of about one day needed for stabilization after the start of gas circulation, any interruption should be avoided whenever

possible to minimize the loss of neutrino mass measurement time. The issue of composition changes between different gas batches on the other hand is inherent to the tritium purification of the TLK infrastructure.

To gain further understanding of these effects, a model using a minimal amount of free parameters has been constructed and compared to LARA measurements. An excellent agreement of model and data has been found with discrepancies below the 0.1 %-level.

With LARA data validating it, the model has then been applied to the tritium+krypton mode in an adapted form to gain a handle on the changes in gas composition. The derived time constant of equilibration is on the scale of 5 days, which restricts changes in the tritium purity in the tritium+krypton mode to be below $0.1\,\%\,\mathrm{h}^{-1}$. Furthermore, the equilibrium tritium purity of 94.8 % is at the level of the neutrino mass mode requirement of 95 %.

A parameter study using the developed model shows that a further increase in tritium purity inside the WGTS is possible. The only way this could be achieved would be by increasing the tritium purity of the gas provided by the Isotope Separation System via a more aggressive, workload-intensive purification scheme.

Summarizing the results of this chapter, all important isotope exchange effects impacting the gas composition in the loop system are well understood and within the requirements for KATRIN.

7. Stability of the Tritium Source Column Density during the KNM1 and KNM2 Measurement Campaigns

Precise knowledge of the column density ρd, or more accurately the product of column density and the inelastic electron scattering cross section, $\rho d\sigma$, with an accuracy $<0.2\,\%$ is essential for the neutrino mass analysis. It constrains the absolute value of the activity entering the neutrino mass analysis, and is necessary to correctly handle the systematic effects of electron scattering on gas inside the source.

This chapter first introduces the methods used to monitor the column density in section 7.1. Observed effects due to outside influences, which negatively impact the column density stability, are discussed in section 7.2 and the achieved stability is presented in section 7.3.

7.1. Determination Methods for the Column Density

The column density of the WGTS can be monitored in several ways by measuring the:

- pressure p_{inj} inside the injection chamber,
- flow rate q_{WGTS} in the IL,
- β-rate with BIXS, the FBM, or the FPD, or the
- energy-dependent response function with mono-energetic electrons from the E-Gun.

Of these methods, only the E-Gun measurements provide results which directly access te parameter $\rho d\sigma$ (see section 7.1.1). This makes the E-Gun the most suitable tool to determine $\rho d\sigma$. However, this method requires scanning of the spectrometer voltage and therefore dedicated measurement time.

The other measurement methods operate in parallel to neutrino mass measurements, but suffer from systematic effects when deriving $\rho d\sigma$. Measurements of pressures and flow rates can be used to determine ρd in the framework of simulating the gas distribution inside the WGTS (see section 7.1.2). In doing so, additional information in

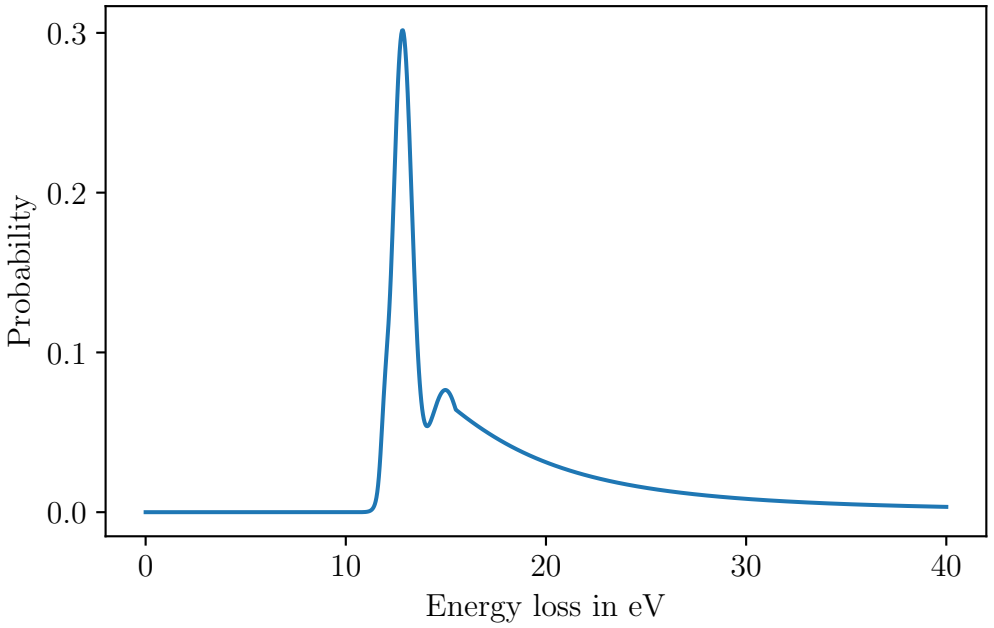

Figure 7.1.: **Energy loss distribution.** Shown is the probability for an electron with 18.6 keV to lose a certain amount of energy in an inelastic collision with a tritium molecule. The used parametrization was derived from E-Gun measurements done with the KATRIN setup [Sch20; Sac20].

form of the inelastic electron scattering cross section σ for tritium is required. This is calculated from theory to be $3.64 \times 10^{-18}\,\mathrm{cm}^2$ at 18.6 keV [Ake+19] with an uncertainty of 0.6 % [Glü19]. Activity measurements require a detailed understanding of the detector response for a given source activity and gas composition to calculate ρd.

While trueness is an issue for these measurement methods, their precision is well below the required <0.2 %. For this reason, E-Gun calibration measurements are used to derive accurate column density values from the continuously available monitoring methods (see section 7.1.3).

7.1.1. Column Density Determination with the Electron Gun

The E-Gun can access $\rho d\sigma$ directly by measuring the energy dependent response function of mono-energetic electrons traveling through the source. These electrons can scatter on gas molecules during their propagation through the WGTS beam tube. In elastic scattering processes, the energy loss of the electrons is negligible. For inelastic scatterings however, they lose energy according to the energy loss distribution f shown in fig. 7.1. The probability P_s of an electron to scatter s times on gas molecules for a specific column density ρd is given by the following formula [Kle+19]:

$$P_s(\rho d\sigma) = \frac{(\rho d\sigma)^s}{s!} \cdot \mathrm{e}^{-\rho d\sigma}\,. \tag{7.1}$$

The response function $R(\rho d\sigma)$ can then be calculated as the superposition of s times self-convoluted energy loss distributions weighted with the scattering probabilities

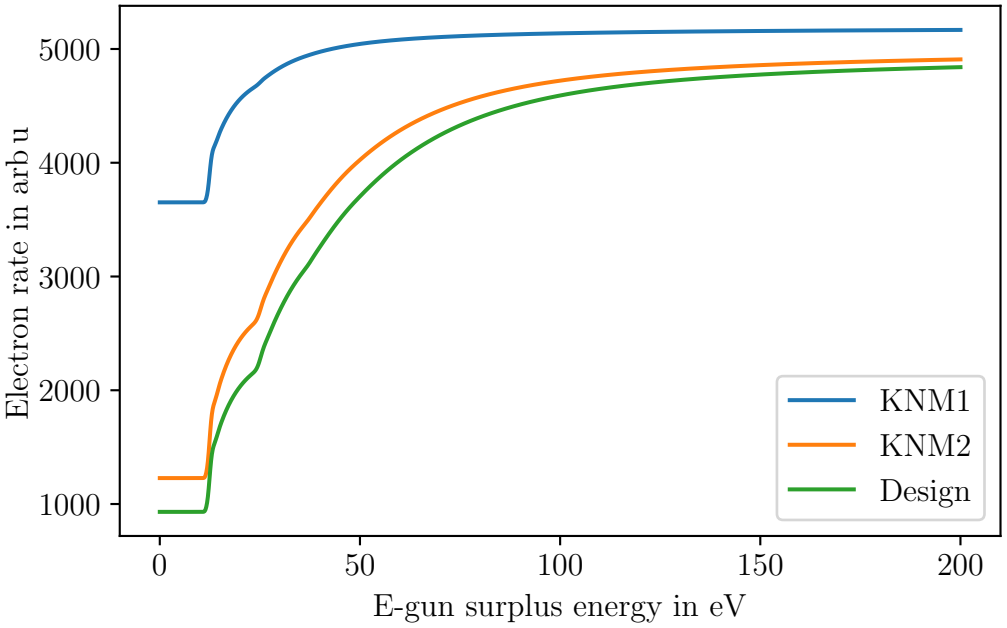

Figure 7.2.: **Column density dependent response function of E-Gun electrons.** Shown are the response functions for the average column densities during KNM1 ($1.1 \times 10^{21}\,\mathrm{m}^{-2}$) and KNM2 ($4.2 \times 10^{21}\,\mathrm{m}^{-2}$), as well as for the design value of $5 \times 10^{21}\,\mathrm{m}^{-2}$. The response functions were calculated using the energy loss distribution from [Sch20; Sac20] with scattering cross section from [Ake+19; Glü19].

P_s [Ake+19]:

$$\mathcal{R}(\rho d\sigma, E) = \int_0^E \sum_s P_s(\rho d\sigma) \cdot f^{*s}(\epsilon) \mathrm{d}\epsilon\,, \tag{7.2}$$

with:

$$\underbrace{f * f * \cdots * f}_{s} \overset{\text{def}}{=} f^{*s}, \qquad f^{*0}(\epsilon) = \delta(\epsilon)\,. \tag{7.3}$$

The transmission function $\mathcal{T}$ describes the probability for electrons to pass the main spectrometer analyzing potential as a function on their energy. This important functions is not considered here, as it is constant in the ρd-related region-of-interest of a few eV below the filter voltage.

With a proper normalization to the rate of mono-energetic electrons supplied by the E-Gun, response functions for different column densities, as shown in fig. 7.2, can be obtained.
For the higher column density in KNM2 of $4.2 \times 10^{21}\,\mathrm{m}^{-2}$ and for the design value of $5 \times 10^{21}\,\mathrm{m}^{-2}$, the kink of two-fold scattered electrons around 25 eV is much more pronounced than for lower column density values such as $1.1 \times 10^{21}\,\mathrm{m}^{-2}$ in KNM1. This difference in shape allows for a measurement of the column density. Experimentally, this is done by scanning the main spectrometer potential to measure the surplus energy the electrons need to pass it for several characteristic energies. The column density is then extracted by fitting eq. (7.2) with a normalization to the measured rates. The accuracy on $\rho d\sigma$ which has been achieved with this measurement

method in KNM2 is smaller than 0.3 %. A general statement about the accuracy is difficult as it depends on a variety of factors[1], one of them being $\rho d\sigma$ itself.

7.1.2. Column Density Determination from Gas Properties

Starting with the initial conceptional design of the WGTS, the gas dynamics of tritium gas flowing through the source tube has been simulated extensively [KAT05; Kuc+18; Hei19]. The main focus of these simulations was to gain an understanding of the gas distribution inside of the source in order to accurately model the emitted β-electron spectrum. As a side effect, there is a good understanding on the dependence of the column density on parameters accessible from the outside such as temperatures, pressures and flows.

The uncertainty on ρd, which can be achieved by using these simulations, is on the order of 2 % [Kuc+18]. While this is not sufficient to fulfill the 0.2 % accuracy requirement, it is the best tool to investigate a large parameter space for e.g. setting new values of the column density at arbitrary temperatures without trial and error E-Gun measurements. For this purpose, the existing simulations have been expanded[2] to allow a direct calculation of the column density from the pressure in the stabilized buffer vessel B1 (for details see appendix B). A comparison of the simulated column density with the column density measured by the E-Gun as described in the previous section is shown in fig. 7.3. In general, the simulated values fit well to the data. They agree to within a value of $1\,\sigma$ for the design value of $5 \times 10^{21}\,\mathrm{m}^{-2}$. However, a systematic shift of the simulated column density values towards lower values by $\approx 1 \times 10^{20}\,\mathrm{m}^{-2}$ is visible. This shift is most likely caused by the imperfect knowledge of the pressure boundary condition p_{out} of the simulation at the two ends of the source tube, towards the DPS1 pump ports. A direct proportionality of injection pressure p_{in} in the center of the WGTS to this outlet boundary pressure was assumed in the simulations, whereas measured pressures indicate a root-like dependence:

$$p_{\mathrm{out}} = a \cdot p_{\mathrm{in}}^{b} + c\,, \tag{7.4}$$

with $b = 0.57 \pm 0.15$. The parameters a and c extracted from measured data can not be used as an input for the simulations as the pressure values are not measured directly at the boundaries and would require further simulations to make use of them.

Regardless of this discrepancy, the simulation provides robust results over the interesting parameter region of source operation and can be used as a cross-reference to notice and identify systematic effects, as will be presented in section 7.2.

7.1.3. Column Density Calibration of Slow Control Sensors with the Electron Gun

For the neutrino mass analysis, a combination of the E-Gun column density measurement and the measurements of pressure and throughput are used. To accomplish

[1] For more details on the uncertainty of this method see [Blo+20; Blo21]
[2] In cooperation with F. Sharipov, sharipov@fisica.ufpr.br

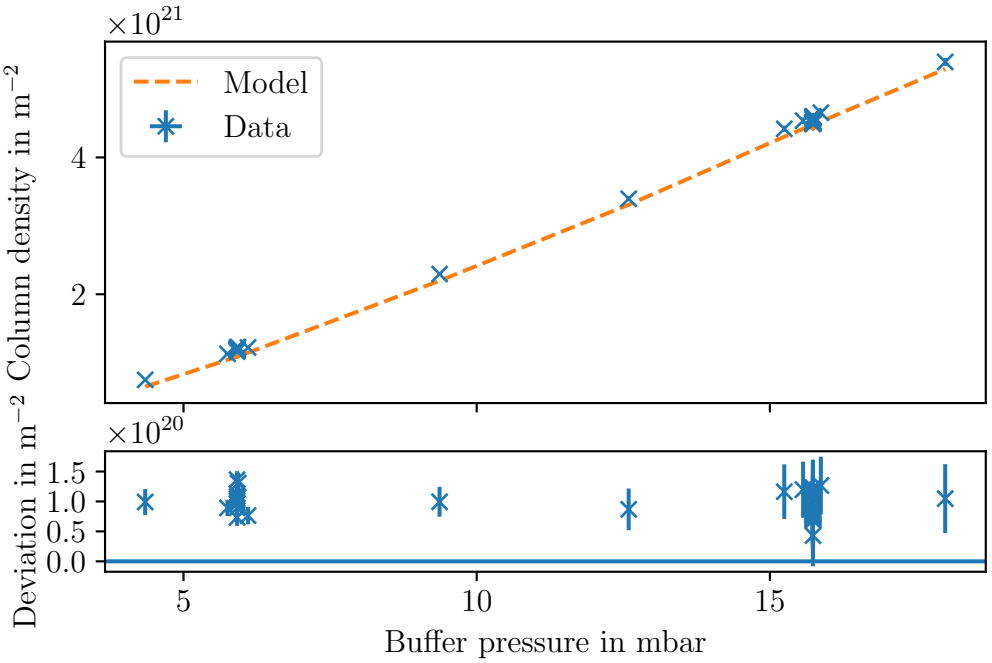

Figure 7.3.: **Comparison of column densities measured with the E-Gun and calculated from gas dynamics.** Shown are column density values in dependence of the stabilized buffer pressure measured with the E-Gun and calculated from gas dynamic simulations using pressures and temperatures as input. The lower plot shows the deviation between simulation and measurement, showing a constat offset of $\approx 1 \times 10^{20}\,\mathrm{m}^{-2}$.

this, the smooth dependence of the column density on the gas dynamical parameters is exploited. As can be seen in the simulated data in fig. 7.4, for parameter regions on the scale of expected fluctuations, the column density can be approximated well by a linear function of a parameter, regardless of the global dependence on this parameter. Using E-Gun measurements at several points in such a region allows for a calibration of the continuously monitored parameters.

This way, the excellent trueness of the E-Gun measurement during dedicated measurements can be combined with the continuously and precisely monitored pressure and throughput to obtain an accurate value for the column density during neutrino mass measurements. One such calibration is shown in fig. 7.5. The dense cloud of measurement points was taken during regular calibration measurements interleaved between neutrino mass measurements, while the data points spaced further apart were taken in dedicated measurements to gain a better sensitivity on the slope of the linear fit. Combining the accuracy of the E-Gun measurement with the reproducibility of the pressure measurements leads to uncertainties on $\rho d\sigma$ of less than 0.3 % for the KNM2 measurement campaign [Blo+20; Blo21].

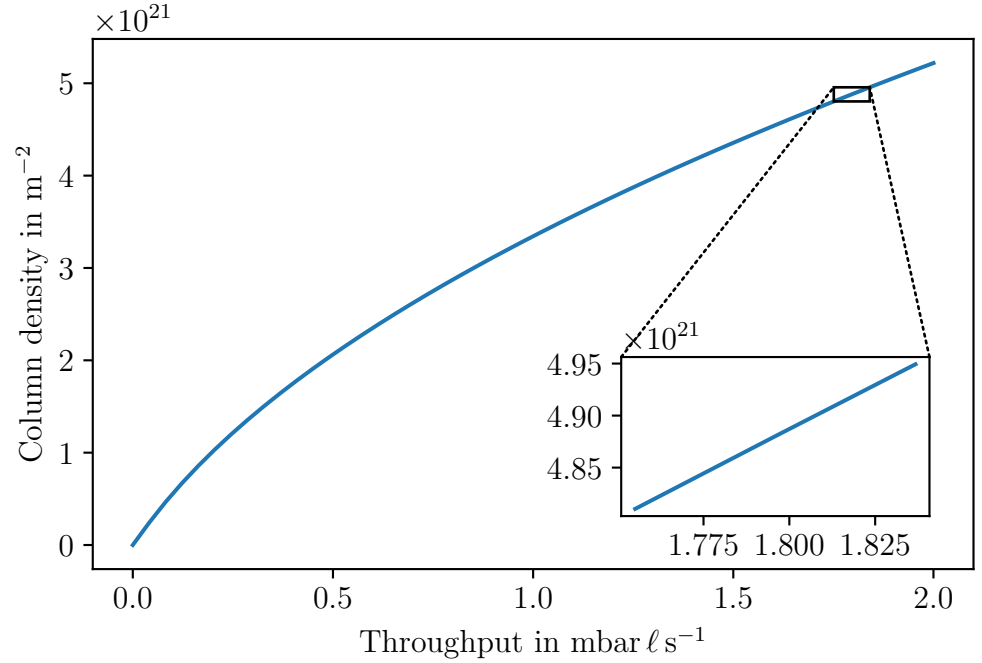

Figure 7.4.: **Linear dependence of the column density on the throughput.** Shown is the simulated column density over a wide range of throughput values for tritium circulating through the WGTS. The inset shows that for small throughput ranges the dependence of the column density on the throughput can be approximated by a linear function.

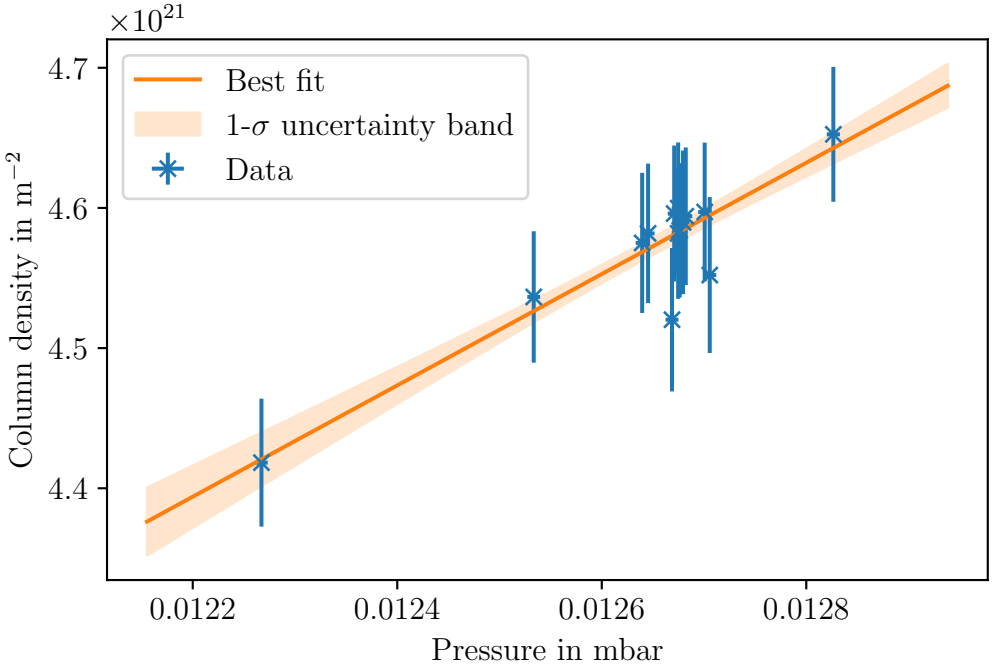

Figure 7.5.: **Calibration of the injection chamber pressure with E-Gun column density measurements.** Shown is the column density measured with the E-Gun over the pressure measured with the sensor connected to the tritium+krypton capillary. The large error bars on the column density result from the uncertainty on the inelastic scattering cross-section needed to calculate ρd from the $\rho d\sigma$ measured using the E-Gun.

7.2. Effects Impacting the Column Density Stability

In order to stabilize the column density of the WGTS to a a given level, all related input parameters need to be stable on at least the same level. These parameters are:

- injection pressure into the WGTS,
- temperature of the WGTS source tube,
- gas composition, and
- conductance of the injection capillary.

The injection pressure and gas composition have been covered in detail in chapters 5 and 6. Effects negatively impacting the remaining factors are investigated in this chapter. This is done using the monitoring methods described in the above section 7.1.3. The first section 7.2.1 investigates the impact of temperature fluctuations of the WGTS source tube and the injection capillary. Section 7.2.2 discusses the impact of changes in the gas composition on conductances in the IL and the resulting impact on the column density. Finally, the impact of a geometry change of the injection capillary due to deposition of impurities is presented in section 7.2.3.

7.2.1. Temperature Fluctuations

The WGTS cryostat contains a gHe (gaseous helium) and a LN_2 (liquid nitrogen) cooling circuit. The gHe circuit provides cooling power to the 2-phase cooling system of the WGTS source tube. Therefore fluctuations of the gHe circuit can strongly affect the source tube cooling and thus the gas density profile of the WGTS, which is discussed in section 7.2.1.1. The LN_2 cooling circuit is only coupled to the primary system via a punctual connection to the injection capillaries. However, as shown in section 7.2.1.2, this connection is sufficient that instabilities of the LN_2 cooling will impact the column density.

7.2.1.1. Temperature Fluctuations of the 30 K Cooling Circuit

Under normal operating conditions, the temperature stability of the WGTS source tube is better than 0.1 % due to the 2-phase cooling system, resulting in a negligible effect on the column density. Problems of the gHe supply can cause much larger fluctuations, as is shown in fig. 7.6. A raise in temperature, as in this case, causes a decrease of the column density, while a decrease of the temperature would correspondingly lead to a rise. It is also of interest that a temperature increase by 1.75 % will cause a column density decrease by 2.75 %. Temperature fluctuations of the gHe circuit can therefore propagate stronger than linear to fluctuations of the column density.

Considering the non-proportional impact on the column density, a temperature stability within the 0.1 % specification would have led to unacceptably high column density fluctuations. As such, the better than required performance of the source tube cooling system plays an important role in achieving the stability requirement of the column density.

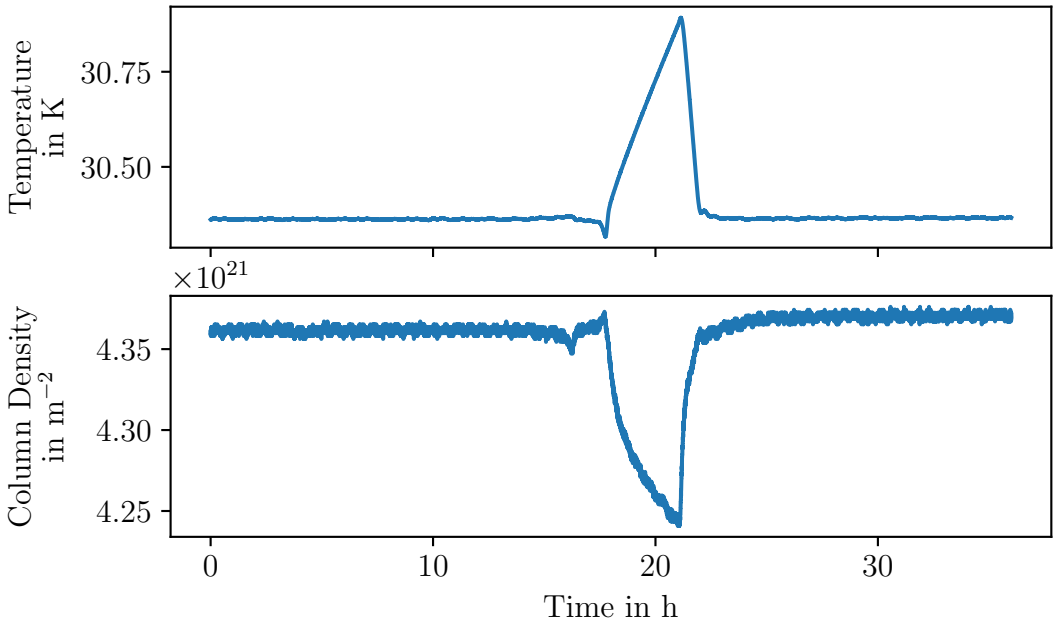

Figure 7.6.: **Influence of fluctuations of the gHe cooling circuit on the source tube cooling and the column density.** Shown is the temperature of the gHe cooling circuit and the monitored column density during a fluctuation in the gHe cooling circuit. An increase in source tube temperature directly leads to a decrease in the column density.

7.2.1.2. Temperature Fluctuations of the LN_2 Shield

The LN_2 shield of the WGTS cryostat minimizes the heat load on the inner components such as the superconducting magnets and the source tube. Temperature fluctuations in the LN_2 cooling circuit of this shield are coupled to the IL via a localized connection to the injection capillaries (see fig. 3.5). A falling temperature of the LN_2 cooling circuit decreases the temperature of the injection capillary and in turn increases its conductance. With increased conductance, the flow through the capillary increases for a given pressure inside the stabilized buffer, resulting in an increase of the column density. This effect is shown in fig. 7.7.

Variations in the WGTS cryostat LN_2 shield temperature of more than 2 K can occur. The origin of these fluctuations is to a large part caused by the refilling process of the on-site tank which provides the LN_2 reservior for the cooling circuit. During a refilling process, the pressure in the LN_2 tank can drop by several bar, causing a drop in temperature of several kelvin, which then propagates to the WGTS cryostat. While a clear correlation in time is visible, the exact impact of these fluctuations on the capillary can not be quantified, as no temperature sensor is connected to the contact point between LN_2 shield and the capillary. THis will cause delays and dampening between measured temperatures and the temperature at the point of contact.

During the KNM2 campaign, the fluctuations of the column density were dominated by this effect. Countermeasures against fluctuations of the LN_2 shield are under investigation and range from operational optimizations of the refilling process to modifications of the cooling system by adding additional buffer vessels.

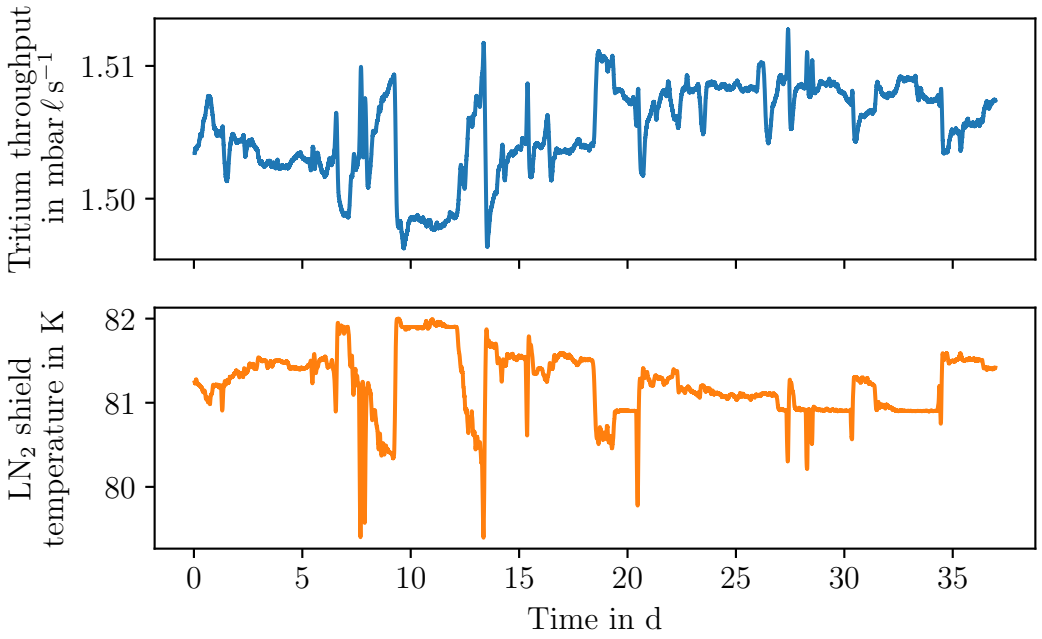

Figure 7.7.: **Influence of the LN_2 shield cooling on the IL throughput.** Shown are the tritium throughput and the temperature of the LN_2 shield over a time period of KNM2. For a constant injection pressure, the temperature of the LN_2 shield has a pronounced impact on the throughput of the gas circulating in the IL, and therefore on the column density.

7.2.2. Composition Changes

The gas composition has an impact on the viscosity of the gas circulating through the IL. Therefore, different gas species (H_2, D_2, T_2) will yield a different circulating throughput and column density for the same injection pressure. The goal of this section is to estimate the magnitude of the column density change due to the sub-% scale changes of gas composition in the IL.

The viscosity μ_m of a mixture can be derived from the viscosities of its n constituents with fractions x_i and molar masses M in approximation by [Wil50]:

$$\mu_m = \sum_{i=1}^{n} \frac{\mu_i}{1 + \frac{1}{x_i} \sum_{j=1, j\neq j}^{n} x_j \phi_{ij}} \tag{7.5}$$

with:

$$\phi_{ij} = \frac{\left(1 + \sqrt{\frac{\mu_i}{\mu_j}} \left(\frac{M_j}{M_i}\right)^{\frac{1}{4}}\right)^2}{\frac{4}{\sqrt{2}} \sqrt{1 + \frac{M_i}{M_j}}} \,. \tag{7.6}$$

Due to the lack of publicly available data on the viscosity of tritiated hydrogen molecules[3], the viscosity of HT was taken to be identical to deuterium due to their similar masses while the viscosity for T_2 was approximated as published in [Kuc+18]. Using the above formula and assuming the above stated viscosities, the effect of an increase of the HT fraction has been simulated. The result of this simulation is shown

[3] A statement on efforts to measure this quantity is given in appendix F

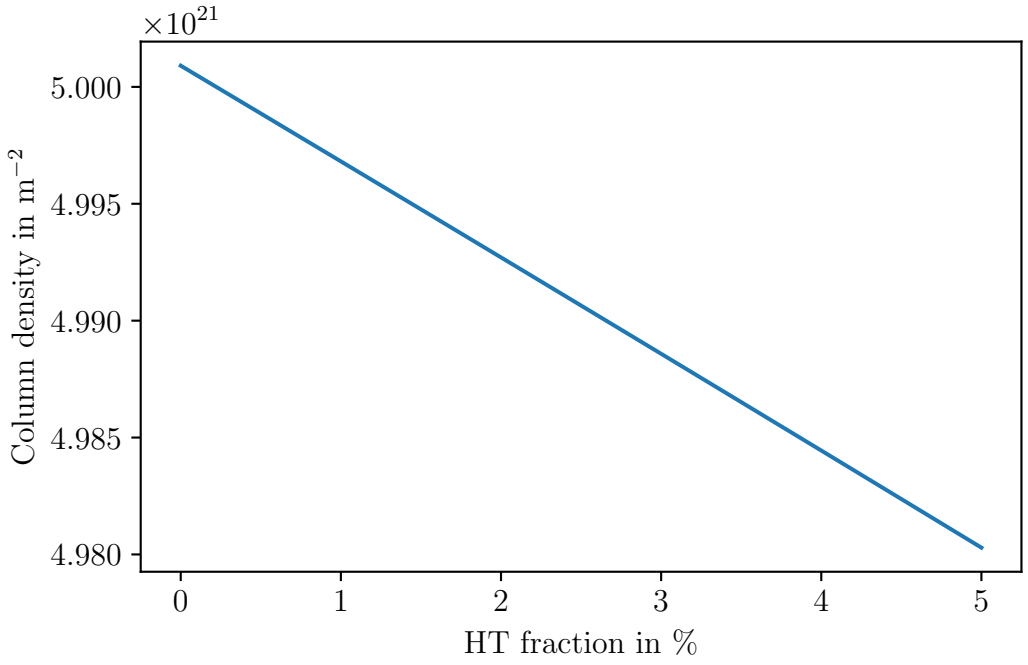

Figure 7.8.: **Change in column density due to increasing HT fraction.** Shown is the simulated column density in dependence of the HT fraction. Increasing the fraction of HT reduces the column density.

in fig. 7.8. From this data, a column density change of 0.04 % per 1 % increase of HT fraction can be extracted.

Consequentially, this effect is below the 0.1 % requirement for the normal KATRIN operation, as the fluctuation of the gas composition due to isotopic exchange effects and different gas batches is much smaller than 2.5 %. To illustrate this, fig. 7.9 shows calculated changes of the column density based on the gas composition measurements of LARA during the KNM2 measurement phase. The calculated column density changes are compared to measured column density data, corrected for the LN_2 shield fluctuations. Therefore, under the assumptions for the viscosities of HT and T_2, the effect of changing gas composition on the column density can be neglected.

7.2.3. Change of Injection Line Geometry

From a point outside of the WGTS cryostat to the injection chamber, the injection capillary is cooled down from room temperature to 30 K (or 80 K/100 K). At these low temperatures, the injection capillary serves as a cryotrap for most gas species. If a large amount of gas freezes out, the deposition of gas inside the injection capillary can lead to the formation of macroscopic frost layers. These layers will reduce the diameter of the capillary, and thereby also its conductance. This then causes a decrease in column density even at a constant injection pressure in the stabilized buffer vessel B1. This behavior was first observed during KNM1, the first measurement campaign using high purity tritium.

In fig. 7.10, data from the first two weeks of circulation is shown. The pressure in the stabilized buffer vessel was increased step-wise. After an increase of the resulting throughput to $>0.5\,\mathrm{mbar}\,\ell\,\mathrm{s}^{-1}$, the throughput started to decrease over

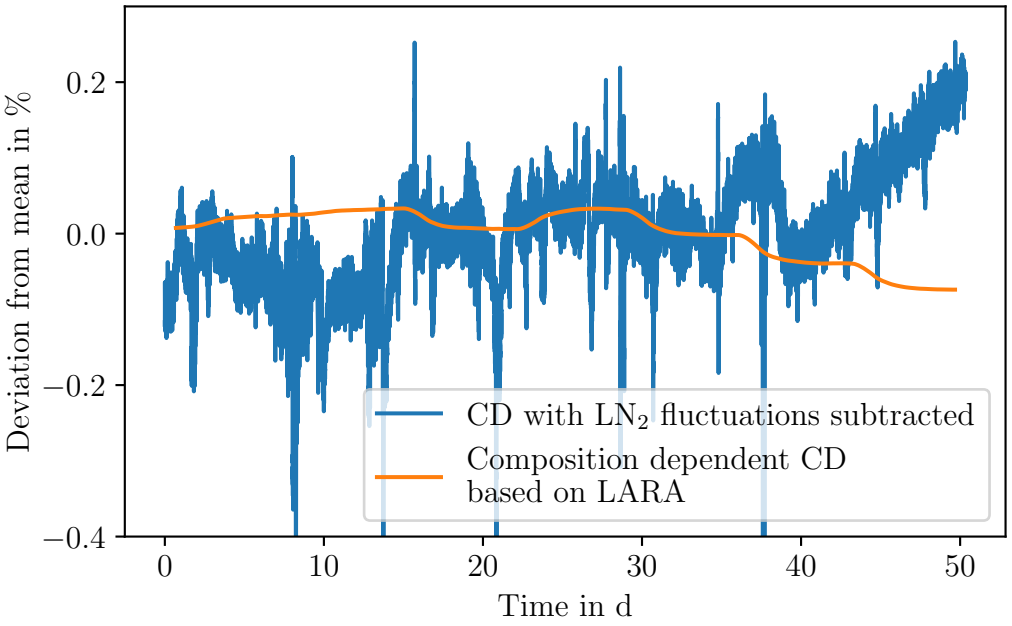

Figure 7.9.: **Comparison of expected effect of gas composition induced column density change to KNM2 column density data.** Shown is modified column density data and an expectation of changes in the column density due to gas composition changes. For the column density data, the major effect of fluctuations of the LN_2 was subtracted to be sensitive to smaller fluctuations.

time, with higher flow rates being accompanied by a faster decrease. The stability of all other parameters such as pressure, temperature, and gas composition, coupled with the continuous decrease of the throughput immediately pointed to a time-dependent reduction of the effective capillary diameter. In the transfer line and injection capillary, such a reduction can only happen due to macroscopic deposition from the gas phase. This also explains the throughput dependence of the throughput decrease, as higher throughputs deliver more depositable material per unit of time to the point of deposition and increase its partial pressure, leading to a larger fraction of the material being deposited. The gas circulating through the IL however is purified continuously to only contain hydrogen isotopes, which would not freeze out and form macroscopic frost layers at 30 K. Furthermore, this effect was not observed during the FT or STS3a measurement phases. Therefore, the gas species causing the diameter reduction need to be produced locally in the IL.

Candidates for this comprise CQ_4 (methane, $Q \in \{H, D, T\}$, mostly tritiated e.g. CT_4) [Mor77], CO, and possibly CO_2, which are known to be potential products of radiochemical reactions of tritium in stainless steel vacuum systems. To confirm this hypothesis, the source tube temperature was elevated to ≈ 85 K. At this new temperature the pressure in the source tube as well as RGA spectra of the gas composition were measured. For these measurements, the pumping power of the DPS1 was reduced in order to achieve a higher pressure and thereby better RGA sensitivity. In the pressure curves shown in fig. 7.11, several clearly distinguishable peaks are visible which correspond to gas species with different vapor pressures. The RGA spectrum for the entire depicted period is shown in fig. 7.12.

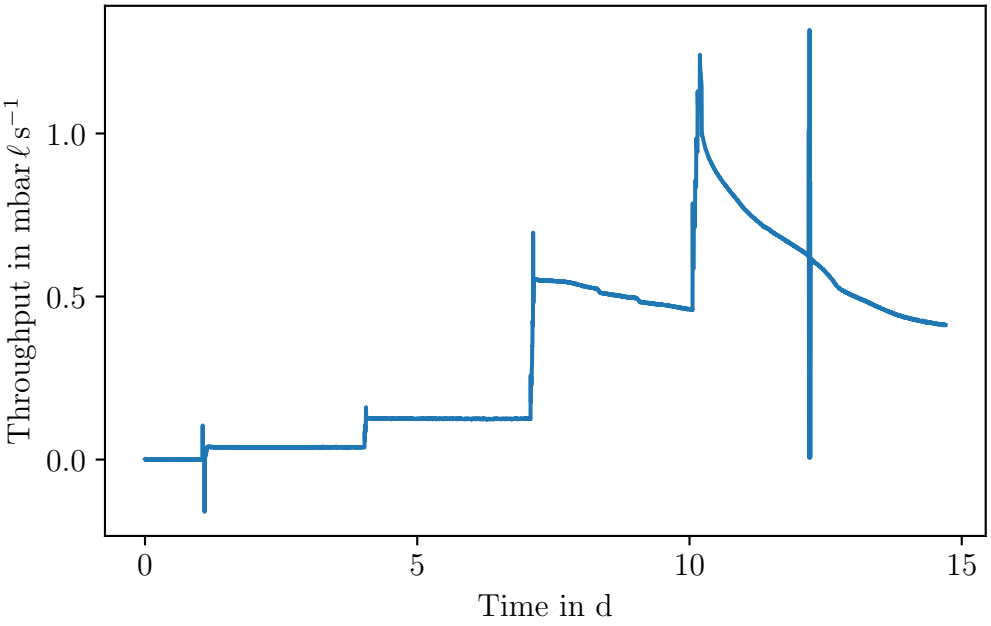

Figure 7.10.: **Throughput decrease induced due to the blocking of the injection capillary caused by deposition of impurities.** Shown is the throughput of gas circulating through the IL at the beginning of KNM1, when high purity tritium was circulated through the IL for the first time.

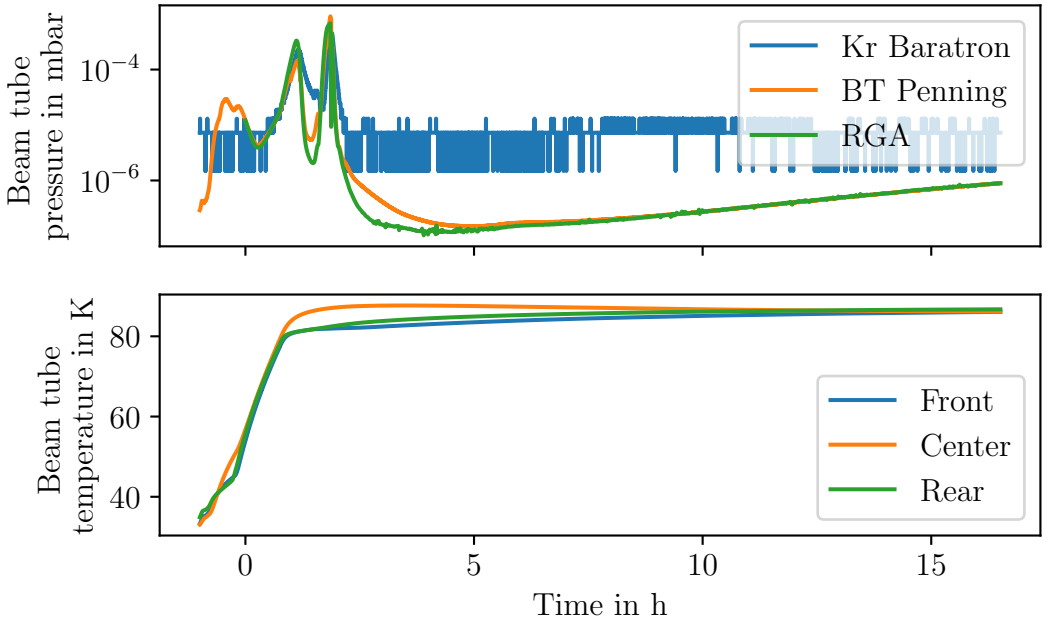

Figure 7.11.: **Pressure and temperature during WGTS cryostat warm-up after blocking caused by deposition of impurities.** For the temperature, sensors at the front, center, and rear of the source tube were used. For the pressure, the Penning sensor connected to the DPS1-R1, the capacitance manometer connected to the injection chamber, and the RGA at DPS1-R2 were used. The pressure spike seen in the Penning gauge and the RGA, but not with the capacitance manometer is desorption of gas from the source tube, not from the injection capillary.

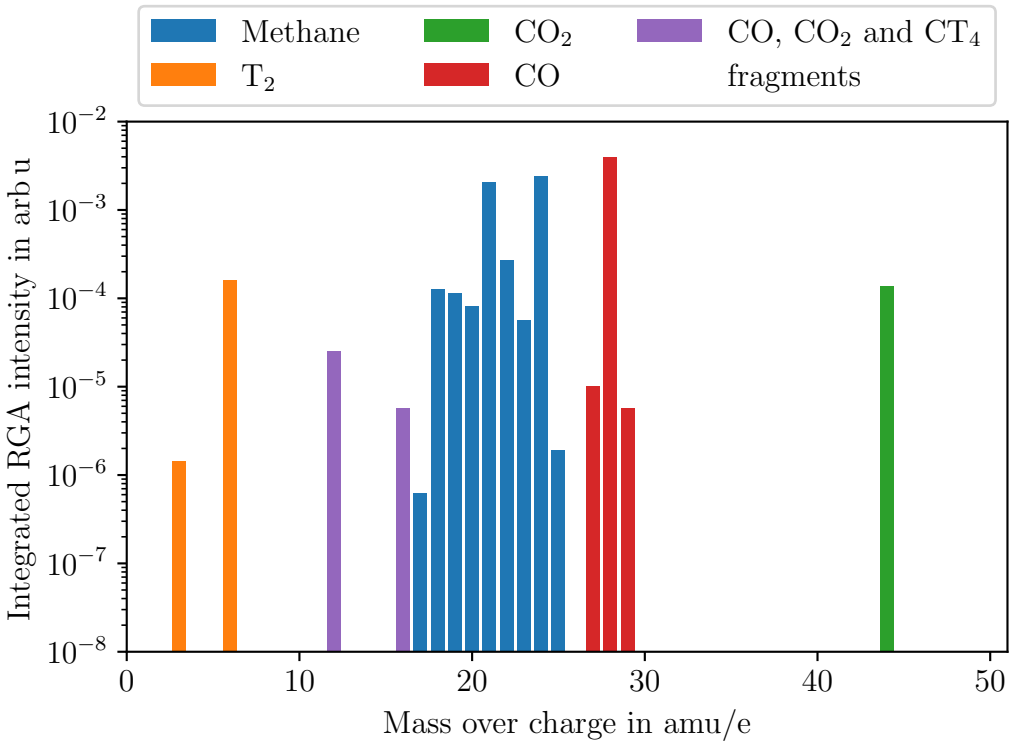

Figure 7.12.: **RGA spectrum of WGTS cryostat warm-up after blocking caused by deposition of impurities.** Shown is the integrated spectrum over the entire warm-up period in order to depict all gas species released at different times in one graphic.

The first pressure peak observed by all pressure sensors in fig. 7.11 corresponds to CO, while the second peak is associated with CQ_4. The long and slow increase of the pressure is produced by CO_2. Considering the peak-like structure of gas desorption for CQ_4 and CO, as well as their presence in the readings of the WGTS beam tube penning, RGA, and the Kr capillary pressure sensor are strong indications of the capillary as the origin of their emission. The CO_2 emission meanwhile is not visible in the Kr capillary pressure sensor. In a separate measurement [Stu20], an emission of CO_2 from the RS as well as desorption of CO_2 from the DPS1-R2 pump port during a different warm-up was observed. Therefore, the CO_2 emission will not be considered further in the following analysis.

An attempt to locate the region of emission can be made by looking at the temporal behavior of the gas desorption. Considering the peak-like structures of CQ_4 and CO desorption, it can be concluded that the temperature at the location of freeze-out slowly changed to values where their saturation vapor pressure[4,5] is far above that of the source tube. For a reference on saturation vapor pressures, refer to appendix I.

In addition, the time difference of the pressure peaks compared to the measured temperature increase allows to constrain the location of the deposition. As the temperature of the source tube was already mostly stable when the peaks for CQ_4 and CO appeared in the pressure, the blockade needs to be in a section of the injection capillary which is not coupled well thermally to the source tube. Additionally, even

[4] CO @ 85 K → >50 mbar
[5] CQ_4 approximated by CH_4 @ 85 K → >1 bar

when increasing the temperature of the source tube cooling, the capillary is still thermally connected to the LN_2 shield. This fixes the capillary temperature at that point to that of the LN_2 shield, which varies from 80 K to 85 K. As the temperature increase of the source beam tube did cause a desorption, the blockade needs colder temperatures than this. Consequentially, it is located behind the coupling to the LN_2 shield. The location of the blockade can therefore be narrowed down to the about 1.2 m long section between the connection to the LN_2 shield and the point from where the capillary is brazed onto the source tube cooling (see fig. 3.5).

With the cause for the throughput reduction identified, a countermeasure to limit deposition of carbonated gases was implemented in the period between KNM1 and KNM2. This countermeasure was based on the exhaustion of the production mechanism for carbonated gases, as their only source is radiochemical reactions with the steel walls of the primary system [Gil80; GME83].

Due to the low-energy nature of the tritium β-decay, ion induced sputtering of the walls can be neglected. Therefore, carbon atoms cannot be extracted from the bulk of the steel walls, meaning only carbon atoms close to the vessel surface are available for the radiochemical formation of impurities. Once this limited reservoir of carbon atoms is depleted via radiochemical conversion, no large-scale synthesis of carbonated gas can be initiated by tritium circulation.

As such, the solution chosen to remove this issue in the IL is the acceleration of this process by increasing the tritium partial pressure. For this purpose, high purity tritium was filled into the vessels B1, B2, and B3 (see fig. 3.3), the transfer line, as well as into the pipes connecting them at a stationary pressure of ≈700 mbar for a duration of 35 d. In case of the stabilized buffer vessel B1 and the transfer line, which account for >70 % of the surface area, this is an increase of more than one order of magnitude in pressure compared to the normal operation pressure scale of <20 mbar. An attempt at quantifying the effectiveness of this procedure is made in appendix E.

After performing the surface depletion of carbon atoms, a decrease of the throughput over time is no longer visible. This is shown in fig. 7.13, where data from KNM1 is compared to data from KNM2. From this data, it can be concluded that the generation of carbonated gases has been successfully reduced to a level which is no longer relevant for KATRIN.

7.3. Achieved Stability of the Column Density

Despite the effects which negatively impact the stability level of the column density, a high degree of stability could be maintained. This section presents the stability in neutrino mass measurement mode in section 7.3.1 and that of the tritium+krypton mode in section 7.3.2.

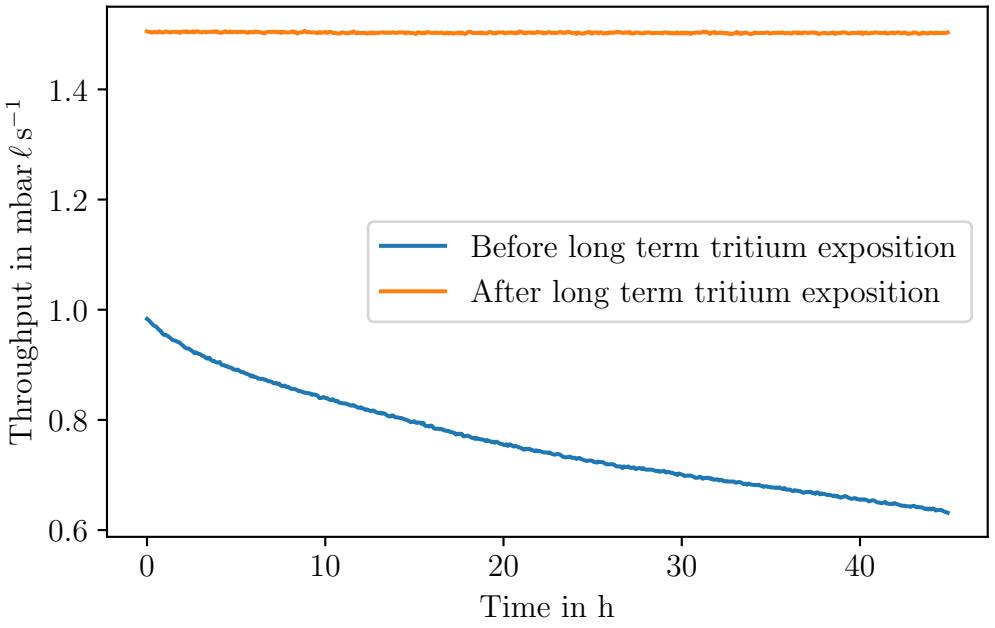

Figure 7.13.: **Throughput stability before and after exposure to elevated tritium pressure levels.** Shown are measured throughputs at the same stabilized buffer pressure taken before and after exposure of the IL vessels to an elevated tritium pressure.

7.3.1. Achieved Stability in Neutrino Mass Measurement Mode

The column density ρd as monitored by the E-Gun calibrated pressure in the injection chamber for the KNM2 campaign is shown in fig. 7.14. With a relative standard deviation of:

$$\frac{\sigma_{\rho d}}{\overline{\rho d}} = 0.14\,\%\,, \tag{7.7}$$

the column density stability for the entire measurement campaign is slightly larger than the requirement of 0.1 %. As the monitored column density values are accounted for in the neutrino mass analysis, fluctuations of the column density on the time scale of a run have the biggest potential to introduce a systematic effect. For the typically 2 h long runs, the column density is much more stable compared to the entirety of the KNM2 measurement phase. When the measurement phase is sliced into 2 h periods, the average value of relative standard deviations is:

$$\overline{\left(\frac{\sigma_{\rho d}}{\overline{\rho d}}\right)} = 0.02\,\%\,. \tag{7.8}$$

A histogram of the relative standard deviations is shown in fig. 7.15. A total fraction of 99.2 % of the 2 h intervals fulfill the 0.1 % requirement, with a vast majority of >80 % of intervals having a standard deviation <0.02 %.

7.3.2. Achieved Stability in Tritium+Krypton Mode

The stability of the column density in tritium+krypton mode is more challenging to monitor. Pressure and flow sensors used for this purpose in the neutrino mass

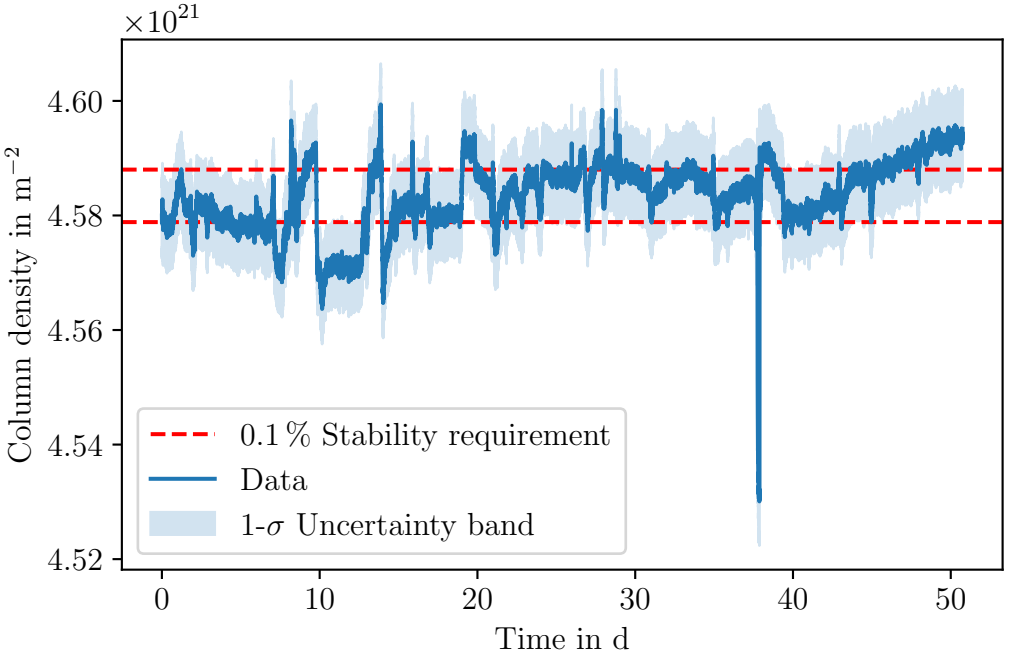

Figure 7.14.: **Column density in neutrino mass measurement mode during KNM2.** Shown is the column density calculated from the injection chamber pressure using the E-Gun calibration. On the timescale of the entire campaign, the 0.1 % requirement is not met, however on the timescale of a 2 h scan, it is met more than 99 % of the time.

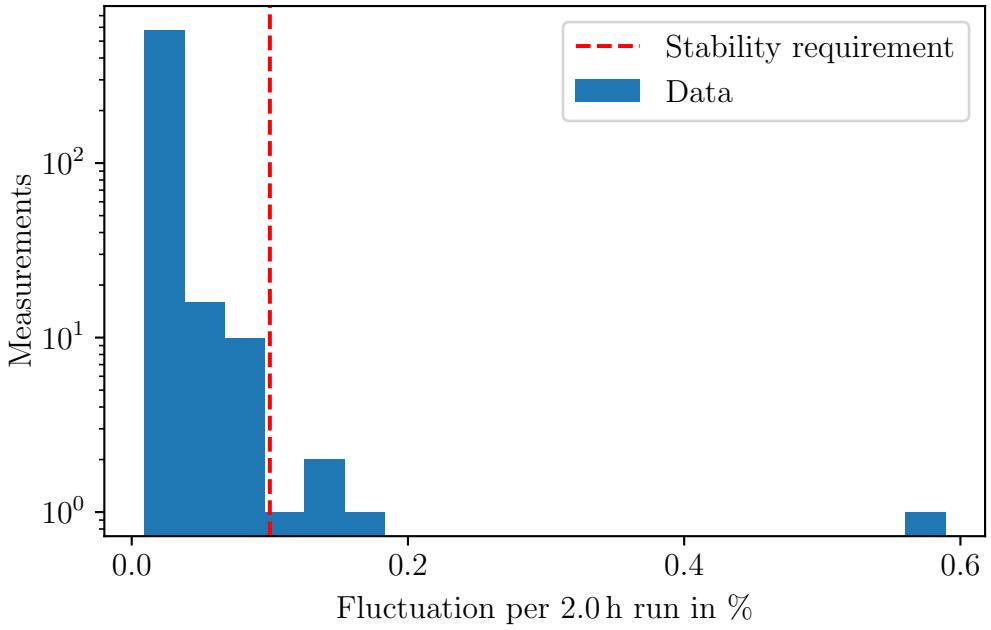

Figure 7.15.: **Histogram of column density fluctuations for 2 h slices of the KNM2 measurement period.** Only for 5 out of the 609 2 h periods, the fluctuations are higher than required. These periods coincide with refilling events of the LN_2 tank.

measurement mode are either not part of the circulation or the value of the measured quantity is outside of their measurement range. The remaining pressure measurement instrumentation is either affected by limited readout resolution or depends on the isotopic composition. The inability to measure changes in the isotopic composition in the tritium+krypton mode also complicates using the source activity, as measured e.g. by the BIXS detectors, for measurement of the column density.

Despite these difficulties, an attempt to quantify the column density fluctuations has been made. A pressure based column density simulation, as well as BIXS rate data combined with a modeled change in tritium purity using the model from section 6.3 were utilized. Due to resolution issues with the pressure based data, this approach is only used as a cross-check for the tritium purity correction to the BIXS values. The fluctuation of these values for the tritium+krypton mode phase of KNM2 is shown in fig. 7.16. For the entire period, the corrected BIXS values lead to a relative standard deviation of:

$$\frac{\sigma_{\rho d}}{\overline{\rho d}} = 0.44\,\% \,. \tag{7.9}$$

Analyzing the data in terms of 2 h slices, as in the case of the neutrino mass measurement mode, the stability is again much better on smaller time scales than for the entire measurement phase. The average standard deviation of the column density in 2 h periods for tritium+krypton mode is:

$$\overline{\left(\frac{\sigma_{\rho d}}{\overline{\rho d}}\right)} = 0.07\,\% \,, \tag{7.10}$$

with a fraction of 96.7 % of 2 h periods fulfilling even the strict 0.1 % requirement of the neutrino mass measurement mode.

7.4. Impact of the achieved Column Density Stability on the Neutrino Mass

The column density is one of the most essential parameters for the neutrino mass analysis with KATRIN. A high stability of the column density of better than 0.1 % is paramount in order for KATRIN to be able to reach the target sensitivity of 200 meV/c^2 (90 % confidence level).
To ensure that this requirement is met, several complementary monitoring systems based on rate, pressure, and flow measurements exist, which allow for continuous high precision measurements of the column density. The downside of these systems are several inherent systematic effects which limit the trueness of the derived column density value. This is mitigated by periodically calibrating the monitoring systems using the scattering of mono-energetic electrons from the E-Gun inside of the WGTS gas column. By using this combined approach, a highly accurate monitoring of the column density on the sub-% level becomes possible.

Several systematic effects were obsered, which negatively impact the column density:

- As a burn-in effect, the radiochemical generation of carbonated gas species (CQ_4, CO) and their subsequent deposition inside the tritium injection capillary resulted in a growing blockage of the capillary and thus led to a steady

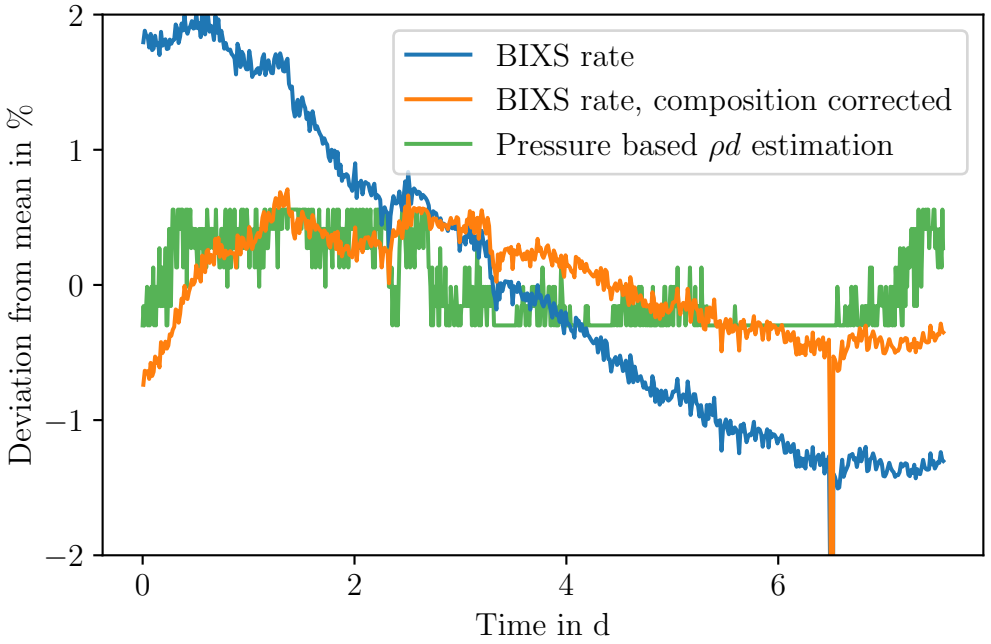

Figure 7.16.: **Deviation from mean of column density in tritium+krypton mode during KNM2.** Shown is the deviation of column density estimates from their mean. The best estimation of the column density can be gained by combining the measured BIXS rate with a modeled decrease in the tritium purity.

decrease of the column density. This effect has been successfully mitigated by exhausting the available carbon on the vessel surfaces of the inner loop, and it is no longer expected to be relevant for future KATRIN operation.

- Temperature fluctuations of the WGTS source tube cause a change in its conductance and thereby the column density. This effect can be neglected for normal KATRIN operation as the the temperature stabilization system reduces these fluctuations to a minimum.
- Temperature fluctuations of the LN_2 shield of the WGTS cryostat cause a change in conductance of the tritium injection capillary, which leads to a change in column density for a constant injection pressure. This effect is the sole reason why a stability of the column density on the <0.1 % level can not be maintained on the timescale of a measurement phase. At the time of writing, the temperature fluctuations in the LN_2 shield persist, however, possible mitigation strategies are currently being evaluated.

These temperature fluctuations of the LN_2 shield were the only effect to cause a significant deviation of the column density in KNM2, the most stable measurement phase so far. When considering the entire KNM2 measurement phase, these fluctuations result in a stability of 0.14 %, slightly exceeding the 0.1 % requirement. This is however only due to several isolated events corresponding to the refilling of the LN_2 tank. On the basis of 2 h runs, more than 99 % of such runs indeed meet the stability requirement of 0.1 %. A vast majority of >80 % of runs achieve a stability better than 0.02 %, significantly surpassing the design requirements.

In conclusion, the column density provided by the tritium loop system of KATRIN fully satisfies and even surpasses the requirement in stability of 0.1 %, with fluctua-

tions exceeding the requirement originating from cryogenic issues outside of the loop system's influence.

8. Summary

The Karlsruhe Tritium Neutrino Experiment (KATRIN) experiment aims to measure the effective mass m_ν of the electron antineutrino with an unprecedented sensitivity of $0.2\,\mathrm{eV/c^2}$ (90 % C.L.), improving upon existing upper limits by one order of magnitude. As the model-independent measurement principle of KATRIN relies on high-precision spectroscopy of the β-decay of molecular tritium, the experimental observable according to Fermi theory is in fact ${m_\nu}^2$. Therefore, an improvement by two orders of magnitude in the key experimental parameters is needed to gain the targeted one order of magnitude in sensitivity improvement on the neutrino mass. This means, that a large amount of statistics has to be accumulated while very strict requirements on systematic effects have to be met during this long-term data taking.

One of the most important experimental parameters which needs to be stabilized in order to minimize systematics, is the column density of the windowless gaseous tritium source (WGTS), which provides the β-electrons with the required source strength of $\approx 1 \times 10^{11}$ Bq. Maintaining the throughput of $\approx 1.8\,\mathrm{mbar}\,\ell\,\mathrm{s}^{-1}$, or $\approx 40\,\mathrm{g\,d}^{-1}$, of tritium necessary to achieve this luminosity, and at a stability level of 0.1 %, is the central responsibility of the tritium loop system (see chapter 3) which is part of the Tritium Laboratory Karlsruhe (TLK).

Over the course of this thesis, the tritium loop system was commissioned and characterized with a focus placed on three major topics, the

- optimization of the stabilized injection of tritium into the WGTS (see chapter 5), the
- characterization and modeling of the isotopic composition inside of the WGTS (see chapter 6), and the
- development of continuous monitoring methods for the column density and characterization of its stability (see chapter 7).

Optimization of the Stabilized Injection of Tritium into the WGTS

After completion of the commissioning of the tritium loop system, it was verified that the system to guarantee injection pressure stabilization fulfills the stability requirement of better than 0.1 % for the neutrino mass measurement mode, and even surpasses it by one order of magnitude. This excellent performance was further improved by an upgrade of the pressure sensor readout system, which minimized fluctuations to the level of 0.0017 %. The upgrade furthermore allowed to stabilize pressures at the 0.1 mbar level. This was also used to create a novel stabilization procedure for the tritium+krypton mode, which is used to investigate source systematic effects with monoenergetic conversion electrons from $^{83\mathrm{m}}$Kr. Using this procedure,

it is possible to meet the new stability requirements of the tritium+krypton mode as well. The performance of this system was unknown prior to the first operation of this mode during the STS3a measurement phase. Similarly, a procedure to prevent transport issues of ^{83m}Kr through the WGTS in the pure krypton mode was developed and successfully implemented.

Characterization and Modeling of the Isotopic Composition inside of the WGTS

When considering the gas composition of the circulating tritium gas, the existing monitoring systems of laser Raman (LARA) spectroscopy and residual gas analysis (RGA) were qualified for their use in KATRIN. The qualitative and quantitative agreement of both systems was verified, and a small time shift between measurements made by LARA and the RGA was found to be the result of the travel time of gas through the piping between the LARA system and the RGA connected to the source tube. Using LARA, two major effects on the gas composition were observed:

- Upon the start of the circulation of tritium gas, the tritium purity exponentially decreases with a time constant of 0.20 d to 0.37 d to a value which is about $\approx$0.5 % less than the starting value. This effect has been found to be caused by isotopic exchange of tritium with hydrogen from the stainless steel walls.
- The tritium gas provided to KATRIN by the TLK infrastructure batch-wise on a weekly basis is subject to slight changes on the sub-percent-level in gas composition due to the necessary purification steps done by the TLK infrastructure. As a result, the gas composition of the gas circulating through the WGTS can change on a weekly basis to a new equilibrium over the course of several days.

To deepen the understanding of these effects and make predictions for the tritium+krypton mode, where no gas composition monitoring is available, a numeric model using a minimal amount of input parameters has been developed. A comparison of this model to the measured LARA data in the neutrino mass measurement mode shows very good agreement to reality. Following that, predictions for the tritium+krypton mode were made, which were then verified using the measured source activity. As a result, the influences on the gas composition observed in the tritium loops system have been sufficiently well understood.

Development of Continuous Monitoring Methods for the Column Density and Characterization of its Stability

Building on the knowledge about the stability of the constituent parameters of injection pressure and gas composition, the column density and effects impacting its stability have been investigated. An accurate monitoring method for the column density during normal KATRIN operation has been devised in the form of a calibration routine based on measured pressures, flow rates, and source activities with scattering measurements of mono-energetic electrons with the gas inside the source. Using this method, it was possible to indirectly observe the deposition of radiochemically produced impurities inside the capillary feeding tritium gas into the WGTS.

The successful mitigation of the deposition process via exposition of the system to tritium at elevated pressures has also been verified using this method. It furthermore allowed to observe an effect where changes in the WGTS cryostat temperature modify the column density. A dependency of the column density on temperature of the LN_2 shield of the WGTS cryostat, which fluctuated on the kelvin-scale, was found to be the largest remaining source of instability for the column density.

Conclusion

Including all these effects, it was demonstrated that the column density fulfills the stability requirement of 0.1 % more than 99 % of the time over long time scales of more than 50 days, with the remainder falling out of the specifications due to issues with the temperatures of the LN_2 shield of the WGTS cryostat. Therefore, the tritium loop system meets all requirements posed to guarantee the expected neutrino mass sensitivity. Some goals were surpassed by more than an order of magnitude. Importantly, the system also fulfills the new requirements of the tritium+krypton mode.

From the perspective of the tritium loops system, the KATRIN experiment will be able to achieve all of its scientific goals.

Open Questions

Over the course of this thesis several new questions arose:

- With all monitoring methods being operational, the unknown viscosity of tritium is a limiting factor for theoretical calculations of gas dynamics models. Measuring this fundamental property would enable more accurate calculations for KATRIN. Furthermore, data of hydrogen isotopologue mixtures would provide data which can be compared to ab initio calculations, allowing the creating of a benchmark against which ab initio theory beyond mono-atomic gases can be tested.
- The interaction of tritium with surfaces, in particular the source tube and the rear wall, has shown to be of great importance for KATRIN. Changes in the work function of these surfaces are expected to cause drifts of the measured spectrum beyond the a level which allows KATRIN to meet its sensitivity goal. Causes for such changes can be the:
  - implantation of tritium ions, the
  - deposition of molecular tritium, the
  - deposition of tritium dimers (or even polymers), or the
  - deposition of impurities.

In addition to these, several topics outside of the scope of this thesis remain which are of high interest for the understanding of the WGTS:

- The presence of free charge carriers in the form of β-decay and secondary electrons as well as ions means that the WGTS is not a column of neutral gas, but rather a weak, self-ionizing plasma. Several properties of the WGTS make it highly non-trivial to derive the property of this cold plasma such as for example the strong magnetic field, the large gradient of neutral particle density, or the low degree of ionization. However, a good understanding of this plasma is necessary in order to rule out complex systematics originating associated with its influence on the β-electrons.
- The formation of clusters of neutral tritium gas molecules (dimers and larger) can harm the KATRIN sensitvity. Electrons produced in β-decay of a tritium atom in such a cluster are subject to slightly different final state distributions, which could distort the shape of the β-spectrum if they are present in sufficiently large numbers and not unaccounted for.

Obtaining answers to these questions would be of great value for KATRIN and future precision experiments using tritium.

Appendix

A. Novel Tritium+Krypton Mode for higher column density and tritium purity

Ongoing analysis of the tritium+krypton mode data have shown the need to replicate the conditions during neutrino mass measurement mode as closely possible. In particular, this concerns the issues of temperature, column density and the gas composition:

- Operation of the krypton modes requires temperatures above at least 40 K to prevent a possible freezing of krypton, and its resulting removal from the circulating gas. This restraint, combined with the required pressure range of the WGTS two-phase cooling, leads to possible operation temperatures of the WGTS at ≈80 K using nitrogen or ≈100 K using argon as two-phase coolant. For this reason, neutrino mass measurements need to be done at either ≈80 K or ≈100 K instead of the originally intended ≈30 K.

- Due to the limitation of a maximum pressure of 3 mbar behind the DPS1 TMPs, the column density in the tritium+krypton as described in section 3.2.2 is limited to $\approx 2 \times 10^{21}\,\mathrm{m}^{-2}$ (40 % of nominal) at 80 K and $\approx 1.8 \times 10^{21}\,\mathrm{m}^{-2}$ (36 % of nominal) at 100 K. However, the maximal column density in neutrino mass measurement mode at these temperatures is $\approx 3.75 \times 10^{21}\,\mathrm{m}^{-2}$ (75 % of nominal) at 80 K and $\approx 3.5 \times 10^{21}\,\mathrm{m}^{-2}$ (70 % of nominal) at 100 K.

- While the gas composition in the neutrino mass mode does change slightly over time, the inner loop permeator ensures that the gas inside the WGTS only consists of hydrogen isotopologues. In contrast, the composition of the gas circulating during tritium+krypton mode changes significantly, as was shown in section 6.3.3. Impurities consisting of hydrogen, oxygen and nitrogen from air, and hydrocarbons from the DPS1 TMPs accumulate in the gas stream during tritium+krypton mode operation. Their relative fraction can reach several percent, possibly inducing a significant change in the WGTS conditions due to different electron scattering and ionization cross-sections, as well as due to different gas dynamical properties.

In order to make the tritium+krypton mode comparable to the neutrino mass measurement mode a new idea was proposed, which lead to the developement a new operation scheme for the tritium+krypton mode. This new scheme discards the goal of maximum $^{83\mathrm{m}}$Kr activity inside the WGTS in favor of a higher column density and less impurities. The following appendix A.1 describes the new scheme. After that, estimations of the expected as well as the measured $^{83\mathrm{m}}$Kr activity in the WGTS using this new tritium+krypton mode are given in appendix A.2. A similar expectation for the amount of impurities is described in appendix A.3. This is followed by several experimental results obtained during the first test operation of the novel tritium+krypton mode. First, appendix A.4 makes a statement about the column density which can be achieved in this mode. Following this, the time until a stable $^{83\mathrm{m}}$Kr rate is achieved is discussed in appendix A.5. Finally, a summary of the novel tritium+krypton mode is given in appendix A.6.

A.1. Novel Tritium+Krypton Mode Operation Scheme

The operating scheme of the novel tritium+krypton mode is described in the following according to the schematic shown in fig. 3.3. The basis for the novel tritium+krypton mode is the neutrino mass measurement mode. By additionally opening the valve AV1, the gas stream pumped by the DPS1 TMPs is split into a fraction being pumped back to the IL inside the ISS glove box, and a fraction which is circulated back into the injection chamber via the tritium+krypton capillary. This leads to an injection of gas from both the tritium injection capillary and the tritium+krypton capillary at the same time. AV8 can then be opened to inject $^{83\mathrm{m}}$Kr into the circulating gas.

Operating the tritium+krypton mode with this alternative scheme leads to several significant differences:

- The volume behind the DPS1 TMPs is pumped by both the IL pumps in the ISS glove box, as well as DPS1 TMPs via the tritium+krypton capillary. As a result, the pressure behind the DPS1 TMPs for a given throughput in this mode is bounded towards higher pressures. This upper bound is given by the throughput-pressure-relation present in the neutrino mass measurement mode. In short, the maximal throughput over the WGTS (and thereby column density) in the novel tritium+krypton mode is at least as high as during the neutrino mass measurement mode.
- The fraction of gas pumped by the IL pumps in the ISS glove box is filtered by the IL permeator. This removes all non-hydrogen isotopologue components from this fractional gas stream, including $^{83\mathrm{m}}$Kr. As a consequence, the concentration of both impurities and $^{83\mathrm{m}}$Kr in the gas circulating through the WGTS is reduced.

A.2. $^{83\mathrm{m}}$Kr Activity in the Novel Tritium+Krypton Mode

In the normal tritium+krypton mode, the total activity in the circulating gas in equilibrium is given by the activity of the ^{83}Rb source $A_{^{83}\mathrm{Rb}}$ of the krypton generator. Due to the continuous extraction and purification of a fraction of the gas stream in the novel tritium+krypton mode this equilibrium is never reached. The total activity in the circulating gas in the novel tritium+krypton mode is given by:

$$A_{^{83\mathrm{m}}\mathrm{Kr}} = \lambda_{^{83\mathrm{m}}\mathrm{Kr}} n_{^{83\mathrm{m}}\mathrm{Kr}} \,. \tag{8.1}$$

The time evolution of the number of $^{83\mathrm{m}}$Kr atoms $n_{^{83\mathrm{m}}\mathrm{Kr}}$ is given by the following differential equations:

$$\frac{\mathrm{d}}{\mathrm{d}t} n_{^{83\mathrm{m}}\mathrm{Kr}} = \lambda_{^{83}\mathrm{Rb}} n_{^{83}\mathrm{Rb}} - \lambda_{^{83\mathrm{m}}\mathrm{Kr}} n_{^{83\mathrm{m}}\mathrm{Kr}} - \frac{q_{\mathrm{ex}}}{n_{\mathrm{tot}}} \,, \tag{8.2}$$

$$\frac{\mathrm{d}}{\mathrm{d}t} n_{^{83}\mathrm{Rb}} = -\lambda_{^{83}\mathrm{Rb}} n_{^{83}\mathrm{Rb}} \,, \tag{8.3}$$

with:

- $n_{^{83}\mathrm{Rb}}$, the amount ob ^{83}Rb inside the krypton generator,

- $\lambda_{^{83}\mathrm{Rb}}$, the decay constant of ^{83}Rb,
- $\lambda_{^{83\mathrm{m}}\mathrm{Kr}}$, the decay constant of $^{83\mathrm{m}}$Kr,
- q_{ex} the flow rate at which the fractional stream of gas is extracted and cleaned at the permeator,
- n_{tot} the total amount of gas in the volume behind the DPS1 from where $^{83\mathrm{m}}$Kr can enter the source.

This approach assumes an equal distribution of $^{83\mathrm{m}}$Kr inside the surrounding gas without any demixing effects.

On short timescales, the decay of ^{83}Rb can be neglected ($A_{^{83}\mathrm{Rb}} = \lambda_{^{83}\mathrm{Rb}} n_{^{83}\mathrm{Rb}} = \text{const.}$). Using this simplification, the solution to eq. (8.2) for an initial $^{83\mathrm{m}}$Kr amount of 0 is given by:

$$n_{^{83\mathrm{m}}\mathrm{Kr}} = A_{^{83}\mathrm{Rb}} \tau \cdot \left(1 - \mathrm{e}^{-\frac{t}{\tau}}\right) , \tag{8.4}$$

with:

$$\tau = \frac{1}{\frac{q_{\mathrm{ex}}}{n_{\mathrm{tot}}} + \lambda_{^{83\mathrm{m}}\mathrm{Kr}}} \tag{8.5}$$

the time constant of equilibration for the number of $^{83\mathrm{m}}$Kr atoms in the novel tritium+krypton mode. For the equilibrium activity of $^{83\mathrm{m}}$Kr in the contained gas, this leads to:

$$A_{^{83\mathrm{m}}\mathrm{Kr}} = \lambda_{^{83\mathrm{m}}\mathrm{Kr}} n_{^{83\mathrm{m}}\mathrm{Kr}} = \frac{\lambda_{^{83\mathrm{m}}\mathrm{Kr}} A_{^{83}\mathrm{Rb}}}{\frac{q_{\mathrm{ex}}}{n_{\mathrm{tot}}} + \lambda_{^{83\mathrm{m}}\mathrm{Kr}}} . \tag{8.6}$$

From this, we can derive the fraction f of activity present in the novel tritium+krypton mode compared to the normal tritium+krypton mode:

$$f = \frac{A_{^{83\mathrm{m}}\mathrm{Kr,alt}}}{A_{^{83\mathrm{m}}\mathrm{Kr,norm}}} = \frac{\lambda_{^{83\mathrm{m}}\mathrm{Kr}}}{\frac{q_{\mathrm{ex}}}{n_{\mathrm{tot}}} + \lambda_{^{83\mathrm{m}}\mathrm{Kr}}} . \tag{8.7}$$

Using the following values:

- $\lambda_{^{83\mathrm{m}}\mathrm{Kr}} = \frac{\ln 2}{\mathrm{T}_{1/2,^{83\mathrm{m}}\mathrm{Kr}}} = 1.03 \times 10^{-4}\,\mathrm{s}^{-1}$ from literature values [Sen+18],
- $n_{\mathrm{tot}} = (84 \pm 4)\,\mathrm{mbar}\,\ell$ as a reasonable empirical value for the gas amount behind the DPS1 TMPs,
- $q_{\mathrm{ex}} \approx (0.90 \pm 0.05)\,\mathrm{mbar}\,\ell\,\mathrm{s}^{-1}$ as an estimate of the extracted gas flow rate.

the fraction of $^{83\mathrm{m}}$Kr activity present in the volume behind the DPS1 TMP in the novel tritium+krypton mode compared to the normal tritium+krypton mode is:

$$f_{\mathrm{theo}} = (0.95 \pm 0.07)\,\% . \tag{8.8}$$

For the activity inside the WGTS, it furthermore needs to be considered that the WGTS beam tube is between the points of injection of fresh tritium and extraction of tritium and krypton. As a result, the fraction of $^{83\mathrm{m}}$Kr inside the beam tube is further reduced by the ratio of the flow rate $q_{\mathrm{inj,Kr}}$ through the tritium+krypton injection capillary to the total flow rate q_{tot} through the WGTS:

$$f_{\mathrm{theo,WGTS}} = f_{\mathrm{theo}} \cdot \frac{q_{\mathrm{inj,Kr}}}{q_{\mathrm{tot}}} . \tag{8.9}$$

For a column density of $3.75 \times 10^{21}\,\mathrm{m}^{-2}$ (75 % of the nominal value), the total flow rate is:

$$q_{\mathrm{tot}} = (1.62 \pm 0.02)\,\mathrm{mbar}\,\ell\,\mathrm{s}^{-1}\,. \tag{8.10}$$

This leads to a expected fractional $^{83\mathrm{m}}$Kr concentration inside the WGTS of:

$$f_{\mathrm{theo,WGTS}} = (0.42 \pm 0.06)\,\%\,. \tag{8.11}$$

Comparing the rates achieved in the first test operation of the novel tritium+krypton mode to those in the pure krypton mode run only a few days prior yielded the a fraction of:

$$f_{\mathrm{exp,WGTS}} = (0.46 \pm 0.03)\,\%\,. \tag{8.12}$$

This result agrees with the theoretical expectation within the respective uncertainties.

A.3. Impurities in the Novel Tritium+Krypton Mode

A similar approach as it was used in the previous section can be used to estimate the amount of impurities n_{imp} due to the DPS1 TMPs inside the circulating gas stream. The governing differential equation in this case is:

$$\frac{\mathrm{d}}{\mathrm{d}t} n_{\mathrm{imp}} = q_{\mathrm{imp}} - \frac{n_{\mathrm{imp}}}{n_{\mathrm{tot}}} \cdot q_{\mathrm{ex}}\,. \tag{8.13}$$

The solution to this equation for no initial impurities ($n_{\mathrm{ex}} = 0$) is:

$$n_{\mathrm{imp}} = n_{\mathrm{tot}} \frac{q_{\mathrm{imp}}}{q_{\mathrm{ex}}} \cdot \left(1 - \mathrm{e}^{-\frac{q_{\mathrm{ex}}}{n_{\mathrm{tot}}} t}\right)\,. \tag{8.14}$$

From this, we can derive the equilibrium concentration of impurities:

$$c_{\mathrm{imp}} = \frac{n_{\mathrm{imp}}}{n_{\mathrm{tot}}}\,. \tag{8.15}$$

Using the following values:

- $q_{\mathrm{imp}} \approx 1.5 \times 10^{-5}\,\mathrm{mbar}\,\ell\,\mathrm{s}^{-1}$ as a reasonable empirical value for the outgassing rate of the DPS1 TMPs,
- $q_{\mathrm{ex}} \approx 1\,\mathrm{mbar}\,\ell\,\mathrm{s}^{-1}$ as an estimate of the extracted gas flow rate.

the equilibrium concentration of impurities is:

$$c_{\mathrm{imp}} = 0.0015\,\%\,. \tag{8.16}$$

This value is much lower than the percent-level concentration of hydrogen and deuterium in the circulating gas. The impact these impurities have on the WGTS conditions in comparison to the operation in neutrino mass measurement mode should therefore be negligible. As the fractional stream of gas passing the permeator also passes the LARA cell, an estimation of the gas composition can be made. In this mode, LARA can only serve as a good estimate of the gas composition as demixing effects can introduce a slight difference between the gas composition of the gas circulating over the LARA cell and the gas circulating over the tritium+krypton injection capillary.

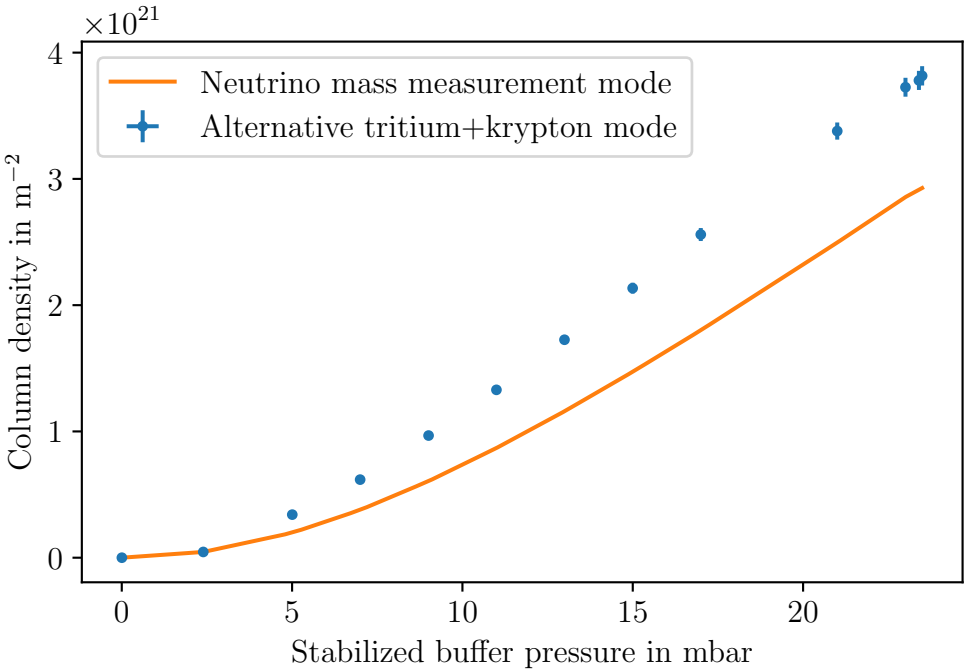

Figure A.1.: **Column density in the novel tritium+krypton mode.** Shown is the measured column density in the novel tritium+krypton mode together with the simulated column density in the neutrino mass measurement mode.

A.4. Column density

During commissioning of the novel tritium+krypton mode several settings of the pressure stabilized buffer vessel B1 (see fig. 3.3) were tested. Using a column density measurement with the E-Gun to calibrate the BIXS rate as described in section 7.1.3, the column density during the different buffer vessel settings could be determined. This is data shown in fig. A.1.

For a given pressure in the stabilized buffer vessel, the column density in the novel tritium+krypton mode is higher than during the neutrino mass measurement mode. The reason for this is found in the throughput dependence of the column density. In the neutrino mass measurement mode the entire throughput is delivered by the stabilized buffer vessel. In the novel tritium+krypton mode, the fraction of gas recirculated via the tritium+krypton injection capillary adds to the throughput from the stabilized buffer vessel, leading to a higher total throughput, and thereby a higher column density.

The novel tritium+krypton does not allow the achievement of significantly higher column densities than the neutrino mass measurement mode. In both modes, the entire throughput of tritium gas needs to be pumped by the DPS1 TMPs. Their maximum throughput limits the column density in long term operation of both modes to the same level of ≈75 %.

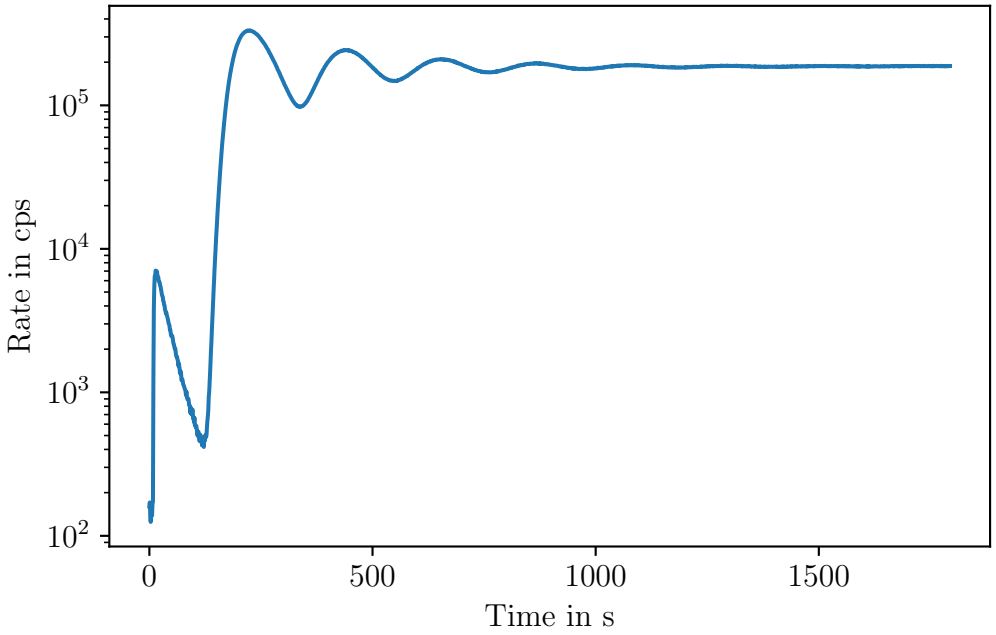

Figure A.2.: ^{83m}Kr **rate after injection in the normal tritium+krypton mode.** Shown is the ^{83m}Kr rate measured with the FPD at a MS retarding voltage of 30 464 V after injection of ^{83m}Kr into the WGTS.

A.5. Time until Stabilization of the ^{83m}Kr rate

Upon injection of ^{83m}Kr into the circulating gas, the ^{83m}Kr needs to be evenly distributed in the circulating gas for the ^{83m}Kr activity inside the WGTS to become stable. This process for the normal tritium+krypton mode is shown in fig. A.2.

After opening of the valve to the krypton generator, an initial, small rise in rate followed by an exponential decline is visible. This feature is caused by the accumulated ^{83m}Kr inside the krypton generator streaming directly into the WGTS beam tube. The exponential decline reflects the pump-out curve of the accumulated ^{83m}Kr through the transfer line connecting the krypton generator to the DPS1-F2 pump port. This feature is followed by a sharp increase in ^{83m}Kr rate which occurs once the ^{83m}Kr pumped by the DPS1 TMPs is first re-injected into the WGTS via the tritium+krypton injection capillary. The initial bunch of ^{83m}Kr is then washed out due to diffusion of ^{83m}Kr in the circulating tritium gas. As a result, the ^{83m}Kr rate which can be measured in the WGTS behaves similar to a dampened oscillator.

As shown in fig. A.3, this behavior is heavily altered in the novel tritium+krypton by the extraction of a significant fraction of the circulating ^{83m}Kr. The initial bunch of ^{83m}Kr is pumped of with a time constant on the order of a single circulation of the bunch. As a result, all accumulated ^{83m}Kr is lost, significantly decreasing the ^{83m}Kr rate compared to the normal tritium+krypton mode. From the data shown in fig. A.3, a time until the ^{83m}Kr rate has stabilized to the level expected from statistical fluctuations on the $3\,\sigma$-level. This particular stabilization time is given by:

$$t_{\mathrm{eq}} = 528\,\mathrm{s}\,. \tag{8.17}$$

This time depends on the amount of circulating tritium gas as well as the flow rate. In general, it is longer for lower flow rates.

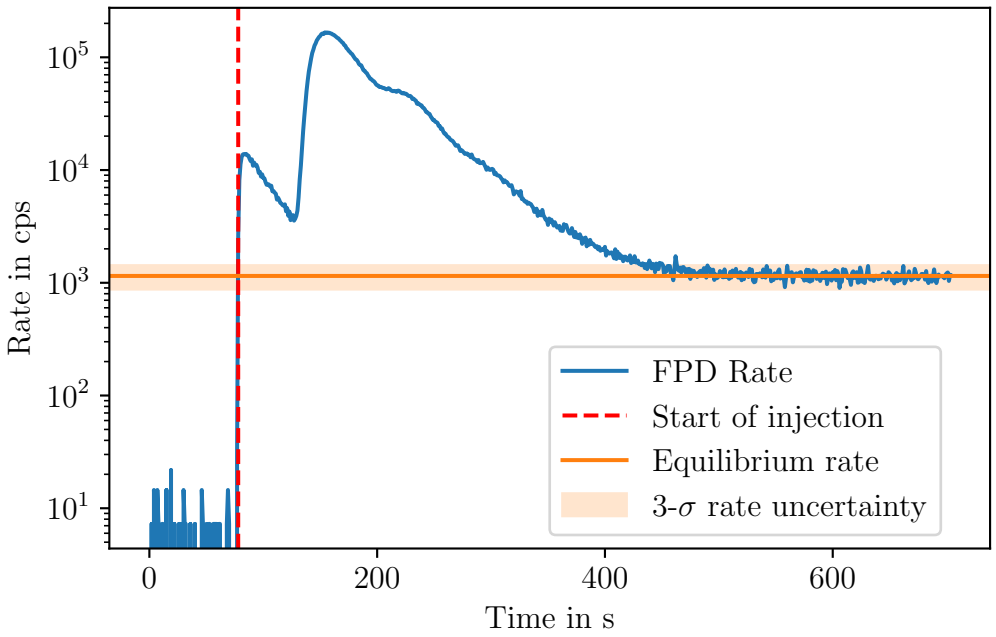

Figure A.3.: **Stabilization of the ^{83m}Kr rate after injection in the novel tritium+krypton mode.** Shown is the the ^{83m}Kr rate at a MS retarding voltage of 30 464 V after injection, the equilibrium ^{83m}Kr rate, as well as the 3 σ statistical uncertainty on the equilibrium ^{83m}Kr rate. After the difference falls below the level which is expected purely by statistical fluctuations, the ^{83m}Kr can be considered to be stable.

A.6. Summary of the Novel Tritium+Krypton Mode

The novel tritium+krypton mode is a novel operation scheme of the WGTS using both tritium and ^{83m}Kr. It changes the focus of the operation from achieving the highest possible ^{83m}Kr rate inside the WGTS to ensuring the best possible comparability to the neutrino mass measurement mode. The main disadvantage of this mode is the strong reduction in ^{83m}Kr rate inside the WGTS down to <1 % of that in the normal tritium+krypton mode. However, this disadvantage can be countered by a stronger ^{83}Rb source or longer measurement times. In contrast, this mode offers the following advantages:

- the possibility to reach column densities of at least $\approx 3.75 \times 10^{21}\,\mathrm{m}^{-2}$ (75 % of nominal) at 80 K,
- a reduction of the amount of impurities induced by the DPS1 TMPs to a negligible amount,
- the possibility to use LARA to measure the composition, and
- fast switching between tritium+krypton and neutrino mass measurement mode.

In conclusion, the novel tritium+krypton mode offers a complementary set of properties to the normal tritium+krypton mode and its high ^{83m}Kr rate. As both modes only differ in their operation scheme and not in any hardware changes, a suitable mode can be chosen to accommodate the needs of the individual measurements.

B. Details on Gas Dynamics Simulations

This section is dedicated to the extension of the gas dynamic models of KATRIN presented in [Kuc+18; Hei19] by performing a simulation of the tritium injection line. First, the necessary terminology will be introduced in appendix B.1. Then the geometry of the injection line will be given in appendix B.2. Following that, the steady state solution of flow through the injection line will be presented and compared to measurement data in appendix B.3.

B.1. General Concepts of Rarefied Gas Dynamics

In the inner loop system of KATRIN, tritium gas is circulated at pressures below 1000 mbar, down to $\approx 10^{-6}$ mbar. While the pressure changes by several orders of magnitude, depending on the actual location inside the inner loop, the geometrical dimensions of the pipes containing the gas is changing by less than a factor of two. As a result, different regimes of gas flow are present in the inner loop. These flow regimes are characterized by the ratio δ of the effective free path length of the gas:

$$\ell = \frac{\mu v_\mathrm{m}}{p}\,, \tag{8.18}$$

to the characteristic length scale a of the gas flow :

$$\delta = \frac{a}{\ell} = \frac{ap}{\mu v_\mathrm{m}}\,, \tag{8.19}$$

with the pressure p and the the most probable velocity:

$$v_\mathrm{m} = \frac{2k_\mathrm{B}T}{m}\,. \tag{8.20}$$

This ratio δ is called rarefaction parameter, and allows to categorize different flow regimes:

- $\delta \ll 1$ the gas particles interact mainly with the walls of the system surrounding the gas flow, making the interaction between particles negligible. This flow regime is usually called free-molecular flow regime.
- $\delta \gg 1$ the equations of fluid mechanics for continuous media are applicable. It is therefore usually called hydrodynamic regime.
- $\delta \approx 1$ the hydrodynamic equations are no longer applicable, but neither can the interactions between particles be neglected. This regime is appropriately called transitional flow regime.

Due to the large changes in pressure at comparable characteristic length scales inside of the inner loop, a large parameter space of δ is covered, requiring the use of equations which properly describe the gas flow in the transitional flow regime.

The basis here is the Boltzmann equation:

$$\frac{\partial f}{\partial t} + \boldsymbol{v} \cdot \nabla_r f = Q(f, \boldsymbol{v})\,. \tag{8.21}$$

This equation connects the velocity distribution function

$$f = f(t, \boldsymbol{r}, \boldsymbol{v}) = \frac{\mathrm{d}^3 N}{\mathrm{d}^3 \boldsymbol{r} \mathrm{d}^3 \boldsymbol{v}}\,, \tag{8.22}$$

which describes the distribution of the gas particles in the 6-dimensional space of position $\boldsymbol{r}$ and velocity $\boldsymbol{v}$, with the collision integral $Q(f, \boldsymbol{v})$ describing the collisions between gas particles.

While eq. (8.21) forms the basis of gas flow calculations in the transitional regime, simplifications are necessary in order to solve this equation. One such simplification is the case of a long, thin tube with circular diameter. For this case, a formula for the mass flow rate $\dot{M}$ through the tube has been derived [Sha16]:

$$\dot{M} = \frac{\pi R^3}{v_\mathrm{m}} \left(-G_\mathrm{P}(\delta) \frac{\mathrm{d}p}{\mathrm{d}z} + G_\mathrm{T}(\delta) \frac{p(z)}{T(z)} \frac{\mathrm{d}T}{\mathrm{d}z} \right)\,, \tag{8.23}$$

with

- R, the radius of the tube,
- v_m, the most probable velocity as defined above,
- z, the length coordinate along the tube axis,
- $p(z)$, the pressure at a given z position,
- $T(z)$, the temperature at a given z position,
- G_P, the Poiseuille coefficient, and
- G_T, the thermal creep coefficient.

The coefficients G_P and G_T are dimensionless flow rates, which characterize the gas flow in dependence on δ. The values of these coefficients have been calculated over a wide range of δ values and can be interpolated by the following equations:

$$G_\mathrm{P} = \frac{8}{3\sqrt{(\pi)}} \frac{1 + 0.04\delta^{0.7} \ln(\delta)}{1 + 0.78\delta^{0.8}} + \left(\frac{\delta}{4} + 1.018 \right) \frac{\delta}{\delta + 1}\,, \tag{8.24}$$

and

$$G_\mathrm{T} = \begin{cases} \frac{4}{3\sqrt{(\pi)}} + 0.825(1 + \ln(\delta))\delta - (1.18 - 0.61\ln(\delta))\delta^2 & \text{for} \quad \delta \leq 1, \\ \frac{1.175}{\delta} - \frac{1.75}{\delta^2} + \frac{1.47}{\delta^3} - \frac{0.5}{\delta^4} & \text{for} \quad \delta \geq 1, \end{cases} \tag{8.25}$$

with sub-% errors.

Using eq. (8.23), the mass flow can be calculated numerically and then be converted into a throughput q via:

$$q = \frac{pV}{t} = \frac{k_\mathrm{B} T}{m} \frac{N \cdot m}{t} = \frac{k_\mathrm{B} T}{m} \cdot \dot{M} = \frac{{v_\mathrm{m}}^2}{2} \cdot \dot{M}\,. \tag{8.26}$$

This procedure has been used successfully to calculate the throughput q and column density:

$$\rho d = \int n(z) \mathrm{d}z\,, \tag{8.27}$$

of the WGTS [Sha10], resulting in a relation of q to ρd. Expanding on this, a calculation of the throughput q based on the pressure p in the stabilized buffer vessel is of experimental interest, as p is the quantity which can be set with a high degree of accuracy. For this purpose, the same procedure applied to the WGTS has been applied to the tritium injection line. However, a difference between the WGTS and the tritium injection line exists. While the WGTS source tube has a uniform diameter, the tritium injection line consists of multiple sections of differing lengths and diameters, the values of which are given in appendix B.2. This means that the radius R in eq. (8.23) has to be replaced by a z-position dependent radius $R(z)$.

B.2. Geometry of the Tritium Injection Line

The tritium injection consists of several sections of varying lengths and diameters. The values for length and diameter of the pipes used to describe the injection line are given in table B.1. A schematic drawing of the injection line between ISS glove box and the WGTS cryostat is shown in fig. B.4. A corresponding visualization of the pipe diameter as a function of the position can be seen in fig. B.7.

Valves in the injection line are approximated by pipes with an effective length, a procedure which was determined in a separate test experiment. As the internal geometry of the valves differs greatly from a straight pipe, including at least two sharp turns, this approximation likely leads to rather large deviations for low pressures.

The temperature of the injection line is only known at several key points where the line is connected to temperature sensors or cooling/heating systems. Between these key points, a linear change in temperature is assumed.

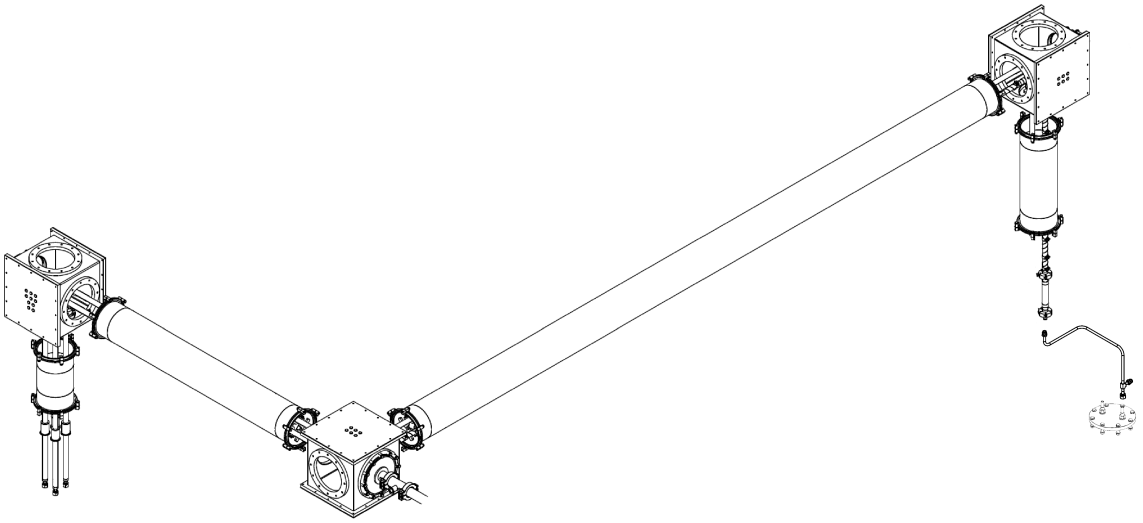

Figure B.4.: **Technical drawing of the tritium injection line between ISS glove box and WGTS cryostat.**

B.3. Steady State Simulation of the Tritium Injection Line

The relation of column density asa function of tritium throughput has been calculated in prior work [Sha10; Kuc+18; Hei19]. This relation together with E-Gun

Table B.1.: **Geometry of the tritium injection line.** Listed are the pipe segments which describe the tritium injection line. In addition to the length l and diameter d of the pipe, the temperatures T_1 and T_2 at the beginning and end of a pipe segment are given.

Segment #	l in m	d in mm	T_1 in K	T_2 in K
1	0.1000	50.0	313.15	313.15
2	0.0400	4.0	313.15	313.15
3	0.0921	4.0	313.15	294.15
4	0.6220	4.0	294.15	294.15
5	0.0921	4.0	294.15	294.15
6	1.2200	9.4	294.15	294.15
7	0.1452	4.0	294.15	294.15
8	10.4770	25.0	294.15	294.15
9	0.1452	4.0	294.15	294.15
10	0.7850	10.0	294.15	294.15
11	0.0921	4.0	294.15	294.15
12	1.2330	6.0	294.15	77
13	0.9390	2.1	77	30
14	4.8780	2.1	30	30

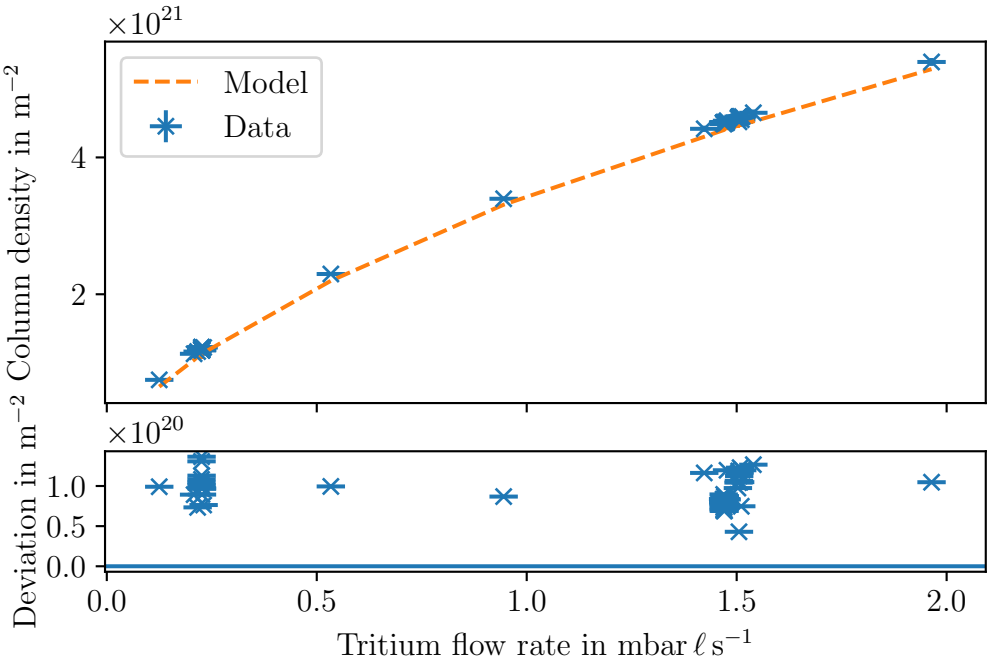

Figure B.5.: **Comparison gas dynamics model to measurement for the column density over tritium throughput relation.** Shown is a comparison of gas dynamics calculations to flow meter and E-Gun column density measurements.

measurements, as described in section 7.1.1, is shown in fig. B.5. The newly derived relation for the throughput relative to the stabilized buffer pressure is shown in fig. B.6. Both relations can be combined as they are strictly monotonous in order to gain a mapping of buffer pressure to column density.

An illustration of the new calculation is shown in fig. B.7, which shows the pressure drop along the tritium injection line and different diameters. Interesting features of this pressure - and therefore gas density - profile are the sharp kinks accompanying changes from larger to smaller diameters, as well as the general influence of the pipe diameter on the pressure drop. The majority of the pressure drop occurs in the final section of the tritium injection capillary with its diameter of only 2.1 mm at 30 K. Accordingly a twice as long section of the injection line with 25 mm diameter outside of the WGTS cryostat does not yield a sizeable pressure drop.

B.4. Transient Simulation of the Tritium Injection Line

The simulations done above are carried out under the assumption of a steady state status where $\dot{M}$ is constant. This is a valid approach when one is interested in fluctuations of the parameters on timescales which are much larger than the characteristic time needed for a sheet of gas to pass through the considered tube. For such a case, the system can be considered to always be in a quasi steady state with $\dot{M}$. When fluctuations on shorter time scales are of interest, this approach can no longer be used. In such a case, the following approach can be used [Sha16]:

$$\frac{\partial p}{\partial t} = \frac{a {v_\mathrm{m}}^2}{2} \frac{\partial}{\partial z} \frac{p}{v_\mathrm{m}} \left(G_\mathrm{P}(\delta) \frac{\partial \ln(p)}{\partial z} - G_\mathrm{T}(\delta) \frac{\partial \ln(T)}{\partial z} \right) + \frac{p}{T} \frac{\partial T}{\partial t} , \tag{8.28}$$

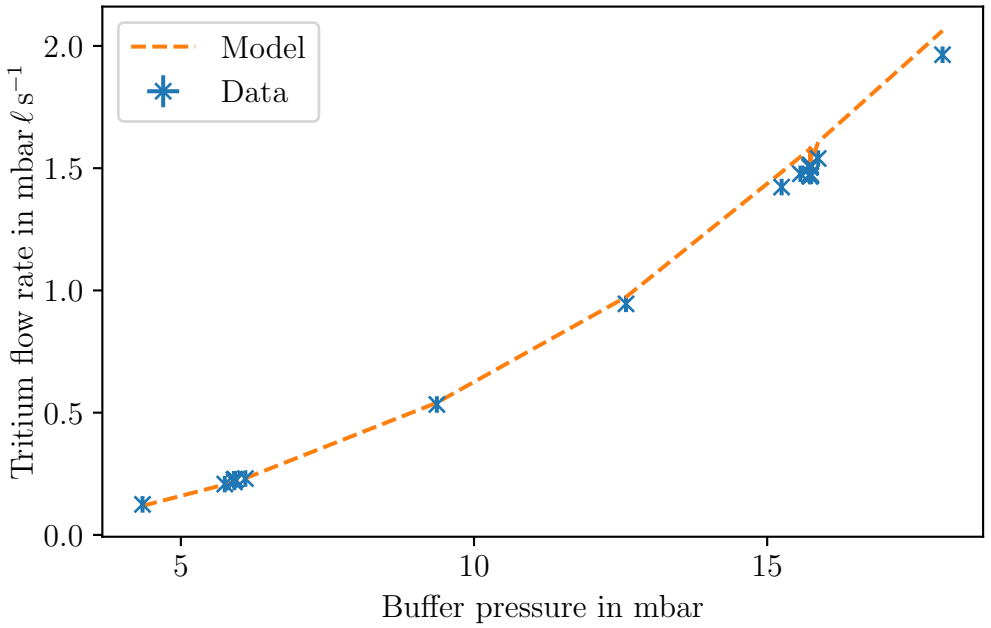

Figure B.6.: **Comparison gas dynamics model to measurement for the tritium throughput over stabilized buffer pressure relation.** Shown is a comparison of gas dynamics calculations to flow meter and pressure measurements.

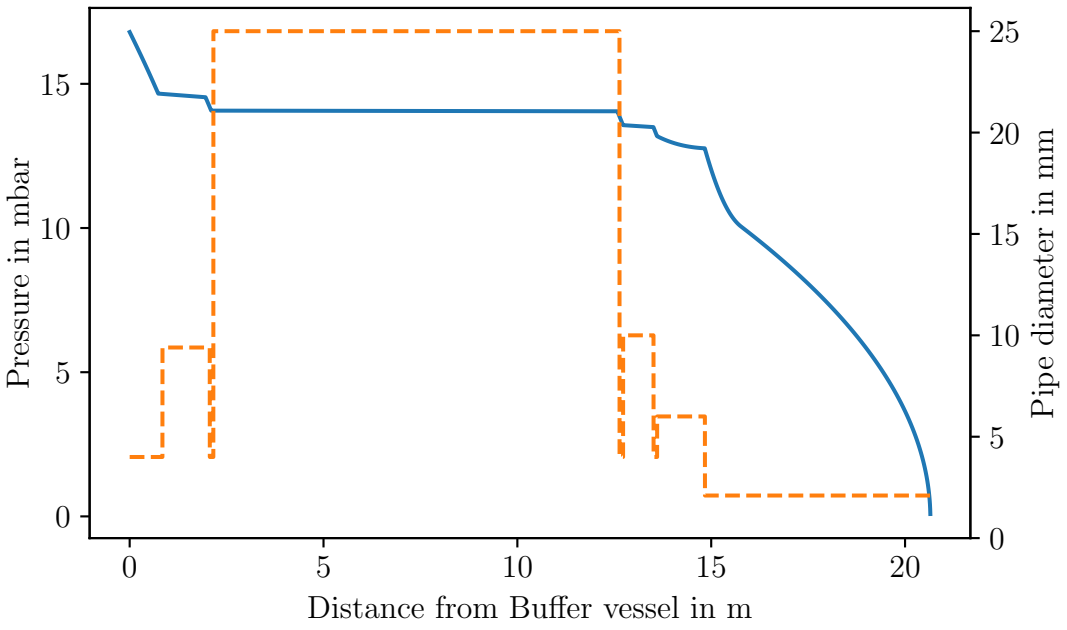

Figure B.7.: **Simulated pressure profile along the tritium injection line.** Shown in addition as a dashed line is the pipe diameter. Sharp changes in the pressure are collocated with changes of the diameter.

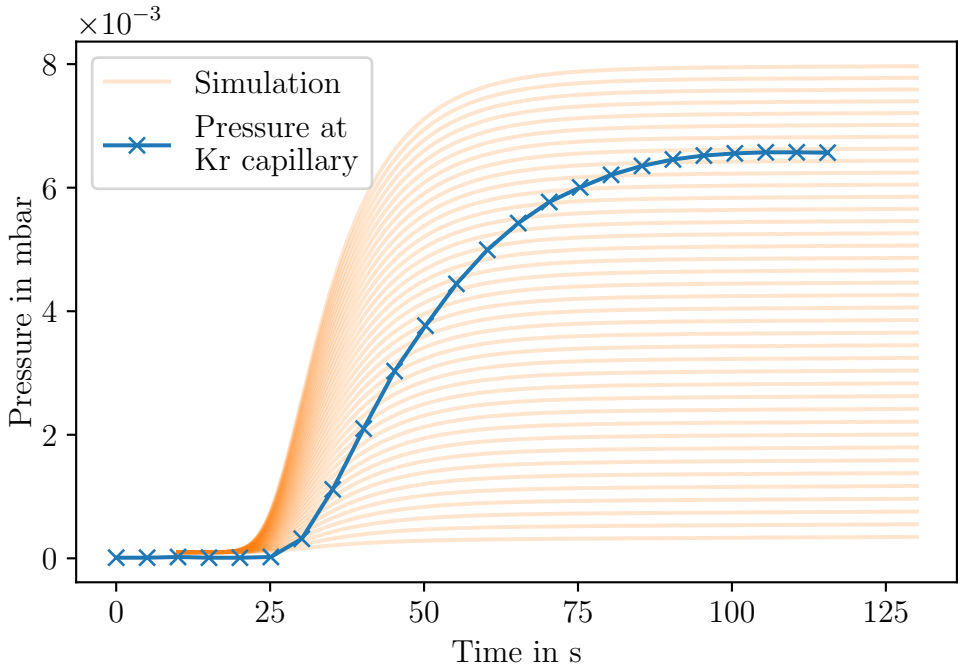

Figure B.8.: **Comparison of simulation and measurement for starting of tritium injection.** Shown is the pressure in the injection chamber as measured with the sensor connected to the tritium+krypton capillary and the simulated pressure at its position. The multitude of simulation lines is the result of slight changes of the mm scale in the choice of choosing the coupling point between tritium injection capillary and the tritium+krypton capillary in the injection chamber. This choice needed to be made somewhat arbitrarily in the process of keeping the problem one dimensional.

to calculate the time dependent pressure profile $p(t, z)$.

An attempt at such a calculation is shown in fig. B.8. For this simulation, the beginning of the gas circulation was simulated, using the measured pressure in the stabilized buffer vessel, and a constant pumping speed via the WGTS source tube as boundary conditions. The pressure measured with the pressure sensor connected to the tritium+krypton capillary is used to compare the simulation results to reality. To do this, the result of the tritium injection line simulation at a certain position was used as a boundary condition for a secondary simulation which produced the pressure at the tritium+krypton capillary sensor. This scheme was necessary due to the need to reflect the Y-junction between tritium injection line, WGTS source tube and the tritium+krypton capillary, while also keeping the problem one dimensional. As a result, the simulated pressure depends on the position chosen to couple the tritium injection line to the tritium+krypton capillary.

From fig. B.8 it can be seen that while the general shape of the pressure curves do look similar, the simulated values show a faster increase in pressure and a shorter time until the transient behavior dies down. This difference is probably a result of the 1D coupling of the tritium injection line to the tritium+krypton capillary which does not take the gas distribution in the injection chamber into account correctly.

As such, the simulation of transients can at the current stage be at most used to gain an insight into short term fluctuations on an order of magnitude scale. They might however still be of interest to investigate the response of the tritium+krypton capillary sensor to a fluctuation of pressure in the injection chamber, as this would allow an estimation of the dampening effect of the tritium+krypton capillary.

However, another issue at the current stage is the computational cost of the transient simulations. To accurately describe the geometry of the tritium injection line, a spatial discretization step size Δz on the mm scale is necessary, leading to a spatial grid of $\approx$ 10000 points on which eq. (8.28) has to be solved. Furthermore, the time discretization step size Δt needs to be chosen on the order of 1×10^{-7} s to 1×10^{-9} s to avoid the appearance of unphysical negative pressures. For a simulation of about 100 s duration, as shown in fig. B.8, it is therefore necessary to evaluate the discretized form of eq. (8.28) roughly $\mathcal{O}\left(10^{13} - 10^{15}\right)$ times. A speed of about 300 µs per single time step could be achieved, leading to a computation time of roughly 10 days for a simulation like this. As the calculation is iterative in time, and all spatial values need to be available for the next time step, parallelization of the problem is difficult. Thread-based parallelization approaches were discarded after the associated overhead and necessity to join the threads after each temporal step proved to be slower than simple sequential calculation. An improvement could be achieved using parallelization based on SIMD (single instruction, multiple data) instructions, which can apply the same operations to multiple sets of data points simultaneously. As no further significant gain on the order of magnitude scale can be expected with this approach, a possible solution could be the change from explicitly solving the differential equation eq. (8.28) to using an implicit solving algorithm.

To summarize, while simulations of the transient behavior of the tritium injection line can be used for rough estimations of the order of magnitude of effects at the moment, there is still potential for further improvement.

C. DAQ Exchange measurement

Before implementing the improved readout for the MKS 690A sensors of the pressure stabilization, it needed to be verified whether the MKS 670 signal conditioner applies some internal digitization and back conversion to analog with a fixed precision, which would limit any improvements. Additionally, it needed to be determined at which point the intrinsic noise characteristics of the pressure sensor become dominant over artifacts due to limited precision readout.

This measurement was done by attaching an external RIGOL DM3052 digital multimeter (DMM)[1] to the 0 V to 10 V output of the signal conditioner. The signal conditioner translates the entire measurement range of 0 mbar to 133.3 mbar of the MKS 690A sensor to 0 V to 10 V. For the later operation however, the range on interest is only 0 mbar to 25 mbar. To make the best use of the external DMM, it was used in its 400 mV F.S. mode with a resolution of 1 µV and only very small pressures applied to the MKS 690A sensor. In this measurement configuration, a resolution of 1.333×10^{-5} mbar on the measured pressure would be the limit. This was judged as sufficient, as this value is close to the lower limit of absolute pressure which can be measured by capacitance diaphragm gauges.

The measurement comparing the PCS7 readout to this external DMM is shown in fig. C.9. It can be seen clearly, that the output of the signal conditioner is free of noise on a level far below the resolution of the PCS7 readout, and no internal digitization seems to happen inside the signal conditioner. An analysis of the periods of constant pressures shows a standard deviation of the measured pressure values of:

$$\sigma_{p,\mathrm{DMM}} = 3.6 \times 10^{-5}\,\mathrm{mbar}\,. \tag{8.29}$$

While this value is above the 1.333×10^{-5} mbar resolution of the DMM, it is below the accuracy stated in the datasheet which corresponds to a value of 4.3×10^{-4} mbar. As no specific information is given on the repeatability precision of the DMM, it can not be conclusively determined whether the remaining fluctuation of the pressure values is caused by the sensor, or the external DMM unit.

However, in either case, a big improvement of the regulation can be achieved by exchanging the readout of the MKS 670 signal conditioner.

[1] see fig. H.19 for specifications

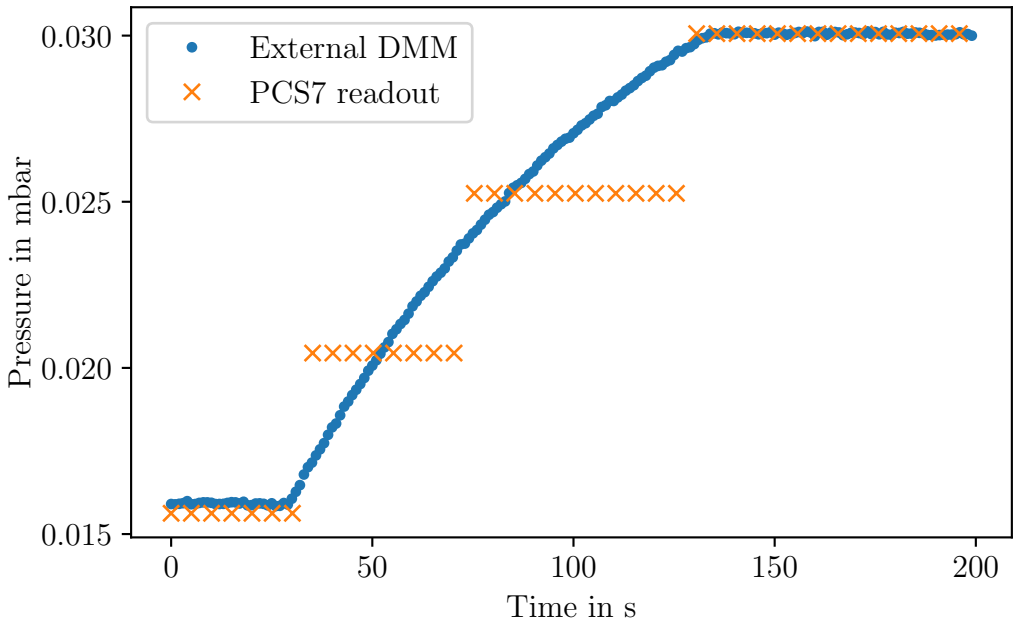

Figure C.9.: **Test of `MKS 670` signal conditioner output with PCS7 and an external `RIGOL DM3052` digital multimeter.**

D. Outgassing Measurement

The outgassing rate of the WGTS and the DPS1 TMPs, including the beam tube and all connecting pipes, can be measured during times when there is no circulation of tritium or krypton through the loops system. This measurement is done by closing the valve of the return line (AV2 in fig. 3.1) with running TMPs. The gas load produced by outgassing is accumulated in the volume behind the TMPs. In order to prolong the lifetime of the pumps providing the TMP forepressure, they are routinely shut down in periods without gas circulation and AV2 is closed, resulting in regular outgassing measurements as a byproduct. These measurements are shown in fig. D.10 and their values tabulated in table D.2.

The outgassing measurements can be split into a section prior to and after start of operation with tritium. Prior to tritium operation, the outgassing rate exponentially decreased over time. This is to be expected as the vacuum system has not been baked, so a significant amount of this outgassing will be due to surface contamination, the majority of which will have been water. After start of operation with tritium, the outgassing rate jumps to a lower value than expected from the prior exponential decrease, and from then on stays at an average outgassing rate q_{imp} of:

$$q_{\mathrm{imp}} = (1.5 \pm 0.2) \times 10^{-5}\,\mathrm{mbar}\,\ell\,\mathrm{s}^{-1}\,. \tag{8.30}$$

The data after start of tritium operation is shown in fig. D.11. While the outgassing rate is stable to within less than a factor of two since start of operation with tritium, distinct trends can be seen, which showcase the issue of history dependence of the outgassing rate: Despite rather comparable time spans between measurement campaigns, the data points of mid 2019 show a steep upward trend, while those of early 2020 show a much smaller increase in outgassing over time while gas is circulated. An explanation for this could be a cleaning effect of tritium circulation on the system. In the data, this can be seen in significant decrease in outgassing after the KNM2 measurement phase in late 2019. This cleaning effect is expected to not only reset the outgassing rate to a lower level, but also deplete the origin for the increase in outgassing rate. In this case it can be expected that the outgassing rate will stabilize further with more periods of tritium circulation. This also means, that impurity accumulation in the circulating gas stream might decrease to a lower level over time.

It needs to be noted, that the outgassing rate by itself does not necessarily reflect the magnitude of isotopic exchange reactions of tritium and hydrogen. If the outgassing gas consists of e.g. a hydrocarbon like methane, it can in principle facilitate twice the exchange of T_2 to HT compared to pure H_2 at the same partial pressure. Isotopic exchange effects with the walls can also be much stronger than the outgassing rate alone would suggest.

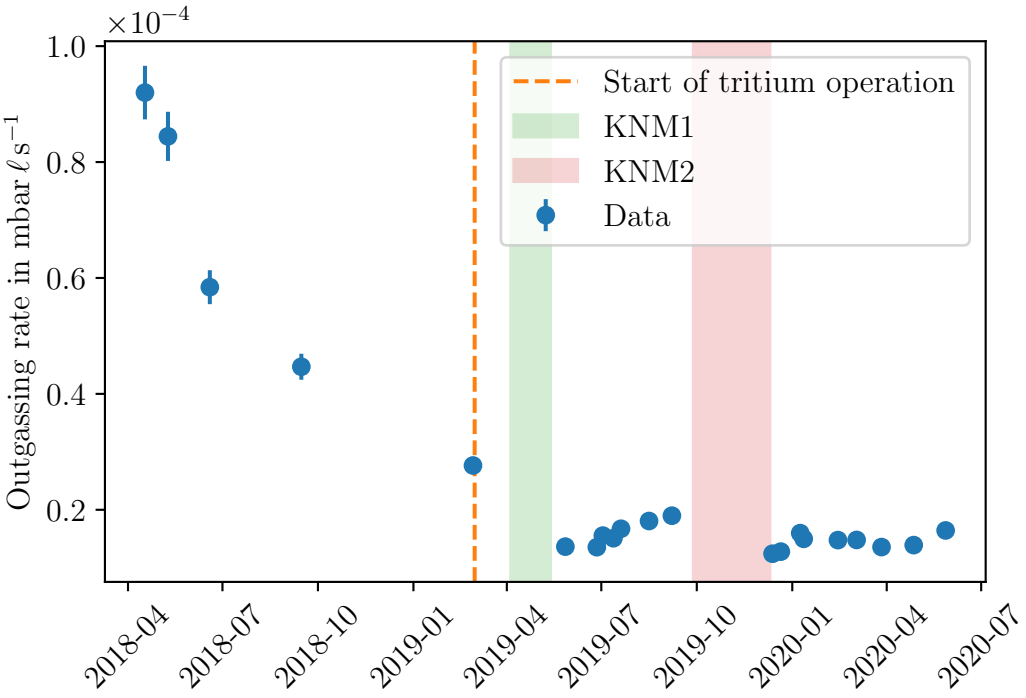

Figure D.10.: **Outgassing rates of the WGTS vacuum system and DPS1 TMPs.** The shown data values are listed in table D.2. The dashed line marks the start of operation with tritium.

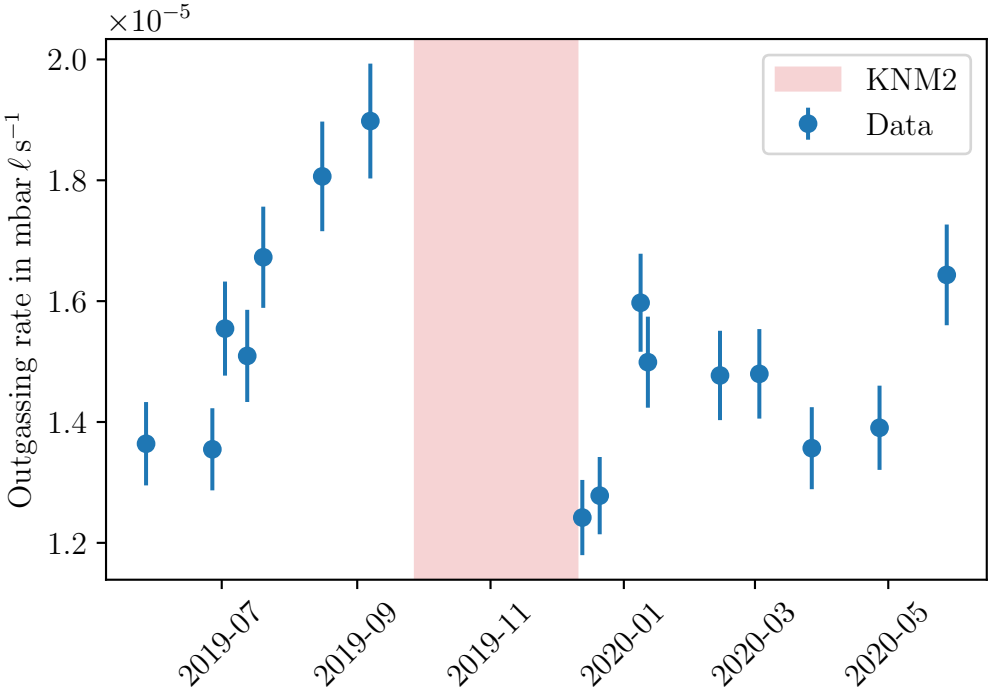

Figure D.11.: **Outgassing rates of the WGTS vacuum system and DPS1 TMPs since start of tritium operation.** The shown data is a zoom on the later part of fig. D.10.

Table D.2.: **Outgassing rates of the WGTS vacuum system and DPS1 TMPs.**

Date/Time	Outgassing rate in $1 \times 10^{-5}\,\mathrm{mbar}\,\ell\,\mathrm{s}^{-1}$	Outgassing rate uncertainty in $1 \times 10^{-5}\,\mathrm{mbar}\,\ell\,\mathrm{s}^{-1}$
2018-04-17 08:00	9.20	0.46
2018-05-09 12:00	8.44	0.42
2018-06-18 20:00	5.84	0.29
2018-09-15 00:00	4.47	0.22
2019-02-27 09:00	2.76	0.14
2019-05-27 09:00	1.36	0.07
2019-06-26 17:00	1.35	0.07
2019-07-02 12:00	1.55	0.08
2019-07-12 16:00	1.51	0.08
2019-07-20 00:00	1.67	0.08
2019-08-16 00:00	1.81	0.09
2019-09-07 00:00	1.90	0.10
2019-12-13 00:00	1.24	0.06
2019-12-20 23:00	1.28	0.06
2020-01-08 16:00	1.60	0.08
2020-01-12 00:00	1.50	0.08
2020-02-14 00:00	1.48	0.07
2020-03-03 00:00	1.48	0.07
2020-03-27 00:00	1.36	0.07
2020-04-27 00:00	1.39	0.07
2020-05-27 18:00	1.64	0.08

E. Estimation of Carbonated Gases

This section contains an estimation of the amount of released carbonated gases in appendix E.1, as well as an estimation of releasable carbonated gases based on literature values in appendix E.2.

Propagation of uncertainties in this section is done via MC-Propagation due to some assumed non-Gaussian uncertainties. The uncertainties given for each listed value are the standard deviation of such a propagated distribution of values. A better feeling for the magnitude of uncertainty can be gained by looking at the distributions in fig. E.12.

E.1. Estimation of generated Carbonated Gases

The amount of carbonated gases which accumulated in the injection capillary during KNM1 can be estimated from the observed pressure rise at the tritium+krypton capillary during several warm-up procedures performed throughout the measurement campaign. For this purpose, the area under the peaks observed in fig. 7.11 was calibrated against a measurement of the total gas amount during the second warm-up. As the warm-up procedures were not all performed with the same configuration, applying this calibration to the other warm-up procedures can induce a large uncertainty, so a conservative uncertainty estimate of 50 % on the derived gas amount is adopted. Larger deviations from the calibration can be ruled out by measurements of the total released gas amount in the large waste buffer vessel, which are however too imprecise to do an estimated based on them. This analysis leads to a total amount of gas containing carbon released during KNM1 of:

$$n_{\mathrm{KNM1}} = (12 \pm 6)\,\mathrm{mbar}\,\ell\,. \tag{8.31}$$

During the production exhaustion process described in section 7.2.3, LARA measurements of the gas were taken. The elevated pressure, in combination with the steady accumulation of CQ_4, allowed for the detection of the CQ_4 concentration with LARA:

$$c_{\mathrm{CQ_4}} = 0.25^{+0.25}_{-0.125}\,\%\,. \tag{8.32}$$

As no gas flow was present to homogenize the gas in the inner loop, this value is not necessarily representative of the entire gas inside the IL. The uncertainty induced by this effect could be very large as the LARA cell is connected via long, thin pipes, which can significantly suppress gas homogenization via diffusion, so considering it in the following analysis would lead to a difficult to interpret result. It is therefore assumed in the following, that the value measured by LARA is representative for the entire gas mixture. A further issue is the lack of good reference values for CQ_4 spectra, for which a high uncertainty on the value of $c_{\mathrm{CQ_4}}$ is taken[2]. Combined with the amount of tritium gas inside the system during the procedure, a total amount of released methane can be calculated:

$$n_{\mathrm{exhaust,CQ_4}} = (46 \pm 20)\,\mathrm{mbar}\,\ell\,. \tag{8.33}$$

[2]Personal communication with G. Zeller, 2020

As the co-production of CO and possibly CO_2 is not well understood, this value is taken as a lower limit on the amount of carbonated gas. An upper limit is estimated using the peak areas of the pressure peaks where the composition is identified. The most extreme case is that all CO and CO_2 molecules result from co-production with CQ_4, in which case the fraction of CQ_4 of the total gas would be:

$$f_{CQ_4} = 0.2 - 1.0 \tag{8.34}$$

This leads to an amount of carbonated gases from the exhaustion procedure of:

$$n_{\text{exhaust,tot}} = (116 \pm 72)\,\text{mbar}\,\ell\,. \tag{8.35}$$

Combining the results from KNM1 and the exhaustion procedure, a total amount of released carbonated gas of

$$n_{\text{tot}} = (128 \pm 72)\,\text{mbar}\,\ell\,, \tag{8.36}$$

can be derived.

E.2. Calculation of Expected Amount of Carbonated Gases from the Inner Loop

Based on literature values for the tritium induced production of carbonated gas species like CQ_4, CO and CO_2 in stainless steel vessels, the total amount $n_{\text{tot,theo}}$ of gas which is expected to be released by the IL can be estimated:

$$n_{\text{tot,theo}} = A_{\text{IL,eff}} \cdot g_{\text{theo}}\,, \tag{8.37}$$

using

- the effective inner surface area $A_{\text{IL,eff}}$ of the IL between the injection capillary and the permeator, as well as of the pure tritium buffer in the FL,
- and the literature value g_{theo} for the amount of carbonated gas which can be released per unit area.

The effective area takes into consideration that the microscopic surface area of vessels and piping important for the radiochemical reactions can differ by one order of magnitude or more from the geometric area of an ideal pipe [GME83]. After comparing the piping used in the IL to those investigated in [GME83], a factor of 10 larger mircoscopic surface area was chosen. Based on the technical drawings of the IL and the pure tritium buffer vessel, their combined geometry surface area is $1.75\,\text{m}^2$. This includes an estimation of the internal surface of the FL Normetex pump, which was also connected to the volume, of $0.3\,\text{m}^2$. Considering the different surface conditions between piping and vessel surfaces, a rectangular distribution from 1 to 10 was taken as an uncertainty to derive the value distribution of $A_{\text{IL,eff}}$.

For g_{theo}, the amount of carbon in the surface layers of the stainless steel vessels is considered. It is assumed that only the topmost $(1.25 \pm 0.25)\,\text{nm}$ contribute. It was found in [GME83] that the mole fraction of carbon in this region for the used 316L steel is around $(50 \pm 5)\,\%$, and therefore much higher than the bulk value of

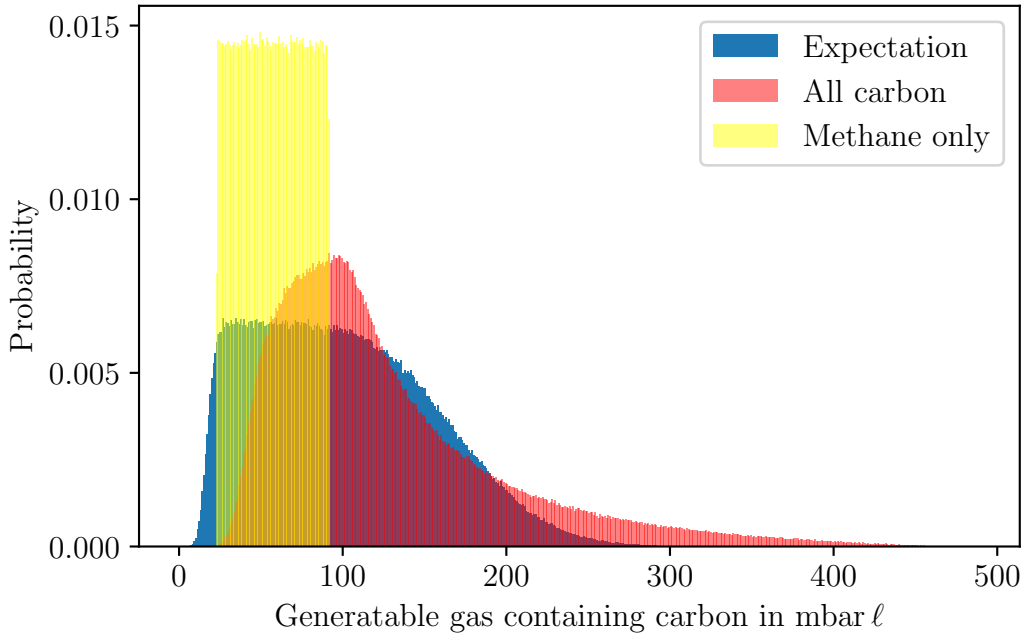

Figure E.12.: **Comparison of theoretical to measured amount of carbonated gas.** Shown are the calculated value distributions for the theoretical and measured amount of carbonated gas. The rectangular shape of the measurement data distribution is caused be the rectangular uncertainty assumed for the methane concentration c_{CQ_4} measured with LARA.

<0.08 %. This high concentration supposedly steams from hydrocarbons left over from the manufacturing process. With this, the amount of carbon atoms which can be used to form carbonated gas species can be calculated, giving the maximal value for the case of total depletion of the surface. This leads to a value of:

$$g_{\text{theo}} = (57 \pm 31)\,\text{mbar}\,\ell\,\text{m}^{-2}\,. \tag{8.38}$$

In [Gil80], methane production of different materials was experimentally investigated. For the material most similar to the one used in the IL piping which was tested (sample #6), a value of $20\,\text{mbar}\,\ell\,\text{m}^{-2}$ of methane generation can be calculated. To compare this to g_{theo}, this value needs to be corrected with f_{CQ_4} determined in appendix E.1 to gain the amount of all carbonated gases, and then derive a reference literature value:

$$g_{\text{theo,ref}} = (20 - 100)\,\text{mbar}\,\ell\,\text{m}^{-2}\,, \tag{8.39}$$

which agrees well with g_{theo}. Using the values for $A_{\text{IL,eff}}$ and g_{theo}, a resulting distribution of values for the theoretically expected amount of carbon containing gas was calculated to be

$$n_{\text{tot,theo}} = (101 \pm 54)\,\text{mbar}\,\ell\,. \tag{8.40}$$

A comparison of the estimated values for the measured released gas and expected releaseable gas is shown in fig. E.12. As can be seen, the distribution of values cover more than an order of magnitude, making definitive statements on whether the expected amount of gas has been removed very difficult.

F. Estimation of Tritium Viscosity

The viscosity of tritium is not available in any publicly available scientific literature. As its value however forms an integral part in gas-dynamical calculations for KATRIN presented in appendix B, knowledge of this quantity is of high interest.

Ideas for possible measurement approaches for a viscometer which can be realized in a tritium-compatible fashion are:

- capillary viscometers, or
- rotational viscometers.

Capillary Viscometer A capillary viscometer is based on the dependence of the conductance of a capillary on the viscosity of the gas flowing through the capillary. Therefore, diverse gas dynamical measurements, such as the pressure drop over the capillary at a constant flow rate through it, can be used to determine the viscosity of gases and liquids. The molar flow $\dot{n}$ through a capillary is given by:

$$\dot{n} = \frac{\pi r^4 (p_1^2 - p_2^2)}{16 L R T \eta_T} C^{\mathrm{gas}}(T, p_1, p_2)\,. \tag{8.41}$$

with:

- p_1, p_2 the pressures at both ends of the capillary,
- r the radius of the capillary,
- L the length of the capillary,
- R the universal gas constant,
- T the temperature of the capillary,
- η_T the viscosity of the gas at temperature T, and
- $C^{\mathrm{gas}}(T, p_1, p_2)$ which includes some corrections.

As the conductance depends strongly on the geometry, the best results with these kinds of viscometers can be achieved by performing ratio measurements. Rather than simply deriving uncertainties on the viscosity from the uncertainty on the geometry, the capillary is calibrated using helium, for which the viscosity has been calculated ab initio with uncertainties in the 0.01 % range. These ratio measurements have been done with accuracies of better than 0.04 % [BMM13].

An issue when transferring these measurements to operation with tritium is the capillary material itself. Due to the possibility to create capillaries with nearly flat internal surface on the atomic scale, glass is the preferred material for capillaries. The danger of cracking however makes glass unsuitable to be used in a primary system without further containment. Furthermore, glass to metal transitions usually limit the temperature range where the system can be operated. This makes working with glass rather problematic considering the cryogenic temperatures necessary to probe the temperature range of interest for KATRIN. Ensuring a good thermal contact to a glass capillary is challenging as well, as differences in thermal expansion of

solid connections can easily cause enough stress to break the capillary. Cooling the capillary via bath solutions on the other hand risk a contamination of the coolant medium with tritium. Using stainless steel or other metals to make the capillary is a possibility, however the surface roughness of the material will lead to larger deviations from an ideal capillary and therefore degrade the quality of the measurement. Neglecting solutions using bath cooling due to the possibility of coolant contamination, the easiest solution would be a metallic capillary connected to a cold finger.

Rotational Viscometer Rotational viscometers are based on the drag a rotating body experiences inside a surrounding medium. This drag is dependent on the viscosity of the gas, making measurements of the rotational frequency of the body a measurement of the viscosity.

Operation with tritium in practice makes direct mechanical feedthroughs into the primary vacuum system impossible. This can be circumvented by magnetic coupling. The rotating body needs to be secured in the vacuum system without friction to the walls, and while specialized mechanical bearings might fulfill the requirements imposed by tritium operation, magnetic bearings are a better solution, as maintenance can be done without opening the primary system.

A commercially available solution to this issue are spinning rotor gauge systems [BTL97]. While they are usually used as pressure measurement devices, they fulfill all requirements needed to measure gas viscosity, and only have UHV compatible stainless steel exposed to the vacuum system, making operation with tritium possible without modifications. Due to the close distance between rotor and the magnetic bearing/readout, it is however not clear, whether such a system can be operated at cryogenic temperatures due to possible adverse effects on the electronics.

G. Detailed KATRIN Loop Flow Diagrams

This section contains the up-to-date flow diagrams of the KATRIN tritium loop system.

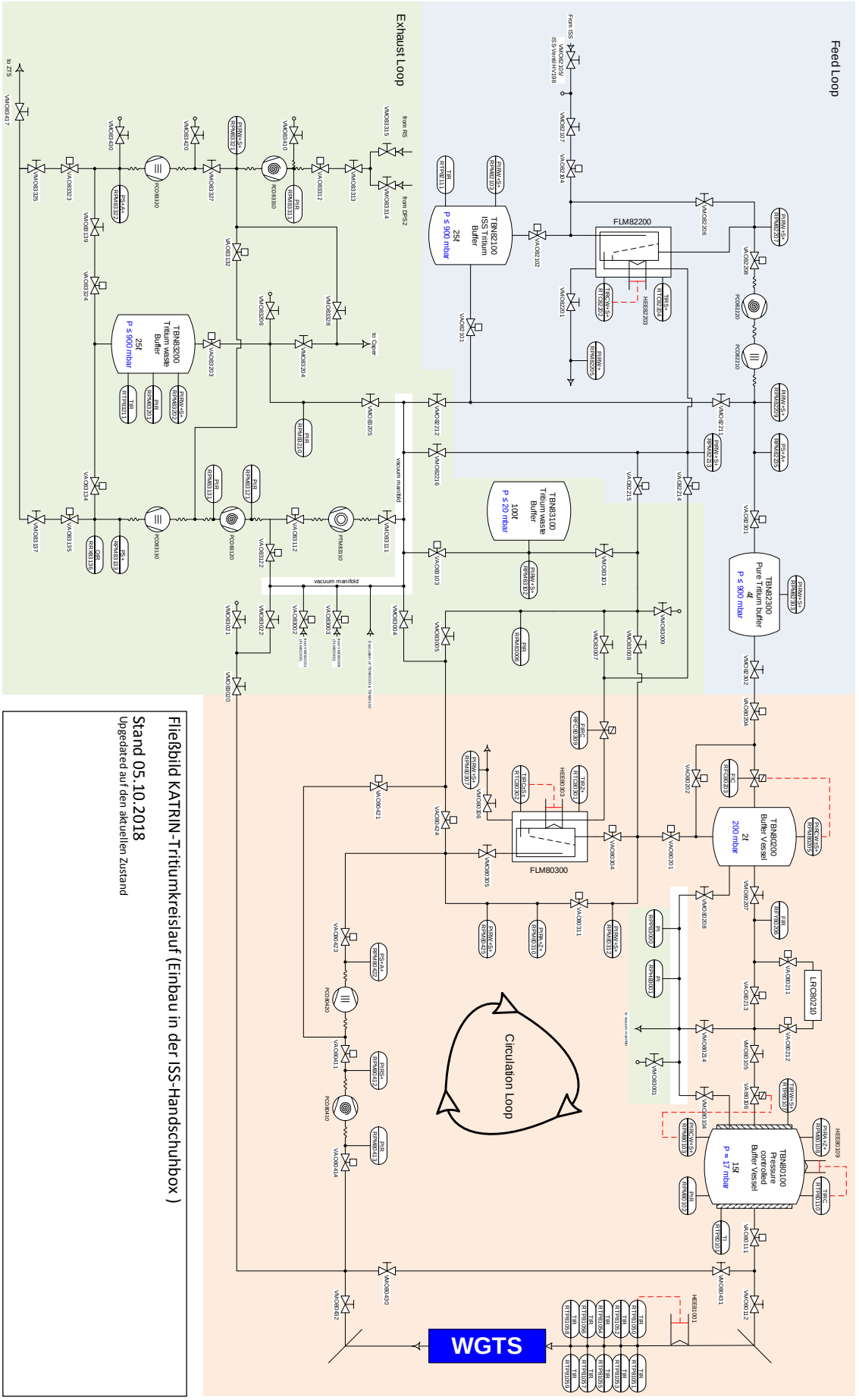

Figure G.13.: **Detailed flow diagram of the loop system components inside the ISS glove box.**

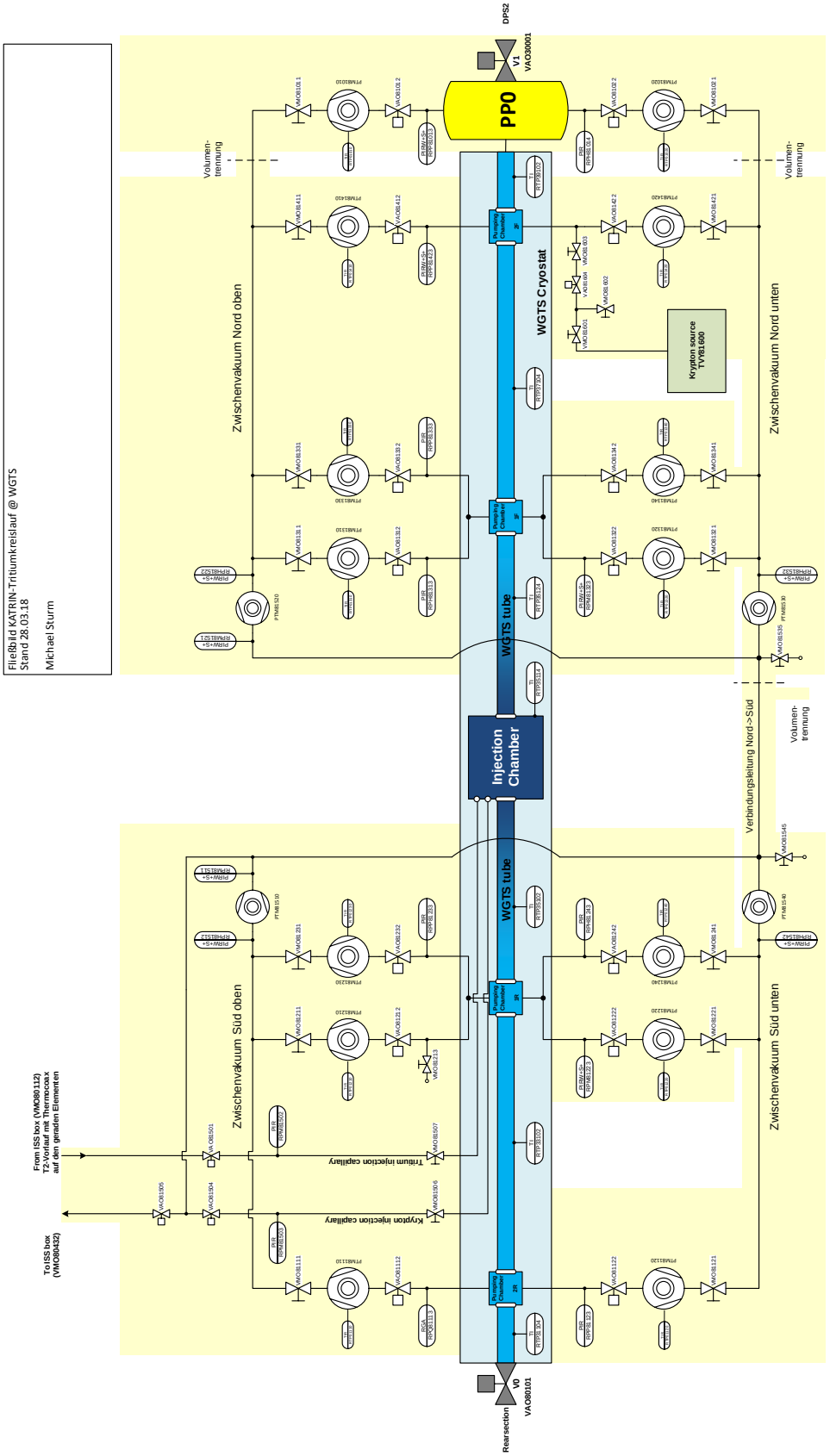

Figure G.14.: Detailed flow diagram of the inner loop system connected to the WGTS.

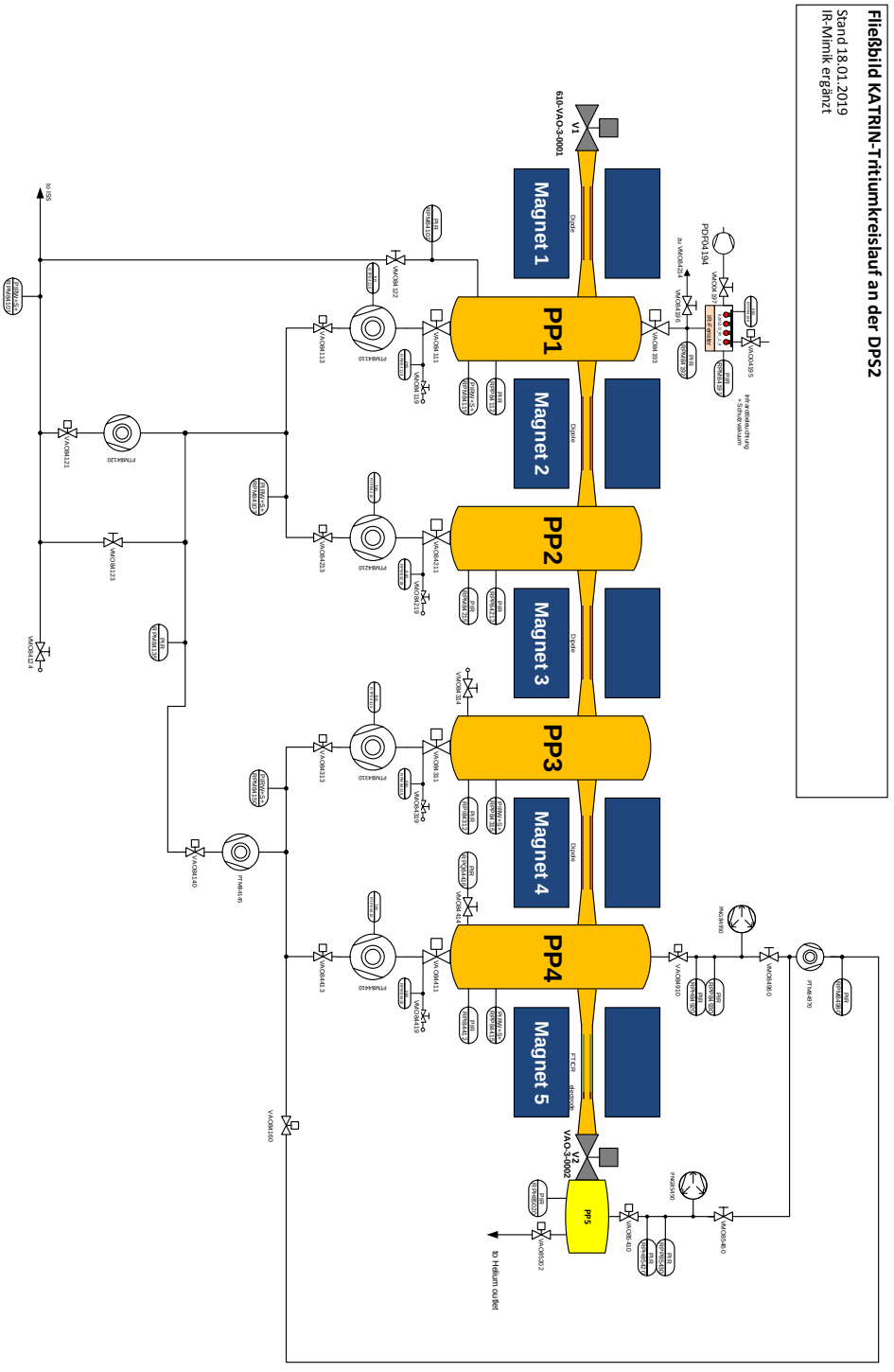

Figure G.15.: **Detailed flow diagram of the outer loop system connected to the DPS2.**

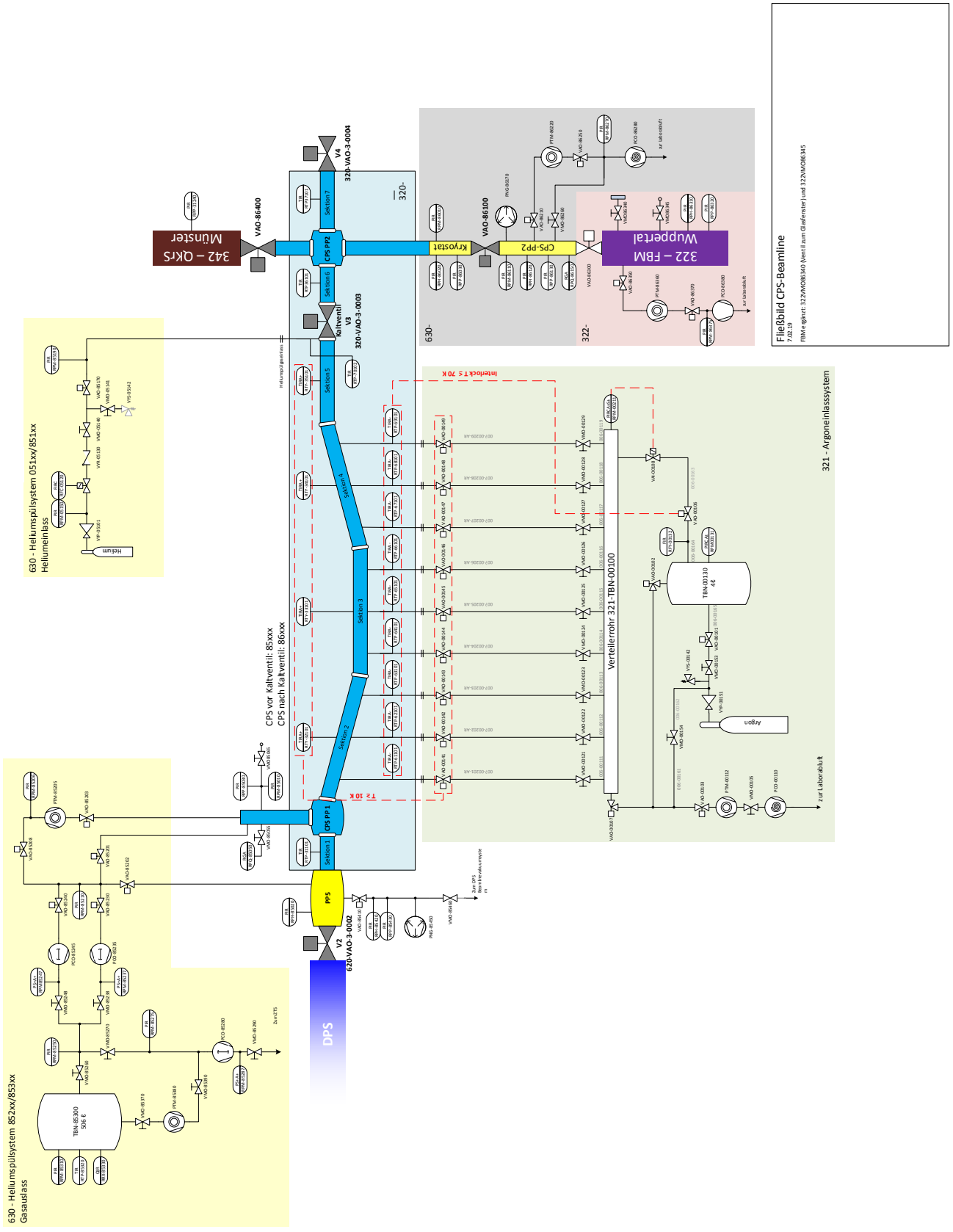

Figure G.16.: **Detailed flow diagram of the outer loop system connected to the CPS.**

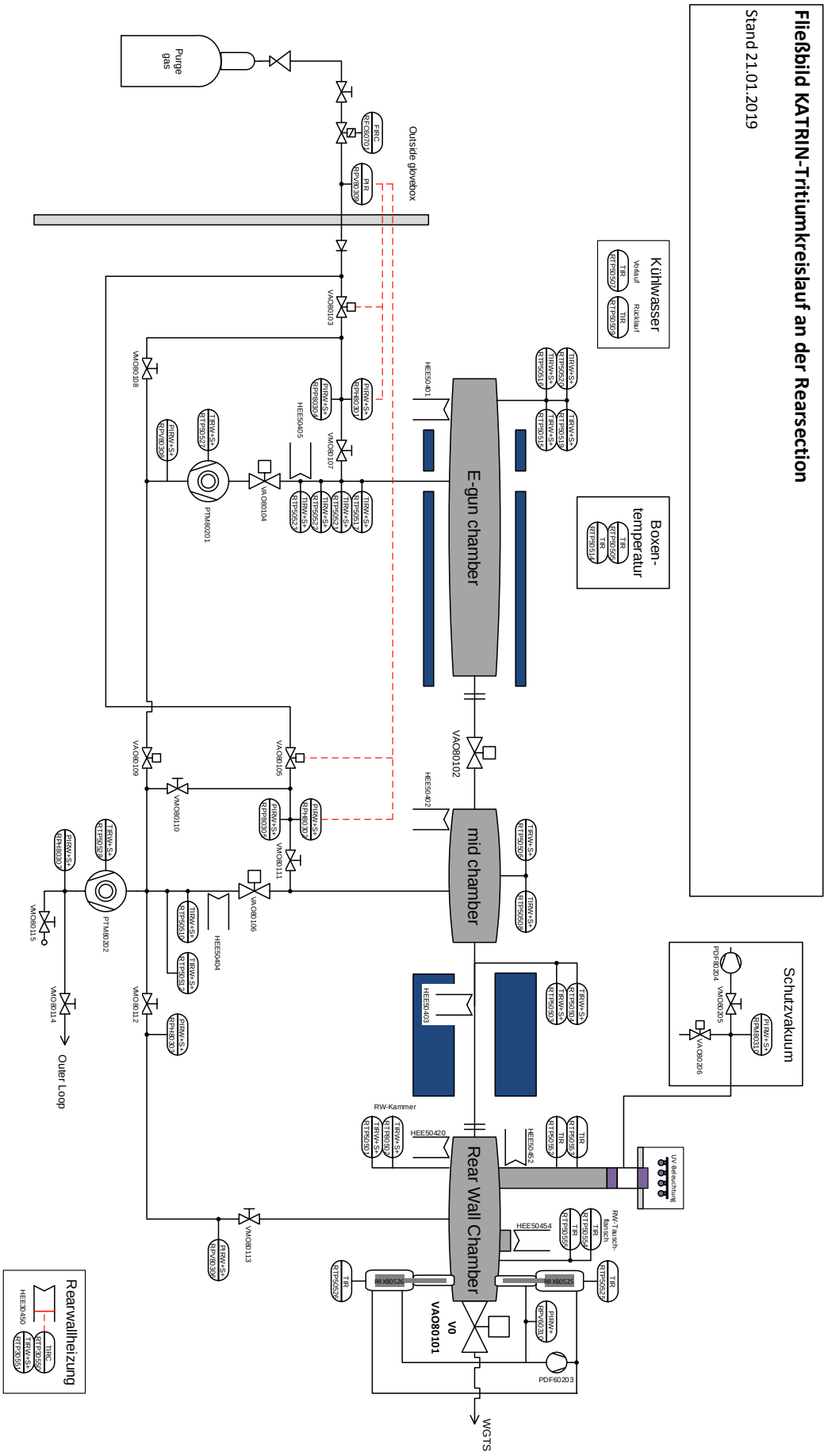

Figure G.17.: **Detailed flow diagram of the outer loop system connected to the RS.**

H. Datasheets

ProfiMessage / ProfiLab

Modul Typ (2 Module je Master / Slave)	ADVT / AAST / ADIT	ADGT	AMDT / ADFT	IOIT / OTPT / DIOT
Analog-Eingänge	**15 / 4 / 10**	**8**	**8 / 8**	**-**
Sensoren	mV, mA, Thermoelemente, Pt100(0) (Pt100(0) nicht bei ADVT)	mV, mA, Thermoelemente, Pt100(0)	mV, mA	-
Summenabtastrate	600 Hz	60 Hz	10 .. 160 KHz / 8 KHz	-
Spannungs- und Strommessbereiche	156 mV .. 10 V, ± 156 mV .. ± 10 V / 0 .. 20 mA, 4 .. mA, ± 20 mA			-
Potentialtrennung zu System	750 VDC			-
Potentialtrennung Kanäle	110 V	650 V	100 V	-
Auflösung / Art ADC	24 Bit Sigma-Delta	24 Bit Sigma-Delta	14 Bit	-
Messgenauigkeit	V / mA: 0,01 % vom Messbereichsendwert Pt100(0): 0,1 K Thermoelemente: 0,1 % EW nach Kompensation	V / mA: 0,01 % vom Messbereichsendwert Pt100(0): 0,1 K Thermoelemente: 0,1 % EW nach Kompensation	± 1,25 V .. ± 10 V: ± 0,1 % EW ± 0,625 V: ± 0,2 % EW ± 0,312 V: ± 0,3 % EW ± 0,156 V: ± 0,4 % EW	- - - -
Analog-Ausgänge	**- / 4 / 1**	**-**	**2 / 2**	**-**
Auflösung	16 Bit	-	12 Bit	-
Potentialtrennung	750 V	-	100 V	-
Ausgang	0/4 .. 20 mA	-	0 .. 10 V	-
Max. Bürde / Min. Last	650 Ω	-	2,5 kΩ	-

Figure H.18.: **Technical data of Delphin ProfiMessage DAQ Systems.** Source: screenshot of https://www.delphin.de/produkte/mess-und-pruefgeraete/profimessage/technische-daten.html taken on the 10th June 2020.

Specifications of DM305X Series

DC Characteristics

Accuracy ± (% of reading + % of range) [1]

Function	Range[2]	Test current or Load voltage	Input Impedance	1 Year 23℃±5℃	Temperature Coefficient 0℃ - 18℃ 28℃ - 55℃
DC Voltage	400.000 mV		10 MΩ 或>10 GΩ	0.025 + 0.008	0.0015 + 0.0005
	4.00000 V		10 MΩ 或>10 GΩ	0.025 + 0.006	0.0010 + 0.0005
	40.0000 V		10 MΩ	0.025 + 0.006	0.0020 + 0.0005
	400.000 V		10 MΩ	0.030 + 0.006	0.0020 + 0.0005
	1000.00 V[4]		10 MΩ	0.030 + 0.005	0.0015 + 0.0005
DC Current	2.00000 mA	<0.03 V		0.050 + 0.070	0.0040 + 0.0070
	20.0000 mA	<0.3 V		0.050 + 0.008	0.0040 + 0.0007
	200.000 mA	<0.3 V		0.050 + 0.009	0.0040 + 0.0008
	1.00000 A	<0.3 V		0.100 + 0.070	0.0100 + 0.0062
	10.0000 A[5]	<0.6 V		0.200 + 0.007	0.0100 + 0.0007
Resistance[3]	400.000 Ω	1 mA		0.050 + 0.010	0.0030 + 0.0005
	4.00000 kΩ	100 μA		0.015 + 0.006	0.0030 + 0.0005
	40.0000 kΩ	10 μA		0.015 + 0.006	0.0030 + 0.0005
	400.000 kΩ	2 μA		0.030 + 0.007	0.0030 + 0.0005
	4.00000 MΩ	200 nA		0.060 + 0.010	0.0030 + 0.0005
	100.000 MΩ	200 nA ||10 MΩ		2.00 + 0.005	0.1500 + 0.0005
Diode Test	2.4000 V[6]	1 mA		0.05 + 0.010	0.0050 + 0.0005
Continuity Test	2000 Ω	1 mA		0.05 + 0.010	0.0050 + 0.0005

Remarks :

[1] Specifications are for 60 minutes warm-up and 5 ¾ digits readings resolution, calibration temperature 18℃ - 28℃.

[2] 20% over range on all ranges except for DCV 1000 V, ACV 750 V, DCI 10 A and ACI 10 A.

[3] Specifications are for 4-wire measure or 2-wire measure under "Null" operation. ± 0.2 Ω of extra errors will be generated if perform 2-wire measure without "Null" operation.

[4] Plus 0.02 mV of error per 1 V after the first ±500 VDC.

[5] 30 seconds OFF after 30 seconds ON is recommend for the continuous current that higher than DC 7 A or AC RMS 7 A.

[6] Accuracy specifications are only for voltage measuring at input terminal. The typical value of current under measure is 1 mA. Voltage drop at the diode junction may vary with current supply.

Setup Time Attentions
The setup time about voltage measurement is influenced by source resistance and media characteristics of cable as well as input signal. Generally, the setup time of readings of lower source resistance (less than 1 kΩ) is1.5 s.

Figure H.19.: **Technical data of RIGOL 3052 Digital Multimeter.** Source: RIGOL Data Sheet DM3000 Series Digital Multimeter DM3061/2/4, DM3051/2/4

1.2 Specifications

Flow volume (converted to N_2)	10 to 50000 SCCM full scale
Flow control resolution	0.2% of FS < 100 SCCM
(Reference value)	0.1% of FS > 100 SCCM
Max. Inlet pressure	10 kgf/cm^{2}G
Response time	15 msec
Operating current	150 mA (max.)
Internal leak standard	1% of FS or less, N_2 (differential pressure 1 kgf/cm^{2}G)
External leak standard	1 x 10^{-10} atm.cc/sec (He) or less
Operating temperature	Specified temperature in the range of 15 to 150°C (adjustment is required at the operating temperature)
Valve type	Normally closed (metal sealed solenoid)
Material in contact with the gas	SUS 316, corrosion-resistant magnetic material, PTFE
Seal material	Nickel C-ring
Piping joints	1/4" VTF male thread (VCR compatible)
Weight	About 0.8 kg

Figure H.20.: **Technical data of MKS 148J full metal regulation valve.** Adapted from [MKS99b] with permission from MKS Instruments.

Ambient Operating Temperature	15° to 40° C (59° to 104° F)
Accuracy	
690A	
Standard	0.12% of reading ±zero/span coeff.
Optional	
All ranges	0.08% of reading ±zero/span coeff.
1, 10, 100, and 1000 Torr units only	0.05% of reading ±zero/span coeff.
Full Scale Pressure Ranges (Torr)	
690A	0.1, 1, 10, 100, 1K, 5K, 10K, 15K, 20K, 25K
Inlet Tube Fitting(s)	Swagelok® 4-VCR® (female)
Measurement Side (P_X) Media Compatibility	Any gas compatible with Inconel®, 304 SS
P_X Overpressure	
100 mTorr (0.1 T) Units	125% FS or 40 psia (whichever is greater)
All other ranges	125% FS or 45 psia (whichever is greater)
Resolution (of FS)	1 x 10^{-6}
Sensor Temperature	Regulated at 45° C
Sensor Type	Single sided, dual electrode
Temperature Effects on Span	
100 mTorr (0.1 T) Units	<0.010% R / °C (100 ppm)
All other ranges	<0.002% R / °C (20 ppm)
Temperature Effects on Zero	
100 mTorr (0.1 T) Units	<30 PPM, F.S./ °C
All other ranges	
at 0.05% or 0.08% of Rdg accuracy	<4 PPM, F.S./ °C
at 0.12% of Rdg accuracy	<15 PPM, F.S./ °C
Time Constant with Signal Conditioner in:	
Fast Position	> 25 ms
Std Position	40 ms
Slow Position	400 ms
Useable Resolution	5 decades

Figure H.21.: **Technical data of MKS 690A high accuracy absolute pressure transducer.** Adapted from [MKS09] with permission from MKS Instruments.

Ranges	x1, x0.1, and x0.01 of full range of the pressure transducer
Analog Signal Output	
Voltage available at rear connector	0 to ±10 V on each range (x1, x0.1, x0.01), into >10K ohm load
Impedance	<1 ohm
Temperature Coefficient (x1 range)	
Zero	± 4 ppm of range/° C (without calibration)
Span	±25 ppm of range/° C (without calibration) ±15 ppm of range/° C (with full scale calibration)
Accuracy[1]	
Zero	
x1	± 100 ppm of range F.S.
x0.1	± 100 ppm of range F.S.
x0.01	± 200 ppm of range F.S.
Span	
x1	± 300 ppm of range F.S.
x0.1	± 350 ppm of range F.S.
x0.01	± 800 ppm of range F.S.
Linearity	
0 to +10 Volts	<±25 ppm F.S.
0 to -10 Volts	<±50 ppm F.S.
Noise	
0.01 - 0.4 Hz	< 70 µVolts peak-to-peak, on the x1 and x0.1 ranges < 350 µVolts peak-to-peak, on the x0.01 range
1 kHz - 1 MHz	<4 mV peak-to-peak, on all ranges
Display and Digital Communications	
Accuracy	
Zero	± 50 ppm F.S.
Span	± 200 ppm F.S.
Update Rate	4 times per second (every 0.25 seconds)
Linearity	
0 to 10 Volts	<± 15 ppm of F.S.
0 to -10 Volts	<± 50 ppm of F.S.
Pressure Units	Torr, mmHg, mbar, Pa, kPa, psi, inHg, inH_2O, cmH_2O, % of Full Scale, ppm, mTorr
Temperature Coefficient	
Zero	1 ppm/° C
Span	25 ppm/° C

[1] Includes non-repeatability

Figure H.22.: **Technical data of MKS 670B high accuracy signal conditioner.** Adapted from [MKS98] with permission from MKS Instruments.

Performance Specifications

Accuracy[1]	± 1% F.S.
Control Range (MFC only)	2.0 to 100% F.S.
Controller Settling Time[4] (MFC only)	<2 seconds (to within 2% of set point)
Full Scale Ranges (nitrogen equivalent)	10, 20, 50, 100, 200, 500, 1000, 2000, 5000, 10,000, 20,000, 30,000 sccm
Maximum Inlet Pressure	150 psig
Operational Differential Pressure[5]	
≤5000 sccm	10 to 40 psid
10,000 to 30,000 sccm	15 to 40 psid
Pressure Coefficient	0.02% Rdg./psi
Repeatability (MFC only)	± 0.2% F.S.
Resolution (measurement)	0.1% F.S.
Temperature Coefficients	
Zero	< 0.05% F.S./° C (500 ppm)
Span	<0.08% of Rdg/° C (800 ppm)
Warm up Time (to within 0.2% of steady-state)	2 minutes

[1]Includes non-linearity, hysteresis, and non-repeatability referenced to 760 mmHg and 0° C.

[4]Controller settling time per SEMI E17-91, specified for flows starting from 0 to 10% (or greater) F.S.

[5]Operational differential pressure is referenced to an MFC outlet pressure at atmosphere.

Figure H.23.: **Technical data of MKS 179A mass flowmeter.** Adapted from [MKS99a] with permission from MKS Instruments.

I. Saturation Vapour Pressure Curves

This section contains saturation vapor pressure curves to be used as reference. A listing of temperatures corresponding to decades of pressure are shown in table I.3. A visualization of this data is given in fig. I.24. The data compilation for vapor pressure curves is based on:

- [SW35] for formaldehyde (CH_2O),
- [Gri51] for tritium (T_2),
- [BZ80] for fluorine, xenon, ethylene, and ethane (F_2, Xe, C_2H_4, C_2H_6)
- [Hae81] for hydrogen, deuterium, neon, nitrogen, argon, carbon monoxide, oxygen, methane, krypton, carbon dioxide, and water (H_2, D_2, Ne, N_2, Ar, CO, O_2, CH_4, Kr, CO_2, H_2O)
- [Luc+05] for methanol (C_2H_5OH).

from [SW35; Gri51; BZ80; Hae81; Luc+05] for several gases found in vaccum systems with a focus on cryogenic temperatures. The data presented in tabular form in table I.3 is shown plotted in fig. I.24.

Not all data has been provided over the entire shown pressure range in the cited publications. For the following gases, the low pressure was extrapolated using the provided calculation formulae in each publication:

- The curve for tritium in [Gri51] is only given down to 13.968 K and 2 mbar.
- The curve for formaldehyde in [SW35] is only given down to 154.85 K and 0.467 mbar.
- The curve for formaldehyde in [Luc+05] is only given down to 130 K and 4×10^{-8} mbar.

The data adapted from [Hae81] were taken without modifications for the entire presented pressure range. The calculation formulae in [BZ80] are all stated to be valid for this pressure range.

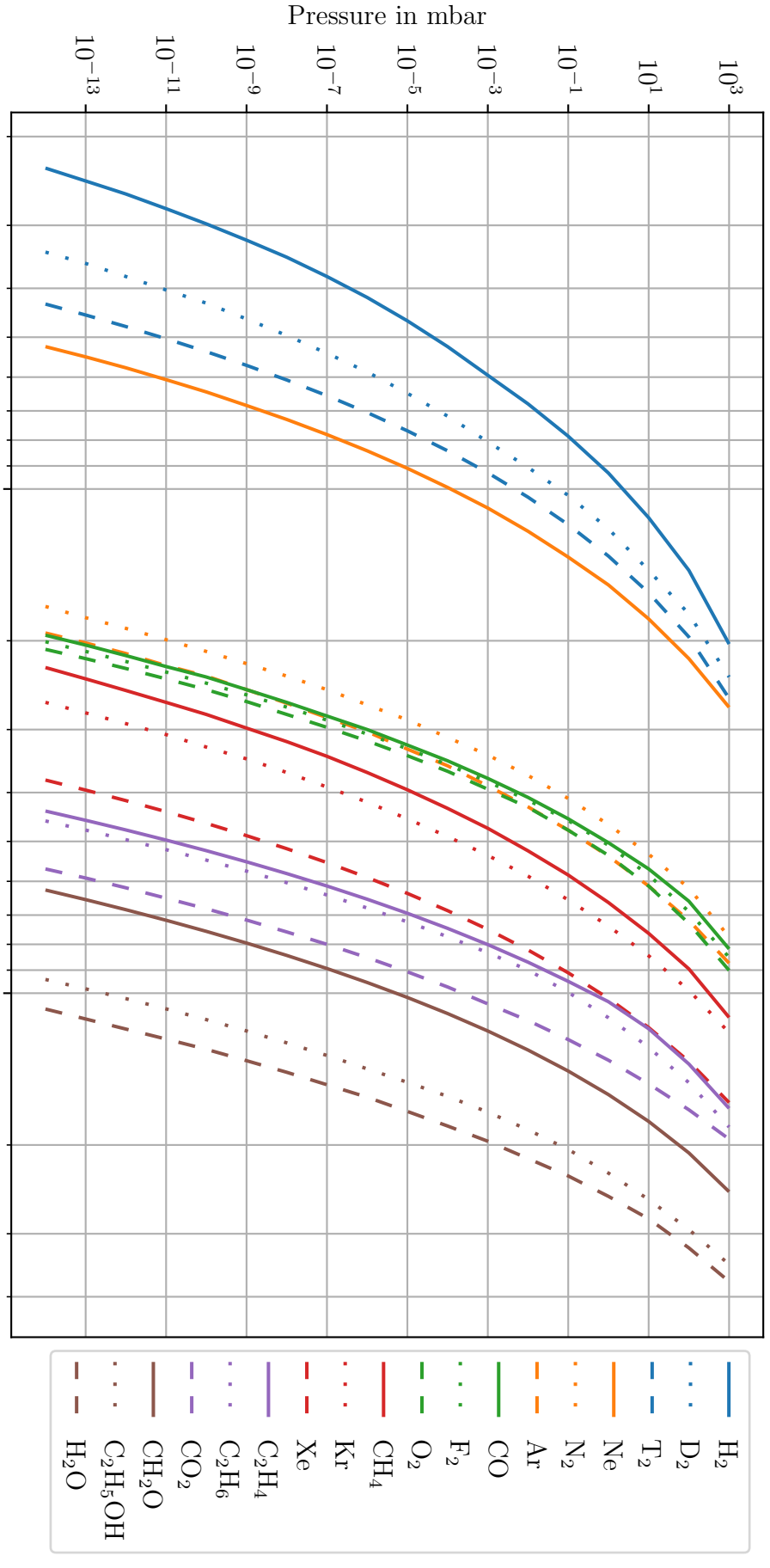

Figure I.24.: **Saturation vapor pressure curves for several gas species.** Based on data from [SW35; Gri51; BZ80; Hae81; Luc+05] shown in table I.3.

Table I.3.: **Saturation vapor pressures in the cryogenic temperature range.** Data adapted from [SW35; Gri51; BZ80; Hae81; Luc+05].

Pressure in mbar	H_2	D_2	T_2	Ne	N_2	Ar	CO	F_2	O_2	CH_4	Kr	Xe	C_2H_4	C_2H_6	CO_2	CH_2O	C_2H_5OH	H_2O
10^{-14}	2.3	3.4	4.3	5.2	17.1	19.3	19.5	20.1	20.8	22.6	26.5	37.8	43.5	45.5	56.7	62.4	93.9	107.5
10^{-13}	2.5	3.6	4.5	5.5	18.0	20.2	20.4	21.0	21.7	23.8	27.8	39.6	45.4	47.5	59.1	65.2	98.0	112.5
10^{-12}	2.6	3.8	4.8	5.8	18.9	21.2	21.4	22.0	22.7	25.1	29.2	41.5	47.5	49.6	61.8	68.3	102.5	117.8
10^{-11}	2.8	4.0	5.0	6.1	19.9	22.4	22.5	23.1	23.8	26.5	30.7	43.7	49.7	51.9	64.8	71.7	107.4	123.3
10^{-10}	3.0	4.3	5.3	6.4	21.0	23.5	23.6	24.3	25.0	28.0	32.5	46.0	52.2	54.5	68.0	75.4	112.8	129.2
10^{-9}	3.2	4.6	5.7	6.8	22.2	25.0	25.0	25.6	26.4	29.8	34.3	48.7	54.9	57.3	71.6	79.5	118.8	136.1
10^{-8}	3.5	5.0	6.1	7.3	23.5	26.6	26.5	27.1	28.0	31.7	36.5	51.7	57.9	60.4	75.6	84.2	125.5	143.5
10^{-7}	3.8	5.4	6.5	7.8	25.0	28.4	28.2	28.7	29.7	33.9	39.0	55.1	61.3	63.9	80.0	89.3	132.9	151.9
10^{-6}	4.2	5.9	7.1	8.4	26.8	30.3	30.0	30.6	31.6	36.5	41.8	58.9	65.1	67.8	85.0	95.2	141.3	160.8
10^{-5}	4.6	6.5	7.7	9.1	28.7	32.8	32.2	32.8	33.8	39.5	45.1	63.4	69.4	72.2	90.7	102.0	150.2	171.6
10^{-4}	5.2	7.2	8.4	9.9	31.1	35.4	34.6	35.2	36.3	43.0	48.9	68.6	74.4	77.3	97.2	109.7	160.2	183.4
10^{-3}	6.0	8.1	9.3	10.9	33.7	38.8	37.5	38.1	39.4	47.1	53.3	74.7	80.1	83.1	105.0	118.8	172.1	196.6
10^{-2}	6.8	9.1	10.4	12.1	37.0	42.7	40.9	41.4	42.8	52.2	58.6	82.1	86.8	90.0	113.3	129.6	186.6	212.8
10^{-1}	7.9	10.3	11.8	13.7	41.1	47.5	45.1	45.5	47.5	58.3	65.3	91.1	94.7	99.6	123.6	142.7	204.1	230.4
1	9.3	12.0	13.6	15.5	46.3	53.5	50.3	50.9	53.3	66.1	73.6	102.4	104.0	111.9	135.8	158.9	227.4	252.9
10^{1}	11.4	14.5	16.1	18.1	53.0	61.3	56.7	58.3	61.3	76.1	84.3	117.0	117.6	128.0	151.3	179.6	256.6	280.2
10^{2}	14.5	17.7	19.7	21.7	61.9	71.7	65.7	68.9	72.7	89.5	98.7	136.5	138.2	150.5	170.3	207.4	294.3	320.0
10^{3}	20.3	23.6	26.0	27.1	77.3	87.2	81.7	84.9	90.1	111.7	119.7	164.8	169.2	184.3	194.7	247.6	345.0	373.1

List of Figures

List of Tables

Bibliography

[Aab+18] M. Aaboud et al. "Measurement of the Higgs boson mass in the $H \to ZZ^* \to 4\ell$ and $H \to \gamma\gamma$ channels with s=13 TeV pp collisions using the ATLAS detector". In: *Physics Letters B* 784 (Sept. 2018), pp. 345–366. DOI: 10.1016/j.physletb.2018.07.050.

[Aad+12] G. Aad et al. "Observation of a new particle in the search for the Standard Model Higgs boson with the ATLAS detector at the LHC". In: *Physics Letters B* 716.1 (Sept. 2012), pp. 1–29. DOI: 10.1016/j.physletb.2012.08.020.

[AAP20] M. A. Acero, A. A. Aguilar-Arevalo, and D. J. Polo-Toledo. "Neutrino Oscillation Analysis of 217 Live Days of Daya Bay and 500 Live Days of RENO". In: *Advances in High Energy Physics* 2020 (Jan. 2020), pp. 1–13. DOI: 10.1155/2020/8526034.

[Abe+11] K. Abe et al. "The T2K experiment". In: *Nuclear Instruments and Methods in Physics Research Section A: Accelerators, Spectrometers, Detectors and Associated Equipment* 659.1 (Dec. 2011), pp. 106–135. DOI: 10.1016/j.nima.2011.06.067.

[Abe+14] Y. Abe et al. "Improved measurements of the neutrino mixing angle θ_{13} with the Double Chooz detector". In: *Journal of High Energy Physics* 2014.10 (Oct. 2014). DOI: 10.1007/jhep10(2014)086.

[Abe+17] K. Abe et al. "Combined Analysis of Neutrino and Antineutrino Oscillations at T2K". In: *Physical Review Letters* 118.15 (Apr. 2017). DOI: 10.1103/physrevlett.118.151801.

[Acq+09] R. Acquafredda et al. "The OPERA experiment in the CERN to Gran Sasso neutrino beam". In: *Journal of Instrumentation* 4.04 (Apr. 2009), P04018–P04018. DOI: 10.1088/1748-0221/4/04/p04018.

[Ada+11] P. Adamson et al. "Improved Search for Muon-Neutrino to Electron-Neutrino Oscillations in MINOS". In: *Physical Review Letters* 107.18 (Oct. 2011). DOI: 10.1103/physrevlett.107.181802.

[Aga+15] N. Agafonova et al. "Discovery of τ Neutrino Appearance in the CNGS Neutrino Beam with the OPERA Experiment". In: *Physical Review Letters* 115.12 (Sept. 2015). DOI: 10.1103/physrevlett.115.121802.

[Ahm+01] Q. R. Ahmad et al. "Measurement of the Rate of $\nu_e + d \to p + p + e^-$ Interactions Produced by ^{8}B Solar Neutrinos at the Sudbury Neutrino Observatory". In: *Physical Review Letters* 87.7 (July 2001). DOI: 10.1103/physrevlett.87.071301.

[Ahn+12] J. K. Ahn et al. "Observation of Reactor Electron Antineutrinos Disappearance in the RENO Experiment". In: *Physical Review Letters* 108.19 (May 2012). DOI: 10.1103/physrevlett.108.191802.

[Ake+19] M. Aker et al. "Improved Upper Limit on the Neutrino Mass from a Direct Kinematic Method by KATRIN". In: *Phys. Rev. Lett.* 123 (22 Nov. 2019), p. 221802. DOI: 10.1103/PhysRevLett.123.221802.

[Ake+20] M. Aker et al. "First operation of the KATRIN experiment with tritium". In: *The European Physical Journal C* 80.3 (Mar. 2020). DOI: 10.1140/epjc/s10052-020-7718-z.

[Ams+15] J. Amsbaugh et al. "Focal-plane detector system for the KATRIN experiment". In: *Nuclear Instruments and Methods in Physics Research Section A: Accelerators, Spectrometers, Detectors and Associated Equipment* 778 (2015), pp. 40–60. DOI: 10.1016/j.nima.2014.12.116.

[AR87] W. D. Arnett and J. L. Rosner. "Neutrino mass limits from SN1987A". In: *Physical Review Letters* 58.18 (May 1987), pp. 1906–1909. DOI: 10.1103/physrevlett.58.1906.

[Are+18] M. Arenz et al. "Calibration of high voltages at the ppm level by the difference of ^{83m}Kr conversion electron lines at the KATRIN experiment". In: *The European Physical Journal C* 78.5 (2018), p. 368. DOI: 10.1140/epjc/s10052-018-5832-y.

[Ase+11] V. N. Aseev et al. "Upper limit on the electron antineutrino mass from the Troitsk experiment". In: *Physical Review D* 84.11 (Dec. 2011). DOI: 10.1103/physrevd.84.112003.

[Ass+96] K. Assamagan et al. "Upper limit of the muon-neutrino mass and charged-pion mass from momentum analysis of a surface muon beam". In: *Physical Review D* 53.11 (June 1996), pp. 6065–6077. DOI: 10.1103/physrevd.53.6065.

[Bab+12] M. Babutzka et al. "Monitoring of the operating parameters of the KATRIN Windowless Gaseous Tritium Source". In: *New Journal of Physics* 14.10 (2012), p. 103046. DOI: 10.1088/1367-2630/14/10/103046.

[Bab14] M. Babutzka. "Design and development for the Rearsection of the KATRIN experiment". PhD thesis. Karlsruher Institut für Technologie (KIT), 2014. DOI: 10.5445/IR/1000045598.

[Bah64a] J. N. Bahcall. "Solar Neutrino Cross Sections and Nuclear Beta Decay". In: *Physical Review* 135.1B (July 1964), B137–B146. DOI: 10.1103/physrev.135.b137.

[Bah64b] J. N. Bahcall. "Solar Neutrinos. I. Theoretical". In: *Physical Review Letters* 12.11 (Mar. 1964), pp. 300–302. DOI: 10.1103/physrevlett.12.300.

[Bah97] J. N. Bahcall. "Gallium solar neutrino experiments: Absorption cross sections, neutrino spectra, and predicted event rates". In: *Physical Review C* 56.6 (Dec. 1997), pp. 3391–3409. DOI: 10.1103/physrevc.56.3391.

[Bar01] B. Barish. "Tau neutrino physics: an introduction". In: *Nuclear Physics B - Proceedings Supplements* 98.1-3 (Apr. 2001), pp. 12–25. DOI: 10.1016/s0920-5632(01)01190-2.

[BDG08] U. Besserer, L. Dörr, and M. Glugla. "Tritium Confinement, Retention, and Releases at the Tritium Laboratory Karlsruhe". In: *Fusion Science and Technology* 54.1 (July 2008), pp. 160–163. DOI: 10.13182/fst08-a1786.

[Beh+17] J. Behrens et al. "A pulsed, mono-energetic and angular-selective UV photo-electron source for the commissioning of the KATRIN experiment". In: *The European Physical Journal C* 77.6 (2017), p. 410. DOI: 10.1140/epjc/s10052-017-4972-9.

[Ber+12] J. Beringer et al. "Review of Particle Physics". In: *Physical Review D* 86.1 (July 2012). DOI: 10.1103/physrevd.86.010001.

[Bet+19] M. Betti et al. "Neutrino physics with the PTOLEMY project: active neutrino properties and the light sterile case". In: *Journal of Cosmology and Astroparticle Physics* 2019.07 (July 2019), pp. 047–047. DOI: 10.1088/1475-7516/2019/07/047.

[Blo+20] F. Block et al. "KATRIN KNM2 Reference ReportSystematic Uncertainty of Column Density / Column Density Times Inelastic Scattering Cross-Section". Mar. 2020.

[Blo21] F. Block. "PhD thesis in preparation, Title pending". (unpublished doctoral dissertation). PhD thesis. Karlsruher Institut für Technologie (KIT), expected 2021.

[BMM13] R. F. Berg, E. F. May, and M. R. Moldover. "Viscosity Ratio Measurements with Capillary Viscometers". In: *Journal of Chemical & Engineering Data* 59.1 (Nov. 2013), pp. 116–124. DOI: 10.1021/je400880n.

[Bor+05a] B. Bornschein et al. "Experimental validation of a method for performance monitoring of the front-end permeators in the TEP system of ITER". In: *Fusion Engineering and Design* 75-79 (Nov. 2005), pp. 645–650. DOI: 10.1016/j.fusengdes.2005.06.038.

[Bor+05b] B. Bornschein et al. "Successful Experimental Verification of the Tokamak Exhaust Processing Concept of ITER with the CAPER Facility". In: *Fusion Science and Technology* 48.1 (Aug. 2005), pp. 11–16. DOI: 10.13182/fst05-a870.

[Bor06] B. Bornschein. "The closed tritium cycle of KATRIN". In: *Progress in Particle and Nuclear Physics* 57.1 (July 2006), pp. 38–48. DOI: 10.1016/j.ppnp.2005.12.004.

[BPB02] U. Besserer, R.-D. Penzhorn, and R. Brandt. "The Behaviour of Zirconium-Cobalt as a Material for Tritium Storage". In: *Fusion Science and Technology* 41.3P2 (May 2002), pp. 793–796. DOI: 10.13182/fst02-a22693.

[BPR15] L. I. Bodine, D. S. Parno, and R. G. H. Robertson. "Assessment of molecular effects on neutrino mass measurements from tritium β decay". In: *Physical Review C* 91.3 (2015), p. 035505. DOI: 10.1103/PhysRevC.91.035505.

[BPT80] G. Beamson, H. Q. Porter, and D. W. Turner. "The collimating and magnifying properties of a superconducting field photoelectron spectrometer". In: *Journal of Physics E: Scientific Instruments* 13.1 (1980), p. 64. DOI: 10.1088/0022-3735/13/1/018.

[Brd+19] V. Brdar et al. "Type I seesaw mechanism as the common origin of neutrino mass, baryon asymmetry, and the electroweak scale". In: *Physical Review D* 100.7 (Oct. 2019). DOI: 10.1103/physrevd.100.075029.

[BS04] S. Bashinsky and U. Seljak. "Signatures of relativistic neutrinos in CMB anisotropy and matter clustering". In: *Physical Review D* 69.8 (Apr. 2004). DOI: 10.1103/physrevd.69.083002.

[BTL97] J. Bentz, R. Tompson, and S. Loyalka. "The spinning rotor gauge: measurements of viscosity, velocity slip coefficients, and tangential momentum accommodation coefficients for N2 and CH4". In: *Vacuum* 48.10 (Oct. 1997), pp. 817–824. DOI: 10.1016/s0042-207x(97)00031-6.

[BZ80] G. N. Brown and W. T. Ziegler. "Vapor Pressure and Heats of Vaporization and Sublimation of Liquids and Solids of Interest in Cryogenics below 1-atm Pressure". In: *Advances in Cryogenic Engineering*. Springer US, 1980, pp. 662–670. DOI: 10.1007/978-1-4613-9856-1_76.

[CH19] S. R. Choudhury and S. Hannestad. "Updated results on neutrino mass and mass hierarchy from cosmology with Planck 2018 likelihoods". In: (July 2019). arXiv: 1907.12598v2 [astro-ph.CO].

[Cha+12] S. Chatrchyan et al. "Observation of a new boson at a mass of 125 GeV with the CMS experiment at the LHC". In: *Physics Letters B* 716.1 (Sept. 2012), pp. 30–61. DOI: 10.1016/j.physletb.2012.08.021.

[Cha14] J. Chadwick. "Verh. d Deutschen Phys". In: *Ges* 16 (1914), p. 383.

[Cho16] S. Choubey. "Atmospheric neutrinos: Status and prospects". In: *Nuclear Physics B* 908 (July 2016), pp. 235–249. DOI: 10.1016/j.nuclphysb.2016.03.026.

[Coc19] A. G. Cocco. "COSMOLOGICAL RELIC NEUTRINO DETECTION WITH THE PTOLEMY EXPERIMENT". In: *Particle Physics at the Silver Jubilee of Lomonosov Conferences*. WORLD SCIENTIFIC, June 2019. DOI: 10.1142/9789811202339_0019.

[Com20] W. Commons. *File:Standard Model of Elementary Particles.svg — Wikimedia Commons, the free media repository*. [Online; accessed 11-May-2020]. 2020. URL: https://commons.wikimedia.org/w/index.php?title=File:Standard_Model_of_Elementary_Particles.svg&oldid=416441632.

[Cow+56] C. L. Cowan et al. "Detection of the Free Neutrino: a Confirmation". In: *Science* 124.3212 (1956), pp. 103–104. ISSN: 0036-8075. DOI: 10.1126/science.124.3212.103.

[Cyb+16] R. H. Cyburt et al. "Big bang nucleosynthesis: Present status". In: *Reviews of Modern Physics* 88.1 (Feb. 2016). DOI: 10.1103/revmodphys.88.015004.

[Dan+62] G. Danby et al. "Observation of High-Energy Neutrino Reactions and the Existence of Two Kinds of Neutrinos". In: *Physical Review Letters* 9.1 (July 1962), pp. 36–44. DOI: 10.1103/physrevlett.9.36.

[Day07] Daya Bay Collaboration. "A Precision Measurement of the Neutrino Mixing Angle θ_{13} using Reactor Antineutrinos at Daya Bay". In: (Jan. 2007). arXiv: hep-ex/0701029v1 [hep-ex].

[Dem+15] D. Demange et al. “CAPER as Central and Crucial Facility to Support R&D with Tritium at TLK”. In: *Fusion Science and Technology* 67.2 (Mar. 2015), pp. 308–311. DOI: 10.13182/fst14-t17.

[DHH68] R. Davis, D. S. Harmer, and K. C. Hoffman. “Search for Neutrinos from the Sun”. In: *Physical Review Letters* 20.21 (May 1968), pp. 1205–1209. DOI: 10.1103/physrevlett.20.1205.

[DM53] L. M. Dorfman and H. C. Mattraw. “The Exchange Reaction of Hydrogen and Tritium”. In: *The Journal of Physical Chemistry* 57.7 (July 1953), pp. 723–725. DOI: 10.1021/j150508a029.

[Doe+02] L. Doerr et al. “Upgrade of the Isotope Separation System at the Tritium Laboratory Karlsruhe”. In: *Fusion Science and Technology* 41.3P2 (May 2002), pp. 1155–1159. DOI: 10.13182/fst02-a22765.

[Dör+05] L. Dörr et al. “The Closed Tritium Cycle of the Tritium Laboratory Karlsruhe”. In: *Fusion Science and Technology* 48.1 (Aug. 2005), pp. 262–267. DOI: 10.13182/fst05-a924.

[Dre+17] M. Drewes et al. “A White Paper on keV Sterile Neutrino Dark Matter”. In: *Journal of Cosmology and Astroparticle Physics* 1701.01 (2017), p. 025. DOI: 10.1088/1475-7516/2017/01/025.

[Dyb19] S. Dyba. “Background reduction by the inner wire electrode and set-up of the condensed krypton source at the neutrino mass experiment KATRIN”. PhD thesis. Westfälische Wilhelms-Universität Münster, 2019.

[Egu+03] K. Eguchi et al. “First Results from KamLAND: Evidence for Reactor Antineutrino Disappearance”. In: *Physical Review Letters* 90.2 (Jan. 2003). DOI: 10.1103/physrevlett.90.021802.

[Eid+04] S. Eidelman et al. “Review of Particle Physics”. In: *Physics Letters B* 592.1-4 (July 2004), pp. 1–5. DOI: 10.1016/j.physletb.2004.06.001.

[Eli+15] S. Eliseev et al. “Direct Measurement of the Mass Difference of ^{163}Ho and ^{163}Dy Solves the Q-Value Puzzle for the Neutrino Mass Determination”. In: *Physical Review Letters* 115.6 (Aug. 2015). DOI: 10.1103/physrevlett.115.062501.

[Ell+17] E. Ellinger et al. “Monitoring the KATRIN source properties within the beamline”. In: *J. Phys. Conf. Ser.* 888.1 (2017), p. 012229. DOI: 10.1088/1742-6596/888/1/012229.

[Ell19] E. Ellinger. “Development and investigation of the Forward Beam Monitor for the KATRIN experiment”. PhD thesis. Wuppertal U., 2019. DOI: 10.25926/r160-7a40.

[Esf+17] A. A. Esfahani et al. “Determining the neutrino mass with cyclotron radiation emission spectroscopy Project 8”. In: *Journal of Physics G: Nuclear and Particle Physics* 44.5 (Mar. 2017), p. 054004. DOI: 10.1088/1361-6471/aa5b4f.

[Est+19] I. Esteban et al. “Global analysis of three-flavour neutrino oscillations: synergies and tensions in the determination of θ_{23}, δ_{CP}, and the mass ordering”. In: *Journal of High Energy Physics* 2019.1 (Jan. 2019). DOI: 10.1007/jhep01(2019)106.

[Fav+16] M. Faverzani et al. “The HOLMES Experiment”. In: *Journal of Low Temperature Physics* 184.3-4 (Feb. 2016), pp. 922–929. DOI: 10.1007/s10909-016-1540-x.

[Fer34] E. Fermi. “Versuch einer Theorie der β-Strahlen. I”. In: *Zeitschrift für Physik* 88.3-4 (Mar. 1934), pp. 161–177. DOI: 10.1007/bf01351864.

[Fis+11] S. Fischer et al. “Monitoring of tritium purity during long-term circulation in the KATRIN test experiment LOOPINO using laser Raman spectroscopy”. In: *Fusion Science and Technology* 60.3 (2011), pp. 925–930. URL: http://www.ans.org/pubs/journals/fst/a_12567.

[Fri+19] F. Friedel et al. “Time-dependent simulation of the flow reduction of D_2 and T_2 in the KATRIN experiment”. In: *Vacuum* 159 (2019), pp. 161–172. ISSN: 0042-207X. DOI: 10.1016/j.vacuum.2018.10.002.

[Fuk+98] Y. Fukuda et al. “Evidence for Oscillation of Atmospheric Neutrinos”. In: *Physical Review Letters* 81.8 (Aug. 1998), pp. 1562–1567. DOI: 10.1103/physrevlett.81.1562.

[Ful18] A. Fulst. “The Condensed Krypton Source (Ckrs) As Calibration Tool For Katrin”. In: (2018). DOI: 10.5281/ZENODO.1300532.

[Gan+16] A. Gando et al. “Search for Majorana Neutrinos Near the Inverted Mass Hierarchy Region with KamLAND-Zen”. In: *Physical Review Letters* 117.8 (Aug. 2016). DOI: 10.1103/physrevlett.117.082503.

[Gas+14] L. Gastaldo et al. “The Electron Capture ^{163}Ho Experiment ECHo”. In: *Journal of Low Temperature Physics* 176.5-6 (May 2014), pp. 876–884. DOI: 10.1007/s10909-014-1187-4.

[GGS58] M. Goldhaber, L. Grodzins, and A. W. Sunyar. “Helicity of Neutrinos”. In: *Physical Review* 109.3 (Feb. 1958), pp. 1015–1017. DOI: 10.1103/physrev.109.1015.

[Gil+10] W. Gil et al. “The Cryogenic Pumping Section of the KATRIN Experiment”. In: *IEEE Transactions on Applied Superconductivity* 20.3 (2010), pp. 316–319. DOI: 10.1109/TASC.2009.2038581.

[Gil80] J. T. Gill. “Effect of container preparation on the growth of protium and methane impurities into tritium gas”. In: *Journal of Vacuum Science and Technology* 17.2 (Mar. 1980), pp. 645–654. DOI: 10.1116/1.570532.

[Gin76] J. Gindler. “The half-lives of 83Rb and 84Rb”. In: *Inorganic and Nuclear Chemistry Letters* 12.12 (Jan. 1976), pp. 931–935. DOI: 10.1016/0020-1650(76)80011-6.

[Glü19] F. Glück. “Internal report: Theoretical total inelastic cross section.” 2019.

[GME83] J. T. Gill, W. E. Moddeman, and R. E. Ellefson. “Chemically polished stainless steel tubing for tritium service”. In: *Journal of Vacuum Science & Technology A: Vacuum, Surfaces, and Films* 1.2 (Apr. 1983), pp. 869–873. DOI: 10.1116/1.572012.

[Got70] R. Goto. “Hyperpure hydrogen from palladium alloy membrane permeation”. In: *Chem. Econ. Eng. Rev.* 2:11 (Jan. 1970).

[Gri51] E. R. Grilly. “The Vapor Pressures of Hydrogen, Deuterium and Tritium up to Three Atmospheres1”. In: *Journal of the American Chemical Society* 73.2 (Feb. 1951), pp. 843–846. DOI: 10.1021/ja01146a103.

[Gro+08] S. Grohmann et al. “Cryogenic Design of the KATRIN Source Cryostat”. In: *AIP Conference Proceedings* 985 (2008), pp. 1277–1284. DOI: 10.1063/1.2908483.

[Gro+11] S. Grohmann et al. “Precise temperature measurement at 30 K in the KATRIN source cryostat”. In: *Cryogenics* 51.8 (2011), pp. 438–445. DOI: 10.1016/j.cryogenics.2011.05.001.

[Hae81] R. A. Haefer. *Kryo-Vakuumtechnik*. Springer Berlin Heidelberg, 1981. DOI: 10.1007/978-3-642-49985-2.

[HAG53] D. R. Hamilton, W. P. Alford, and L. Gross. “Upper Limits on the Neutrino Mass from the Tritium Beta Spectrum”. In: *Physical Review* 92.6 (Dec. 1953), pp. 1521–1525. DOI: 10.1103/physrev.92.1521.

[HAS81] M. J. Henchman, N. G. Adams, and D. Smith. “The isotope exchange reactions $H^+ + D_2 \rightleftarrows HD + D^+$ and $D^+ + H_2 \rightleftarrows HD + H^+$ in the temperature range 200–300 K”. In: *The Journal of Chemical Physics* 75.3 (Aug. 1981), pp. 1201–1206. DOI: 10.1063/1.442168.

[Hau19] N. Haußmann. “Simulation and measurement of the Forward Beam Monitor detector signal for the KATRIN experiment”. en. PhD thesis. Wuppertal U., 2019. DOI: 10.25926/8Q1Y-6752.

[Hei19] F. Heizmann. “Analysis tools and methods for tritium data taking with the KATRIN experiment”. en. In: (2019). DOI: 10.5445/IR/1000093536.

[Hig64] P. W. Higgs. “Broken Symmetries and the Masses of Gauge Bosons”. In: *Physical Review Letters* 13.16 (Oct. 1964), pp. 508–509. DOI: 10.1103/physrevlett.13.508.

[Hir+87] K. Hirata et al. “Observation of a neutrino burst from the supernova SN1987A”. In: *Physical Review Letters* 58.14 (Apr. 1987), pp. 1490–1493. DOI: 10.1103/physrevlett.58.1490.

[Hub20] A. Huber. “Analysis of first KATRIN data and searches for keV-scale sterile neutrinos”. (unpublished doctoral dissertation). PhD thesis. Karlsruher Institut für Technologie (KIT), 2020.

[HW91] E. Hairer and G. Wanner. *Solving Ordinary Differential Equations II*. Springer Berlin Heidelberg, 1991. DOI: 10.1007/978-3-662-09947-6.

[Jou04] K. Jousten, ed. *Wutz Handbuch Vakuumtechnik*. Vieweg+Teubner Verlag, 2004. DOI: 10.1007/978-3-322-96971-2.

[Kar19] Karlsruhe Institute of Technology (KIT). *New Results for the Mass of Neutrinos. Press Release 119/2019*. Sept. 2019. URL: http://www.kit.edu/kit/english/pi_2019_119_new-results-for-the-mass-of-neutrinos.php?fbclid=IwAR2N70g-y1oswUmC-SmnKfNHzUFOUvWmND49xTHY-TpTVQU7oTzIVy5ljDA (visited on 09/17/2019).

[KAT05] KATRIN collaboration. *KATRIN Design Report*. FZKA scientific report 7090. 2005. DOI: 10.5445/IR/270060419.

[KD19] V. Kotu and B. Deshpande. "Data Exploration". In: *Data Science*. Elsevier, 2019, pp. 39–64. DOI: 10.1016/b978-0-12-814761-0.00003-4.

[KG17] M. Klein and F. Glück. "Tritium ion blocking and detection in the KATRIN experiment". In: *Journal of Physics: Conference Series* 888.1 (2017), p. 012073. DOI: 10.1088/1742-6596/888/1/012073.

[Kle+19] M. Kleesiek et al. "β -Decay spectrum, response function and statistical model for neutrino mass measurements with the KATRIN experiment". In: *The European Physical Journal C* 79.3 (Mar. 2019). DOI: 10.1140/epjc/s10052-019-6686-7.

[Kod+01] K. Kodama et al. "Observation of tau neutrino interactions". In: *Physics Letters B* 504.3 (2001), pp. 218–224. ISSN: 0370-2693. DOI: 10.1016/S0370-2693(01)00307-0.

[Kra+05] C. Kraus et al. "Final results from phase II of the Mainz neutrino mass searchin tritium β-decay". In: *The European Physical Journal C* 40.4 (Apr. 2005), pp. 447–468. DOI: 10.1140/epjc/s2005-02139-7.

[Kuc+18] L. Kuckert et al. "Modelling of gas dynamical properties of the KATRIN tritium source and implications for the neutrino mass measurement". In: *Vacuum* 158 (2018), pp. 195–205. DOI: 10.1016/j.vacuum.2018.09.036.

[Las06] M. G. T. Lasserre. "Double Chooz, A Search for the Neutrino Mixing Angle θ_{13}". In: (June 2006). arXiv: hep-ex/0606025v4 [hep-ex].

[Lin+20] Y.-T. Lin et al. "Beta decay of molecular tritium". In: (Jan. 2020). arXiv: 2001.11671v2 [nucl-ex].

[LL02] T. J. Loredo and D. Q. Lamb. "Bayesian analysis of neutrinos observed from supernova SN 1987A". In: *Physical Review D* 65.6 (Feb. 2002). DOI: 10.1103/physrevd.65.063002.

[LLS14] A. J. Long, C. Lunardini, and E. Sabancilar. "Detecting non-relativistic cosmic neutrinos by capture on tritium: phenomenology and physics potential". In: *Journal of Cosmology and Astroparticle Physics* 2014.08 (Aug. 2014), pp. 038–038. DOI: 10.1088/1475-7516/2014/08/038.

[LM52] L. M. Langer and R. J. D. Moffat. "The Beta-Spectrum of Tritium and the Mass of the Neutrino". In: *Physical Review* 88.4 (Nov. 1952), pp. 689–694. DOI: 10.1103/physrev.88.689.

[LS85] V. M. Lobashev and P. E. Spivak. "A method for measuring the electron antineutrino rest mass". In: *Nuclear Instruments and Methods in Physics Research Section A: Accelerators, Spectrometers, Detectors and Associated Equipment* 240.2 (1985), pp. 305–310. DOI: 10.1016/0168-9002(85)90640-0.

[LU00] L. Lucas and M. Unterweger. "Comprehensive review and critical evaluation of the half-life of tritium". In: *Journal of Research of the National Institute of Standards and Technology* 105.4 (July 2000), p. 541. DOI: 10.6028/jres.105.043.

[Lub+80] V. Lubimov et al. "An estimate of the ν_e mass from the β-spectrum of tritium in the valine molecule". In: *Physics Letters B* 94.2 (July 1980), pp. 266–268. DOI: 10.1016/0370-2693(80)90873-4.

[Luc+05] S. Lucas et al. “Vapor Pressure and Solid Phases of Methanol below Its Triple Point Temperature”. In: *The Journal of Physical Chemistry B* 109.38 (Sept. 2005), pp. 18103–18106. DOI: 10.1021/jp053313v.

[Mac20] M. Machatschek. “A Phenomenological Theory of KATRIN Source Potential Systematics and its Application in Krypton-83m Calibration Measurements”. (unpublished doctoral dissertation). PhD thesis. Karlsruher Institut für Technologie (KIT), expected 2020.

[McC15] E. McCutchan. “Nuclear Data Sheets for A = 83”. In: *Nuclear Data Sheets* 125 (Mar. 2015), pp. 201–394. DOI: 10.1016/j.nds.2015.02.002.

[Mer+13] S. Mertens et al. “Background due to stored electrons following nuclear decays in the KATRIN spectrometers and its impact on the neutrino mass sensitivity”. In: *Astroparticle Physics* 41 (2013), pp. 52–62. DOI: 10.1016/j.astropartphys.2012.10.005.

[MKS09] MKS Instruments. *MKS Type 690A Absolute andType 698A Differential High Accuracy Pressure Transducers*. Version Rev F, 4/09. Jan. 1, 2009.

[MKS98] MKS Instruments. *MKS Type 670B High AccuracySignal Conditioner Instruction Manual*. Version Rev B, 1/98. Jan. 1, 1998.

[MKS99a] MKS Instruments. *MKS Type 1179A and 2179AMass-Flo® Controllerand-Type 179A Mass-Flo Meter*. Version Rev A, 1/99. Jan. 1, 1999.

[MKS99b] MKS Instruments. *MKS Type 148J Pressure and Flow Control Valve*. Version Rev E, 3/99. Jan. 1, 1999.

[MNS62] Z. Maki, M. Nakagawa, and S. Sakata. “Remarks on the Unified Model of Elementary Particles”. In: *Progress of Theoretical Physics* 28.5 (Nov. 1962), pp. 870–880. DOI: 10.1143/ptp.28.870.

[Moh+07] R. N. Mohapatra et al. “Theory of neutrinos: a white paper”. In: *Reports on Progress in Physics* 70.11 (Oct. 2007), pp. 1757–1867. DOI: 10.1088/0034-4885/70/11/r02.

[Mor77] G. A. Morris. “Methane growth in tritium gas exposed to stainless steel”. In: (Mar. 1977).

[Mün19] G. Münster. *Von der Quantenfeldtheorie zum Standardmodell*. De Gruyter, Aug. 2019. DOI: 10.1515/9783110638547.

[Mye+15] E. G. Myers et al. “Atomic Masses of Tritium and Helium-3”. In: *Physical Review Letters* 114.1 (Jan. 2015). DOI: 10.1103/physrevlett.114.013003.

[OW08] E. W. Otten and C. Weinheimer. “Neutrino mass limit from tritium β decay”. In: *Reports on Progress in Physics* 71.8 (2008), p. 086201. DOI: 10.1088/0034-4885/71/8/086201.

[Pan03] N. Panagia. “A Geometric Determination of the Distance to SN 1987A and the LMC”. In: (Sept. 2003). arXiv: astro-ph/0309416v1 [astro-ph].

[Pau30] W. Pauli. “Offener brief an die gruppe der radioaktiven bei der gauvereinstagung zu Tübingen”. In: *Open letter to the group of radioactive people at the Gauverein meeting in Tübingen*. 1930.

[PB13] F. Priester and B. Bornschein. "TriToP – A compatibility experiment with turbomolecular pumps under tritium atmosphere". In: *Vacuum* 98 (Dec. 2013), pp. 22–28. DOI: 10.1016/j.vacuum.2012.09.006.

[Pee73] P. J. E. Peebles. "The Role of Neutrinos in the Evolution of Primeval Adiabatic Perturbations". In: *The Astrophysical Journal* 180 (Feb. 1973), p. 1. DOI: 10.1086/151936.

[Pet20] W. C. Pettus. "Overview of Project 8 and Progress Towards Tritium Operation". In: *Journal of Physics: Conference Series* 1342 (Jan. 2020), p. 012040. DOI: 10.1088/1742-6596/1342/1/012040.

[Pic+92] A. Picard et al. "A solenoid retarding spectrometer with high resolution and transmission for keV electrons". In: *Nuclear Instruments and Methods in Physics Research Section B: Beam Interactions with Materials and Atoms* 63.3 (1992), pp. 345–358. DOI: 10.1016/0168-583X(92)95119-C.

[PM68] J. R. Penton and E. E. Muschlitz. "Ionization of Hydrogen, Hydrogen Deuteride, and Deuterium on Impact of Metastable Helium Atoms". In: *The Journal of Chemical Physics* 49.11 (Dec. 1968), pp. 5083–5088. DOI: 10.1063/1.1670002.

[Pon58] B. Pontecorvo. "Mesonium and antimesonium". In: *Soviet Phys. JETP* 6 (1958).

[Pon68] B. Pontecorvo. "Neutrino experiments and the problem of conservation of leptonic charge". In: *Sov. Phys. JETP* 26.984-988 (1968), p. 165.

[Pri+20] F. Priester et al. "Tritium Processing Systems and First Tritium Operation of the KATRIN Experiment". In: *Fusion Science and Technology* (May 2020), pp. 1–5. DOI: 10.1080/15361055.2020.1730118.

[Pri13] F. Priester. "Tritiumtechnologie für die fensterlose Quelle WGTS von KATRIN". German. PhD thesis. Karlsruher Institut für Technologie (KIT), 2013. DOI: 10.5445/IR/1000035699.

[PSB15] F. Priester, M. Sturm, and B. Bornschein. "Commissioning and detailed results of KATRIN inner loop tritium processing system at Tritium Laboratory Karlsruhe". In: *Vacuum* 116 (June 2015), pp. 42–47. DOI: 10.1016/j.vacuum.2015.02.030.

[RA10] RENO Collaboration and J. K. Ahn. "RENO: An Experiment for Neutrino Oscillation Parameter θ_{13} Using Reactor Neutrinos at Yonggwang". In: (Mar. 2010). arXiv: 1003.1391v1 [hep-ex].

[RC53] F. Reines and C. L. Cowan. "Detection of the Free Neutrino". In: *Physical Review* 92 (3 1953), pp. 830–831. DOI: 10.1103/PhysRev.92.830.

[Res+19] O. Rest et al. "A novel ppm-precise absolute calibration method for precision high-voltage dividers". In: *Metrologia* 56.4 (July 2019), p. 045007. DOI: 10.1088/1681-7575/ab2997.

[Rob+91] R. G. H. Robertson et al. "Limit on ν_e mass from observation of the β decay of molecular tritium". In: *Physical Review Letters* 67.8 (Aug. 1991), pp. 957–960. DOI: 10.1103/physrevlett.67.957.

[Rod21] C. Rodenbeck. "Investigation of inelastic scattering of beta electrons in KATRIN's gaseous tritium source using time of flight methods to determine the neutrino mass". (unpublished doctoral dissertation). PhD thesis. Institut für Kernphysik, Westfälische Wilhelms-Universität Münster, expected 2021.

[Röl15] M. Röllig. "Tritium analytics by beta induced X-ray spectrometry". PhD thesis. Karlsruher Institut für Technologie (KIT), 2015. DOI: 10.5445/IR/1000054050.

[Röt17] C. Röttele. "Results of the first Cool-down of the KATRIN Cryogenic Pumping Section". In: *Journal of Physics: Conference Series* 888.1 (2017), p. 012228. DOI: 10.1088/1742-6596/888/1/012228.

[Röt19] C. Röttele. "Tritium suppression factor of the KATRIN transport section". en. PhD thesis. Karlsruher Institut für Technologie (KIT), 2019. DOI: 10.5445/IR/1000096733.

[Sac20] R. Sack. "Measurement of the energy loss of 18.6 keV electrons on deuterium gas and determination of the tritium Q-value at the KATRIN experiment". (unpublished doctoral dissertation). PhD thesis. University of Münster, expected 2020.

[Sch+13] M. Schlösser et al. "Accurate calibration of the laser Raman system for the Karlsruhe Tritium Neutrino Experiment". In: *Journal of Molecular Structure* 1044.0 (2013), pp. 61–66. DOI: 10.1016/j.molstruc.2012.11.022.

[Sch+91] P. Schira et al. "The Tritium Laboratory Karlsruhe: Laboratory design and equipment". In: *Fusion Engineering and Design* 18 (Dec. 1991), pp. 19–26. DOI: 10.1016/0920-3796(91)90101-u.

[Sch20] L. Schimpf. "Characterization of energy loss processes of 18.6 keV electrons inside the windowless tritium source of KATRIN". (unpublished doctoral dissertation). PhD thesis. Karlsruher Institut für Technologie (KIT), expected 2020.

[Sei19] H. Seitz-Moskaliuk. "Characterisation of the KATRIN tritium source and evaluation of systematic effects". PhD thesis. Karlsruher Institut für Technologie (KIT), 2019. DOI: 10.5445/IR/1000090748.

[Sen+18] J. Sentkerestiová et al. "Gaseous ^{83m}Kr generator for KATRIN". In: *Journal of Instrumentation* 13.04 (2018), P04018. DOI: 10.1088/1748-0221/13/04/P04018.

[Sha10] F. Sharipov. *Tritium flow through a non-symmetrical source. Simulation of gas flow through an injection hole*. Tech. rep. Departamento de Fısica, Universidade Federal do Parana, Sept. 2010. URL: http://fisica.ufpr.br/sharipov/KATRIN/report6.pdf (visited on 03/16/2020).

[Sha16] F. Sharipov. *Rarefied Gas Dynamics*. Wiley-VCH Verlag GmbH & Co. KGaA, Jan. 2016. DOI: 10.1002/9783527685523.

[Sha96] F. Sharipov. "Rarefied gas flow through a long tube at any temperature ratio". In: *Journal of Vacuum Science & Technology A: Vacuum, Surfaces, and Films* 14.4 (July 1996), pp. 2627–2635. DOI: 10.1116/1.579991.

[Sib19] V. Sibille. "First tritium results of the KATRIN analysis". In: *Proceedings of Neutrino Oscillation Workshop — PoS(NOW2018)*. Sissa Medialab, Apr. 2019. DOI: 10.22323/1.337.0072.

[SJF00] A. Saenz, S. Jonsell, and P. Froelich. "Improved Molecular Final-State Distribution of HeT^+ for the β-Decay Process of T^2". In: *Physical Review Letters* 84.2 (Jan. 2000), pp. 242–245. DOI: 10.1103/physrevlett.84.242.

[Stu20] M. Sturm. "Investigation of WGTS and RW chamber outgassing". Tech. rep. Jan. 15, 2020.

[SW35] R. Spence and W. Wild. "114. The vapour-pressure curve of formaldehyde, and some related data". In: *Journal of the Chemical Society (Resumed)* (1935), p. 506. DOI: 10.1039/jr9350000506.

[Tan+18] M. Tanabashi et al. "Review of Particle Physics". In: *Physical Review D* 98.3 (Aug. 2018). DOI: 10.1103/physrevd.98.030001.

[TK79] S. Tanaka and R. Kiyose. "Isotope Separation of Hydrogen and Deuterium by Permeation through Palladium Membrane". In: *Journal of Nuclear Science and Technology* 16.12 (Dec. 1979), pp. 923–925. DOI: 10.1080/18811248.1979.9730997.

[TM05] R. Trotta and A. Melchiorri. "Indication for Primordial Anisotropies in the Neutrino Background from the Wilkinson Microwave Anisotropy Probe and the Sloan Digital Sky Survey". In: *Physical Review Letters* 95.1 (June 2005). DOI: 10.1103/physrevlett.95.011305.

[Van10] G. VanRossum. *The Python language reference*. Hampton, NHRedwood City, Calif: Python Software FoundationSoHo Books, 2010. ISBN: 9781441412690.

[Vén+05] D. Vénos et al. "^{83m}Kr radioactive source based on ^{83}Rb trapped in cation-exchange paper or in zeolite". In: *Applied Radiation and Isotopes* 63.3 (2005), pp. 323–327. DOI: 10.1016/j.apradiso.2005.04.011.

[VEŠ12] J. D. Vergados, H. Ejiri, and F. Šimkovic. "Theory of neutrinoless double-beta decay". In: *Reports on Progress in Physics* 75.10 (Sept. 2012), p. 106301. DOI: 10.1088/0034-4885/75/10/106301.

[Vir+20] P. Virtanen et al. "SciPy 1.0: fundamental algorithms for scientific computing in Python". In: *Nature Methods* 17.3 (Feb. 2020), pp. 261–272. DOI: 10.1038/s41592-019-0686-2.

[WA03] K. Winter and G. Altarelli, eds. *Neutrino Mass*. Springer Berlin Heidelberg, 2003. DOI: 10.1007/b13585.

[Wel+15] S. Welte et al. "Tritium Laboratory Karlsruhe: Administrative and Technical Framework for Isotope Laboratory Operation". In: *Fusion Science and Technology* 67.3 (Apr. 2015), pp. 635–638. DOI: 10.13182/fst14-t98.

[Wel+17] S. Welte et al. "Experimental Performance Test of Key Components of the KATRIN Outer Tritium Loop". In: *Fusion Science and Technology* 71.3 (Mar. 2017), pp. 316–320. DOI: 10.1080/15361055.2017.1291233.

[Wel+20] S. Welte et al. "Tritium Supply and Processing for the First KATRIN Tritium Operation". In: *Fusion Science and Technology* (Mar. 2020), pp. 1–5. DOI: 10.1080/15361055.2019.1705681.

[Wil50] C. R. Wilke. “A Viscosity Equation for Gas Mixtures”. In: *The Journal of Chemical Physics* 18.4 (Apr. 1950), pp. 517–519. DOI: 10.1063/1.1747673.

[WO15] R. Wendell and K. Okumura. “Recent progress and future prospects with atmospheric neutrinos”. In: *New Journal of Physics* 17.2 (Feb. 2015), p. 025006. DOI: 10.1088/1367-2630/17/2/025006.

[Wu+57] C. S. Wu et al. “Experimental Test of Parity Conservation in Beta Decay”. In: *Physical Review* 105 (1957), pp. 1413–1414. DOI: 10.1103/PhysRev.105.1413.

[Zub20] K. Zuber. *Neutrino Physics*. CRC Press, May 2020. DOI: 10.1201/9781315195612.

Symbols

a	Characteristic length scale of a vacuum system
A	Mass number
A	Area
A	Activity
AU	Astronomical unit
A_{WGTS}	Cross sectional area of the WGTS
$A_{\alpha\to\beta}$	Transition amplitude from state α to state β
α	Index variable used for flavor states
α_j	Majorana phase of the PMNS matrix
$\vec{B}$	Magnetic field strength
B	Absolute value of the magnetic field strength
B_{max}	Maximal magnetic field strength of a MAC-E filter
B_{min}	Minimal magnetic field strength of a MAC-E filter
β	Index variable used for flavor states
β^-	Particle released in β^--decay (electron)
β^+	Particle released in β^+-decay (positron)
c	Speed of light in vacuum
c	Concentration
C	Conductance of a vacuum system
d	Diameter
d	Total differential
∂	Partial differential
δ	Rarefaction parameter
δ_{CP}	CP violating phase of the PMNS matrix
δ_{ij}	Kronecker delta
e	Euler's number
e^-	Electron
e^+	Positron
E	Energy

E_{rec}	Recoil energy of a nucleus in β-decay
E_0	Endpoint of an β-spectrum with a massless neutrino
ε_{T}	Tritium purity
$\varepsilon_{\mathrm{FPD}}$	Focal plane detector efficiency
$f(t, \boldsymbol{r}, \boldsymbol{v})$	Velocity distribution function
F	Fermi function
$\vec{F}$	Force
G	Two-body phase-space factor
G_{F}	Fermi coupling constant
G_{P}	Poiseuille coefficient
G_{T}	Thermal creep coefficient
γ	photon
γ	Realtivistic Lorentz factor
Γ	Decay rate
$\mathcal{H}$	Hamiltonian
$\hbar$	Reduced Planck constant
i	Index variable
i	Imaginary unit
j	Index variable
k	Index variable
k_{B}	Boltzmann constant
l	Index variable
ℓ	Effective mean free path length
L	Length
$\mathcal{L}$	Lagrangian
$\mathcal{L}_{\mathcal{D}}$	Lagrangian Dirac mass term
$\mathcal{L}_{\mathcal{M}}$	Lagrangian Majorana mass term
λ	Decay constant
m	Mass
m_{e}	Rest mass of the electron
m_ν	Neutrino rest mass
m_i	i-th neutrino mass eigenstate
$m_{\beta\beta}$	Effective neutrino mass in neutrinoless double β-decay

m_D	Dirac mass of the neutrino
m_R	Majorana mass of the neutrino
Δm_{ij}^2	Difference of squared masses of neutrino mass eigenstates m_i and m_j
μ^-	Muon
μ^+	Antimuon
$\vec{\mu}$	Magnetic moment vector
μ	Magnetic moment
μ	Dynamic viscosity
M_{nuc}	Nuclear matrix element of β-decay
M	Molar mass
$\dot{M}$	Mass flow rate
ν	Neutrino
$\bar{\nu}$	Antineutrino
ν_e	Electron neutrino
$\bar{\nu}_e$	Electron antineutrino
ν_μ	Muon neutrino
$\bar{\nu}_\mu$	Muon antineutrino
ν_τ	Tauon neutrino
$\bar{\nu}_\tau$	Tauon antineutrino
$\lvert\nu_\alpha\rangle$	Neutrino flavor eigenvector for flavor α
$\lvert\nu_i\rangle$	Neutrino mass eigenvector for mass eigenstate i
ν_L	Left-handed neutrino
$\bar{\nu}_L$	Left-handed antineutrino
ν_R	Right-handed neutrino
$\bar{\nu}_R$	Right-handed antineutrino
n	Neutron
n	Number of particles
N_T	Number of tritium atoms in the WGTS
$\mathcal{O}$	Bachmann-Landau notation (Big O notation)
p	Proton
p	Momentum
p	Pressure
p_{B1}	Pressure in the stabilized buffer vessel B1
$\bar{p}$	Mean pressure

p_{inj}	Pressure inside the IL stabilized buffer vessel
p_{Kr}	Pressure measured at the tritium+krypton injection capillary.
p_{DPS1}	Pressure behind the DPS1 TMPs
p_{eq}	Equilibrium pressure
π	Archimedes' constant
π^0	Pion, neutral
π^+	Pion, positively charged
π^-	Pion, negatively charged
$P_{\alpha\to\beta}$	Transition probability from state α to state β
P_j	Probability for a tritium molecule to be in the j-th exicited final state after β-decay
Φ	Magnetic flux
q	Flow rate
q_{feed}	Feed flow rate into the IL from the FL
q_{WGTS}	Flow rate of gas through the WGTS
q_{out}	Flow rate of outgassing
q_{loss}	Flow rate of gas from the IL lost to the DPS2 and RS
q_{imp}	Flow rate of gas from outgassing or isotopic exchange used in simulation
q_{circ}	Flow rate through the IL used in simulation
Q	Energy corresponding to the mass defect in nuclear decay
Q	Collision Integral
$\boldsymbol{r}$	Position vector
r	Rate
R	Radius of a tube
$\mathcal{R}$	Response function
ρd	Column density
$\rho d\sigma$	Column density times total inelastic scattering cross section for electrons with energies close to 18.6 keV on T_2 molecules
σ	Standard deviation
σ	Total inelastic scattering cross section for electrons with energies close to 18.6 keV on T_2
t	Time

Δt	Time difference
τ	Time constant
T	Temperature
τ^-	Tauon
τ^+	Antitauon
$\mathcal{T}$	Transmission function
θ_{ij}	Mixing angle of the PMNS matrix
θ	Mixing angle of a 2×2 neutrino mixing matrix
Θ	Heaviside function
Θ_C	Cabibbo angle
U	The PMNS matrix
$U_{\alpha i}$	Element of the PMNS matrix for flavor eigenstate α and mass eigenstate i
U_ana	Voltage applied to the analyzing plane of a MAC-E filter
v	Velocity
$\boldsymbol{v}$	Velocity vector
v_m	Most probable velocity velocity of gas particles
v_gas	Macroscopic velocity of a gas bunch
$\boldsymbol{v}$	Velocity vector
V_0	Energy of the ground state of a tritium molecule after β-decay
V_j	Energy of the j-th exicited final state of a tritium molecule after β-decay
x	First spatial coordinate
X	Element name place holder
Y	Element name place holder
z	Third spatial coordinate
Z	Atomic number

Acknowledgments

As a closing note, I would like to thank the multitude of people who have accompanied and helped me along the way during this thesis:

- Prof. Dr. G. Drexlin for giving me the possibility to do this interesting thesis work in the KATRIN collaboration, as well as for the support in all the optimization endeavors presented in this thesis.
- Prof. Dr. B. Holzapfel for evaluating this thesis as the second reviewer.
- My supervisor Michael Sturm for his relentless support in every phase of this doctoral project.
- My colleagues Florian Priester and Marco Röllig who were always willing to help with any practical questions and the banter that made working on this doctoral project several times more enjoyable.
- Beate Bornschein for the many nice discussions, scientific and otherwise, as well as her support for improvement ideas.
- Lutz Bornschein for the fun conversations as well as teaching me a lot about the practical side of super conducting magnet operation.
- Max Aker, Simon Niemes, and Carsten Röttele as fellow PhD students for sharing the experience and making the busy and trying times a lot more fun.
- Robin Größle for the many interesting scientific discussions and for sharing his wisdom about the properties of hydrogen and its isotopologues.
- Fabian Block for his cooperation in devising the column density analysis
- Magnus Schlösser, Bennet Krasch, and Genrich Zeller for their support with everything related to LARA.
- Stefan Welte and his group for their capable help in all things tritium processing and process engineering in general.
- Peter Schäfer and the TLK measurement and automation technology group for their support in commissioning the tritium loops system and always quickly implementing changes and improvement.
- Norbert Kernert for suffering with me through hours of leak testing.
- Lutz Schimpf and Caroline Rodenbeck for their help in using the E-Gun for column density measurements.
- Felix Sharipov for introducing me to the interesting topic of rarefied gas dynamics and his help in developing the model of the tritium injection line.

All of this wouldn't have been possible without the following people supporting my life outside of university:

- My family for the support in taking this path and continuing it up to this point. In particular, I would like to thank my sister Jeanette for proofreading this thesis and correcting the oh so many comma mistakes.
- My friends Lukas and Valentin for the countless hours of recreative gaming without which I would have probably burned out during the frustrating parts of this PhD project.
- My friends Florian, Krissi, and Simon for the relaxing evenings of ritualized movie/series evenings, as well as all the roleplaying weekends. In particular, I would like to thank Florian for introducing me to Python and Rust, without which I would have been lost in the hell of C++ and ROOT.

This thesis wouldn't have been possible without: